

Aging Studies of Drift Chambers of the HERA-B Outer Tracker Using CF₄-based Gases

D I S S E R T A T I O N

zur Erlangung des akademischen Grades
doctor rerum naturalium
(dr. rer. nat.)
im Fach Physik

eingereicht an der
Mathematisch-Naturwissenschaftlichen Fakultät I
Humboldt-Universität zu Berlin

von
Herrn Dipl.-Phys. Alexander Schreiner
geboren am 11.12.1968 in Frunse

Präsident der Humboldt-Universität zu Berlin:
Prof. Dr. Jürgen Mlynek

Dekan der Mathematisch-Naturwissenschaftlichen Fakultät I:
Prof. Dr. Bernhard Ronacher

Gutachter:

1. Prof. Dr. H. Kolanoski
2. Prof. Dr. T. Lohse
3. Prof. Dr. B. Schmidt

eingereicht am:	5. Juli 2001
Tag der mündlichen Prüfung:	15. November 2001

Abstract

The intense radiation environment in the HERA-B experiment, being comparable to that of LHC experiments, requires that the detector be very resistant to high radiation loads. The Outer Tracker of HERA-B consists of drift tubes folded from polycarbonate foils (honeycomb) and is operated with a CF_4 -containing gas mixture. Aging tests made in HERA-B, under hadronic irradiation, using prototype drift chambers showed a rapid rise of self-sustaining dark currents (Malter effect). Extensive aging studies were carried out with the objective to find an appropriate set of construction materials as well as optimal operational parameters. It was shown that the gain loss (anode aging) and the Malter effect could be avoided after replacing the methane in the counting gas, $\text{Ar}/\text{CF}_4/\text{CH}_4$, by CO_2 and applying cathode coating. However, other, relatively less known aging effects appeared: rising conductivity of the wire-supporting strips and wire corrosion. These two aging effects could also be prevented keeping water at a proper concentration. The aging tests showed that a too high water content (above about 500 ppm) gives rise to strip conductivity, conversely, a too low water content (below about 100 ppm) enhances anode wire corrosion. In an attempt to interpret the test results, plasma phenomena like quenching by different admixtures, production of molecular species, concentration of long-lived HF produced via CF_4 dissociation in the avalanche were semi-quantitatively estimated. This work contains also a comprehensive summary of all aging studies for the Outer Tracker and an overview of the literature on wire chamber aging, in particular with CF_4 -based counting gas mixtures.

Keywords:

drift chamber, aging, corrosion, CF_4

Zusammenfassung

Die intensive Strahlungsumgebung im HERA-B-Experiment, vergleichbar mit der von LHC-Experimenten, erfordert einen gegen hohe Strahlenbelastung sehr widerstandsfähigen Detektor. Das Äußere Spurkammersystem von HERA-B besteht aus wabenförmigen Driftröhren, die aus Polycarbonatfolie gefaltet sind und mit einer CF_4 -haltigen Gasmischung betrieben werden. Alterungsversuche, durchgeführt in HERA-B unter hadronischer Bestrahlung mit Prototyp Driftkammern, zeigten einen schnellen Anstieg von sich selbsterhaltenden Dunkelströmen (Maltereffekt). Ausgedehnte Alterungsuntersuchungen mit dem Ziel, geeignete Materialien und optimale Arbeitsparameter zu finden, wurden durchgeführt. Es wurde gezeigt, dass Verstärkungsverlust (Anodenalterung) und Maltereffekt vermieden werden konnten, nachdem Methan im Zählgas $\text{Ar}/\text{CF}_4/\text{CH}_4$ durch CO_2 ersetzt und die Kathode beschichtet wurde. Es traten jedoch andere, weniger bekannte Alterungseffekte in Erscheinung: Ansteigende Leitfähigkeit der Drahtunterstützungstreifen und Drahtkorrosion. Beide Alterungseffekte konnten ebenfalls vermieden werden, wenn eine geeignete Wasserkonzentration eingehalten wurde. Die Alterungsteste zeigten, dass ein zu hoher Wassergehalt (über etwa 500 ppm) Streifen-Leitfähigkeit verursacht, während umgekehrt ein zu niedriger Wassergehalt (unter etwa 100 ppm) die Anodendraht-Korrosion verstärkt. Um die Testresultate zu interpretieren, wurden Plasmaphänomene, wie Quenching durch verschiedene Beimischungen, Produktion bestimmter Moleküle und die Konzentration von langlebigem HF, das durch CF_4 -Dissoziation in der Lawine erzeugt wurde, näherungsweise abgeschätzt. Die Arbeit enthält außerdem eine Zusammenfassung aller Alterungsuntersuchungen für das Äußere Spurkammersystem und eine Literaturübersicht zur Alterung von Drahtkammern, insbesondere mit CF_4 -basierten Zählgasen.

Schlagwörter:

Driftkammer, Alterung, Korrosion, CF_4

Für Gruppe HERA-B Zeuthen

Acknowledgement

It is pleasure to acknowledge vital contribution of many people who have made the work on this thesis not only possible but enjoyable as well.

First of all, I would like to thank my supervisor, Prof. H. Kolanoski, who is responsible for changing my views on several important aspects of writing papers. A lot of his questions and suggestions turned out to be highly rewarding (For example, test at different humidity was his idea). I am also indebted to Gerhard Bohm for many ideas of his that have sipped into this work, in some cases without my fully realizing it. A lot of clarity of the text is due to the artistry of Mike Walter who also made invaluable work on this thesis, though of course any errors which remain are entirely my responsibility.

Many thanks to Seva Suvorov, who brought me into understanding of this interesting field of research within several weeks. He will certainly see his ideas and views represented here.

I would like to thank Michael Jablonski, Christian Stegmann and their team for the preparation of unbreakable chambers for my aging tests and also people who heavily contributed to aging studies of the OTR and thus to this paper: Andreas Schwarz, Ulrich Uwer, Marcus Hohlmann, Klaus Dehmelt, Mar Capeans, Cristobal Padilla and many others.

I am grateful also to DESY Zeuthen for the supportive and stimulating home it has given to me over the last three years.

Contents

Introduction	1
1 HERA-B experiment	3
1.1 Beam and target	3
1.2 HERA-B spectrometer	3
1.2.1 Main Tracking System	6
1.2.2 Particle Identification System	8
1.2.3 Trigger system	9
1.3 Outer Tracker	11
1.3.1 Honeycomb chambers of the HERA-B detector	11
1.3.2 Superlayer structure	14
1.3.3 Front-end electronics	15
1.3.4 Gas System of the OTR	16
1.3.5 Materials used in the OTR gas system	17
2 Drift chamber operation and gas composition	20
2.1 Principles of operation	20
2.2 Gas composition	20
2.3 Electron drift velocity in gases based on Ar/CF ₄	22
2.4 Quenching mechanism in a mixture Ar/CF ₄ and a quencher	26
2.4.1 Experimental evidence	26
2.4.2 Radiative de-excitation and photoelectron emission	27
2.4.3 Quenching of luminescence	30
2.4.4 Photoabsorption	32
2.4.5 Quenching of electronically excited atoms (molecules) in collisions	33
2.4.6 Ion-molecular reactions	34
2.4.7 Experimental definition of the mechanism limiting the maximum gain	36
2.5 Other factors for defining the gas composition	37

3	Aging processes in drift chambers	39
3.1	Introduction	39
3.2	Anode aging	39
3.3	Cathode aging	44
3.4	Outgassing of materials	45
3.5	Materials which should be avoided in the gas system	47
3.6	Formalism of the test procedure	48
4	History of aging studies of HERA-B honeycomb chambers	50
4.1	Introduction	50
4.2	First tests	51
4.2.1	Aging test with X-rays in Zeuthen	51
4.2.2	Aging test with prototypes in HERA-B	51
4.3	Aging tests with clear indications of the Malter effect	57
4.3.1	Aging test in π /proton beam (PSI I)	57
4.3.2	Aging test in a proton beam (PSI II)	58
4.3.3	Exploratory aging test with an α -beam	58
4.4	Aging tests without clear evidence of the Malter effect	59
4.4.1	Other aging tests with X-rays	59
4.4.2	Irradiation test with α -particles (Rossendorf I)	60
4.4.3	Test in 13 MeV proton beam (Rossendorf II)	60
4.4.4	Other aging tests	61
4.5	Definition of materials, production processes, operating parameters	63
4.5.1	Coating of the cathode	63
4.5.2	Tests of the glue	63
4.5.3	Choice of the mixture	65
4.6	Validation of parameters with α -beam	65
4.6.1	Second aging test in Karlsruhe (Karlsruhe II)	65
4.6.2	Third aging test in Karlsruhe (Karlsruhe III)	68
4.7	Summary	73
5	Aging tests with X-rays	75
5.1	Aging studies of 10 cm long chambers	75
5.1.1	Aging study on FR4 strips	75
5.1.2	X-ray aging tests of chambers with different cathode coatings	86
5.1.3	Conclusion	94
5.2	Aging studies of 40 cm long chambers	95
5.2.1	Introductory test	95
5.2.2	Test with a water content of 50 and 200 ppm	106
5.2.3	Aging test with straws	115
5.2.4	Test with a water content of 350 and 700 ppm	118
5.2.5	Irradiation in dry environment	125
5.2.6	Conclusion	128

6	Aging tests with an α-source	131
6.1	Introduction	131
6.2	Setup	131
6.3	Specific problems with perforated chambers	132
6.4	Detection of electronegative species produced in plasma chemistry	134
6.5	First aging tests	136
6.6	Aging tests with Ar/CF ₄ /CH ₄ and Ar/CF ₄ /CO ₂	137
6.7	Sealer paste “Sista F109” in an aging test	138
6.8	Electron microscopy and X-ray spectroscopy	142
6.9	Summary and conclusions	143
7	Aging tests with Ar/CO₂	144
7.1	Introduction	144
7.2	X-ray aging test	144
7.3	Aging test with α -source	146
7.4	Conclusion	148
8	HERA-B run in 2000	150
9	Plasma chemistry in the avalanche in Ar/CF₄/CO₂	154
9.1	Introduction	154
9.2	Dissociation	154
9.3	Production rate of fluorine species in Ar/CF ₄ /CO ₂	157
9.4	Chemistry	160
9.5	Estimation of HF concentration	163
9.5.1	Thermal convection	163
9.5.2	HF concentration	165
9.6	Concluding remarks	167
10	Summary and conclusions	169
A	Study of the eccentricity and wire tension influences on the chamber operation	173
B	Useful tests	179
B.1	Gas gain and counting characteristic in the gas Ar/CF ₄ /CO ₂	179
B.2	Gas gain in Ar/CO ₂	180
B.3	Measurement of the cathode heating	180

Introduction

One of the interesting features of nature is the different behaviours of matter and antimatter. This effect is one of the conditions of the observed absolute dominance of matter over antimatter in the big bang universe. The effect, which is known as CP-asymmetry, can be implemented in the Standard Model by a complex phase in the Cabibbo-Kabayashi-Maskawa Matrix (CKM).

A CP-symmetry violation has been observed so far only in decays of neutral kaons, where the effect is rather small and the theoretical uncertainties are relatively big, restraining a strict check of the Standard Model. On the other hand, a high statistics analysis of beauty meson decay modes, which are predicted to have a larger effect, represents a unique opportunity where data can be compared with predictions at high precision. One example of such decay modes is

$$B^0 \rightarrow J/\psi K_S$$

called *the golden decay* because of its clear signature.

At present two experiments at asymmetric e^+e^- colliders (B-factories) are running: BaBar at SLAC¹ and BELLE at KEK². They are tuned to the center-of-mass energy of $\sqrt{s} = 10.6$ GeV corresponding to the mean of the $\Upsilon(4s)$ resonance. Since the cross-section is relatively small, the collider has to provide high luminosity. Conversely, the beauty production cross section on hadronic machines is higher. However, a study of CP-asymmetry is not easier because of a very high background and requires sophisticated detectors resistant to high irradiation intensities. The HERA-B experiment was designed to study CP asymmetry in the golden decay using the proton beam of the HERA storage ring and a fixed-target spectrometer.

The production cross section of beauty quarks in hadronic interactions at centre-of-mass energies of about 40 GeV, like in HERA-B, is 6 orders of magnitude smaller than the total inelastic cross section. Furthermore, a branching ratio of the golden decay

$$B^0 \rightarrow J/\psi K_S \rightarrow l^+ l^- \pi^+ \pi^-$$

is also very small, 2×10^{-5} , resulting in a very small signal-to-background ratio of the order 10^{-11} . In order to accumulate enough statistics, the detector should

¹Stanford Linear Accelerator Center

²High Energy Accelerator Research Organisation in Japan

operate at a very high interaction rate of the order of about 40 MHz, generating an extreme radiation environment. The irradiation load of HERA-B could be compared to those of experiments at LHC³. These severe conditions impose considerable requirements on the detector: a sophisticated trigger system and a high radiation resistance of all the detector components.

One of the delicate components of the detector is the Outer Tracker consisting of honeycomb drift chambers. A functional feature of drift chamber operation is the electron avalanche multiplication involving plasma chemistry processes near very thin anode wires. Chemically aggressive species produced via dissociative processes in the avalanche react with each other forming large clusters. The clusters can deposit on the electrodes forming polymerization films, whiskers, dust, etc. Other species can chemically attack and corrode the wire.

Drift chambers are thus prone to different kind of radiation damages. The high risk of damages coming from the intense radiation in HERA-B constitutes one of the crucial problems which needs to be solved. Aging tests made in the true HERA-B environment with prototype drift chambers showed a rapid rise in self-sustaining currents. This effect was not observed up to a dose four orders of magnitude higher under X-ray irradiation. Consequently, aging effects depend on many factors and should be systematically studied. Extensive aging studies of honeycomb drift chambers were planned with an objective to find an appropriate solution for a set of construction materials which could be introduced into the gas system of the Outer Tracker as well as optimum parameters for chamber operation. This work details the test accomplishments and the obtained results in the R&D program as well as suggests theoretical models of the effects found in the process of investigation. Chapter 1 provides an overview of the detector and its components mainly focusing on the OTR design and its gas system. A semiquantitative analysis was made in chapter 2 to substantiate the choice of the mixture Ar/CF₄/CO₂ (65:30:5)⁴ as well as to describe the properties of this mixture using theoretical and experimental data as a background. The phenomenon “aging of drift chambers” and the related theory are presented in chapter 3. The R&D program presented in chapter 4 was carried out by different groups using different types of irradiation in different places before the work on this thesis started. The aging studies with descriptions of the test procedures, the results, as well as theoretical explanations of observed effects carried out in context of this thesis are detailed in chapters 5 to 7. In addition, gas parameters, aging and high-voltage problems in the Outer Tracker during the HERA-B run over the year 2000 were shortly described in chapter 8. A semi-quantitative analysis including an estimation of production rates and lifetimes of species produced in the avalanche in the counting gas with a possible influence of contaminants like oxygen or water is given in chapter 9. The important results of the aging program are summarised in chapter 10.

³the Large Hadronic Collider to be built at CERN.

⁴Denotation Ar/CF₄/CO₂ (65:30:5) means, by default, that the numbers of Ar, CF₄ and CO₂ molecules constitute 65%, 30% and 5% of the total number of molecules in the gas composition, respectively.

Chapter 1

HERA-B experiment

HERA-B is an experiment designed to study CP-violation in the B-system using the HERA¹ proton beam and a fixed-target forward spectrometer.

1.1 Beam and target

HERA, the Electron Proton Storage Ring with a circumference of 6.3 km (see fig.1.1), provides protons with energies of 920 GeV and a bunch frequency of about 10 MHz. A wire target is positioned in the halo of the HERA-B proton beam. The target scrapes the protons diffused from the beam center.

The wire target consists of two parallel sets separated by 4 cm with respect to the beam direction. At least two sets are required to insure a sufficient interaction rate and at the same time the precise measurement of B-decay length. Each set consists of 4 wires strung perpendicular to the beam forming a square around the beam.

1.2 HERA-B spectrometer

HERA-B is a fixed-target forward spectrometer designed for the efficient reconstruction of the golden decay. Fig. 1.2 shows the decay pattern of the golden decay. A scheme of the HERA-B detector is shown in figure 1.3. The spectrometer consists of a Silicon Vertex Detector (SVD), a Ring Imaging Čerenkov Counter (RICH), a Main Tracking System, a dipole magnet, a Transition Radiation Detector (TRD), an Electromagnetic Calorimeter (ECAL) and a Muon System. The Main Tracking system consists of the Inner (Microstrip Gaseous Chambers) and the Outer (Honeycomb Chambers) Trackers [47].

Because of the small b-quark production cross section and the branching ratio of the golden decay

$$\sigma_{b\bar{b}}/\sigma_{in} = O(10^{-6}), \quad (1.1)$$

¹Hadron-Electron-Ring-Anlage

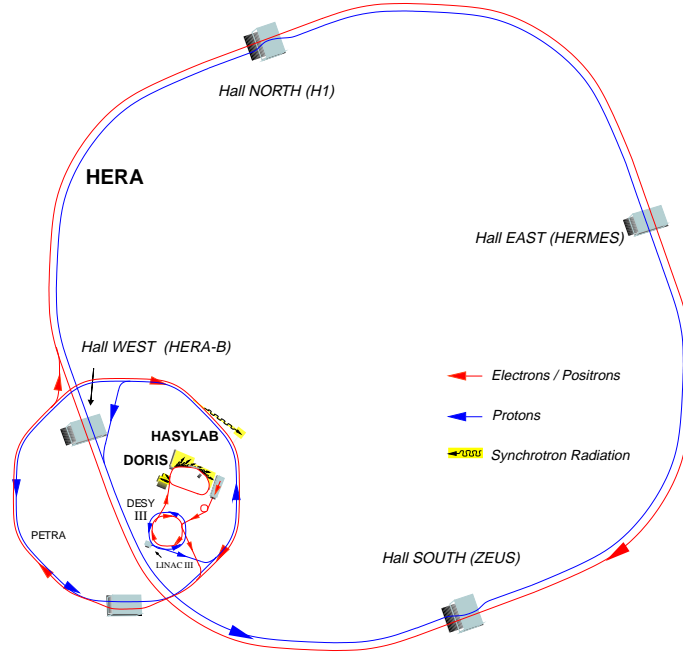


Figure 1.1: HERA storage ring at DESY. HERA consists of electron (blue inner line) and proton (red outer line) beams oppositely directed.

$$Br(B \rightarrow J/\psi K_S \rightarrow l^+ l^- \pi^+ \pi^-) \approx 2 \times 10^{-5} \quad (1.2)$$

HERA-B has to operate with an interaction rate of about 40 MHz to reach the goal of measuring CP violation. Figure 1.4 shows expected particle fluxes in HERA-B and in future LHC experiments. The lines represent a simple $1/r^2$ dependence where r is the distance from the beam. The irradiation loads are comparable for drift chambers in HERA-B and at LHC. The detector has to withstand the rather high radiation load for several years of operation.

To hold the occupancy below a limit which is acceptable for the read-out electronics, a high granularity is required. This leads to a rather large number of about 600 000 channels for all the detector components.

As can be seen in figure 1.2, the requirement of high background suppression implies that kaons and leptons are well identified, secondary vertices from B-decays are well separated from the primary. J/ψ 's of the golden decays must be identified with high efficiency in the large background. Thus a sophisticated 4-level trigger system was designed to suppress the background of hadron tracks identified with high efficiency. The fastest and very delicate first level trigger (FLT), runs on hardware processors. Using reduced data from fast links, it suppresses the background by a factor of 200 and thus provides the CPU time for the higher level triggers. Figure 1.5 shows an example of an event with four interactions at the

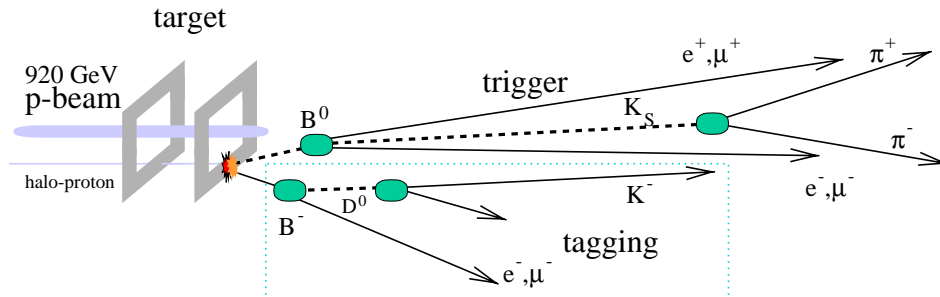


Figure 1.2: Schematic representation of the golden decay, a best candidate for the study of CP asymmetry. The decay has a clear signature and the Standard Model prediction of CP-asymmetry of this decay is very precise. The initial flavour of a triggered B needs to be determined from the other B in the event (flavour tagging).

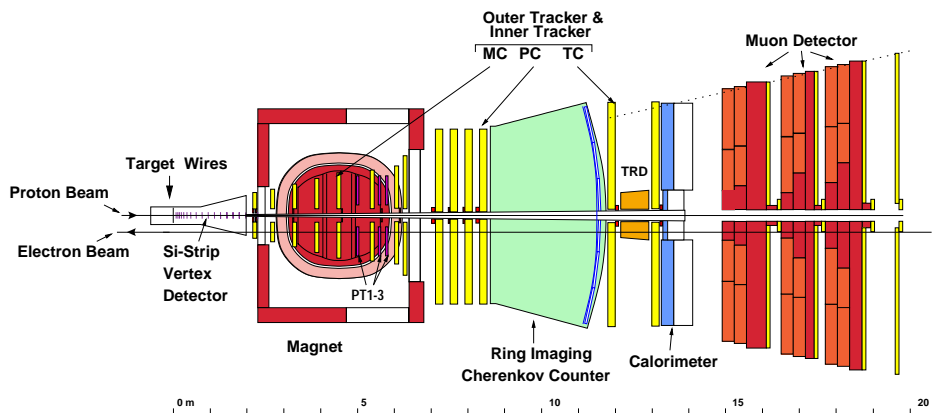


Figure 1.3: HERA-B Spectrometer. The detector should efficiently trigger and reconstruct the golden decays as well as determine (tag) the flavour of the decaying B meson. The tagging of the B flavour proceeds through an identification of the charge sign of a lepton or a kaon coming from the other B meson decay.

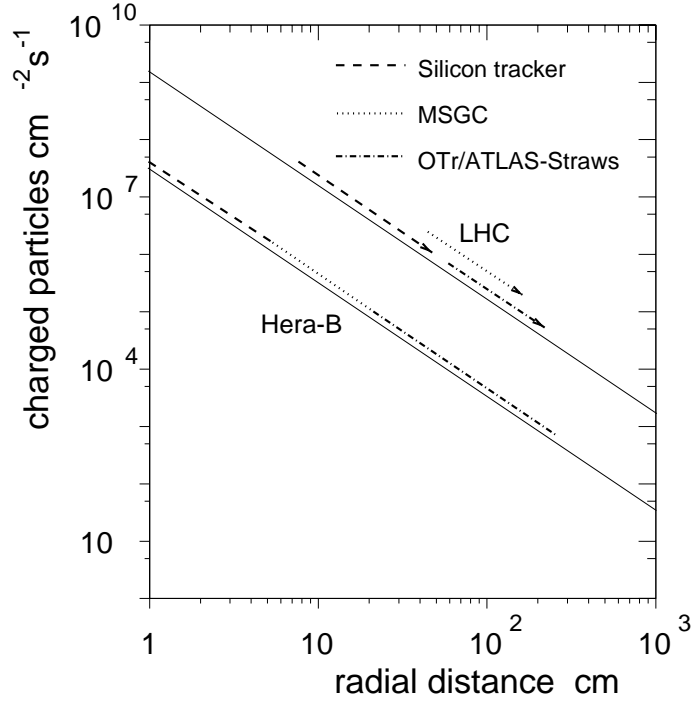


Figure 1.4: Particle flux in two experiments, HERA-B and LHC, as a function of the radial distance.

target wire (40 MHz rate) and more than 200 tracks.

In addition to the efficient reconstruction of the golden decay, the detector provides a high time resolution to be able to measure time-dependent CP violation, lifetimes and flavour mixing.

1.2.1 Main Tracking System

The Main Tracking System was designed to provide efficient track reconstruction of charged particles in a large angular range, precise momentum measurement and fast delivery of signals to the trigger system in a high rate environment.

The particle density varies with the radial distance from the beam as $1/r^2$ (see figure 1.4). Three different types of tracking technologies were used in the detector depending on the distance from the beam to limit the occupancy and the number of read-out channels. The Main Tracking System consists of:

- a Silicon Vertex Detector covering an area with R of 1 - 6 cm;
- an Inner Tracker for R in the range from 5 cm to 25 cm;

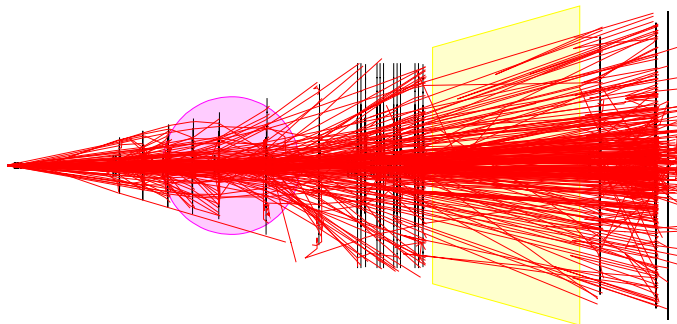


Figure 1.5: *The high mean track multiplicity per bunch crossing (BX) in HERA-B of ≈ 150 imposes particular demands on the detector: radiation hardness of its components and sophistication of the trigger and reconstruction system.*

- an Outer Tracker covering a large angular range at distances larger than 20 cm from the beam;
- a Dipole Magnet with a field integral of 2.2 T·m.

The **Silicon Vertex Detector** (SVD) has to fulfill two main requirements: 1) precise reconstruction of secondary vertices to measure life-times, time-resolved CP-asymmetry, flavour oscillation; 2) radiation hardness to withstand at least one year in the region of extreme particle densities of the order of $10^7 \text{ cm}^{-2}\text{s}^{-1}$. The SVD consists of 8 superlayers, containing four views oriented $\pm 2.5^\circ$ and $90^\circ \pm 2.5^\circ$ with respect to the vertical. One view consists of four elements with a strip pitch of $25 \mu\text{m}$. Every second strip is read out. The measured track resolution of the detector is $12 \mu\text{m}$.

The **Inner Tracker** (ITR) consists of Micro-Strip Gaseous Chambers (MSGC) combined with Gas Electron Multiplier foils (GEM). The MSGCs are made up of alkali-free glass plates coated with an 60-nm-thick amorphous carbon layer and a golden strip pattern. The strip pattern consists of $10 \mu\text{m}$ wide anode strips and $170 \mu\text{m}$ wide cathode strips with $60 \mu\text{m}$ wide gaps between them. The GEM foil was introduced to provide an additional multiplication and thus soften the main multiplication of the MSGC preventing sparking [112]. The chambers are filled with Ar/CO₂ (70:30) as a drift gas which does not react with the detector components, provides good aging characteristics and does not cause such a strong abrasion as CF₄-containing gases [112].

The **Outer Tracker** (OTR) consists of Honeycomb Drift Chambers (HDC). The OTR is used to measure tracks in a large volume and cover a wide angular range. It is described in detail in section 1.3.

High- p_T Chamber. Inner and Outer Tracker chambers are installed into the Dipole Magnet for precise momentum measurement. In addition, three High- p_T chamber stations PT1-PT3 provide a selection of high- p_T tracks. The high- p_T

pretrigger selects candidates of high- p_T tracks by their hit-patterns. All the PT stations are positioned within the magnet, PT1 between MC5 and MC6, PT2 and PT3 between MC6 and MC8 (see figure 1.3). Each PT station, covering a region of approximately 2.5 m^2 down to a distance of 25 cm from the beam insures two-dimensional reconstruction of the tracks. Depending on the distance from the beam, two different technologies of drift chambers were used. Near the beam gas-pixel chambers are installed, further away from the beam straws with “pick-up” pads. The gas-pixel chambers contain anode wires strung parallel to the beam. The straws contain printed circuits with pad patterns placed very close to or in contact with the cathode.

1.2.2 Particle Identification System

The Particle Identification System consists of:

- a Ring Imaging Čerenkov Counter for separation of kaons from pions and protons with momenta from a few GeV to 50 GeV;
- an Electromagnetic Calorimeter for separation of electrons and positrons from hadrons;
- a Muon System for muon identification in the momentum range from 5 GeV to 200 GeV;
- a Transition Radiation Detector for an additional electron-hadron separation in the momentum region from 5 to 150 GeV in the area of high particle density near the beam.

The **Ring Imaging Čerenkov Counter** (RICH) consists of a *radiator*, *mirrors*, and *photo multiplier tubes* (PMT). The radiator is a big tank filled with C_4F_{10} (Freon). The operation of the RICH is based on the Čerenkov effect. A charged particle traveling in a substance with a velocity \vec{v} higher than the velocity of light in this substance radiates light in a cone. The mirrors focus the emitted light into a circle on the focal plane, where PMTs are positioned. From the radius of the circle the velocity v is determined.

The **Electromagnetic Calorimeter** (ECAL) should fulfill the following objectives:

- detection of electrons, positrons and photons as showers and separation from hadrons;
- measurement of their energies in the region from 5 GeV to 200 GeV;
- providing a fast signal for the trigger of J/ψ decay candidates.

The ECAL has a geometrical acceptance of 68% for an electron coming from the golden decay. The ECAL consists of three sections with varying granularity to reduce the occupancy and the number of channels. The calorimeter is made up

of alternating layers of absorber and scintillator with wavelength shifter fibers (WSF) running perpendicular to the layers of absorber and scintillator (“Shashlik” arrangement). The WSFs are connected to the PMTs positioned behind the modules.

The **Transition Radiation Detector** (TRD) should improve the electron and hadron separation in a region of high particle density close to the beam between the RICH and the ECAL. It is based on Kapton straws embedded in a polypropylene fiber radiator. Given a number of sensitive layers of 32, a pion rejection factor of more than 10 can be reached.

The straws were also used in aging tests of the OTR as described in section 4.6.1. They have a cathode tube with a diameter of 6 mm of a specially prepared Kapton foil:

- $2 \times 18\text{-}\mu\text{m}$ -thick Kapton (polyimide) foil for mechanical robustness;
- $6\text{-}\mu\text{m}$ -thick welding layer made up of polyurethane composite;
- $2 \times 0.2\text{-}\mu\text{m}$ -thick aluminium layer to increase conductivity;
- $2 \times 4\text{-}\mu\text{m}$ -thick polyimide foil enriched with carbon.

The anode is a gold-plated tungsten wire with a diameter of $50\text{ }\mu\text{m}$.

The **Muon System** (MS) detects muons in an energy range from a few GeV to 200 GeV and is included in the fast trigger to select muon pair candidates from the J/ψ decay. The MS consists of four superlayers of drift chambers interleaved by absorber layers made up of armoured concrete and steel. Each superlayer is made up of: pixel chambers covering the area between 14 and 40 cm from the beam; drift tube or pad chambers covering the area in the outer region.

The pad chambers are introduced to reduce the occupancy in the region of high particle density near the beam. A drift cell ($9 \times 9\text{ mm}^2$) of a pad chamber is formed by a 30-mm-long sense wire surrounded by four potential wires (all wires are directed along the z-axis).

A drift tube chamber consists of 2×16 cells with a rectangular profile ($15 \times 12\text{ mm}^2$). Two layers of the cells are needed to obtain an overall efficiency of the chamber of more than 99% providing a trigger efficiency greater than 95%. The chambers are filled with the gas $\text{Ar}/\text{CF}_4/\text{CO}_2$ (65:30:05) (the same as in the Outer Tracker) to ensure good aging characteristics and a short electron drift time.

1.2.3 Trigger system

HERA-B was designed to operate at a very high interaction rate to accumulate enough statistics. The combination of a tight bunch spacing and a high track multiplicity in HERA-B results in an enormous data flow that could not be entirely stored on tape. Before logging, the data should be transferred through a filter reducing the original rate of 10 MHz to tens of Hz. This is only reachable using fast modern electronics and well concerted cooperation of the Data Acquisition System and the Trigger System.

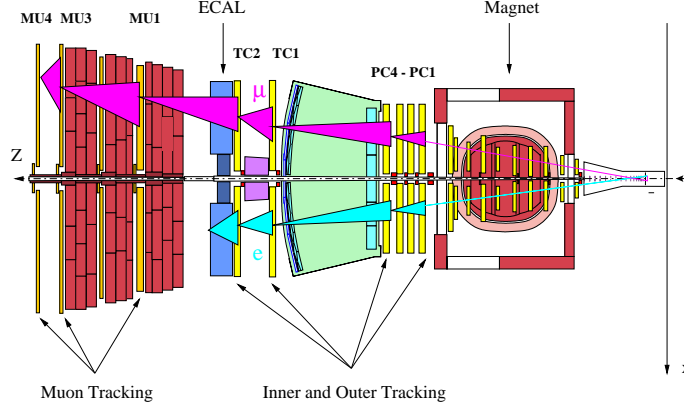


Figure 1.6: *Basic method of the FLT operation.*

The trigger was organized in four levels being mainly aimed on selection of the following decays:

$$B^0(\bar{B}^0) \rightarrow J/\psi + X \rightarrow l^+ l^- + X$$

However the trigger can be reconfigured to select other decay channels. Conventional configurations and performances of each level of the sophisticated Trigger System are summarised in the following:

The **pretrigger** identifies electrons as high- p_T clusters in the ECAL, muons as coincidences in the muon chamber pads and high- p_T tracks as corresponding patterns in the high- p_T chambers. The track parameters (first estimate) of candidates are transferred to the first level trigger.

The **First Level Trigger (FLT)**, running on the hardware processors (Track Finding Units), at first determines the Regions of Interest (ROI) for every candidate identified by the pretrigger (see fig1.6). Then, the FLT searches a hit in the next tracking chambers using a Kalman algorithm. The information for the FLT comes from the superlayers PC1, PC4, TC1, TC2, Mu1, Mu3, Mu4 via fast links. Estimating coordinates and angles of tracks deflected by the magnet, the FLT quickly calculates the momentums of the particles using look-up tables (it is assumed that the tracks originate near the target). Afterwards, the FLT estimates invariant masses of lepton pairs (in different combinations but with opposite charges) notifying the second trigger level if any invariant mass lies in the J/ψ region. Given the input event rate of 10 MHz, the FLT trigger should be very fast. It is aimed to reduce the event rate approximately 200 times.

The **Second Level Trigger (SLT)** should reduce the event rate approximately 100 times to a level of 50 kHz. It refits the tracks more precisely using more superlayers and, also, the drift time information for the ROIs. A narrower cut is applied on the invariant masses. The SLT also extrapolates tracks into the vertex detector where it reconstructs the primary and the secondary vertices and

Trigger level	Pretrigger	FLT	SLT	TLT	4LT
input	10 MHz	10 MHz	50 kHz	500 Hz	50 Hz
latency	1 μ s	10 μ s	7 ms	100 ms	4 s
reduction	1	200	100	10	2.5

Table 1.1: *The performance of the HERA-B trigger levels.*

can apply cuts on vertex separations. If a secondary vertex is found, the event is directly transferred to the forth level trigger. The first two trigger levels FLT and SLT are supposed to ensure the total background suppression for the golden decays.

Switching and buffering is implemented on SHARC cluster boards, the SLT farm is running on 240 Pentium II PCs, on which also the third level trigger is implemented.

If any event is accepted, the whole event data (not only from ROIs) are assembled in one node of the SLT farm for further processing on the higher trigger levels.

The **Third Level Trigger** (TLT). The design and the role of the third level trigger is under study. Supposedly, it will run on typically 20 % CPUs of common SLT/TLT farm PCs. The TLT is now considered to extend physics in HERA-B with non- J/ψ events and additionally suppress the background for some event classes which can not be sufficiently reduced by the SLT.

The **Fourth Level Trigger** (4LT) should perform: full online event reconstruction, event classification, filtering (with an event rate reduction from 50 Hz to 20 Hz), data logging and archiving, data quality monitoring (DQM), preparation of data for calibration and alignment (CnA).

The 4LT runs on 200 CPUs in 100 dual-CPU PCs with 256 MB SDRAM each, which allows to buffer tens of events.

The performance of the trigger levels which could be represented by the rate reduction factor and by the latency (time allocated for one event) is summarised in table 1.1.

1.3 Outer Tracker

1.3.1 Honeycomb chambers of the HERA-B detector

The high rate environment in HERA-B imposes particular demands on the chambers:

- small cell diameters to limit the occupancy;
- good aging characteristics to survive several years of operation;
- drift time shorter than 96 ns to avoid piling-up of signals from different bunch crossings;

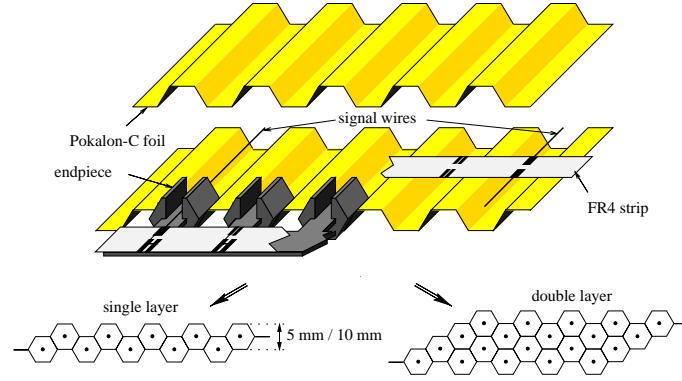


Figure 1.7: *Structure of honeycomb chambers used in the Outer Tracker.*

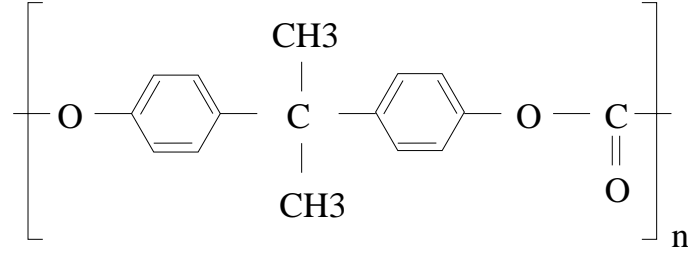


Figure 1.8: *Chemical formula of polycarbonate.*

- cheap and modular construction;
- a stable self-supporting structure and a minimum of material in the sensitive volume.

The OTR Honeycomb Drift Chambers (HDC) filled with a fast CF_4 -based gas mixture fulfill all these needs. The structure of a HDC module is shown in fig.1.7.

The cathode is a polycarbonate foil (the chemical formula of polycarbonate is shown in fig. 1.8) loaded with 6% carbon (Pocalon-C) for conductivity. In order to prevent the Malter effect (see section 3.3), the foil is covered with copper and gold (40/50 nm). The anode is a gold-plated tungsten wire with a diameter of 25 μm . The wires are supported by FR4 strips which are placed approximately every 50 cm along the cells. They are soldered to the FR4 strips (while the cells are still open) with a precision of 50 μm . End-pieces made up of Noryl are placed at the ends of the cells to provide a mechanical robustness and to support external FR4 strips. The end-pieces have openings for gas circulation. The gas is exchanged by laminar flow, diffusion and convection caused by temperature differences. To increase the gas flow through the cells, the gas flow in the box outside the cells is

blocked. As opposed to straw tube detectors, there is no individual gas supply to every cell.

The chambers are operated with an Ar/CF₄/CO₂ (65:30:5) gas mixture which provides short electron drift times (less than bunch spacing of 96 ns even in 10 mm chambers) and relatively good aging characteristics.

The operational parameters of the chambers are summarised in the table 1.2.

parameter	value
gas	Ar/CF ₄ /CO ₂ (65/30/5)
part. flux	10 ⁵ cm ⁻² s ⁻¹
charge/year	0.6 C/cm
flow	1 box vol/h

Table 1.2: *Working parameters of the OTR honeycomb chambers.*

The charged particle flux in HERA-B of approximately 30 MHz/r² (fig.1.4) restricts the dimensions of the cells of the honeycomb chambers. Both the cell diameter and the cell length should be small enough to limit the occupancies. In order to restrict both the number of channels and the occupancies, the cell diameter in the most exposed sections is 5 mm and further outside 10 mm. In addition, occupancies were also reduced subdividing the superlayers into smaller sectors. Some chambers near the beam have a reduced active area. Signals from the active area are transmitted to the external read-out by means of 75- μ m-thick Cu/Be wires (the gas amplification in the area with a thick anode is negligible).

Standard HERA-B OTR honeycomb modules with 5 mm cells have four layers of 32 cells each (see fig. 1.7). Modules with 10 mm cells have 2 or 4 layers of 16 cells each. To increase the effective surface conductivity as well the mechanical robustness, each module is covered on both sides with 100 μ m thick Al-foils. In addition, the modules are longitudinally strengthened with several carbon fiber roads with a diameter of 2 mm to reduce the danger of module buckling. In the box the modules are mounted on aluminium base plates.

In total the OTR consists of about 1000 modules covering an area of ≈ 1000 m² and representing 115000 channels.

Chamber production

Folding of a foil is carried out using the technique described in [5].

Tempering. The folded foil is placed between two accurately machined metal templates with half-hexagonal relief geometry. After the foil is kept between two templates at the temperature of up to 150 °C for 20 minutes it exactly copies the form of the templates.

Coating with a 50 nm thick copper layer followed by coating with a 40 nm thick gold layer are performed using a new method “arc enhanced thermal evaporation technique” [48].

Assembly. Before the modules could be produced, about 1200 foils of 1 m length and 30 cm width have to be prepared in the following steps. The foils are cut and thoroughly checked: the angle of the folded foil should be correct, there are no scratches on the coating, the surface is clean. Then, the first foil layer is placed into the clean template with the same relief as for the tempering and fixed by vacuum. It should be noted that the template is prepared by applying a thin uniform layer of anti-contact paste to avoid the adherence of the foil to the template. After the glue is applied on the FR4 strips, they get fixed on the template with special pins. Then, the strips are precisely aligned under a microscope and kept straight during curing of the glue. Later, when the glue is cured wires are strung one after another at a tension of 50 ± 3 g. The wire position is determined by the slit in the FR4 strip (Therefore, the correct alignment of FR4 strips is of great importance). After the final check of wire positions with magnifying glasses, the wires are soldered to the strips. After soldering it is checked that no wire is sticking out of the soldering point, the solder point is round and smooth. Afterwards, the tension of all wires of the layer is measured. If some wire tension is not in the tolerance region it is replaced. In the next step, the layer is cleaned of dust with a vacuum cleaner. Cleaning is followed by a HV stability test. The maximum dark current at 2000 V should not exceed 30 nA. Subsequently, end-pieces are glued into the foil at both ends. A second prepared foil is placed on top of the first one. This procedure continues until a single (double) layer is completed. After the top template is removed, the fiber roads are glued to the top and the bottom foils. Next, the aluminium foil is glued on both sides of the layer using a special method allowing the different material elongations due to temperature changes (see [16] for more details). The module production finishes with the soldering of HV boards to the module.

Great attention was paid to the cleanliness of the room where the modules were produced. Caps, special shoes, and latex gloves were worn by all the personnel working in the room.

After modules were completed a high-voltage training was performed followed by the gain uniformity check along some wires with ^{55}Fe . Unstable wires were trained again and disconnected if the procedure was not successful, shorts were repaired or disconnected. A similar quality check was implemented during superlayer assembly. On the average, less than 1% bad wires were detected during these check procedures.

1.3.2 Superlayer structure

The main objective of the Outer Tracker is the measurement of tracks of charged particles in a large volume and in a large geometrical acceptance, down to a distance of 20 cm from the beam. The Outer Tracker consists of 13 superlayers (see figure 1.9) which are able to measure the track coordinates [15]. In general, a superlayer consists of 3 stereo-layers with modules positioned at 0° , $\pm 5^\circ$ with respect to the vertical. This construction allows to reconstruct two coordinates of a track.

Seven superlayers MC1-MC6, MC8 are placed after the SVD within the mag-

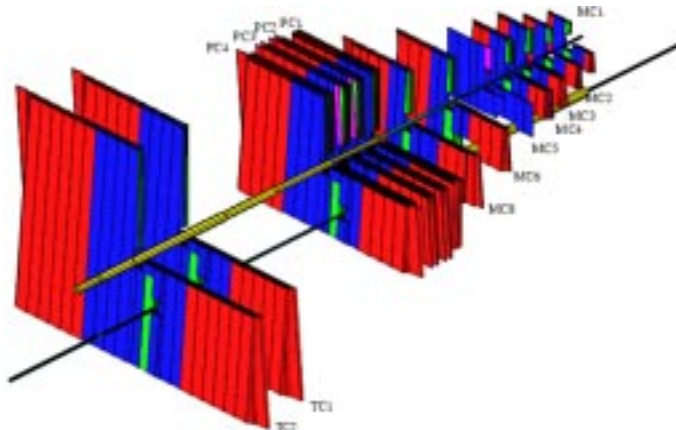


Figure 1.9: *OTR superlayers.*

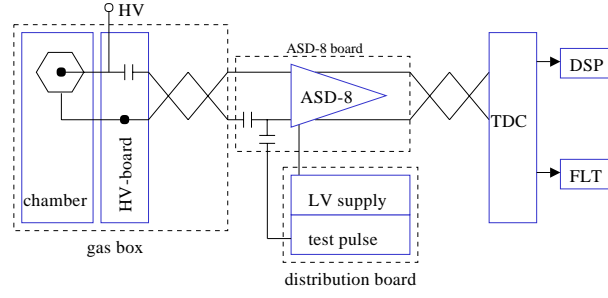
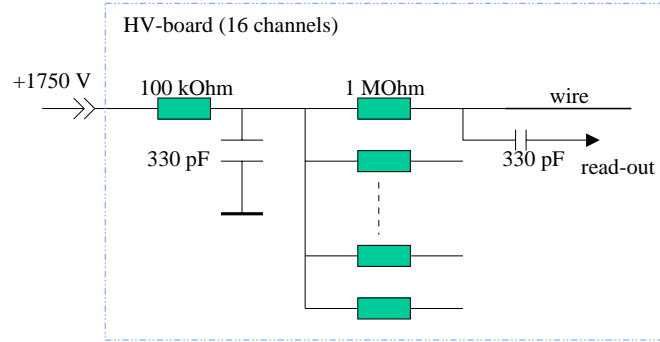
net. They allow reconstruction of curved tracks and improve momentum resolution. Four superlayers PC1 - PC4 are placed between the end of the magnet and the RICH. They provide data for the pattern recognition of straight tracks for higher level triggers and for the online and offline analysis. TC1 and TC2 placed between the RICH and the ECAL are used for extrapolation of tracks to the ECAL and muon chambers. They are included into the First Level Trigger together with chamber PC1 and PC4. The size of the superlayers increases when increasing z , from $0.9 \times 0.6 \text{ m}^2$ as for MC1 to $6.5 \times 4.6 \text{ m}^2$ as for TC2.

Each superlayer is divided into two independent halves. This allows to move them away from the beam pipe for a better access. The superlayer modules are contained in a big box filled with the counting gas.

1.3.3 Front-end electronics

A single channel of the OTR front-end electronics is shown in fig.1.10. The readout is based on the ASD-8 chip which contains eight channels with an Amplifier, a Shaper and a Discriminator each (ASD) [7]. A signal from a wire is transferred via a HV-board and a twisted pair cable to an ASD-8 board. The outputs of ASD-8 boards are connected via 5 to 10 m long shielded twisted pair cables to the time-to-digital converters (TDC). These digitize the arrival time of the pulse in 0.5 ns bins delivering 8 bit output. Digital data from the TDC are transferred to a Digital Signal Processor (DSP). From superlayers PC1, PC4, TC1 and TC2 data are also transferred via Trigger Link Boards (TLB) to the FLT.

The HV-board distributes the high-voltage to a group of 16 wires and connects the wires with the inputs of amplifiers via coupling capacitors (see fig 1.11). The HV-boards are placed at the end of each module within the gas box. The electrical connections from the “outer” HV-supply and read-out to the “inner” HV-boards is realized through feed-through boards.

Figure 1.10: *Front-end electronics of the OTR.*Figure 1.11: *Electrical scheme of the HV-board.*

The signal from a wire is read out by an ASD-8 chip, originally developed by the University of Pennsylvania for drift chamber applications in a high rate environment at SSC experiments. It meets the following requirements: low cost per channel, small rate dependence, fast signal shaping, low cross talks, radiation hardness, high integration density, precise timing, low power consumption.

Besides in the OTR, the chips find applications in other HERA-B subdetectors: in the RICH, in the Muon System and in the High- p_T Chambers.

1.3.4 Gas System of the OTR

The OTR counting gas must be fast to avoid piling-up of signals from different bunches. An admixture of CF_4 fulfills the requirements but makes the gas also rather expensive. Therefore, a closed gas system with a purification system can considerably moderate expenses. Besides gas purification, the OTR gas system mixes the gas, pumps the gas through the chambers, controls the flow, regulates the gas mixing and quantitatively analyses the gas composition (including also small impurities).

A scheme of the gas system is shown in fig.1.12. From two 450-liter tanks, one filled with liquid argon and another with liquid CO₂, and from a 600-liter tank filled with CF₄ the components flow into a mixer reservoir in regulated fractions. The allowed variation of the gas composition is 65 ± 0.7 , 30 ± 0.6 and 5 ± 0.3 for Ar, CF₄ and CO₂, respectively.

Being mixed, the fresh gas flows into a store tank which is also filled with the “impure” gas coming from the chambers. The addition of fresh gas during the HERA-B run in 2000 was about 1% per hour. Before being introduced into the drift chambers, the gas is purified from oxygen and water by the catalyst R3-11G and by the mole-sieve 3A (K₉Na₃ [(AlO₂)₁₂(SiO₂)₁₂]_y H₂O), respectively. Water decontamination also effectively occurs in the oxygen purifier [50]. The oxygen purifier can purify the mixture for about ten days keeping the oxygen content below 200 ppm and water content below 20 ppm (however, leaks can considerably increase the concentration of atmospheric contaminants as was observed during the run in 2000). Then, the oxygen purifier has to be regenerated, which takes about three days [50].

The gas system keeps the gas pressure by 0.3-0.6 mbar higher than atmospheric pressure. In case of a dangerous increase or a decrease in the pressure, safety valves connect a tank with pre-mixed counting gas to the gas system preventing entry of air into the chambers.

The gas analysis chain consists of a Gas Chromatograph (GC), a hygrometer, a monitor chamber (drift tube) and an oxygen analyzer. Program controlled, the analysis chain is sequentially connected to the common input and to the outputs of each half-superlayer of the OTR. The levels of nitrogen, oxygen and water are required not to exceed 1000, 200 and 500 ppm, respectively [39].

1.3.5 Materials used in the OTR gas system

The materials used in the chamber and box production as well as plumbing are summarised in table1.3. An extensive R&D program showed that such materials like gas, cathode foil, glue strongly influence the chamber aging characteristics. The selection of these materials was defined by aging test results described in chapter 4. The use of a gold-plated anode wire suppresses the anode aging considerably as mentioned in section 3.2. The use of FR4 (G10) in the OTR (feed-through boards, wire-supporting strips, HV boards) is unavoidable. The presence of FR4 in the gas system is “probably OK” according to [58] with the indispensable condition that the FR4 board has a surface cleaned off the possible silicon contamination. In another test, see [46], no outgassing was observed from a FR4 printed circuit board. Metallic tubing like, for example, stainless steel tubing does not have such a high outgassing as a plastic tubing and is non-transparent to air components.

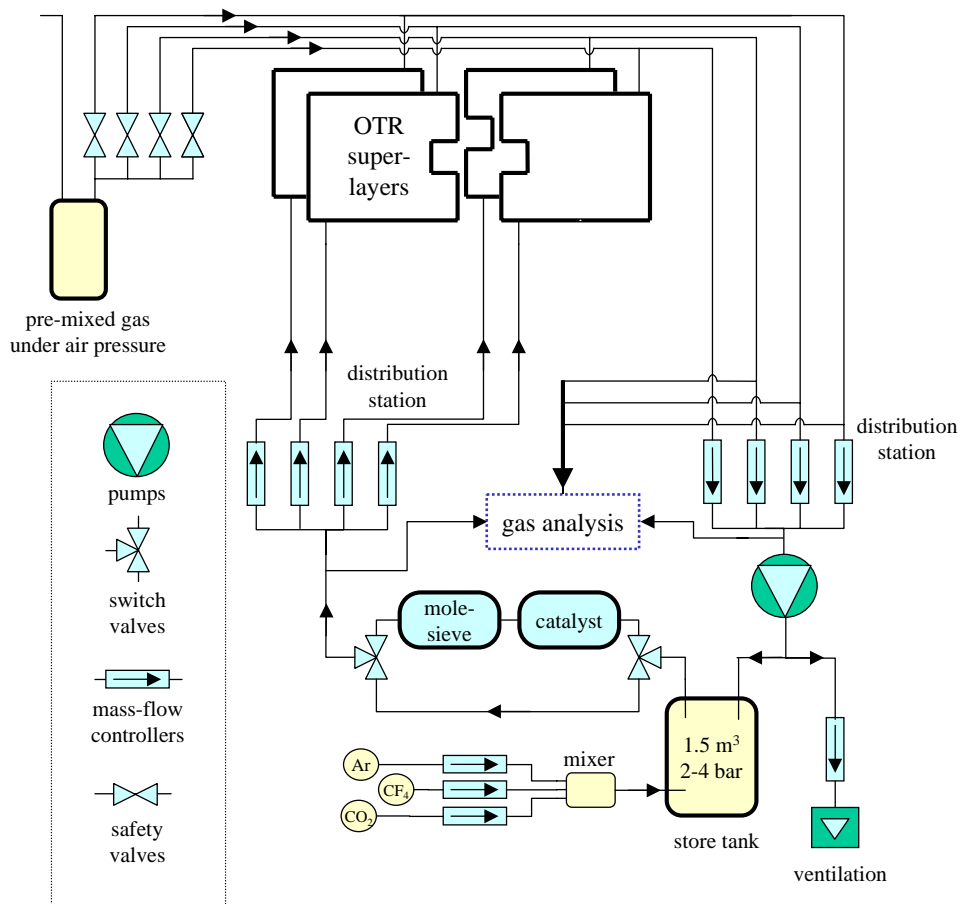


Figure 1.12: *Gas system of the OTR.*

Chamber Construction		
Item	Material	Producer
cathode	75 μm thick Pokalon-C ^a foil covered with Cu (50 nm) and Au (40 nm)	LONZA (coating by APVV, Essen)
signal wire	25 μm gold-plated tungsten wire gold content 6%	California Fine Wires
thick wire	75 μm Cu + Be wire	Little Falls Alloys
end-pieces	Noryl (polyphenylene ether) ^b	
wire support strip	FR4 (G10) ^c	NELCO
solder tin	FLUITIN Sn60Pb DIN1707 F-SW32 DIN8516 ^d	Küppers Metallwerk GmbH
glue	Stycast 1266 A and Catalyst 9 ^e	Emmerson & Cummings
conductive glue ^f	E-solder 3025 A+B	IMI
aluminium cover foil	100 μm thick Al-foil	
carbon fiber roads	carbon fiber composite	
base plates	FR4	
Box Construction		
Item	OTR Materials	Aging Test Materials
frame	stainless steel	aluminium
glue	the same as in chamber production	the same as in chamber production
windows	not in design	100 μm thick aluminized Mylar foil and (or) 70 μm thick Kapton foil
walls	MC: carbon fiber plates PC: carbon fiber honeycomb TC: glass fiber honeycomb	not in design
superlayer caps	carbon fiber	not in design
feed-through boards	FR4	FR4
Gas System		
Item	Material	Producer
gas	Ar/CF ₄ /CO ₂ (65:30:5) ^g + 300 ppm H ₂ O	Ar: MESSER, CO ₂ : Linde Gas, CF ₄ : AIR PRODUCTS
HV-board	FR4 circuit boards	assembly in Ljubljana, Slowenien
connectors	polyester with an addition of glass type "Scotchflex"	3M
wire connection to HV board	pretinned Cu-wire	Wanit GmbH
twisted pair cable	PVC insulation	Lemo
non-flexible tubes	stainless steel	Dockweiler (Hamburg)
flexible tubes	stainless steel	Swagelok
tube connectors and valves	stainless steel	Swagelok

^aPokalon-C is based on polycarbonate (polymerized bisphenol A) with an addition of 6% C (soot), the chemical formula of polycarbonate is shown in fig.1.8.

^bNoryl is prepared by oxidative coupling of phenylene oxide monomer (C₆H₅)₂O using oxygen and a copper-based catalyst. The polymer is blended with polystyrene to produce a high-strength, moisture-resistant engineering plastic.

^cFR4 is based on glass fiber laminate, matrix epoxy resin, modified with bromine derivatives to lower inflammability.

^dTin contains 3.5% halogen free flux.

^eThis glue was used since the middle of 1998. Araldite AW-106 (modified epoxy resin based on bisphenol A) and hardener HV953V produced by CIBA-GEIGI were used before the middle of 1998 in aging tests described in chapter 4.

^fThis glue was applied for a good electrical contact between foils.

^gThe documented impurity of the gas is approximately 5 ppm.

Table 1.3: *Materials used in the Outer Tracker gas system and in aging tests (according to [16, 9, 107]). Materials used in the chamber construction and in the gas system in aging setups were mostly identical to those used in the OTR (an exact list of included materials is given in the descriptions of every particular aging test). However, the boxes used in the aging tests differed from the OTR half-superlayer boxes. See section 3.6 for the explanation.*

Chapter 2

Drift chamber operation and gas composition

2.1 Principles of operation

The principle of drift chamber operation is shown in fig.2.1. A charged particle crossing a drift chamber ionizes the gas along its track. The electrons drift along the electric field lines to the anode and are multiplied in an avalanche process close to the wire due to the high field. Movement of ions and electrons induces a current on the wire, which is read out at the end of the wire by an amplifier. The output signal from the amplifier triggers a discriminator. After discrimination of the signal, a Time-to-Digital Converter (TDC) digitizes the arrival time of the pulse, i.e. the drift time of the electrons from the place of ionization. The drift time is then converted to a distance through a space-time relation (rt-relation).

The electron drift velocity, the detection efficiency, the stability of operation and the aging characteristics strongly depend on the counting gas. A semiquantitative estimation of the counting gas properties can be very helpful in the choice of gas components. A discussion of gas properties is given in the sections below.

2.2 Gas composition

A choice of components for the gas mixture should be made following the requirements imposed by the given experiment. There is no unique solution which fulfills all the possible demands. An optimum set of parameters should be found for every specific case.

The Outer Tracker should: provide data for efficient reconstruction of tracks in a large volume with a good precision, cope with the high event rate, stably operate at high gain for a long time.

Consequently, the gas should:

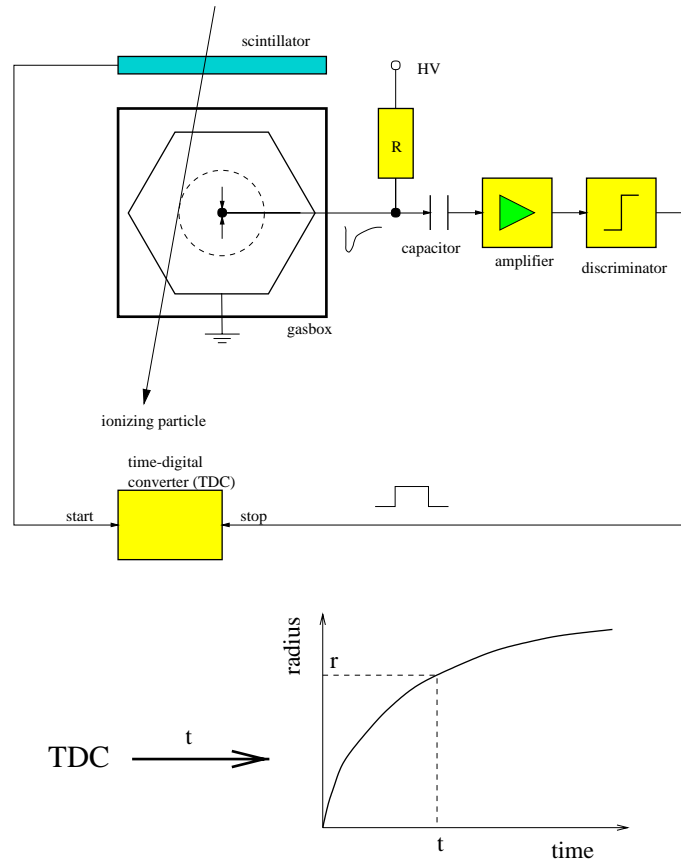


Figure 2.1: *Principle of drift chamber operation. The electron drift time is measured and converted to a distance from the anode wire through a space-time relation (rt-relation).*

- be not too expensive to be circulated in the OTR chambers (however, if it is necessary, people operate even with Xe);
- be fast, with electron drift times not exceeding the time period between bunches (96 ns) in 10 mm chambers;
- have a low electron diffusion constant affecting the resolution;
- provide good aging characteristics for the chambers;
- it should be non-inflammable, non-corrosive and non-poisonous.

As will be shown in the following section, gases based on Ar/CF₄ have high electron drift velocity. Section 2.4 details the need for addition of a third gas, which is referred to as a quencher. As will be shown in chapter 4, hydrocarbon-containing mixtures cause rapid aging processes in the chambers, which were not observed when CO₂ was used as a third component. It might be useful to analyze semiquantitatively properties of an Ar/CF₄-based gas including admixtures of CO₂ or other gases.

2.3 Electron drift velocity in gases based on Ar/CF₄

An Ar/CF₄-based gas was chosen for the OTR because of its high electron drift velocity. The only known mixtures fast enough to provide drift times less than 96 ns in 10 mm chambers are those containing CF₄.

The high electron drift velocity in CF₄-based mixtures, which could also contain a large fraction of a gas without dipole or quadrupole moments (like Ar, Xe, CH₄, etc), is a result of a combination of two effects which are described below.

The electron drift velocity w is a function of the electric field E , the concentration N and the momentum transfer cross section¹ σ_m .

To calculate the electron drift velocity, one should know the electron energy distribution function. Under the assumption that all electrons have the same energy ϵ_0 , it is easy to deduce a simplified formula for w :

$$w = \frac{Ee}{\sigma_m(\epsilon_0)N} \frac{1}{\sqrt{2m\epsilon_0}} \quad (2.1)$$

where e and m are the electronic charge and the electronic mass, respectively.

The momentum transfer cross section for CF₄ has a very deep minimum of 1.1×10^{-17} cm² at electron energies of around 0.13 eV [74] as shown in fig.2.2. This quantum effect, known as the Ramsauer effect, occurs when the de Broglie wavelength of a moving electron becomes similar to the size of the collision molecules. Furthermore, the rotational excitation cross section of a CF₄ molecule is expected to be small because of the absence of dipole and quadrupole moments [12]. The

¹Momentum transfer cross section is the total elastic cross section obtained by integrating the differential elastic cross section over all angles weighted by the factor $(1 - \cos \theta)$.

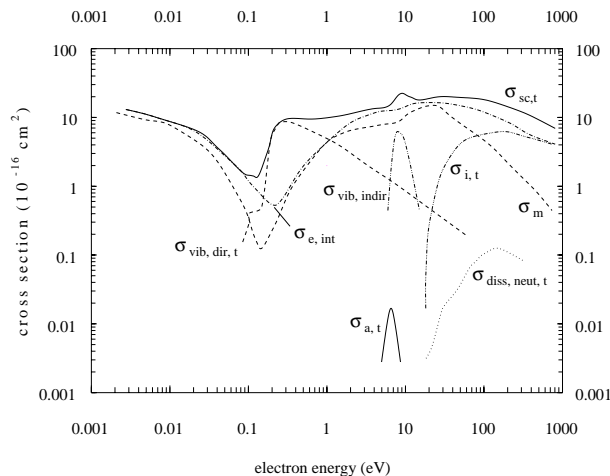


Figure 2.2: *Electron impact cross sections for CF_4 [22] where $\sigma_{sc,t}$ is the total scattering cross section, σ_m is the momentum transfer cross section, $\sigma_{e,int}$ is the total elastic scattering cross section, $\sigma_{vib,dir,t}$ is the total cross section for vibrational excitation, $\sigma_{vib,indir}$ is the indirect electron scattering cross section through the negative ion resonances, $\sigma_{i,t}$ is the total ionization cross section, $\sigma_{a,t}$ is the total electron attachment cross section, $\sigma_{diss,neut,t}$ is the total cross section for production of neutral species.*

large vibrational excitation cross section, which increases rapidly in the energy region around 0.15 eV when increasing the electron energy [11, 8] leads to high losses of the electron energy. This increase occurs due to the excitation onset of the asymmetric stretch mode ν_3 . The very strong inelastic scattering peaking at 0.25 eV keeps the electron energy low, slightly above the gas thermal energy unless a rather high electric field is applied [94]. The electron drift velocity is high only if electron energies lie near the Ramsauer minimum.

In fact, such a deep Ramsauer minimum also exists in argon, being shallower in other gases without dipole and quadrupole momenta as summarised in table 2.1. However, the effect constraining the electron energy around the Ramsauer minimum is not so pronounced because the inelastic scattering cross sections in these gases increase not so rapidly as in CF_4 when increasing the electron energy (see, for example, [31] and [32] for CH_4 and C_2H_6 , respectively). Since the inelastic scattering cross section is very small in argon at low energies [78], the mean energy of a free electron in a drift chamber near the cathode is 5-6 eV, far beyond the Ramsauer minimum. An addition of CF_4 to argon results in cooling down the free electrons to energies near the Ramsauer minimum leading to a strong increase in the electron drift velocity [23].

A small addition of CH_4 as a quencher (the quencher effect is described in the next section) does not lead to such a strong reduction in the electron drift velocity as that of CO_2 [13], because: 1) the Ramsauer effect occurs in CH_4 ; 2) it occurs

gas	$\sigma_{m,min} (\times 10^{-17} \text{ cm}^2)$	$\epsilon(\text{eV})$	ref.
CF ₄	1.1	0.13	[74]
Ar	1.5	0.3	[41]
Kr	6	0.6	[41]
Xe	15	0.7	[41]
CH ₄	10	0.2	[31]
C ₂ H ₆	10	0.13	[32]

Table 2.1: Momentum transfer cross section and electron energy corresponding to the Ramsauer minima in different gases. Gases H₂O and CO₂ are not presented here since the Ramsauer effect is not pronounced in them (the Ramsauer effect occurs when the molecules have zero dipole and quadrupole moments).

gas	Ar	CF ₄	CO ₂	CH ₄	N ₂	O ₂	H ₂ O
$\sigma_m \times 10^{-17} \text{ cm}^2$	2	1.3	400	12	70	50	1700
reference	[41]	[74]	[13]	[31]	[101]	[70]	[22]

Table 2.2: Momentum transfer cross sections of different gases measured at the electron-impact energy of 0.13 eV, the mean electron energy in the counting gas Ar/CF₄/CO₂ (65:30:05) at a distance 2.5 mm from the wire (which is calculated using the Magboltz-2.2).

in the same energy region as in CF₄ and Ar.

A semiquantitative estimation using formula (2.1) already shows the influences of different species on the drift velocity in the OTR drift chambers filled with Ar/CF₄/CO₂ (65:30:05). A calculation using Magboltz-2.2 program shows that the electron temperature in nearly the whole volume of honeycomb chambers filled with Ar/CF₄/CO₂ (65:30:05) is not much higher than the gas temperature and roughly equals 0.13 eV at a radius of 2.5 mm. The momentum transfer cross sections of different gases measured at the electron-impact energy of 0.13 eV are shown in table 2.2. The momentum transfer cross section for a mixture is the weighted mean of the momentum transfer cross sections for the mixture components. For Ar/CF₄/CO₂ (65:30:05) the momentum transfer cross section can be estimated to be $2.2 \times 10^{-16} \text{ cm}^2$. Using formula (2.1) for the electric field of 1.3 kV/cm (field at the radius of 2.5 mm), we obtain w to be approximately 150 $\mu\text{m}/\text{ns}$, while the Magboltz calculation yields 90 $\mu\text{m}/\text{ns}$. This shows the validity of (2.1) as an order of magnitude estimate.

An addition of a third gas (see section 2.4) would change both the electron temperature and the total momentum transfer cross section. Then, the influence of different admixtures on the electron drift velocity is defined by the resulting σ_m and $\langle\epsilon\rangle$.

As can be seen in table 2.2, a CO₂ molecule has a large momentum transfer cross section. Thus, an addition of this gas to a fast gas can result in a considerable

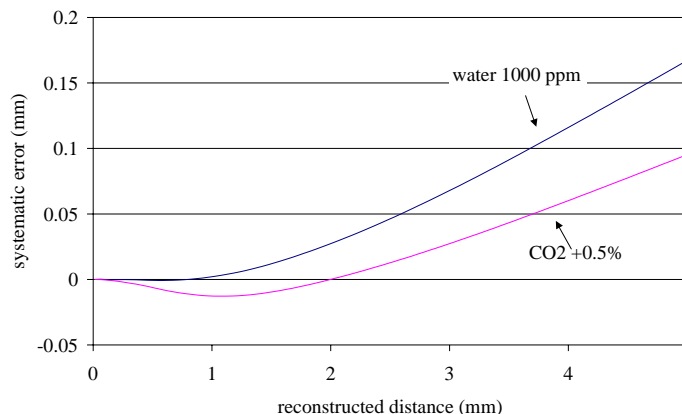


Figure 2.3: *Systematic deviations in the reconstructed distance caused by an 0.5%-increase in the CO_2 content and a 1000-ppm-increase in the water content. The data are calculated for 10-mm chambers at 1900 V and can be also used for 5-mm chambers at 1700 V since the electric fields at the given radius are almost equal in both types of chambers.*

change of the electron drift velocity. Furthermore, contaminants like N_2 and O_2 would only slightly change the drift velocity; still, the presence of water in a concentration of one part per thousand could result in a loss of the electron drift velocity by several percent.

A change in the drift velocity causes a change of the calibrated rt-relation. A calculation of the drift velocities in the gas $\text{Ar}/\text{CF}_4/\text{CO}_2$ (65:30:05) with and without a 1000-ppm water admixture and also for the mixture $\text{Ar}/\text{CF}_4/\text{CO}_2$ (64.5:30:5.5) was made using the Magboltz-2.2 program. Deviations from the normal gas composition lead to systematic errors in the reconstructed distance. The errors as functions of the distance are shown in figure 2.3.

It should be noted that the Magboltz calculation gives a rather moderate dependence on the CO_2 and the water contents. A direct comparison of the cross sections given in table 2.2 hints on a more rapid reduction in the drift velocity when increasing the water and CO_2 contents. To check the correctness of the Magboltz program, we compared experimental data obtained in [44] for the mixture $\text{Ar}/\text{CF}_4/\text{CO}_2$ (65:28:07) with the prediction of Magboltz. The Magboltz and the experiment curves agreed very well, as can be seen in fig.2.4.

Measuring the drift velocity in very fast gases, one should be sure that the water content is small. Similarly, the water content, which leads at 1000 ppm to systematic errors in the reconstructed distance of up to $170 \mu\text{m}$, should be well controlled in the OTR.

Also, the concentration of CO_2 should be well regulated, as a 0.5%-deviation from the normal CO_2 content causes a deviation of up to $100 \mu\text{m}$ of the reconstructed distance.

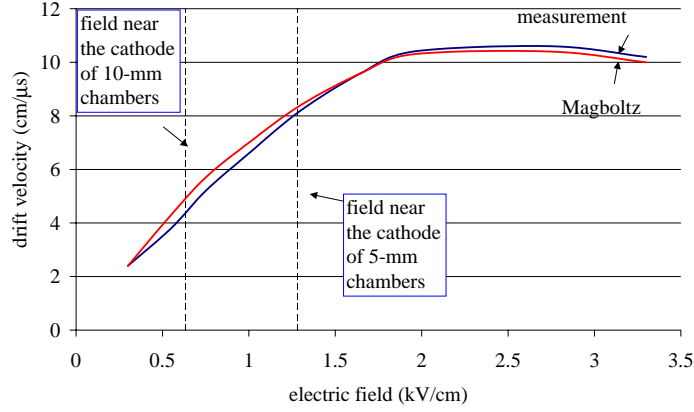


Figure 2.4: Comparison of electron drift velocity measured in [44] with that of calculated by Magboltz-2.2 (released in 2000).

Because CO_2 reduces the electron drift time, the concentration of it should be not higher than 5% for the given CF_4 content [44]. The drift time would exceed the allowed limit when decreasing the CF_4 content or increasing the CO_2 content. Also, an addition of admixtures which are believed to prolong the operating lifetime, methylal or ethanol, is undesirable for the same reason. A maximum addition of 1% methylal is allowed and no ethanol at all [44].

2.4 Quenching mechanism in a mixture Ar/CF_4 and a quencher

The stability of drift chamber operation and the maximum working gain can be increased when adding a relatively small quantity of another gas (usually called quencher). As a discussion of quenching effects, in general, would be too complicated, let us restrict our choice to the mixture Ar/CF_4 (+ quencher), which provides a high electron drift velocity.

2.4.1 Experimental evidence

The addition of a quencher can be substantiated, for example, by the results of a test described in [27] where the voltage dependencies of the counting rates in four mixtures $\text{Ar}/\text{CF}_4/\text{CH}_4$ (74:20:6), $\text{Ar}/\text{CF}_4/\text{CH}_4$ (67:30:3), $\text{Ar}/\text{CF}_4/\text{CO}_2$ (65:30:5) and Ar/CF_4 (70:30) were measured. The plateau² widths of the rate curves in mixtures $\text{Ar}/\text{CF}_4/\text{CH}_4$ (74:20:6), $\text{Ar}/\text{CF}_4/\text{CH}_4$ (67:30:3), $\text{Ar}/\text{CF}_4/\text{CO}_2$

²Plateau is the flat part of the curve representing counting rate as a function of voltage. Below the plateau not all the ionizing particles are counted due to an insufficient gas gain, above the plateau noise and the secondary avalanche starts contributing to the counting rate.

(65:30:5) were almost identical (≈ 360 V), whereas the plateau in a mixture Ar/CF₄ (70:30) was narrower (≈ 220 V). It suggests that the maximum gain at stable operation in the binary mixture Ar/CF₄ is 4 times lower than in the ternary mixtures additionally containing methane or CO₂.

The increase in the maximum gain can be explained by the following mechanism. Ion recombination as well as molecular de-excitation are often accompanied by emission of UV photons. An emitted photon can excite another molecule or strike the cathode. An interaction with the cathode can proceed through the photo-effect resulting in the release of an electron, which in turn drifts to the wire and causes a secondary avalanche. Therefore, one adds quenching gases which absorb photons or quench excited molecules. Additionally, ion-molecular reactions in collisions with quenching molecules leading to formation of larger ions or ions with lower ionization potentials are sometimes mentioned in the literature to explain the quenching mechanism. It is instructive to analyze these effects semiquantitatively.

2.4.2 Radiative de-excitation and photoelectron emission

The amplitude of the secondary avalanche is directly proportional to the number of emitted photons, which is partially defined by cross sections for electronic state excitation in electron-molecule impact collisions. Since we did not find the cross sections for argon, we compared electronic excitation cross sections with ionization cross sections for different atoms and molecules given in [60]. The probability for electronic excitation and ionization in the avalanche in close proximity to the anode (see electron energy distribution function in fig.9.3) were estimated to be always of the same order of magnitude. This means that the number of electrons and the number of excited atoms produced in the avalanche are comparable.

As the number of photons reaching the cathode depends on the overlapping region between the emission and the absorption spectra of the gas, the measurements of the form and the extent of the emission spectrum and the absorption coefficient in the same energy region are important.

In atoms the only degrees of freedom are translational and electronic. Therefore, in atomic gases under a low pressure radiation occurs only due to electronic transitions. The electronic transitions result in characteristic series of lines in the emission spectrum.

Under a higher pressure when the time between collisions becomes less or comparable with the lifetime of the excited states (10^{-8} s) additional forms of de-excitation arise. An atom A having an excited electronic state lying below the ionization potential can dissipate its energy usually through the following processes [21]:

- **Spontaneous emission:**

$$A^* \leftrightarrow A^{(*)} + h\nu' \quad (2.2)$$

with transitions directly or stepwise to the ground state. This radiation is typical for atomic gases under low pressure. When increasing the pressure, the spectrum

lines become wider due to broadening of electronic states during collision periods and weaker due to the growing competition of the other dissipation energy processes (2.4). In the emission spectrum **Resonance radiation:**

$$A^* \leftrightarrow A + h\nu_R \quad (2.3)$$

often dominates. Such radiation is observed when the only possible radiation transitions from the excited state is to the ground state, which is the case for the lowest excited level, or for a higher level if intermediate transitions are forbidden [21].

- **Fluorescence and phosphorescence.** The short-time emission of photons having lower energies than the energy absorbed by a molecule is called fluorescence, long-time one is phosphorescence. In atomic gases it normally occurs in collisions with an unexcited atom through excimer formation followed by emission

$$A^* + A \leftrightarrow A_2^* \rightarrow A + A + h\nu_{\text{continuum}}. \quad (2.4)$$

This emission spectrum is a structureless band shifted to longer wavelengths compared to the A^* emission [21]. As the gas concentration increases, the A_2^* emission increases whereas that of A^* decreases due to self-absorption and depletion of A^* via the excimer formation process (2.4). Thus the form of the spectrum depends on the pressure.

- **Energy transfer to other species** with lower-lying excitation states

$$A^* + X \leftrightarrow A^*X \rightarrow A + X^* \quad (2.5)$$

Generally speaking, when an excited state of a molecule lies higher than its ionization potential, it is called superexcited state. An atom being in a superexcited state usually undergoes autoionization.

In molecules other mechanisms of relaxation are possible: dissociation and internal conversion (radiationless rearrangement of discrete electronic states within a molecule, which relaxes the molecule into its lowest excited state of a given multiplet).

Luminescence under pressures of tens of millibars or higher is observed to have a continuum spectrum extending over several eV. The highest energy limit ϵ of the spectrum corresponds to the transition between the lowest electronic excited state and the ground state [102].

An explanation for this fact can be as follows. An atom or a molecule (excited e.g. through e-impact) can emit a photon relaxing to a lower excited state or to the ground state. In the first case, the photon is absorbed after $O(10 \mu\text{m})$ and can be re-emitted again. This process continues until one molecule dissociates or the photon has an energy below ϵ : a photon of an energy below the lowest electronic

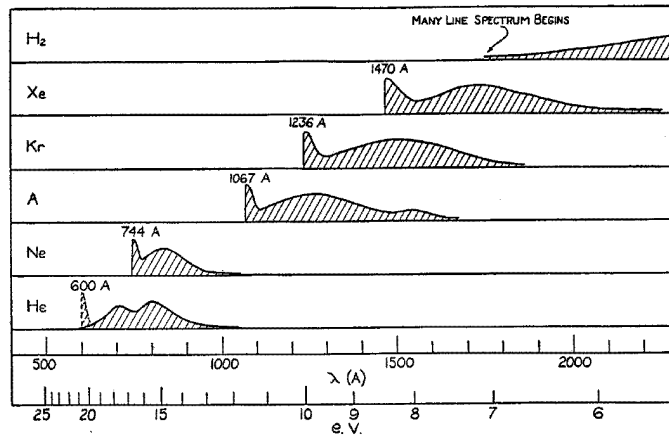


Figure 2.5: *Schematic representation of noble gas and H_2 continua measured under pressures of several hundred millibars [102]. A continuum of argon under atmospheric pressure is shown in figure 2.8.*

excited state cannot be absorbed. Thus the observed photons are of energy ϵ or below. This spectrum consists of a big number of lines (transitions between a lot of different states) which are wide due to “disturbance” of electronic states during molecular (atomic) collisions.

Approximate forms of noble gas continua measured under pressures of several hundred millibars are shown in fig.2.5. The continuum from pure argon measured under atmospheric pressure in [100] covers the region from 4.5 eV to 11 eV (see fig. 2.8). The argon continuum, being similar to that of other noble gases, consists of two bands. The first narrow band is related to resonance radiation from the lowest excited states (11.5 eV) and the second wide band is probably emitted in processes with excimer formation (see process (2.4)). Studies of noble gases showed that under a low pressure (the pressure of neon was less than 140 mbar) only the first band exists. When increasing the pressure, the first band becomes weaker and wider and moves to the region of lower energies due to increasing self-absorption at the region of the lowest excited state [102]. Conversely, the second band appears when increasing the pressure. It dominates the first band under atmospheric pressure.

If an emitted photon striking the cathode has an energy higher than the work function of the cathode material, it can produce a photoelectron. This effect is called photoemission or photoeffect.

A typical photon energy dependence of the photoemission probability is illustrated for a copper cathode in fig.2.6. According to [36], usually (not only for copper) the photoemission efficiency does not exceed 1% for photon energies less than 10 eV.

Photoemission from the cathode does not allow to operate stably a drift cham-

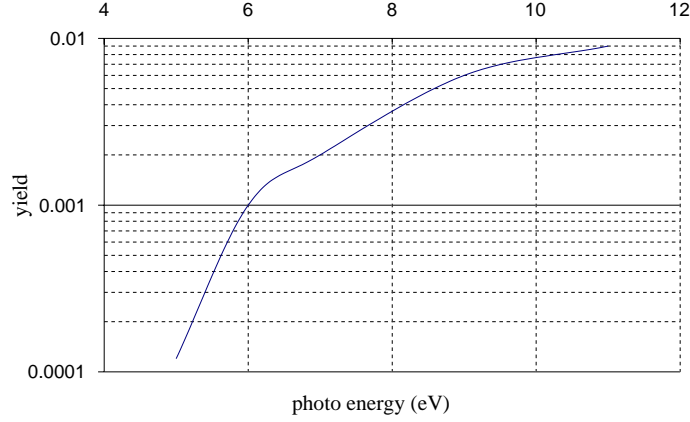


Figure 2.6: *Photoemission quantum yield of copper with clean surface [36]. The probability for emission of an electron drops very fast as the photon energy approaches the work function of copper (4.4 eV) from above.*

ber filled with pure noble gas at a gas gain of more than $10^3 - 10^4$.

2.4.3 Quenching of luminescence

As was noted before, the form and the intensity of the emitted spectrum is environment-dependent. Even a small addition of an appropriate gas can lead to a considerable suppression of the emission intensity. This effect is called quenching.

Emission-quenching studies of argon adding traces of CH_4 , CO_2 , O_2 , N_2 , Kr and Ne were performed by [100]. The discussion in this section is mainly based on the explanations in this article. It was found that the emission intensity is quenched by a factor of more than 10 when adding about 2% of CH_4 , CO_2 , O_2 or N_2 . The quenching efficiency was about 2 times lower for the addition of Kr. When adding 10% Ne, the emission intensity was reduced by a factor of 5. An 0.1%-addition of N_2 resulted in an appearance of several pronounced emission bands with similar intensity as the rest of the spectrum. These bands, lying in the region around 3.5 eV, were related to emission of N_2 .

Quenching by the gases CH_4 , CO_2 , O_2 and Kr was explained to result from ionization of these gases since a large increase in the number of free electrons from ionization was observed in discharge processes in [77] when adding traces of gases with the ionization potentials considerably less than 15.8 eV, the ionization potential of Ar. The ionization potential of N_2 is 15.6 eV, thus quenching by N_2 could not be related to ionization. The appearance of a strong low-energy emission of N_2 when traces of N_2 are added to argon is a hint that quenching occurs due to electronic excitation of N_2 followed by emission (as explained in [100]).

The argon emission was most effectively quenched by CH_4 and CO_2 . The dependence of the emission intensity on the quencher concentration taken from

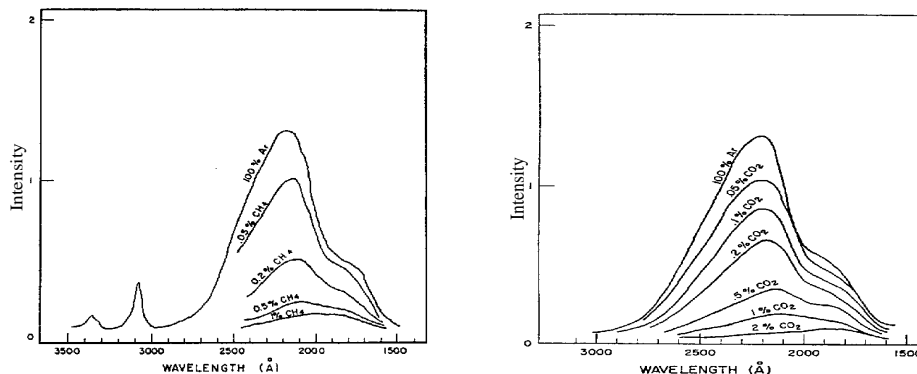


Figure 2.7: Quenching of the argon emission by CH_4 (left) and CO_2 (right) at different quencher concentrations. The quenching efficiencies of CH_4 and CO_2 were similar. It was shown that the band at 3100 \AA in the left figure was emitted by water, the concentration of which was estimated to be in the region of 1-10 ppm. The right parts of the emission spectra are cut due to the short wavelength limit of the quartz window transmission.

gas	Ne	CF_4	Ar	Kr	Xe	O_2	CO_2	CH_4	H_2O	N_2
$E_{\text{lowest}}, \text{eV}$	17	12.6	11.5	10	8.2	4	7.5^a	7.5^a	6^a	6
reference	[43]	[24]	[43]	[43]	[43]	[42]	[22]	[22]	[22]	[51]

^aLowest state energies are assumed approximately equal to electronic excitation onsets observed in electron-impact interactions.

Table 2.3: Energy of the lowest electronic excitation state for different atoms and molecules.

[100] is shown in figure 2.7.

It should be remarked that an effective quenching of the argon emission occurs when a second gas having the electronic excitation states lower than that of argon (see table 2.3) is present. Indeed, an addition of traces of Kr to argon also effectively quenched the argon emission. Conversely, a small addition of Ar to Kr does not seem to provide quenching of the Kr emission. However, a moderate quenching was observed when adding neon to argon in spite of the fact that the neon electronic excitation states are higher.

The high efficiency of quenching by polyatomic molecules like CH_4 and CO_2 could be explained by a larger phase space due to a bigger number of electrons occupying the electronic shells than in atomic gases.

Although the lowest excitation state of a CF_4 molecule is higher than that of argon, CF_4 can probably quench rather efficiently via dissociation as described in section 2.4.5. A CF_4 molecule seems to dissociate with a high probability [110]. This is in good agreement with [87]. According to this paper, the absence of optical emission from CF_4 was observed. Although a continuum ranging from 2 eV to 5

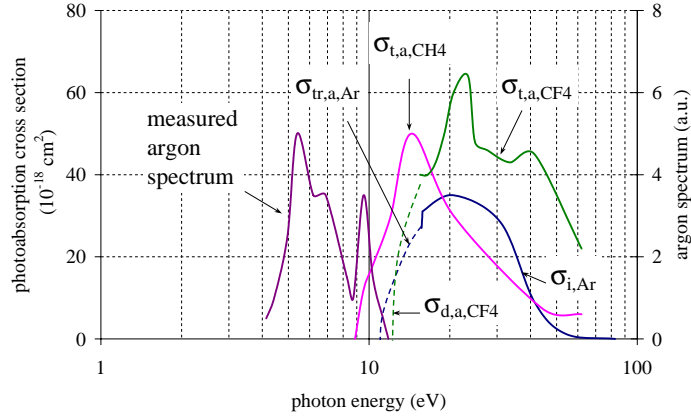


Figure 2.8: Argon luminescence spectrum and photoabsorption by different gases. The spectrum was measured in pure argon under approximately atmospheric pressure [100]. The measured total photoabsorption cross section for CH_4 is denoted by σ_{t,a,CH_4} [29, 90]; σ_{t,a,CF_4} is the measured total photoabsorption cross section for CF_4 [71, 20]; $\sigma_{i,\text{Ar}}$ is the measured total photoionization cross section for Ar [91]; σ_{d,a,CF_4} is the supposed dissociative photoabsorption cross section for CF_4 ; $\sigma_{tr,a,\text{Ar}}$ is the supposed photoabsorption cross section for Ar at the photon energy below ionization potential. When an atom of argon absorbs a photon with energy lower than its ionization potential, it re-emits a photon relaxing to a lower excitation state or to the ground state, sometimes, via processes of excimer formation (see process (2.4)).

eV was observed in electron-impact interactions [6], the source of this emission was attributed to the species CF_3^{+*} .

Because the photon energy is less than the work function of gold (5.1 eV), this radiation will not produce photoeffect in gold-coated chambers. Thus CF_4 molecules (without admixture of argon or other luminescent gases) do not require quenching by another gas.

The considerable reduction in the emission intensity observed in [100] can imply an increase in the photoabsorption coefficient or in the efficiency of energy transfer mechanism (2.5) followed by ionization or dissociation. These two processes are analysed semiquantitatively below.

2.4.4 Photoabsorption

Photoabsorption takes place via electronic excitation of atoms or molecules. Unlike the emission spectrum, the absorption spectrum is a characteristic of single atoms (molecules) and its form does not depend on the concentration [21]. The absorption coefficient at a given photon energy should be proportional to the concentration. The long wavelength threshold of absorption commonly lies at the level of the lowest electronic excitation state unless this electronic transition is forbidden.

The threshold for electronic excitation of a CF_4 molecule is rather high, 12.6

eV [67]. Thus the photoabsorption starts at this energy. Argon probably absorbs photons from 11 eV to 50 eV as shown in figure 2.8. The measured photoionization cross section of argon could be extended to lower energy, where absorption occurs via electronic excitation with a subsequent radiative electron transfer to a lower excited state or to the ground state.

According to the data in figure 2.8, in the mixture Ar/CF₄ the absorption length for a photon with an energy higher than the ionization potential (16 eV for CF₄ and 15.76 eV for Ar) is short

$$\frac{1}{\sigma_{ph,abs}N} \approx 6 \mu\text{m}$$

where N is the concentration of the gas and $\sigma_{ph,abs}$ is the photoabsorption cross section. Photons with energies below 11.5 eV could be absorbed by another quencher like CH₄. As can be seen in figure 2.8, a photon can only be absorbed by CH₄ if its energy is higher than 9 eV. The absorption length for a 10 eV photon in Ar/CF₄ with 5% CH₄ is about 400 μm . Thus the emission intensity from the avalanche in the energy band around 10 eV will be suppressed at the radius of 2.5 mm by a factor of about 500. However the photons with an energy of less than 8 eV can not be absorbed by CH₄ and by CO₂. Thus the effect of quenching seen in figure 2.7 is probably caused by another mechanism described in section 2.4.5.

It is worth to mention, however, that an addition of a small amount of gas with the ionization potential lower or within the range of the argon emission spectrum like methylal could be harmful. Ignition of a discharge at a relatively low gas gain can occur due to photoionization processes in this gas. Given a typical photoionization cross section of the order of $20 \times 10^{-18} \text{ cm}^2$ [21], a photoionization process would occur at a distance, on the average, of 1 mm to the avalanche if a methylal content is 0.2%. The probability of a photoelectron production becomes very high, about unity, in comparison to the rather low probability of photoemission on the cathode (see figure 2.6). One of the conditions for development of an undesired discharge is a very small content of this gas. When methylal is added in a higher concentration, the ionization would occur near the avalanche and will be taken by the read-out electronic as one avalanche process. In this case, the effect would not be dangerous since it would be observed as an increase in gain, which can be regulated with high-voltage.

The increase in ionization when adding a small concentration of species with low ionization potential is well-known (see, for example, [21]) and is referred to as Jesse effect.

2.4.5 Quenching of electronically excited atoms (molecules) in collisions

The suppression of the secondary avalanche amplitude and thus an increase in the maximum gain can also be explained by quenching of excited atoms (molecules) in collisions. The quenching rate constant of electronically excited electronic states

depends on the collision partner. Some high electronic excitation modes, for example, $\text{Ar}(4d[3/2])$ could be quenched in collisions with argon atoms at almost the same rate as with CH_4 , CF_4 or CO_2 molecules [98]. However, for low lying states $\text{Ar}(^3P_2)$, $\text{Ar}(^3P_0)$ quenching efficiencies of modes in collisions with argon atoms at room temperature is very small, more than 10^5 times lower than for $\text{Ar}(4d[3/2])$, however, is still high in collisions with CO_2 or CH_4 molecules [98]. Most probably, the excited states of argon, lying lower than the lowest excitation energy of a CF_4 molecule (12.6 eV) cannot be quenched by CF_4 .

Let us estimate an excited state lifetime limited by quenching collisions neglecting radiative de-excitation when 5% of a quencher is added to pure argon. Given a quenching rate constant for $\text{Ar}(^3P_2)$ and $\text{Ar}(^3P_0)$ of approximately $k_{\text{quen}} = 5 \times 10^{-10} \text{ cm}^3/\text{s}$ [98], the life time of these excited states should be

$$\tau = \frac{1}{k_{\text{quen}} * N} \approx 1.5 \text{ ns.}$$

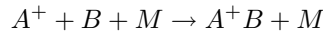
The lifetime is similar to a typical radiative de-excitation time (For example, the lifetimes of resonance lines $^1P_1^0$, $^3P_1^0$ of Xe and Kr, corresponding to energies 5-7 eV, lie in the range of 3-5 ns [21]). The quenching factor of more than 10 when 2% of the quencher is added (see section 2.4.3) probably builds up in stages of the multiple resonance re-emission process. Being excited, an atom can emit a photon with some probability p or be quenched in collisions with another molecule. The emitted photon is absorbed after $O(10 \text{ } \mu\text{m})$ and is re-emitted again with a probability p . After n such stages the probability to find the photon will be p^n . Therefore, the intensity of the observed emission gets considerably suppressed when adding another gas.

2.4.6 Ion-molecular reactions

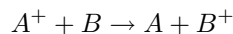
There is another possibility to produce a secondary avalanche. Positive ions formed in avalanches or in ion-molecular reactions recombine interacting with the cathode. The energy remaining after recombination is usually transferred to the molecules (or to the lattice) of the cathode material through an electronic excitation. However, an emission of an electron is also possible.

Since interactions between ions and molecules are stronger than between neutral species, there are much more varied reactions between ions and molecules than between neutrals. The long-range Coulomb field of an ion attracts polarizable molecules at large distances. A strongly inhomogeneous electric field induces a dipole potential between an ion A^+ and atom B given by $-\alpha_B e/2r^4$ where α_B is the polarizability of atom B (the polarizability of atoms and molecules is commonly several \AA^3), e is the electronic charge, r is the distance between the ion and B . Also, the chemical properties of an ion A^+ are completely different from that of the neutral parent A . For example, Ar^+ is chemically aggressive.

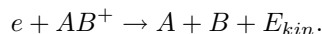
Usually, two mechanisms can reduce the probability of production of a free electron in ion-electrode interactions.



or



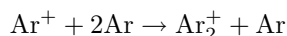
where A and B are molecules (atoms), M is a quenching partner. An ion AB^+ has more degrees of freedom for energy dissipation in the recombination than A :



Also, the ionization potentials of AB or B are lower than that of A (otherwise, the reactions would not take place) so that the excitation energy remaining after recombination is lower. Hence, the probability of knocking out an additional electron in an interaction of the ions AB^+ or B^+ with the cathode should be lower than in an interaction of the original ion A^+ .

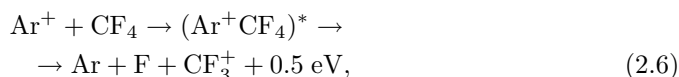
Ion-molecular reactions in collisions with quenching molecules leading to formation of larger ions can partially explain the quenching effect seen in [27] and described in section 2.4.1.

In pure argon a positive ion of argon has a short lifetime at room temperature and reacts in a three body process as follows



This reaction occurs with a rate coefficient of $2.2 \times 10^{-31} \text{ cm}^6/\text{s}$ [97] corresponding to a lifetime of 6 ns. An ion Ar_2^+ is stable at room temperature and the ionization potential of Ar_2 (14.5 eV) [43] is lower than that of Ar (15.76 eV). Because ions move in an electric field typically three orders of magnitude more slowly than electrons, the drift time of Ar_2^+ in the chamber should be of the order of 100 μs .

If CF_4 is present, the behaviour of Ar^+ is not known. A direct electron transfer process from CF_4 to Ar^+ is not possible since the ionization potential of Ar (15.76 eV) is slightly lower than that of CF_4 (16 eV). But if we assume that Ar^+ and CF_4 can form a complex ion



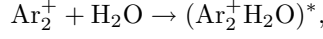
the probability of the reaction with CF_4 could be much higher. The energy release of the reaction can be estimated as

$$E = I_{\text{Ar}} - I_{\text{CF}_3} - \nu_{\text{CF}_3-\text{F}}$$

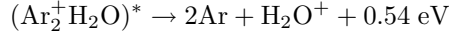
where I_{Ar} (15.76 eV), I_{CF_3} (10.1 eV) are the ionization potentials of Ar and CF_3 , respectively, and $\nu_{\text{CF}_3-\text{F}}$ (5.2 eV) is the binding energy between CF_3 – F . The process (2.6) could occur because CF_4 is a polarizable molecule (so that it is attracted by an ion), and Ar^+ as chemically aggressive species could combine with CF_4 .

Taking this reaction into account, the prediction of the fluorine production rate should be considerably higher than when considering only CF_4 electron-impact dissociation.

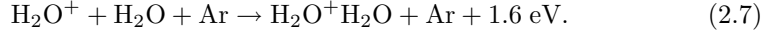
Most probably, Ar^+ and Ar_2^+ react with H_2O molecules, which are present in honeycomb chambers in small concentrations. Possible reactions are:



which can continue as



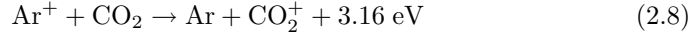
followed by



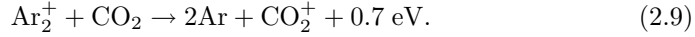
According to [97], the binding energy of an ion and H_2O being typically 1 eV for the first attached H_2O molecule converges to 0.42 eV (this is the binding energy of a H_2O molecule to the surface of a water drop) when increasing the number of attached H_2O molecules. The affinity of a complex ion with four attached H_2O molecules to one H_2O molecule is usually close to 0.42 eV. Since the binding energy of 0.42 eV is too low to hold the molecule for a relatively long time, the probability to find complex ions with more than four attached water molecules is low (as explained in [97]).

Since a water molecule has a large dipole moment, it is attracted to an ion from a relatively long distance. Most probably, process (2.7) would occur long before the ion reaches the cathode even if the concentration of water is as low as several ppm.

An addition of a quencher with a lower ionization potential to a mixture Ar/CF_4 could change the way of ion-molecular interaction, for example:



or



The cross section of such charge transfer processes can be estimated to be of the order 10^{-15} cm^2 [85], which yields a value for the time constant of the order of 10 ns (the CO_2 content is assumed to be 5%). Similar charge transfer processes occur with CH_4 .

Addition of CH_4 or CO_2 to a dry gas can lead to formation of ions with lower ionization potentials. However, at the presence of water traces, it seems to be unlikely that a quencher would initiate formation of complex ions with the ionization potential lower than those of $\text{H}_2\text{O}^+(\text{H}_2\text{O})_n$ clusters.

2.4.7 Experimental definition of the mechanism limiting the maximum gain

To find out what limits the maximum operating gain (ions or photons), we measured the time interval between the pulses and their after-pulses. We used a monitor chamber (a drift chamber with a gold coated cathode having a diameter

of 15 mm) filled with the gas Ar/CF₄/CO₂ (65:30:05) and radiated with ⁵⁵Fe (5.9 keV photons from ⁵⁵Fe produce a point-like region of ionization). Because of a rather long electron drift time of ≈ 100 ns in the monitor chamber, the pulses and their after-pulses resulting from photoemission on the cathode could be clearly separated.

Results. The HV of the monitor chamber could be increased until the amplitude of the primary pulses and that of their after-pulses, which came approximately 100 ns later, became comparable.

Conclusion. The delay between the pulses and after-pulses of 100 ns means that after-pulses restricting the maximum gain are generated by photoemission rather than by ion recombination on the cathode followed by emission of electrons. If the maximum gain were limited by the latter process, we would have breakdown at a voltage lower than the voltage at which primary pulses and after-pulses become of equal amplitude.

2.5 Other factors for defining the gas composition

As was shown before, an Ar/CF₄-based mixture is fast: the electron drift time is less than the bunch separation of 96 ns. It was also shown that an addition of quencher to Ar/CF₄ gas helps to increase the stability. Additional factors influencing the choice of the mixture components are given below.

The maximum gas gain increases when increasing the concentration of polyatomic gases and thus the quenching efficiency. On the other hand, hydrocarbons like isobutane (iC₄H₁₀) or methane can lead to polymerization on the anode surface. Methane or other hydrocarbons when disintegrated in the avalanche recombine in different species. Large species with large electric dipole moments are attracted by the strongly inhomogeneous electric field near the wire and condense on the wire surface as a solid or a liquid substance. This effect is dangerous because it causes fast gain loss.

Aging investigations revealed that an introduction of hydrocarbons led to a strong anode aging and the Malter effect. However, these problems were not observed with CO₂ as a quencher (see section 4). On the other hand, introduction of CO₂ in a concentration larger than 5% is also undesirable since the mixture becomes too slow.

Since the electron impact inelastic cross section in CF₄ is higher than in argon, a chamber filled with a gas having higher CF₄ content should operate at higher voltage to provide the same gas gain than those filled with a mixture containing less CF₄. However, an increase in the operating high-voltage is always unattractive for different reasons.

The gas CF₄, with a price of approximately 70 DM/kg, mainly defines the cost of a mixture. From this point of view a lower CF₄ content in the mixture is preferable.

Another factor making an increase of CF₄ concentration unfavorable is disso-

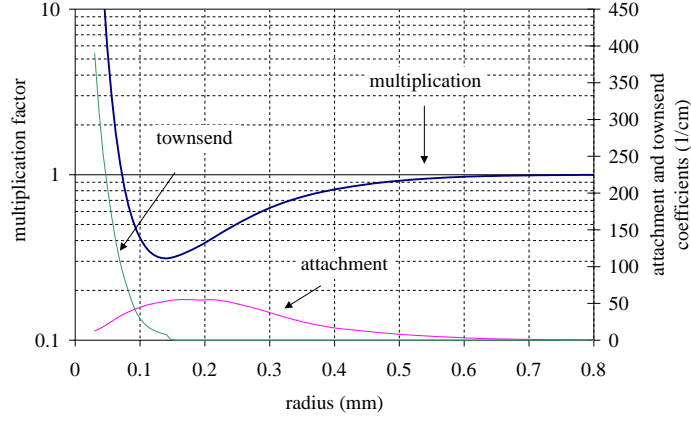


Figure 2.9: Multiplication factor of electrons drifting to the anode from the distance larger than 0.6 mm, attachment and Townsend coefficients as function of the radius in Ar/CF₄/CO₂ (65:30:5). The Townsend and the attachment coefficients were calculated using the Magboltz-2.2 program.

ciative attachment by CF₄ via processes



occurring with an approximately equal probabilities. The cross section for this process is denoted as $\sigma_{a,t}$ in figure 2.2. As a result of attachment, an electron from the ionization can be captured during its drift to the anode wire. With the help of the Magboltz-2.2 program it was shown that approximately 70% of the electrons starting at a radius larger than 0.6 mm are captured (see figure 2.9) in Ar/CF₄/CO₂ (65:30:5). A minimum ionizing particle ionizes, on the average, 50 atoms and molecules in a 5 mm cell. Only approximately 15 of them reach the radius of 150 μm , where the Townsend and the attachment coefficients become equal. The high attachment coefficient of the gas can, in fact, badly influence the spacial resolution of the chamber and the efficiency (detection probability).

Chapter 3

Aging processes in drift chambers

3.1 Introduction

HERA-B was designed to operate at a high rate, which is comparable to the rate at which LHC experiment will operate. This requires a good radiation resistance of the honeycomb chambers as one of the indispensable conditions for the OTR drift chambers to survive for several years annually accumulating a dose of approximately 0.6 C/cm in the hottest region. The drift chambers are delicate devices and prone to a lot of different types of damages. A generic term for these problems is “aging”. In drift chamber nomenclature it comprises a lot of different effects (called “aging effects”): gas gain losses, dark currents or self-sustaining currents, increased currents, anode wire corrosion, sparking and other effects. These effects are usually caused by the formation of deposits on the wire surface or on the cathode or chemical attacks by aggressive radicals (species with unpaired valence electrons) originating in the avalanche.

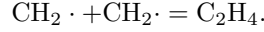
3.2 Anode aging

One of the functional features of drift chambers is the presence of a very high field near the thin anode wire near which dissociation and ionization processes occur. Highly aggressive radicals produced in the avalanche recombine in different species or join already formed large molecules forming even larger ones (polymerization). The growth of the molecules is usually accompanied by the increase in their dipole moments. Finally, a molecule, being attracted by the highly inhomogeneous electric field near the wire, condenses on the wire surface as a solid or a liquid substance. The deposits could have various forms: thin films, whiskers, powder, liquid drops. They could be insulating or electrically conductive. Deposits usually cause a gain loss due to the increase in the effective diameter of the

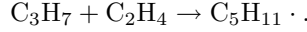
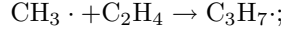
wire unless the conductive deposit has some spiky shape. In the latter case corona discharges lead to dark pulses (noise). An additional gain drop occurs due to the reduction of the electric field caused by an accumulation of charge on an insulating layer. The variation of the deposit thickness along the wire causes a variation of the gain and, consequently, a loss in pulse-height resolution.

Progenitors of today's drift chambers are Geiger counters, which are sealed and contained argon with an addition of a quenching gas. An increase in after-pulsing and noise is observed after typically $O(10^{10})$ counts in sealed Geiger counters and explained to be caused by a lack of the quenching gas, which is consumed in the dissociation processes [40]. Later, proportional counters and multiwire proportional chambers partially replaced Geiger counters. They usually contained argon and 10-20% methane. A serious gas gain loss occurring after some running time is caused by a deposit on the anode wire. The disappearance of the plateau in the voltage dependence of the counting rate (see appendix B.1) could be explained by the presence of deposits on the electrodes.

Polymerization via the dissociation of CH_4 , which is often used as a quencher, can occur via the following processes. The methane ionization in the avalanche results in the formation of positive ions CH_4^+ , CH_3^+ , CH_2^+ , CH^+ , C^+ , H^+ . Also neutral species called radicals $CH_3\cdot$, $CH_2\cdot$, $CH\cdot$, $C\cdot$, $H\cdot$ are produced in the avalanche with unpaired valence electrons. Relatively stable species are also produced, for example, ethylene (C_2H_4), which can be formed in the avalanche via the reaction



In the avalanche C_2H_4 induces formation of polymer chains [106]:



Similarly, these reactions are also characteristic for other unsaturated hydrocarbons. The polymer chain grows and becomes heavier until it deposits on an electrode surface.

In the literature the aging loss rate, R , is usually expressed as a normalized derivative of the gas gain with respect to the accumulated charge per unit length:

$$R = -\frac{1}{G_0} \frac{dG}{dQ}$$

where G_0 is the initial gain, G is the current value of the gain and Q is the accumulated charge. R is expressed in $\frac{\%cm}{C}$.

Anode aging rates measured in six different setups with different hydrocarbons were compared in [93]. The comparison yields that the use of lighter hydrocarbons leads to lower aging rates than in tests with heavier ones. However, another study of plasma polymerization showed that polymerization rate varies as follows: $i(CH_4) > i(C_2H_6) > i(C_3H_8)$ [62].

As hydrocarbons are usually responsible for polymerization, their avoidance should be one of the trends in the choice of materials for the gas system. The

replacement of hydrocarbons with CO_2 often results in a considerable prolongation of the life expectancy of drift chambers. A gain recovery when using a CO_2 -based gas was, for example, reported in [38]. Creating discharge in $\text{Ar}/\text{C}_2\text{H}_6$ or Ar/CH_4 whiskers on the wire were grown. After the replacement of the counting gas with Ar/CO_2 whiskers were etched away.

A gain loss in a chamber filled with a mixture composed of gases not containing hydrocarbons is usually caused by a pollution from leaks or by an outgassing of materials used for chamber construction. These admixtures could be present in traces and the measurement of them requires the use of sensitive tools. For example, analysis of deposits formed when operating with a CO_2 -based gas showed the presence of Si (and sulphur) [17, 37].

A Monte-Carlo simulation of aging with a known gas is difficult because most of the cross sections for collisions of electrons, photons, atoms, molecules, ions, radicals with each other are not known. A model of anode aging in a detector with CO_2 as a quencher, which could result from the unknown outgassing of the used material in the boxes or plumbing is even more difficult.

In [93, 106, 58, 92, 69] it was shown that the gain loss rate depends on: the gas gain, the gas flow, the irradiation area, the size and the geometry of the chambers.

Wire coating. Since the avalanche occurs in close proximity to the anode wire, the wire coating plays a significant role in anode aging. Large molecules (probably with high polarity) are attracted by strongly inhomogeneous field near the wire. If the wire surface is not chemically inert the species react with the wire material “sticking” to it. Usually, one uses a gold-plated wire as the anode. It was shown, for example, in [111] that the gain loss of a drift chamber filled with $\text{CF}_4/\text{iC}_4\text{H}_{10}$ was very fast when using Cu, Al, Ni or Stablohm¹ wires.

Intensity. The intensity dependence of the gain loss rate is rather complicated. It is assumed that anode aging (almost) does not depend on the intensity. In this believe, one makes accelerated tests to reduce the test time. Since in these tests the chambers are usually subjected to higher doses than expected in the real detector, possible underestimations of the aging rate can be compensated by higher doses. The radiation intensity dependence of the aging rate was shown, for example, in [83]. Irradiating a chamber filled with $\text{Ar}/\text{C}_2\text{H}_6$ (50:50) at a current density of $1.4 \mu\text{A}/\text{cm}$, the aging rate was relatively low at $5 \frac{\% \text{cm}}{\text{C}}$. However, the operation with a rather low current density of $0.1 \mu\text{A}/\text{cm}$ resulted an aging rate of $60 \frac{\% \text{cm}}{\text{C}}$.

Purity. The gain loss rate also depends on the purity of the counting gas. Probably, the most “dangerous” species is silicon (see discussion in section 3.5). The influence of different species on the anode aging rate, which depends, of course, on many parameters, is a very difficult question and therefore will not be discussed here. Certainly, to avoid some unexpected phenomena the gas should be as pure as possible. Here one example: according to [55], an irradiation test was made with a chamber filled with DME having a rather high content of contaminants: 870 ppm of Freon 22 (CHF_2Cl), 270 ppm of iC_4H_{10} , 120 ppm of propylene (C_3H_6), 45 ppm

¹Stablohm wire is a resistive wire used as the anode wire for the charge division read-out technique.

of Freon 12 (CF_2Cl_2). The test showed a gain loss rate more than 10 times higher than with a pure mixture (in which the content of any contaminant was lower than 15 ppm). For instance, in another report [57], the gain loss rate increased ten times when high purity gases were exchanged for a technical grade purity mixture. It should be remarked however that the chambers filled with CF_4 -based mixtures are usually not so sensitive to contaminations due to the etching mechanism by F-containing species produced via CF_4 dissociation (see i.g. [37]).

Irradiation particles. As it will be shown later, development of aging effects strongly depends on the type of irradiation. The Malter effect in drift chambers of the HERA-B Outer Tracker usually seen in hadronic environments using CF_4/CH_4 -based mixtures after several mC/cm never developed with X-rays. Also, in later tests of the HERA-B muon group (see [27]) the aging rate increased by more than two orders of magnitude after replacing 5.9 keV photons with 100 MeV α -particles when using Ar/ CF_4/CH_4 (74:20:6).

Good additives. The aging rate can also be considerably decreased when adding some admixtures in small concentrations. For example, in drift tubes filled with the mixture Ar/ CH_4/N_2 (91:5:4) the gain fall was stopped after water or ethanol ($\text{CH}_3\text{CH}_2\text{OH}$) were added. The continuous fall of the gain disappeared after H_2O was added into the counting gas having only a technical grade purity [57] (The same results were obtained with ethanol). In another group, an addition of isopropyl alcohol ($\text{C}_3\text{H}_7\text{OH}$) or methylal ($[\text{OCH}_3]_2\text{CH}_2$) to the “magic gas” (Ar/ $\text{iC}_4\text{H}_{10}/\text{CF}_3\text{Br}$ (75:24.5:0.5)) prolonged the chamber lifetime by three orders of magnitude [17].

One of the common features of the curative admixtures (water, alcohols, ethers) is the possibility of oxygen (or OH) production via the dissociation of these molecules. Oxygen, as suggested in [58], can probably stop chain-radical polymerization. However, Si polymerizes very eagerly in combination with oxygen, as mentioned in section 3.5. Another common property: they are polar gases [18]. Molecules with large dipole moments considerably reduce electron temperature in a low electric field (if their fraction is comparable with 1% or larger). However, in the avalanche, where electronic state excitation and ionization cross sections become very large, they contribute rather moderately to cooling electrons.

Hydrogen is another admixture that sometimes slows down aging. For example, positive influence of hydrogen was observed in [96]. However, an extensive analysis of species produced under a glow discharge in methane showed the production of species like H_2 , C_2H_6 (ethane), C_2H_4 (ethylene) and C_2H_2 (acetylene). Polymers were produced as $(\text{CH}_2)_n$ chains. The polymerization rate was considerably increased when adding hydrogen. Also, it was mentioned in [106] that results with the use of hydrogen are contradictory.

CF_4 -based mixtures drew much attention in drift chamber applications owing to their high electron drift velocity (see section 2.3) and good aging features. For instance, chambers filled with a CF_4 -based mixture appear to age rather slowly or not to age at all even without high purity conditions. For example, no anode aging was observed when using Xe/ CF_4/CO_2 mixed in different ratios (50:30:20), (60:25:15), (70:20:10) [4]. Gain loss recoveries are reported rather often. For in-

stance, a chamber which was aged by bubbling Ar/C₂H₆ (50:50) through silicon oil during the irradiation was recovered with a rate of more than 1000 $\frac{\%cm}{C}$ when changing the mixture to CF₄/iC₄H₁₀ [111]. In another aging test, chambers filled with Ar/C₂H₆ showed strong anode aging, which was completely stopped after 4% CF₄ had been added [83].

The good aging characteristics of CF₄-based mixture could be related to etching by F-radicals. In fact, CF₄ finds a wide application in the etching technology [68, 75]. The production of species in the avalanche via dissociation of CF₄ will be estimated in section 9.3. CF₄ dissociates easily and mostly into CF₃ and F radicals. The latter is a highly aggressive radical, which reacts with almost all the plastics and polymers.

Transient aging. It might be mentioned here that the use of CF₄ lead to observations of another kind of effects not connected to the aging of chambers and is often referred to as “transient aging”. When using the mixture Xe/CF₄/CO₂ in different proportions a transient (not-permanent) reduction in the gain was observed [4]. The higher the intensity was, the deeper the gain dropped. The gain recovered after a relatively short relaxation time. Since a transient gain loss was observed in a control chamber connected to the output of the gas box with the irradiated chamber when the irradiation began [14], it could be concluded that the effect is caused by neutral, long-lived, highly electronegative species created in the avalanche.

Rejuvenation procedures. The methods applied to prolong the lifetime of the chambers vary widely. There are construction allowing opening the chambers and replacement or repair of the wires. The wire deposit could be partially removed by wiping or scrubbing the wires or by solving with acetone or something else. For example, rejuvenation of a damaged chamber was possible in [76] because the chambers had a small modular construction. The chambers were inserted into an ultrasonic bath with ethanol for two minutes. As a result of the procedure, the chamber gain recovered from 15% to 65% relative to the initial gain.

Since most of the polymer deposits are highly branched and cross-linked, they are difficult to remove or solve [58]. However, there are methods which can lead to partial or complete restoration of the gain even without opening the chambers. The gain recovery can be reached by etching (chemical reaction with species produced in the plasma) or/and by sputtering (“erosion” via momentum transfer processes when reversing the HV) or by heating (evaporation of liquid deposit). For example, when reversing the HV and setting the current to 0.7-23 $\mu A/cm$ for one or two weeks, the chamber filled with pure argon was considerably resuscitated (the gain recovered from very small to 80-100%) [65].

Anode corrosion. Another only recently observed aging effect, “anode wire corrosion”, should also be mentioned here. This effect was observed, for example, in ATLAS [88, 66]. In the process of operation the wires in a chamber filled with Xe/CF₄/CO₂ having a relatively high water content of several percent swelled, the gold coating splitted off. An analysis showed a more than 2.5- μm -deep permeation of oxygen into the wire material [66]. According to the paper, atomic oxygen, which is produced via O₂ or H₂O dissociation, strongly speeds up the wire corrosion. The

wire swelling and etching of the wire was seen in the OTR already after about 0.2 C/cm and will be described in section 5.2.

3.3 Cathode aging

The degradation of functional characteristics of drift chambers can also occur due to damages of the cathode. The cathode aging of chambers usually takes place via two mechanisms: etching (abrasion) or polymerization of the cathode.

Cathode etching. A metallic cathode coating can be damaged after some running time due to the etching by neutral or charged products of the CO_2 or CF_4 dissociations. For instance, a rapid deterioration of an aluminum layer in a polycarbonate straw filled with $\text{Xe}/\text{CF}_4/\text{CO}_2$ began after 0.2 C/cm followed by total evaporation after 1 C/cm, whereas a Kapton straw with an Al-layer is covered by polyimide showed only a slight decrease in the electrical conductivity after 2.6 C/cm [4]. The Kapton straw cathode foil had an outer layer of polyimide with an addition of C protecting the intermediate aluminum layer, which was needed to obtain a high bulk conductivity of the foil (see section 1.2.2).

A CF_4 plasma model seems to require more sophistication than the simple assumption that etching results from chemical attacks by F-radicals alone. Here is one example showing that etching depends on many factors (not only on the presence of CF_4 in the gas). It was reported in [33] that CF_4 with the help of oxygen could remove the copper coating from a Mylar cathode. The etching damage occurred only if air traces were present in the gas. Tests with a controlled addition of N_2 , H_2O or by changing radiation particles did not show etching at all.

Malter effect. Another equally dangerous cathode aging effect is polymer formation on cathode surfaces. This effect is often called the Malter effect. A model of the Malter effect can be seen in figure 3.1.

An insulating layer is formed by polymerization of the cathode which prevents the neutralization of positive ions leading to the formation of a surface charge. The charge induces a high electric field extracting electrons from the cathode. Many of them recombine with positive ions immediately, but some of them drift to the anode and generate avalanches. This process can develop into a continuous, self-sustaining current in the chambers without an external flux of ionizing particles. The effect was studied and described for the first time in [73]. The development of the Malter effect depends on gas, cathode material and production technology.

Sometimes, the effect can be cured by water. For example, ARGUS drift chambers filled with propane/methylal (97:3) developed Malter currents of $1\mu\text{A}/\text{wire}$ after 1.5 years of data taking [26]. An addition of 1% water helped to suppress the current completely.

Or another example: Malter-like discharges developed also in straws filled with $\text{Ar}/\text{C}_2\text{H}_6$ after 0.02 C/cm, as reported in [79]. It was also shown in the paper that the discharge development time could be prolonged by 50% when adding 0.2%

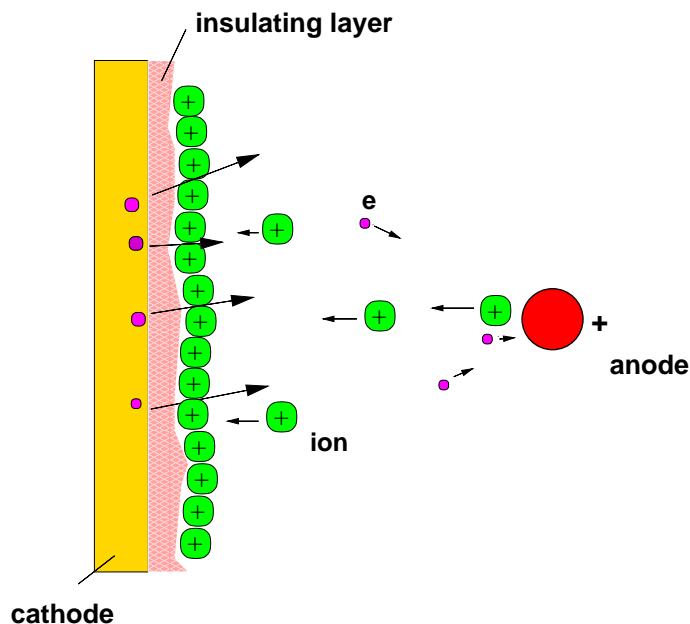


Figure 3.1: *Model of the Malter effect.*

water. The effect of water suppression of the Malter effect can be attributed to the property of water to increase the conductivity of various materials.

3.4 Outgassing of materials

As the use of plastics, glues and other organic materials in chambers and gas systems is unavoidable, one should choose materials with lower outgassing. One of the important parameters in aging studies is the G-value, the number of desorbed molecules per 100 eV of the absorbed radiation. G-values for different plastics are summarized in the table 3.1.

As can be seen, the G-value of polycarbonate, which is used as the cathode in the OTR chambers, is rather high in comparison, for example, with Kapton, which is used in the TRT ATLAS straws (see description in [3]). In spite of the large G-value, polycarbonate as foil material for the honeycomb chamber cathode could not be replaced with, for example, Kapton because of its good folding characteristics.

We can roughly estimate how dangerous cathode material with a high G-value like that of polycarbonate could be. A minimum ionizing particle (MIP) dissipates in a $70\text{ }\mu\text{m}$ thick polycarbonate foil approximately 50 keV of its energy. The cathode absorbs roughly ten times higher radiation energy from UV photons emitted in the avalanche per MIP. Furthermore, approximately 10 MeV is dissipated on

material	G-value
low density polyethylene	3.86
high density polyethylene	3.06
polystyrene	0.026
plasticised PVC	1.16
non-plasticised PVC	0.77
polymethyl methacrylate	1.18
polytetrafluorethylene	0.098
Nylon 6	1.02
polycarbonate	0.86
polyethylene terephthalate	0.17
polysulphone	0.13-10
epoxide resins	0.12-0.57
polyimide (Kapton)	0.00276
polyetherether ketone (PEEK)	0.005
polyetherimide (PUI, ULTEM)	0.014

Table 3.1: *G-values of plastics irradiated at 20 °C in air (from [19]).*

the cathode due to bombardment by positive ions per MIP. This estimation of the energy directly follows from the fact that the number of produced electrons is approximately equal to the number of produced positive ions, each of which dissipates, roughly speaking, 5 eV. Thus one hit should result in a release of approximately 10^5 molecules by a polycarbonate cathode foil. This number is by more than one order of magnitude lower than the number of species originating in the avalanche due to CF_4 dissociation when using the counting gas $\text{Ar}/\text{CF}_4/\text{CO}_2$ (65:30:05). Indeed, the production rate of species in the avalanche is approximately equal to that of free electrons (see section 9.3), but, recombination of one positive ion on a polycarbonate foil results in desorption, on the average, of only approximately 0.04 molecules.

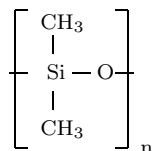
However, CF_4 dissociation causes usually ablation rather than polymerization, as it was reported, for example, in [111]. Conversely, the tests with an application of CH_4 clearly showed the proneness to polymerization on the wire surface. Since the total cross sections for electron impact dissociation of CF_4 and CH_4 are comparable (see figure 9.2) and the concentration of methane (used as a quencher) in gas mixtures is usually of the order of several percent, the dissociation rate of methane in the avalanche should be approximately comparable with that of molecules emitted by a polycarbonate foil. According to [89], besides H_2 , the main component in the outgassing of organic materials, also a considerable amount of heavy molecules is emitted which can cause or enhance deposit formation on electrodes.

It might be mentioned that a metallic coating of plastic foils, preventing the absorption of UV photons and positive ions by plastic, should lead to a reduction in the outgassing rate by several orders of magnitude.

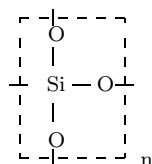
3.5 Materials which should be avoided in the gas system

Among all the materials which are unattractive for the use in the drift chamber construction, one should pay particular attention to a group of silicon-containing materials. Silicon is the second most abundant element of the earth's crust, being exceeded only by oxygen. Silicon is present in FR4, oils and molecular sieves. A rather high concentration of SiF_4 can be found in CF_4 -based mixtures depending on producer.

Since the valence of silicon and carbon are the same, the behaviour of these chemical elements are similar. Combining with hydrogen, silicon forms several hydrides or silanes, the simplest being monosilane (SiH_4), which is a volatile species. Si also forms numerous organo-silicon compounds in which Si atoms are linked in open or cyclic polymeric chains with a lot of different elements like C, N, O as well as halogens, sulphur, and nitrogen [1]. It shows an unusually strong proneness to polymerization especially in combinations with oxygen usually forming polysilicon



or silicate



As explained in [106], owing to the relatively large weight of a Si atom, silicon compounds are not so volatile as those of carbon and some of them could not be removed by the gas flow and deposit readily on electrodes. A high rate aging caused by silicon traces was observed, for example, in [53, 37].

However, traces of silicon can be tolerated in CF_4 -based gases, because fluorine produced in the avalanche willingly reacts with silicon, forming, for example, volatile SiF_4 species [52]; $\text{CF}_{1,2,3}$ prefers to etch SiO_2 [84]. As mentioned already in section 3.2, recovery of a gas gain loss with a rate of $1000 \frac{\%_{\text{cm}}}{\text{C}}$ was observed in [111] using the mixture $\text{CF}_4/\text{iC}_4\text{H}_{10}$ (80:20). In spite of the use of a CF_4 -based mixture, materials containing silicon should be avoided in the OTR. This concerns molecular sieves, oil traces in the gas, silicon glues and rubber (RTV²), large amount of G10 [106, 58].

²Room Temperature Vulcanizer

3.6 Formalism of the test procedure

As was shown above, the appearance of aging effects depends on many factors, therefore, the aging test should be made as realistic as possible. This should imply a setup with a realistic geometry, operating at true parameters, the use of gases from vendors capable to supply gases for the real detector, and the presence of all the materials intended to be used in the real detector.

However, there are certain parameters that could not be reached, for example, the duration of the test could not be as long as 5 years or more. Assuming that aging depends on the total dose, which is proportional to an accumulated charge, and does not depend on the irradiation intensity, aging tests are usually made with increased intensities.

Acceleration of the tests raises a lot of questions: what should be the gas flow? Should the voltage or be increased to compensate the space charge? If the voltage should be increased, then how would it effect the stability of the operation in the non-irradiated region, where the space charge does not exist? Should the flow be changed, etc. These questions are not simple, and the answers depend on the aging effect to be studied.

The voltage could be increased in accelerated tests to maintain the gain at the true value if an increase in the voltage would not effect the stability of operation in the non-irradiated region. This measure is motivated by the intention to keep the plasma density in the avalanche at the same value as in the real detector.

The increase in the current made in accelerated tests leads to an increase in the cathode temperature which in turn can enhance gas convection in tube chambers with an open geometry. The term “open geometry” means the chamber geometry which implies the use of end-pieces with openings for free gas circulation. Within a gas box, unlike straws, the HERA-B Outer Tracker honeycomb chambers have an open geometry construction. The introduction of metal or plastic tubes (capillaries) conveying the gas to every cell would stabilize the gas flow in honeycomb chambers in aging tests, on the other hand, would create a separation between the gas inside and outside the cell in the gas box. Consequently, “internal” and “external” gases would have different purity, which can lead to another outcome of an aging test.

Another problem arises when using X-rays as irradiation. In this case, the gas boxes should have windows which should be transparent for X-rays and consequently be thin and thus probably be permeable for some atmospheric components. The presence of windows leads to an increase in the impurity content of the gas and thus causes a difference between the parameters of the real detector and the aging setup. In order to achieve a gas high purity, the windows should be made as small as the irradiated region.

Another example of unavoidable differences between the real detector and an aging setup is the size of boxes and chambers. The volume of a gas system should be relatively large to insure that contributions from diffusion, laminar flow, and convection caused by temperature differences are similar to those of the real detector.

According to these consideration, we changed from irradiation of short 10 cm long chambers to 40 cm long, comparable with the OTR chambers. We used the chambers with open geometry as well as with capillaries and compared results. Thin windows, transparent to X-rays, were made as small as the irradiated region. We tried to use different particles for irradiation: X-rays and alphas. Chapter 4 describes the history of the OTR tests made with different parameters: gas composition and used materials, size of chambers and irradiated areas, chamber construction, cathode coating, irradiation particles. Such an extensive R&D program should have narrowed the assortment of various surprises during exploitation of the detector.

Chapter 4

History of aging studies of HERA-B honeycomb chambers

4.1 Introduction

The annual radiation dose of the honeycomb chambers in HERA-B in the hottest region is ≈ 0.6 C/cm, thus comparable with that of LHC experiments. The high radiation level in HERA-B puts particular demands on the radiation resistance of the detector. Therefore, extensive aging studies of the drift chambers had to be launched, which led to substantial parameter changes.

As already mentioned in section 1.3, the honeycomb chambers were chosen because of: cheap and modular construction, good aging characteristics, stable self-supporting structure minimizing the amount of material in the sensitive volume (see section 1.3). Pokalon-C (polycarbonate foil enriched with 6% carbon to increase the bulk conductivity) was used as the cathode for honeycomb chambers. Polycarbonate was the only choice since it had high bulk conductivity, small multiple scattering defined by thickness and density, good folding and tempering characteristics. Since it was believed that Pokalon-C foil has a sufficiently high surface conductivity, no coating was applied in the early tests.

As explained in section 2.3, a CF_4 -based mixture, was chosen for the honeycomb chambers to obtain high electron drift velocity. Previous aging test by other groups with CF_4 -based mixtures showed good aging characteristics and even rapid recovery of the gain loss without requirements of high purity conditions and using hydrocarbons as quenchers (see [111, 30, 83, 37, 4]). According to earlier tests described in [58, 49], the drift chambers filled with the mixture CF_4/CH_4 (80:20) showed high radiation resistance. Therefore this gas was initially chosen for the OTR (There was also successful test described in [2] made in the slightly different mixture CF_4/CH_4 (90:10)).

The first OTR aging test was made with X-rays in Zeuthen in 1996 (see section 4.2.1 or the full report [95]). The chambers showed good aging behaviour and no damage up to a dose of 4.5 C/cm. Therefore it was temporarily concluded that honeycomb chambers are radiation-resistant. However, in the next aging tests of the OTR chambers it was observed that the aging behaviour strongly depends on the type of irradiation: tests in the hadronic radiation environment of HERA-B showed the appearance of aging effects 4 orders of magnitude faster than, for example, with X-rays. It became necessary to make systematic aging studies under conditions as close as possible to those of the real experiment and to find a working set of parameters. These studies have been made within a very restricted time. The sections below describe the investigation program carried out by different crews, in different laboratories, in different countries, using different irradiating facilities. The description was based on the following information sources [63, 64, 104, 45, 9]. As a result of this program, significant changes were introduced into the design, set of parameters, and materials (mainly, the counting gas, the surface coating, glue and gluing technique were affected).

4.2 First tests

4.2.1 Aging test with X-rays in Zeuthen

The first OTR aging test was launched in 1996 in Zeuthen. A detailed report is given in [95]. The main parameters of the test are listed in table 4.1. Four cells of 15 cm long chambers with uncoated Pokalon-C¹ were irradiated with X-rays collimated to a width of 1 cm.

Results. The chambers showed good aging behaviour and no damage up to a dose of 4.5 C/cm.

With the estimated maximum dose per year in HERA-B this test suggested that the chambers would resist radiation much longer than the expected lifetime of HERA-B. The later tests showed that this result could not be extrapolated to the hadronic beam in HERA-B and probably also different chamber size and different gas flow conditions.

4.2.2 Aging test with prototypes in HERA-B

After the radiation resistance of honeycomb chambers had been verified with X-rays, the chambers had to undergo a final check in the true HERA-B environment.

Materials and parameters

Prototypes of the OTR chambers were used to test the aging behaviour under realistic conditions. Three double layer modules with 5 mm cells and three single layer modules with 10 mm cells were installed in HERA-B about 8 m downstream

¹ “Uncoated Pokalon-C” means normal polycarbonate foil enriched with 6% soot without any additional treatment of the surface.

parameter	value
irradiation	X-ray tube, U=35 keV
mixture	CF ₄ /CH ₄ (80:20)
chamber	monolayer/8 cells
chamber length	15 cm
cell diameter	5 mm
cathode	uncoated Pokalon-C
irr. area	1 cm×4 cells
glue	Araldite
box	aluminium box
box window	Kapton foil
tubing	copper, teflon and rubber
current	1.5 μ A/cm
HV	2250 V
integrated dose	4.5 C/cm

Table 4.1: *Main parameters of the test made with X-rays in Zeuthen.*

from the target so that the distance between the beam and the cell nearest to the beam was 20 cm. The parameters of the aging test are summarised in table 4.2. The foils and FR4 strips were glued with Araldite AW-106, the solder points were also covered with Araldite. Besides the 1 m long chambers, also one 10 cm long chamber was irradiated in HERA-B. It might be mentioned here that the detector was almost empty, therefore the radiation level was lower since the background from the secondary interactions was small.

Result

Several hours after the target rate was increased to 40 MHz, the chambers started showing excessive and persistent currents (currents which remain high after the irradiation is interrupted but the high-voltage is still on). A typical time evolution of the currents can be seen in figure 4.1.

The current behaviour suggests that the Malter effect (see section 3.3) seems to have developed in the modules.

During the remaining running time of HERA (until September 1997) various attempts were made to suppress these Malter currents. Because of the time pressure, these tests could not be very systematic and the interpretation of the results was not so easy. Later measures undertaken to get rid of the rest currents were made in a hurry since the time of HERA beam exposures was very limited.

Attempts were made to avoid the Malter effect by adding healing admixtures, water (see description of successful tests, for example, in [26, 79, 59]) or ethanol. An addition of 0.5% water did not suppress the Malter currents. Although at the beginning the addition of ethanol helped to extinguish the Malter effect, however, later it was found that all chambers in the box which saw alcohol for 2 weeks

parameter	value
target rate	up to 40 MHz
mixture	CF ₄ /CH ₄ (80:20)
chamber	3 x single-l. ($l=1$ m, $cd=5$ mm) ^a 3 x double-l. ($l=1$ m, $cd=10$ mm) 1 x mono-l. ($l=10$ m, $cd=5$ mm)
cathode	uncoated Pokalon-C
glue boxes	Araldite ^b prototypes for the proposed half superlayers
tubing	stainless steel
max. current	O(0.06 μ A/cm)
HV	2250 V (5 mm)
integrated dose	few mC/cm

^aThe chamber length is denoted by l and cd is the cell diameter.

^bAraldite AW-106 and hardener HV953V were used before the middle of 1998. The same glue was used in the chamber and in the box production.

Table 4.2: *Materials and parameters of the aging tests made with prototype chambers in HERA-B (1996/97).*

became soft and looked very wavy. Most probably, ethyl alcohol reacts with the glue and Pokalon-C used in the chambers. Additional measures like exchange of CF₄/CH₄ for Ar/CF₄/CH₄² reducing the voltage from 2250 V to 1600 V or transition to Ar/CF₄/CO₂ (50:30:20) did not suppress the effect.

It might be worth to mention here that later tests showed high etching property of Ar/CF₄/CO₂ but it was not known at the time when this test was made otherwise some efforts to continue with Ar/CF₄/CO₂ for a longer time would be made.

All the 1 m long chambers showed development of the Malter effect, while the 10 cm long chamber did not show any degradation. This indicate that the Malter effect depends on chamber size and geometry.

After removal of the chambers from the experiment, the scanning of one of the chambers with ⁵⁵Fe showed local gain losses probably caused by anode aging. The Malter effect could be reignited with the X-rays of a ⁵⁵Fe source.

Although the Malter effect was obviously initiated by a hadronic beam, a visual inspection revealed another aging effect which resulted from the gluing procedure. As was said before, the solder points were covered with Araldite. The glue turned bluish-green after the irradiation. Also, burning processes seemed to have occurred on some solder points during this test in HERA-B.

The cathodes were investigated using Electron Spectroscopy for Chemical Analysis (ESCA, see method description in figure 4.2) made by Bundesanstalt für Ma-

²Here and below Ar/CF₄/CH₄ means the mixture Ar/CF₄/CH₄ (74:20:06) and Ar/CF₄/CO₂ means Ar/CF₄/CO₂ (65:30:05) by default.

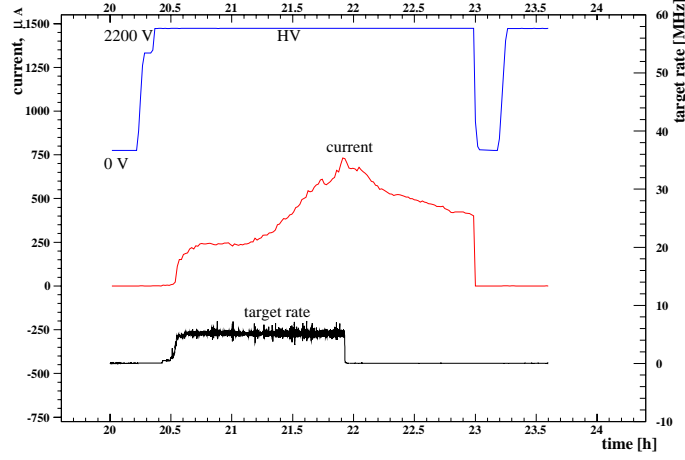


Figure 4.1: *An example of the time evolution of the currents in prototype chambers in HERA-B. As can be seen, at a constant high-voltage and relatively stable target rate the chambers started drawing increasing currents. The current continued even after the irradiation was stopped. The behaviour of the current indicates the development of the Malter effect (see section 3.3).*

terialprüfung in Berlin.

Figure 4.3 shows ESCA spectra of non-irradiated and irradiated foils. As can be seen, besides carbon and oxygen of polycarbonate, fluorine and nitrogen were found on the irradiated foil surface. Furthermore, a high resolution scan of the C-peak indicated that polymer-like films were present on the irradiated surface. The line shape pointed to the presence of C with C-O, C-F and C-N bonds. On non-irradiated foils only C-O bonds were found in the ESCA spectrum. The analysis of non-irradiated Pokalon-C (soot enriched polycarbonate foil) also showed the absence of soot particles on the surface. These results are consistent with later analyses which will be described in section 4.5.1.

The surface of the cathode was also analysed using Raster Electron Microscopy (SEM). The contrast image of the surface under the raster electron microscope is only obtained if the investigated probe is electrically conductive and electrically connected to ground so that no charge is accumulated. The picture was observed to loose contrast suddenly and reproducibly when the electron beam energy decreased to less than 0.9 keV. Such a behaviour can be explained by the presence of an insulating layer with an approximate thickness of 100 nm or less on the surface. The charge would not accumulate if the electrons have an energy high enough to cross the non-conductive film.

Besides the cathode deposit, strong anode aging was observed. The wire deposit was investigated using ESCA. Despite the golden surface of the wire, only 0.15% Au were measured. The deposit consisted of C(73%), O(17%), F(3%),

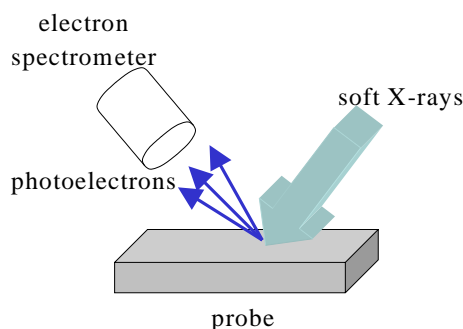


Figure 4.2: *Electron Spectroscopy for Chemical Analysis (ESCA)*. ESCA is used for surface analysis. A probe is irradiated with soft monochromatic X-rays, the kinetic energy of electrons produced via the photoeffect is measured. Typical energies vary from 100 eV to 1000 eV. A layer depth of 30-100 Å can be analysed in polymers [103]. Not only atomic composition but also interatomic bonds are influenced by the electron emission spectrum.

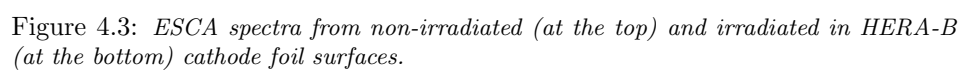
N(2%) and Si(4%). Fluorine was present as CF_2 and half as much as CF. Nitrogen was found as amide (NH_2) and silicon as SiO-polymers.

Discussion

Most likely, the excessive and persistent currents seen in HERA-B were caused by the Malter effect. A model of the Malter effect was explained in section 3.3.

Species containing carbon bounded to fluorine presumably originate from CF_4 dissociation processes in the avalanche. The origin of molecules containing nitrogen is not known, but N could be present in the epoxy hardener HV953V [9]. Also, an outgassing study of different materials and glues showed the presence of 2-pyrrolidinone containing nitrogen in the outgassing of Araldite AW-106 after the glue was cured [46]. Since the glue changed the colour after the irradiation and seems to have burnt on some solder points the outgassing of the glue could be strong enough to make, in combination with avalanche dissociation products, a 100 nm thick insulating deposit on the surface.

The observation of severe aging effects such as the Malter effect and anode aging made an extensive R&D program necessary. To be independent of the HERA-B running and shutdown conditions, the first, very important step in the program was the reproduction of the aging in a test setup outside of HERA-B and to find new operating parameters. Since the Malter effect maybe caused by insufficient surface conductivity of the cathode, it was necessary to change to a more conductive cathode material or to apply a surface treatment. Furthermore, the change of the quencher from hydrocarbons (iC_4H_{10} or CH_4) to CO_2 could stop polymer formation on the cathode. The change of Araldite to another glue with weaker outgassing could be also helpful.



4.3 Aging tests with clear indications of the Malter effect

4.3.1 Aging test with π /proton beam (PSI I)

Setup

The high intensity hadron beam of the ring cyclotron at the PSI³ was used by many groups for aging studies. Having the momentum of 350 MeV/c, pions are minimum ionizing particles (MIPs), protons of this momentum produce an ionization one order of magnitude larger than MIPs, which is probably not yet dangerous. But interacting with nuclei, hadrons can produce heavily ionizing nuclear fragments which have a higher probability to cause damages or aging effects in detectors.

The parameters of the aging tests made with the PSI beam are given in table 4.3. In the setup one 46 cm long, one 30 cm long and two 10 cm long chambers with

parameter	value
mixture	CF ₄ /CH ₄ (80:20)
irradiation	π/p (p=350 MeV/c)
irr. area	$\Delta x=12$ cm, $\Delta y=22$ cm
box	alum., Araldite, Kapton foil
tubing	stainless steel
glue	Araldite
current	0.02 $\mu A/cm$
HV	2250 V
integrated dose	few mC/cm

Table 4.3: *Materials and parameters of the aging test made with the 350 MeV/c hadron beam at PSI.*

uncoated Pokalon-C cathodes and a 30 cm long chamber with a graphite-coated Pokalon-C foil were used.

Results

After 10 hours of irradiation (0.5 mC/cm) the Malter effect started showing up in the long uncoated chambers, but not in the 10 cm long and the graphite coated chamber. Anode aging was not observed.

The fact that the Malter effect in the graphite-coated chamber was not observed made the uncoated Pokalon-C cathode foil suspicious.

³Paul Scherrer Institut, Switzerland

4.3.2 Aging test in a proton beam (PSI II)

Three 30 cm long chambers were tested with 70 MeV protons of the PSI beam. The test parameters are given in table 4.4.

parameter	value
mixture	CF ₄ /CH ₄ (80:20)
irradiation	p, 70 MeV
irr. area	$\varnothing = 3.2$ mm
box	alum., Araldite, Kapton foil
tubing	stainless steel
chamber length	30 cm
cathodes	2 uncoated 1 graphite-coated
glue	Araldite
max. current	0.2 μ A/cm
integrated dose	few mC/cm

Table 4.4: *Materials and parameters of the aging test made with a 70 MeV proton beam.*

Results. When irradiating with a 3.2 mm wide p-beam, no module showed damage up to a few mC/cm. However, the Malter effect was observed in one untreated module when the diameter of the beam was increased. Observed rest currents were in the range of a few μ A. A later scanning check with a ⁵⁵Fe source having high emission intensity “ignited” the Malter effect in the other untreated module. The graphite-coated module did not show rest currents even after intensive X-ray irradiation.

Discussion. A possible explanations of the occurrence of the rest currents after widening the beam is that the wider beam has irradiated a problematic area of the module which was not irradiated before. It was also assumed that the 70 MeV proton beam damaged both untreated modules but produced not sufficient ionization density to make the damage of the second untreated module observable.

As conclusion, we should mention that the π -beam initiated the Malter effect clearer and better reproducible. This fact could be attributed to a higher production rate of nuclear fragments with 350 MeV/c pions than with 70 MeV protons.

4.3.3 Exploratory aging test with an α -beam (Karlsruhe I)

This introductory test was made with the highly ionizing 100 MeV α -beam of the cyclotron in the research center “Forschungszentrum Karlsruhe GmbH” to probe for the Malter effect aiming to find a “good” test facility for a more systematic investigation.

Setup. Two 10 cm long honeycomb chambers, uncoated and graphite-coated, filled with Ar/CF₄/CH₄ were irradiated up to few mC/cm.

Results:

- The uncoated chambers showed the Malter effect after approximately 5 mC/cm.
- The graphite-coated chamber did not show the Malter effect but a slowly decreasing current indicating decreasing gain, probably, due to anode aging.

Thus the 100 MeV α -beam was proven to be a good tool for studies of the Malter effect and was used for further investigations (see section 4.6).

4.4 Aging tests without clear evidence of the Malter effect

4.4.1 Other aging tests with X-rays

Aging test in Heidelberg

The test parameters are summarised in table 4.5.

parameter	value
irradiation	8 keV photons from Cu-anode
gas	Ar/CF ₄ /CH ₄ (74:20:6)
box	alum., Araldite, Kapton foil
cathode	1 uncoated Pokalon-C 1 graphite-coated Pokalon-C
chamber length	46 cm
glue	Araldite
irr. area	whole chambers
current	O(0.1 μ A/cm)
integrated dose	few mC/cm

Table 4.5: *Materials and parameters of the aging test made with X-rays in Heidelberg.*

Results. No Malter effect but 40% gain drop was observed in both chambers.

The gain loss is likely caused by anode aging, which was also observed in other tests with Ar/CF₄/CH₄. Since in the X-ray tests the Malter effect was not observed, it was concluded that the Malter effect prefers hadronic beams.

Aging test in Zeuthen using Ar/CF₄/CH₄

The aging test was made with the same parameters as the test described in section 4.2.1 except that the mixture CF₄/CH₄ was replaced with Ar/CF₄/CH₄. The

objective was to validate the gain loss observed in Heidelberg (see the subsection above).

Results: although the chambers obtained up to 5 C/cm, no aging effects was observed.

The difference between aging results of this test and those of the test made in Heidelberg could be a result of the considerable difference in some parameters like chamber size or irradiated area.

Aging test in Dubna

The parameters of the test are listed in table 4.6.

parameter	value
irradiation	8 keV photons from Cu-anode
gas	Ar/CF ₄ /CO ₂ (30:20:50)
chambers	5 uncoated Pokalon-C chambers
glue	Araldite
irr. area	$\Delta y=0.5$ cm
current	5 μ A/cm
HV	2000 V
integrated dose	6 C/cm

Table 4.6: *Materials and parameters of the aging test made with 8 keV photons in Dubna.*

Results: No aging effects were observed in this test. The only significant difference with the Heidelberg X-ray test was a different gas, Ar/CF₄/CO₂ (30:20:50), instead of Ar/CF₄/CH₄ (74:20:6). These test results gave a hint that the choice of the gas can be essential for anode aging.

4.4.2 Irradiation test with α -particles (Rossendorf I)

The test parameters are summarised in table 4.7.

It should be remarked that the intensity control was difficult in this test. Thus a gain measurement was impossible.

Results. No Malter effect was observed in the coated chambers. Although Malter-like currents of O(5 μ A) were observed in one uncoated chamber, it could not be reproduced in the others.

Discussion. The test did not clearly show the Malter effect even with a rather heavily ionizing α -beam. The fact could be attributed to the too low α -particle energy, which limits the production of nuclear fragments.

4.4.3 Test in 13 MeV proton beam (Rossendorf II)

The parameters of the test are given in table 4.8.

parameter	value
irradiation	α , 28 MeV α -particles stop in the first module
gas	Ar/CF ₄ /CH ₄ (74:20:6)
chambers	5 monolayers×16 wires
chamber length	30 cm
cathodes	2 uncoated 2 graphite-coated 1 Cr-coated
glue	Araldite
irr. area	$\Delta y=1$ cm
current	0.6 $\mu\text{A}/\text{cm}$
HV	1600 V
integrated dose	3 mC/cm

Table 4.7: *Materials and parameters of the aging test made under irradiation with α -particles.*

Results: A gain loss could not be measured because of intensity fluctuations. Although the Malter effect was not observed at the nominal high-voltage of 1600 V, an increase up to 1750 V (equivalent to a gain boost factor of ≈ 5) resulted in the appearance of rest currents of 10-15 μA in the uncoated chamber. In spite of the HV increase, no Malter effect was observed in the graphite-coated chamber.

4.4.4 Other aging tests

Aging tests with electron irradiation

It should be remarked, that the Malter effect had never been observed in X-ray aging tests of the OTR chambers but sometimes observed in hadronic beams after some mC/cm. To perform study of the dependence on the beam particle type, the chambers were irradiated with electrons in the energy region of up to 2.5 MeV using the beam of the Van der Graaf accelerator of the Hahn Meitner Institut (HMI) in Berlin. The test parameters are listed in table 4.9. Before this test was made, the chamber had been irradiated with X-rays up to 0.6 C/cm without showing any of the aging effects. The chambers had 10 mm wide FR4 wire-supporting strips in the middle as in the HERA-B aging test with the prototypes.

Results. No Malter effect and no anode aging but currents starting at about 200 V with a non-linear current-voltage dependence were observed.

parameter	value
irradiation	protons, 13 MeV
gas	Ar/CF ₄ /CH ₄ (74:20:6)
chambers length	30 cm
cathodes	1 uncoated Pokalon-C 1 graphite-coated
glue	Araldite
irr. area	9x9 cm ²
current	0.3 μ A/cm
HV	1600 V \rightarrow 1750 V
integrated dose	5 mC/cm

Table 4.8: *Materials and parameters of the aging test made with 13 MeV protons.*

parameter	value
irradiation	electrons, 2.5 MeV
gas	Ar/CF ₄ /CH ₄ (74:20:6)
chambers length	1 m
cathodes	1 uncoated Pokalon-C
glue	Araldite
irr. area	whole chambers
current	0.01-3.6 μ A/cm
HV	1600 V
integrated dose	10 mC/cm

Table 4.9: *Materials and parameters of the aging test made with a 2.5 MeV electron beam.*

Aging tests with α -source

In view of the fact that the Malter effect tends to appear under hadronic irradiation, it could be assumed that the reason for this tendency is that hadrons produce higher ionization densities. Then, the Malter effect could appear in chambers irradiated with a ²⁴¹Am source, which emits α -particles with an energy of 4.5 MeV. Aging tests were made with 10 cm long, differently coated chambers filled with Ar/CF₄/CO₂ or Ar/CF₄/CH₄. The cathodes were perforated since low energy α -particles cannot cross the cathode foil.

Results. Although the Malter effect was not distinctly seen, a gain loss was observed with Ar/CF₄/CH₄ (76:20:6) but not with Ar/CF₄/CO₂ (65:30:5).

Discussion. The fact that the Malter effect was not reproducible with α -particles of a ²⁴¹Am source could not be clearly explained. The reasons could be as follows: too small chambers and irradiation spot or too low energy of α -particles, not sufficient to cause nuclear fragmentation.

4.5 Definition of materials, production processes, operating parameters

4.5.1 Coating of the cathode

As it was shown in different aging tests (PSI, Rossendorf), the graphite coating of Pokalon-C seems to prevent the Malter effect.

AFM⁴ investigations did not reveal any significant differences between pure polycarbonate foil and Pokalon-C (soot enriched polycarbonate foil). This fact could be explained by the absence of soot particles on the Pokalon-C surface (this was observed by ESCA and mentioned in section 4.2.2 above), which could somehow relate to the occurrence of the Malter effect.

Search for a replacement of polycarbonate failed because the foil should satisfy the following requirements:

- high bulk and surface conductivity,
- small multiple scattering depending on the amount of material in the sensitive volume,
- mechanical folding and tempering must be possible.

Sticking to Pokalon-C as the basic cathode material, it became clear that the surface has to be treated applying coating (graphite, chromium, gold, copper, etc). Plasma etching has also been tested. The Malter effect had never appeared in chambers if any of the cathode foil treatments mentioned above was applied.

The final choice was a Pokalon-C foil coated with 50 nm thick layer of copper and a 40 nm thick layer of gold. This choice was based on:

- production possibility,
- chemical inertness,
- mechanical rigidity.

4.5.2 Tests of the glue

Since the solder points on the FR4 strips, covered with Araldite, appeared to be not HV stable, the influence of glue in aging tests was also studied. A series of more than 20 irradiation tests were made in Zeuthen with X-rays, using 10 cm long uncoated Pokalon-C chambers. Sparking processes were observed if the solder points were covered with glue. Therefore, it was decided not to apply glue on solder points in the later production.

In outgassing tests of different glues made in CERN using the RD-10 analysis system [46] also Araldite glue was investigated. The system consists of:

- Mass Spectrometer (MSD), which has a sensitivity of the order of ppm.

⁴Atomic Force Microscopy. The device measures the attraction of a needle by the surface molecular forces.

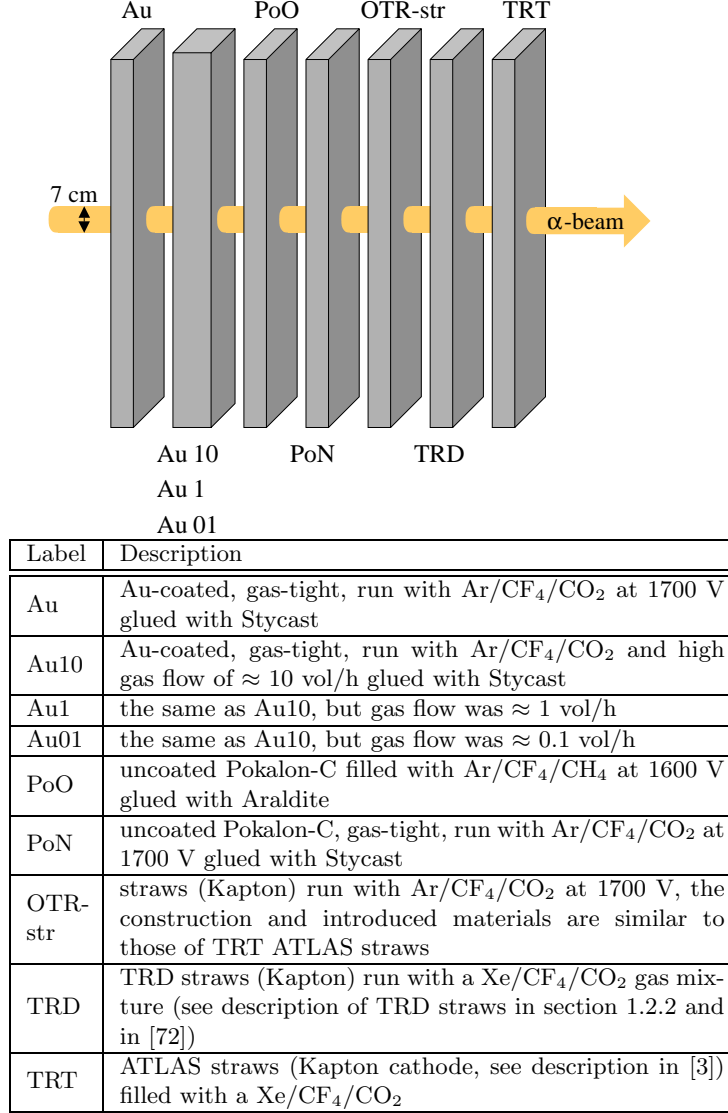


Figure 4.4: Schematic view of modules irradiated with the α -beam (top) and description of the test chambers (bottom).

- Electron Capture Device (ECD), which detects only electronegative species with a sensitivity of the order of one ppb.

Araldite was observed to intensely outgas different hydrocarbons. The presence of C-N bonds in cathode deposits (see section 4.2.2) can also be attributed to outgassing of this glue since 2-pyrrolidinone, containing nitrogen, was also detected by the RD-10 system. A good substitute for Araldite could be Stycast, which was found to have very low outgassing and does not cause aging (according to the numerous OTR tests).

As a result of the tests performed since the beginning of 1998, Stycast (see table 1.3) was used in the production of chambers and boxes until today.

4.5.3 Choice of the mixture

It could be concluded from aging test described in sections 4.2.2 (in HERA-B, with CF_4/CH_4), 4.5 (with X-rays, with $\text{Ar}/\text{CF}_4/\text{CH}_4$), 4.3.3 (in α -beam, with $\text{Ar}/\text{CF}_4/\text{CH}_4$) that the use of mixtures containing hydrocarbons sometimes results in anode aging. However anode aging was never observed with $\text{Ar}/\text{CF}_4/\text{CO}_2$ mixtures. Furthermore, chambers with uncoated Pokalon-C cathodes filled with CF_4/CH_4 and $\text{Ar}/\text{CF}_4/\text{CH}_4$ mixtures sometimes showed the Malter effect, which was probably caused by some polymerization processes initiated by hydrocarbons. However, in numerous aging tests with an α -source (see section 4.4.4) using $\text{Ar}/\text{CF}_4/\text{CO}_2$, the Malter effect was not observed.

On the basis of the previous tests the mixture $\text{Ar}/\text{CF}_4/\text{CO}_2$ was found to be a promising candidate for the OTR, therefore, it was extensively explored in the further aging tests.

4.6 Validation of parameters with α -beam

4.6.1 Second aging test in Karlsruhe (Karlsruhe II)

Since the aging test with the 100 MeV α -beam of the cyclotron in the research center “Forschungszentrum Karlsruhe GmbH” showed a rapid development of the Malter effect (see section 4.3.3), this facility was chosen for more extensive aging studies.

The aging test had the goal to validate:

- the gas mixture $\text{Ar}/\text{CF}_4/\text{CO}_2$,
- the Au/Cu-coating of the cathode,
- the glue Stycast and other parameters.

Setup. The setup of the aging test and the main test parameters are shown in figure 4.4 and table 4.10, respectively.

It has to be noted that “gas-tight” means that the gas input and the output of the chamber were made up of stainless steel capillaries conveying the gas to every

parameter	value
irradiation	α -beam, 100 MeV
chambers	monolayers/16 cells
chamber length	40 cm
cell diameter	5 mm
irr. area	$\varnothing=7$ cm
tubing	stainless steel
box	alum., Stycast, Kapton foil
current	$0.2 \mu\text{A}/\text{cm}$
integrated dose	$0.3 \text{ C}/\text{cm}$

Table 4.10: *Main parameters of the aging test “Karlsruhe II”.*

cell and controlling the flow. In contrast to the previous tests were the chambers had standard open geometry, in this test the gas inside the cells was completely separated from the gas outside of the cells in the gas box. All the chambers were “gas-tight” except chamber “PoO”, which had standard, open geometry. For the production of “PoO” and its box Araldite was used. All the other chambers and boxes were produced with the new glue, Stycast (see table 1.3). In addition, straw chambers were tested because of their good aging characteristics (see, for example, [4]). The water content in boxes is believed to have been rather high because of the use of Kapton foil windows, which are water-transparent. The humidity was unfortunately not measured, however, according to some estimations, the moisture content was about 3000 ppm.

Results

Both untreated Pokalon-C chambers showed anode aging and the Malter effect. Figure 4.5 shows an example of development of Malter-like currents in the Karlsruhe setup. As the figure shows, the development of high currents during the irradiation and persisting after the beam was switched off was observed after $10 \text{ mC}/\text{cm}$ in uncoated Pokalon-C chambers. After replacement of $\text{Ar}/\text{CF}_4/\text{CH}_4$ by $\text{Ar}/\text{CF}_4/\text{CO}_2$ the Malter effect disappeared and the gain was even recovered (see figure 4.6).

The other chambers did not show problems for doses below $0.2 \text{ C}/\text{cm}$. At about this dose the Au-plated chambers started drawing strong dark currents which increased continually during the irradiation and reached several $\mu\text{A}/\text{cell}$. A test showed that the currents were not Malter-like but showed rather ohmic behaviour. After opening the chamber it was found that the currents were caused by an increased conductivity of wire-supporting strips in the irradiated cells (see the chamber construction in figure 1.7). The bottom strips of chamber Au01, positioned at the lower end of the chamber and 10 cm away from the center of the irradiated region, had about 1000 times higher conductivity than the upper strips, positioned at the upper end of the chamber and 20 cm away from the center of

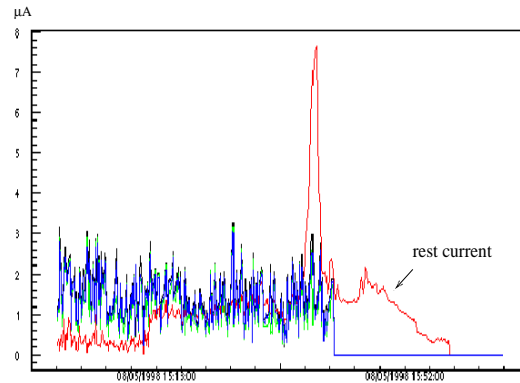


Figure 4.5: Example of the Malter effect at the α -beam. The current in uncoated module is denoted by red curve. The curves of other colours are currents in some other modules. Development of excessive currents was observed in uncoated module during the irradiation. After the beam had been switched off, the uncoated Pokalon-C chamber drew high persistent currents whereas the other modules did not.

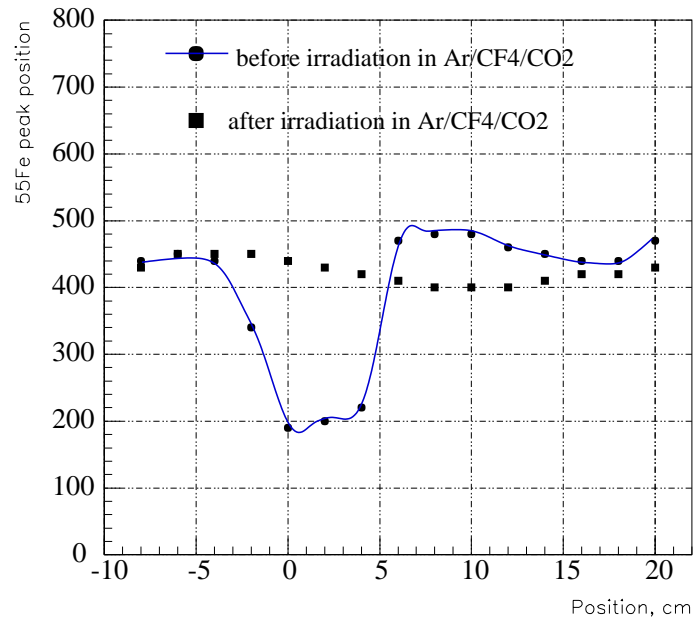


Figure 4.6: The chamber PoO lost gain during irradiation using $\text{Ar}/\text{CF}_4/\text{CH}_4$, however, recovered almost completely in $\text{Ar}/\text{CF}_4/\text{CO}_2$.

chamber	Au10	Au1	Au01
R	50 GOhm	100 MOhm	30 MOhm

Table 4.11: *Typical resistance of the bottom FR4 wire-supporting strips in irradiated cells of the chambers with a gold-plated cathode. The strip resistance seemed to vary inversely with the flow.*

the irradiated region (The chambers were positioned like in the OTR and in most of the aging tests: the wires were directed vertically and the strips horizontally). It should be remarked that although the gas conveyed by the capillaries flowed upwards along the chambers (as in many other aging tests), the flow was very slow in this chamber (0.1 vol/h) and diffusion played a dominant role in the gas exchange.

The typical resistance of the bottom strips is given in table 4.11. As can be seen, in chambers with the higher flow conductivity was smaller. The strips in the PoO drew a dark current several orders of magnitude lower than those of Au-coated ones.

The bottom FR4 strips looked very damaged in irradiated cells but could not be analysed by electron microscopy. Only conductive probes can be investigated using this method. This new effect, conductivity of the wire-supporting strips, was extensively studied in this thesis and will be described in chapter 5.

Energy Dispersive X-ray Spectroscopy analysis (see figure 4.7) of wires, cathodes and solder points on the FR4 strips of PoN chambers showed the presence of Si, O, Al, Mg and traces of C on an investigated wire of PoN, but Au01 had wires with very clean golden surface. Solder points were not shiny in Au01. Fluorine was present on the solder points (more in Au01 and less in PoN). In Au01 a much smaller amount of fluorine was observed on the solder points of the upper strips positioned further from the irradiated region than on those of the bottom, “near” strips. The cathode of Au01 was covered with brown spots which was found to be Cu, however, such spots were not observed in PoN.

4.6.2 Third aging test in Karlsruhe (Karlsruhe III)

As was shown above, the previous test “Karlsruhe II” failed to validate the important parameters due to the development of rather strong dark currents. However, there were some indications that the dark current was a consequence of the high humidity of the gas, since water-transparent Kapton windows were used. It was necessary to repeat the test with a dry gas. Therefore, the Kapton foil windows were additionally covered with an aluminized Mylar foil. The humidity in the gas box was controlled.

Purpose. The main objectives of the test were:

- to validate the set of parameters and construction materials found in the previous tests: the gas mixture Ar/CF₄/CO₂, Cu/Au-coating of the cathode foil (see section 4.5.1), glue for the chamber production;

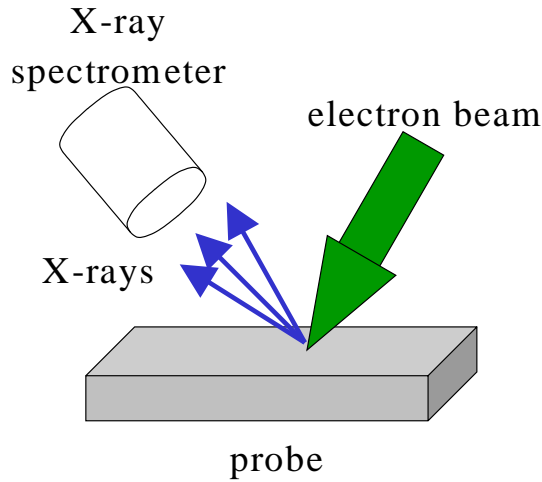


Figure 4.7: *Energy Dispersive X-ray Spectroscopy (EDS) is a supplement to the raster electron microscope. X-ray fluorescence radiation of materials is emitted when an electron in a neutral atom is removed from an inner shell by bombarding the atom with electrons of the raster beam. The shells in an atom, designated as $n = 1, 2, 3, 4, 5$ by optical spectroscopists, are labeled K, L, M, N, O . . . by X-ray spectroscopists. If an electron is removed from a particular shell, electrons from all the higher-energy shells can fill that vacancy, emitting photons in a spectrum of series of lines characterizing the probe material. The shortest discrete wavelengths are produced by materials having the highest atomic numbers. The resultant series of X-ray lines, the characteristic spectrum, is superimposed on a spectrum of continuous radiation resulting from accelerated electrons (bremsstrahlung). Such methods are used in the analyses of materials of unknown composition.*

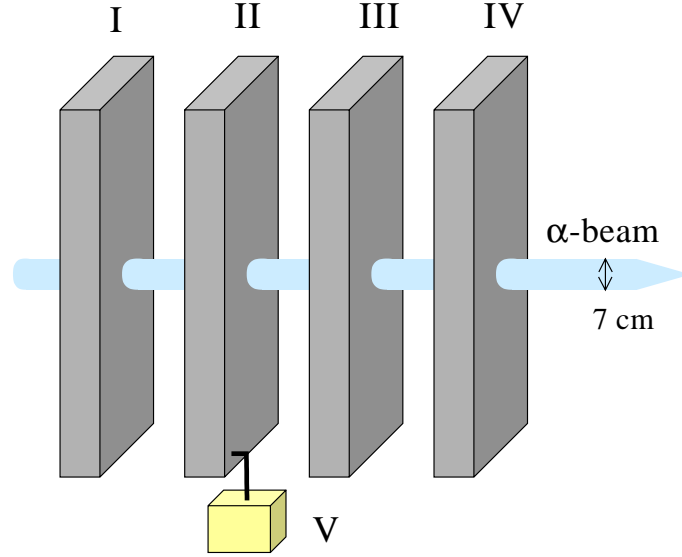
- to find out the origin of the wire-supporting strip conductivity (therefore, the chambers contained strips in irradiated and non-irradiated areas);
- to answer additional technology questions like the presence of colophony on the solder points and anticontact paste⁵ “QZ5111” on the foil.

Setup. Four 16-cell modules were installed in separate gas boxes as shown in figure 4.8. The main test parameters are listed in table 4.12.

To avoid anode aging, which appeared in all the chambers working with Ar/CF₄/CH₄, the mixture Ar/CF₄/CO₂ was used. Since the Malter effect occurred in uncoated Pokalon-C chambers, Au/Cu-coating was applied to the foils.

To check the influence of colophony on the aging behaviour, on the one side of the chambers the surface of the solder points was cleaned, on the other side it was not.

⁵Anti-contact paste was applied on the templates during the module production to avoid the adherence of the foil to the template material.



Label	Description
I	a box with Cu/Au-coated Pokalon-C chamber with one FR4 wire-supporting strip separating 75 μm thick Cu/Be and 25 μm thick gold-plated wires in the middle of the irradiated spot
II	a box with Cu/Au-coated Pokalon-C chamber (without FR4), the gas inputs of some of the cells were connected to an outgassing box V containing Cu/Au-coated foil with anti-contact paste
III	a box with Cu/Au-coated chamber, with a Kapton strip in the middle, filled with Ar/CO ₂ (80:20)
IV	a box with an uncoated Pokalon-C chamber

Figure 4.8: *Karlsruhe III setup (top) and description (bottom).*

All the chambers were equipped with Rilsan capillaries only at the bottom (upper ends of the chambers were open to the gas box). Some of the chambers had FR4 strips directly irradiated and other strips placed in the non-irradiated area.

parameter	value
irradiation	α , 100 MeV
gas	Ar/CF ₄ /CO ₂ (I,II,IV) Ar/CO ₂ (80:20) (III)
box frame	aluminium
windows	Kapton foil & aluminized Mylar foil
chambers length	40 cm
irr. area diam.	7 cm
current	0.2-0.9 μ A/cm
humidity (inp)	<10 ppm
humidity (box outp)	O(300 ppm)
integrated dose	1.1 C/cm (I, II) \approx 0.5 C/cm (III, IV)

Table 4.12: *Main parameters of the aging test “Karlsruhe III”.*

Results. Up to a dose of 1.1 C/cm the chambers showed no Malter effect, however, some gain loss was observed. The largest gain drop was 11% in one cell which did not see outgassing of anticontact past as shown in figure 4.9. The typical gain drop was less than 6%.

However, no organic deposit was observed under the optical and electron microscopes. The gold layer on a gold-plated tungsten wire in the irradiated region seems to have partially split off, as can be seen in figure 4.10. Almost on every irradiated wire splits were visible. EDS showed tungsten on the wire, on some places the signal of W dominated. Thus a new effect was observed, which will be further referred to as wire “etching” or “corrosion”.

No dark current was observed in any chamber unless water was added to the counting gas by means of a bubbler. The humidity dependence of the dark current was measured relatively fast for several tens of hours varying the humidity in module I after a dose of 1.1 C/cm interrupting the irradiation. The dependence of the dark current on the water content in module I is shown in figure 4.11. According to this figure, the assumption that high water content was the reason for strong dark currents in the test “Karlsruhe II” was experimentally substantiated.

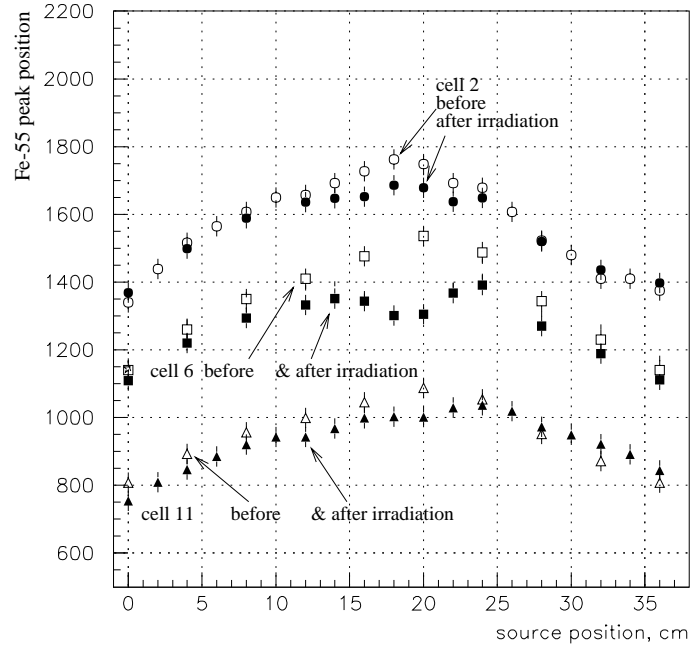


Figure 4.9: Scanning with ^{55}Fe along wires of module II (according to figure 4.8). Gain loss of the order of about 11% was observed in one cell. No significant aging was observed in cell 11, which was exposed to the outgassing of anticontact paste. Inhomogeneity of the gas gain along the cells, which was measured before the irradiation test started, is probably an effect of the mechanical flexibility of monolayers.

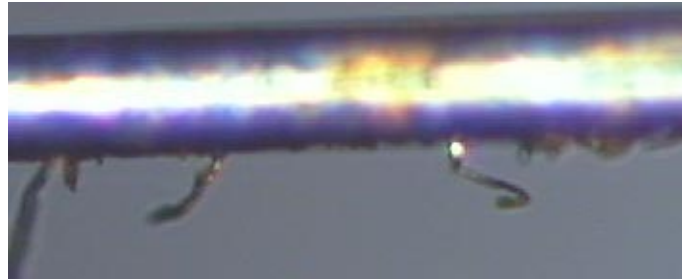


Figure 4.10: Middle wire of module I (see figure 4.8) in the irradiated region near the strip. It shows the splitting of the Au-layer.

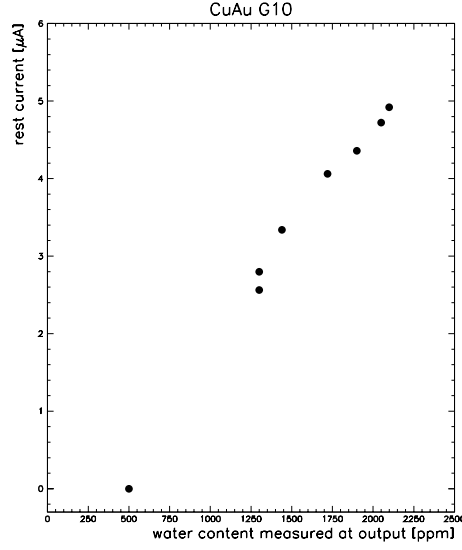


Figure 4.11: *The total dark current in the module I as a function of water content.*

4.7 Summary

Using different beams, materials, gas mixtures, the Malter effect observed in HERA-B was reproduced in some cases. Table 4.13 summarizes the development of anode aging and the Malter effect in different tests.

As was shown, X-rays, electrons, low energy protons and α -source could not unambiguously generate the Malter effect. However, the effect observed in HERA-B could be reproduced in a 350 MeV/c π /proton beam and in a 100 MeV α -beam in Karlsruhe. Most probably, this is an effect of high ionization density. Difference to e.g. α -source is probably higher local energy deposition by nuclear fragments resulting from nuclear interactions (flight-length of fragments is very short). Positive ions and radicals, which are produced in the plasma, bombarding the cathode could favour polymerization. The latter leads to formation of an insulating layer on the surface.

Three important changes were introduced as a result of the systematic investigations:

- untreated Pokalon-C foil was coated with copper and gold to avoid the Malter effect;
- mixtures containing CH_4 (CF_4/CH_4 , $\text{Ar}/\text{CF}_4/\text{CH}_4$) were replaced by the gas $\text{Ar}/\text{CF}_4/\text{CO}_2$ to avoid anode aging;
- glue Araldite was replaced by Stycast to reduce the problems with outgassing components.

Test facility	Charge	Gain loss	Malter effect	Section
no (unclear) Malter effect				
all X-ray tests	<5 C/cm	yes (Ar/CF ₄ /CH ₄) depending on ch. size	not observed but could be (re)ignited from X-rays	4.2.1 4.4.1 4.2.2 4.3.2
2.5 MeV e ⁻ -beam	≈ 10 mC/cm	no measurement	no	4.4.4
28 MeV α -beam	≈ 3 mC/cm	=	unclear (Ar/CF ₄ /CH ₄ , untreated c.)	4.4.2
13 MeV p-beam	≈ 5 mC/cm	=	unclear (Ar/CF ₄ /CH ₄ , untreated c.)	4.4.3
4.5 MeV α 's from ²⁴¹ Am	≈ 150 mC/cm	yes (Ar/CF ₄ /CH ₄)	unclear (Ar/CF ₄ /CH ₄ , untreated c.)	4.4.4
clear Malter effect				
HERA-B	few mC/cm	yes (CF ₄ /CH ₄)	yes (CF ₄ /CH ₄)	4.2.2
350 MeV/c π /p-beam	few mC/cm	no measurement	yes (CF ₄ /CH ₄ , untreated c.)	4.3.1
70 MeV p-beam	≈ 3 mC/cm	=	yes (CF ₄ /CH ₄ , untreated c.)	4.3.2
100 MeV α -beam	≈ 10 mC/cm	yes (Ar/CF ₄ /CH ₄)	yes (Ar/CF ₄ /CH ₄ , untreated c.)	4.6.1

Table 4.13: *Appearance of aging effects in different tests. If effects appeared, the conditions of the effects are also given.*

Aging tests of gold-plated Pokalon-C chambers glued with Stycast and filled with Ar/CF₄/CO₂ did not show a significant gain drop and the Malter effect but revealed two new effects: development of conductivity of wire-supporting strips and wire etching. The first effect, as was shown in the test Karlsruhe III, can be suppressed by reducing the water content in the chambers to a level of less than 500 ppm. Strip conductivity behaviour was also extensively studied in X-ray tests, as described in the section 5.1. Wire etching was studied and will be described in section 5.2. The studies which will be discussed in the following chapters pursued the aim to study the main observations in more detail.

Chapter 5

Aging tests with X-rays

5.1 Aging studies of 10 cm long chambers

5.1.1 Aging study on FR4 strips

Introduction

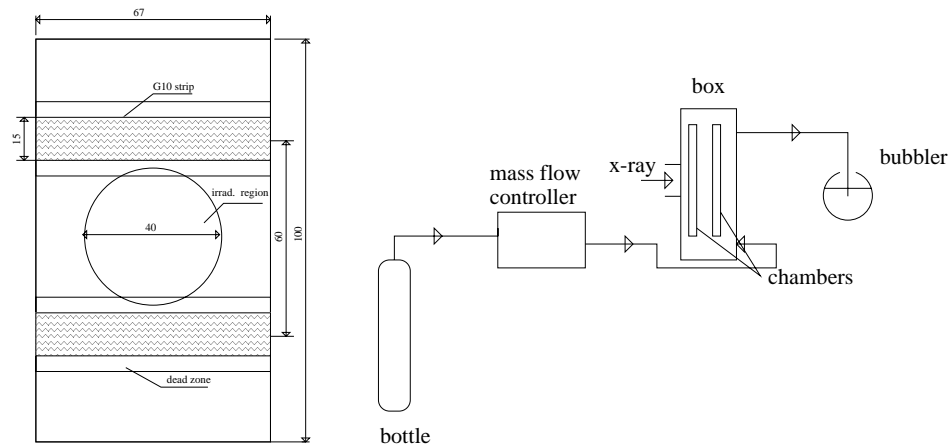


Figure 5.1: *Schematic view of the chamber nearest to the X-ray tube (left) and gas flow in the X-ray setup (right). The length of the chamber is 10 cm. End-pieces, FR4-strips and other materials used in building of this chamber were identical to those used in the OTR chambers.*

An important result of the test “Karlsruhe II” (see section 4.6.1) is that the FR4 support strips became conductive after irradiation of the cells with the α -particle beam. After accumulation of 0.3 to 0.4 C/cm (corresponding to 0.5 years

of OTR operation in HERA-B) the dark current in the irradiated cells of the Au01 chamber was $O(1 \mu\text{A}/\text{cell})$.

To study the behaviour of FR4 strips in a harsh radiation environment (and to search for other effects in addition), a series of tests was made.

Setup

Two gold-plated Pokalon-C mono-layer (honeycomb made up of only two folded foils) chambers of 10 cm length each consisting of 8 cells were manufactured for irradiation with an X-ray tube (Mo at -35 kV). They were placed in a box vertically, one after another. The chamber nearest to the X-ray tube was equipped with two 15 mm FR4 strips located on both sides of the irradiated region (see figure 5.1), the other chamber with a strip of the same type located in the middle of the chamber, directly in the irradiated region.

The gas flow in the X-ray setup is shown in the right part of figure 5.1. The gas flowed from a bottle through a stainless steel pipe of about 18 m length through a mass flow controller into the inlet at the bottom of the box. The output at the upper part of the box was connected to an about 3 m long pipe which was insulated from the atmosphere by a bubbler filled with vacuum oil “ALCATEL-Spezial-Öl”. The test was performed using the nominal mixture $\text{Ar}/\text{CF}_4/\text{CO}_2$ (65:30:5) and an operating voltage of 1700 V.

Each irradiated wire was connected to an individual microammeter as shown in figure 5.2. The chambers had no capillaries just as the OTR chambers. The gas box with a volume of about 500 cm^3 had two aluminized Mylar windows.

X-ray aging tests (Tests 1,2,3)

Measured parameters. During the aging tests the following parameters were measured: the current in every irradiated cell, the total dark current, the ambient temperature (in the X-ray setup: the temperature of the box), atmospheric pressure, humidity of air. After some periods of irradiation ^{55}Fe spectra were taken from each irradiated and non-irradiated cell.

Purity test of the gas system. Besides the desired gas mixture a gas system always contains pollutants. Their possible chemical reactions can significantly influence the results of aging tests. Therefore, it is necessary to check the contamination of the gas system before an aging test. The pollution takes place due to leaks, diffusion of air through the windows or outgassing from materials in the gas system. Also, some species can be produced by plasma chemistry in the avalanche.

Gas leaks were checked with a “Guepo” leak detector. Furthermore, leaks were controlled with an exhaust gas bubbler. When the gas flow was set to zero, a remaining bubble in the gas bubbler should stay for several minutes, indicating excellent gas-tightness.

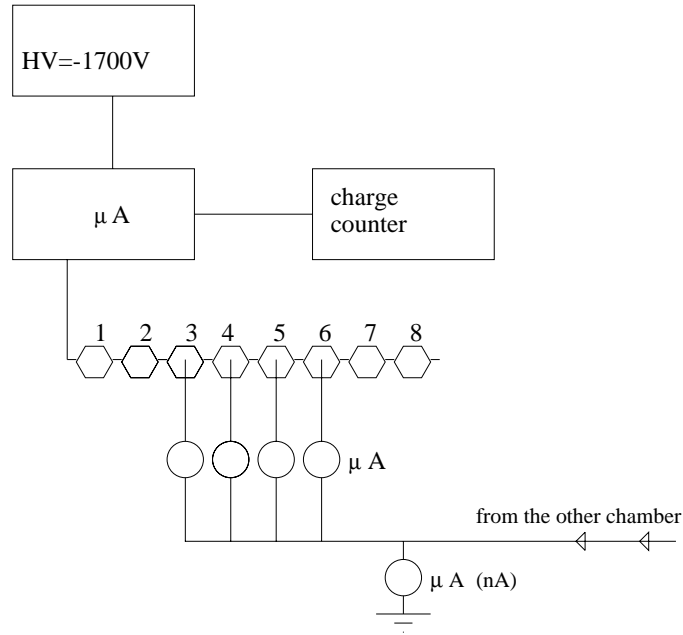


Figure 5.2: Scheme of current measurement for one of the test chambers in the X-ray setup.

Electronegative contaminants like oxygen lead to a drop of the gas gain.¹ As was shown in [105], the intensity of oxygen outgassing by plastic drops considerably for several hours after separation of plastic from air. Then the oxygen content is defined by transparency of the gas box and tubing. In order to detect the oxygen in our test, ^{55}Fe pulse height spectra were taken at gas flow rates of 0.1 volume/h and at 10 vol/h. If the difference in amplitudes was less than 10%, the gas tightness was considered to be acceptable.

Results. In these tests the chambers obtained the following irradiation doses:

Test 1: 1 C/cm

$$(F = 1 \text{ vol/h}, i \approx 1.8 \mu\text{A/cm}),$$

Test 2: 0.22 C/cm

$$(F = 1 \text{ vol/h}, i \approx 0.75 \mu\text{A/cm}),$$

¹Since the electron impact cross section of water attachment is comparable, for example, with that of CF_4 and resonance attachment is at the high electron energy of about 7 eV [22] (i.e. in a small region near the wire), an influence of water on the gain for water concentrations of less than 1% can be neglected.

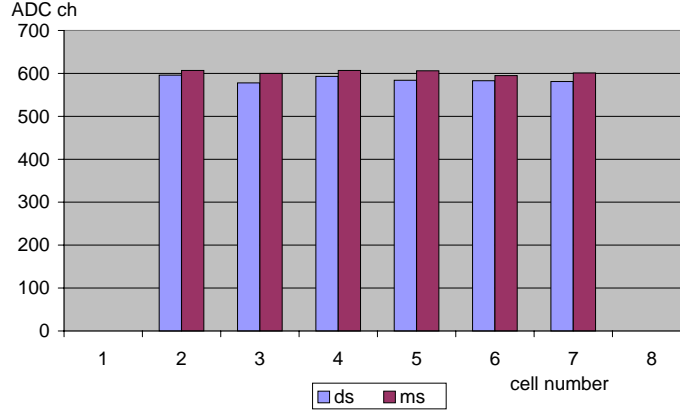


Figure 5.3: Mean of ^{55}Fe spectra in cells of X-ray setup in the new chambers. The cell of the double strip chamber are denoted by “ds”, those of the mono-strip chamber by “ms”.

Test 3: 0.37 C/cm
($F = 0.1$ vol/h, $i \approx 0.75$ $\mu\text{A}/\text{cm}$)

where i is the current density.

After each test ^{55}Fe pulse height spectra were taken. They did not show any observable reduction in the gas gain in the irradiated region. Quite the contrary, a slight increase in the gas gain, about 3%, was observed in irradiated cells (see figure 5.4). Such a tendency was certainly not observed before irradiation (see figure 5.3).

After **Test 1** the dark current measured about one hour after stop of the irradiation was, on the average, about 100 pA in the irradiated cells, which was about five times higher than in the non-irradiated ones (see figure 5.5).

As can be seen in figure 5.6, during **Test 2** the dark current was, on the average, 250 pA/cell (measured immediately after the stop of irradiation).

In **Test 3** the dark current was increasing continuously from about 250 pA/cell to about 700 pA/cell. This increase can be explained by an increase in the water concentration at the lower gas flow (see the section below) because of a possible contamination of the gas system by water.

After having been irradiated (**Tests 1,2,3**) the X-ray chambers were in air for about 2 days (the gas box was open). Closing the gas box and starting to flush with the mixture $\text{Ar}/\text{CF}_4/\text{CO}_2$ we observed high dark currents, on the average, about 3 $\mu\text{A}/\text{cell}$ in each irradiated cell (the HV was as usual 1700 V). The non-irradiated ones showed a dark current two orders of magnitude lower. We did not irradiate the chambers and observed the time evolution of the dark current. About 1.5 h later the dark current was measured again in each cell yielding an average value of about 0.4 $\mu\text{A}/\text{cell}$. The dark current measured after 12 hours was 10 times lower. The time dependence seemed to be an exponential-like convergence to zero.

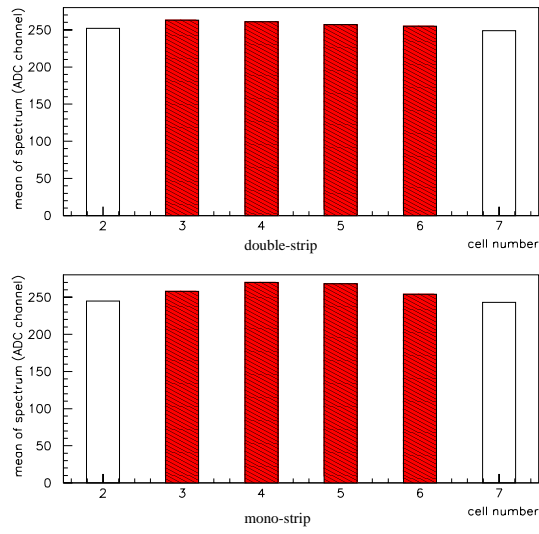


Figure 5.4: Mean of ^{55}Fe spectra in cells of X-ray setup after **Test 3**. Red bars indicate measurements in irradiated cells, unfilled bars in non-irradiated ones.

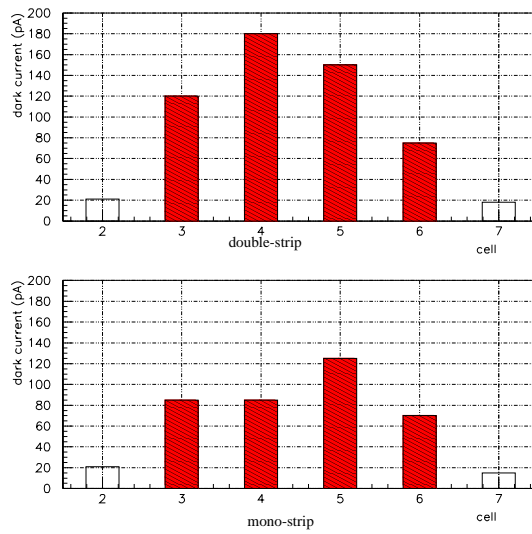


Figure 5.5: Distribution of dark currents in cells of X-ray setup chambers after **Test 1**.

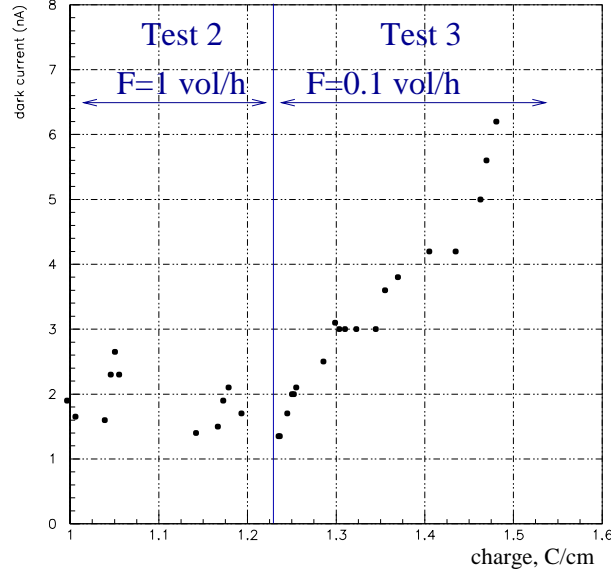


Figure 5.6: Dark current in **Tests 2** ($F=1$ vol/h) and **3** ($F=0.1$ vol/h) as a function of accumulated charge. The dose accumulated in **Test 1** was added.

The very large dark current after closing the chambers was probably induced by water contained in air. To test this hypothesis, we added water vapour into the gas system of the X-ray setup by means of a water bubbler.

Aging test with addition of water (Test 4)

Approximately a week after we made **Test 3** described in the previous section, we added water via a bubbler. The chambers were irradiated to a dose of about 0.6 C/cm at a current density of $0.5 \mu\text{A}/\text{cm}$ and a gas flow rate of 0.5 vol/h. The evolution of the dark current during this irradiation from the moment when we applied the HV is shown in figure 5.7. The addition of 0.6% of water at a gas flow rate of 0.5 vol/h resulted in a mean dark current of about 50 nA/cell in the previously irradiated cells. The dark current in the non-irradiated cells was, on the average, about 250 pA/cell. One of the cells, which had shown the largest dark current before, went out of operation during the test. As was seen later, a kind of “carbon bridge” was formed on the strip, between a solder point and the cathode.

Although with addition of water the dark current showed fluctuations in the region from 100 nA to 200 nA, its final value of about 170 nA or 40 nA/cell was not larger than the initial one. To summarise, water addition caused a high strip conductivity but did not lead to a further increase of the dark current.

After irradiation the dark current was measured in each cell, It was $40 - 100$ nA/cell in the irradiated region of the chamber with one strip and two times

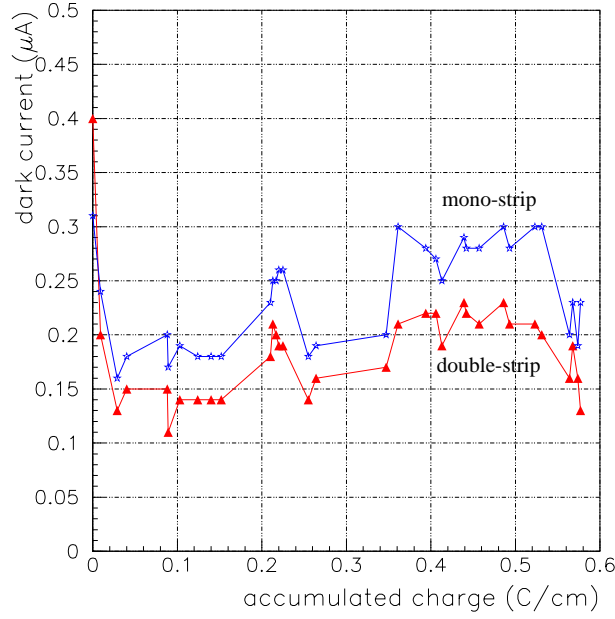


Figure 5.7: Total dark current per chamber in the aging test with water addition (0.6%).

lower in the cells with two strips (see figure 5.8). The dark current in irradiated cells was about 200 times higher than in non-irradiated ones.

After this aging test, ^{55}Fe pulse spectra were taken. As figure 5.9 indicates, the gain is even slightly higher in the irradiated cells than in non-irradiated ones. It should be remarked, that the wide deviation of gains in cells of irradiated chambers is a typical phenomenon. It can result from reaction of the cathode foil with aggressive species leading to buckling of chambers, which in turn results in displacements of wires from its centres.

Aging test with maximal X-ray intensity and very small gas flow (Test 5)

Since a strong increase in the dark current was observed before (see section 5.1.1) at a small gas flow rate $F = 0.1$ vol/h the following test was made at maximal intensity of the X-ray tube ($I=1.8 \mu\text{A}/\text{cm}$).

This test was made with the chambers we used in the previous tests (**Tests 1, 2, 3, 4**) and after we irradiated the same chambers filled with a mixture Ar/CO_2 up to $0.7 \text{ C}/\text{cm}$ (see a description of this test in section 7.2). We replaced the gas Ar/CO_2 by $\text{Ar}/\text{CF}_4/\text{CO}_2$.

The behaviour of the measured dark current is shown in figure 5.10. As this figure indicates, the dark current started growing from $\approx 40 \text{ pA}/\text{cell}$ at the begin-

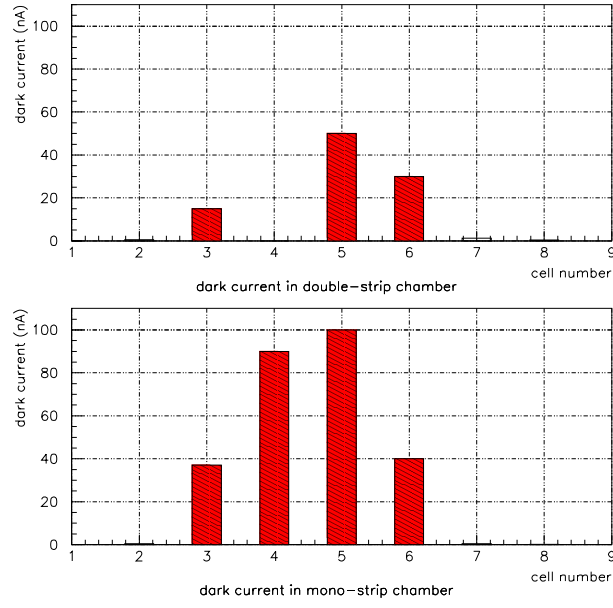


Figure 5.8: *Distribution of dark current in cells during the test with water addition.*

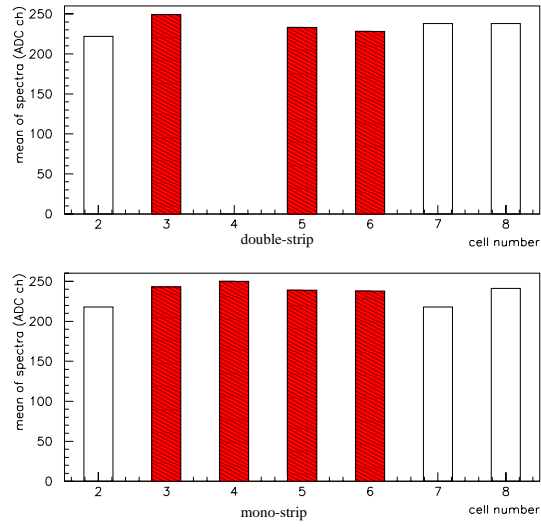


Figure 5.9: *Mean of ^{55}Fe spectra measured in chambers of X-ray setup after irradiation with water admixture. The red bars indicate the dark currents in irradiated cells, the unfilled bars in non-irradiated ones.*

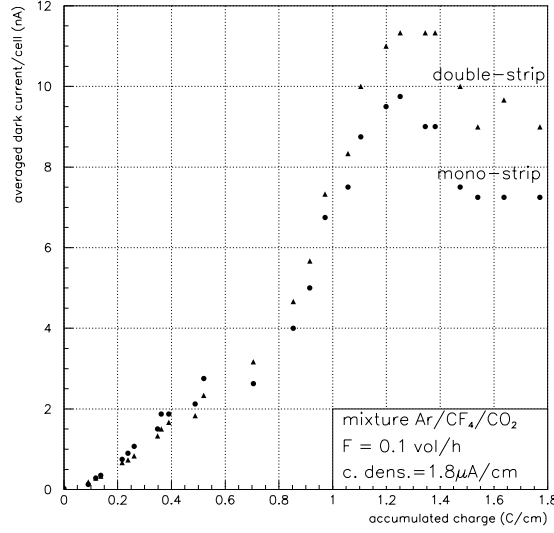


Figure 5.10: *Dark current as a function of accumulated charge in Test 5.*

ning and reached its maximum of ≈ 10 nA/cell. After 1.2 C/cm the dark currents stopped increasing. Other tests on FR4 strips also showed that the dark current increased continuously at the beginning of the test but the gradient became smaller and even compatible with zero after some dose.

The distribution of the dark currents in the cells is shown in figure 5.11. As can be seen, the dark current for irradiated cells is approximately two times higher. Using this ratio and assuming a linear dependence of the strip conductivity on the concentration of responsible species, we would obtain about two times lower concentration in the non-irradiated cells (i.e. in the box) than in the irradiated cells. But this comparison is not correct because the HV was not applied on non-irradiated wires during the irradiation and was, of course, applied on irradiated wires. The dark current is probably defined by the concentration of “charge carriers” in the strips, which, certainly, depends on the pre-history.

Measurements made in air one month after the stop of irradiation

In order to study if the dark current changes after a relatively long non-irradiated pause, we stopped irradiating for 30 days, during which the box was open and the chamber exposed to air. During measurements made afterwards the chambers were also in air. The results are: Just after application of the HV the dark current was very high, $\approx 3 \mu\text{A}$, in the irradiated cells. At the same time it was only ≈ 1 nA in non-irradiated ones. The dark current dropped by about 10 times for

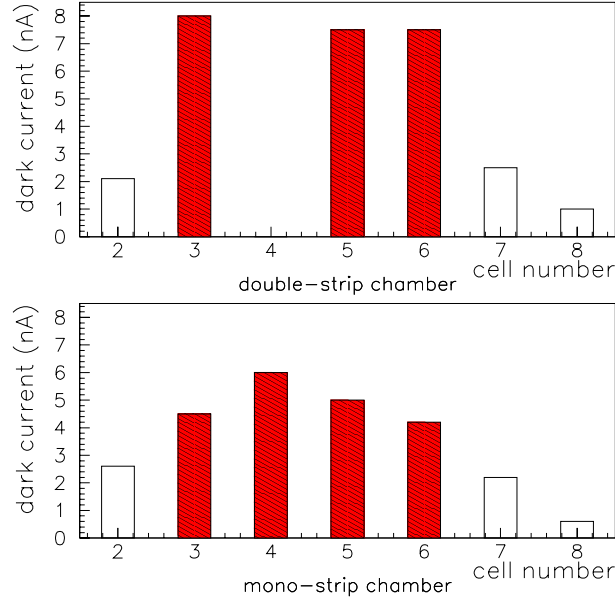


Figure 5.11: *Distribution of the dark current in the double- and mono-strip chambers after test 5.*

the first 24 hours and 20 times for 72 hours (The HV was always applied).

Dark pulses (≈ 3000 Hz) were observed in all the irradiated cells. The nature of dark pulses is studied more comprehensively in section 5.1.2. After opening the chambers and cutting the wires the current was measured on each strip. In the double-strip chamber the ratio of the dark current in the upper strip and in the lower one was

$$\frac{I_{upperstrip}}{I_{lowerstrip}} \approx 8.$$

The difference between conductivity of the lower and the upper is, most probably, caused by an upward movement of the gas. As will be shown in section 9.5.1, the gas flow is strongly enhanced by thermal convection (The chambers were positioned vertically and had free gas circulation).

The wires were investigated under the electron microscope. The typical surface of the wire in the irradiated region is shown in figure 5.12. It looks the same as the surface of a new wire. An X-ray spectroscopy showed neither the presence of any elements on the surface except gold nor a significant difference between irradiated and non-irradiated regions.

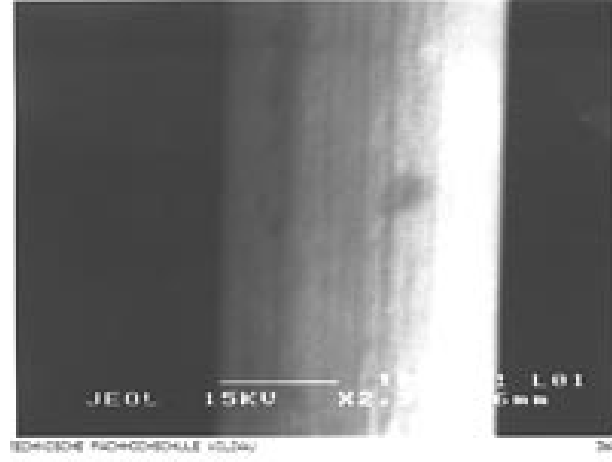
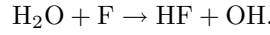


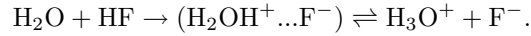
Figure 5.12: Micrograph of the wire surface made under the electron microscope. This region was subjected to a dose of ≈ 4 C/cm in the mixture Ar/CF₄/CO₂ and of ≈ 0.6 C/cm in the mixture Ar/CO₂.

Discussion

The dark current behaviour described in the previous subsection is not understood but can be explained as follows. The process of dissociation in the avalanche leads to the creation of species which flow (or diffuse) to the strip. These species are probably HF, as discussed in chapter 9, which form via reaction:



The enrichment of FR4 material with these species continues until an equilibrium is reached. The equilibrium is defined by absorption and desorption processes. HF, being not very aggressive, forms together with water hydrofluoric acid, which is conductive because in the presence of water the species dissociate into ions, charge carriers:



These charge carriers can live in a FR4 strip relatively long. If the HV is not applied the density of the charge carriers is high because they do not drift to the electrodes in the electric field. After switching on the high-voltage the leakage current is high because of the high density of charge carriers. Without a new supply of charge carriers, that is without irradiation, the density of them falls down, resulting in a decrease of the current.

Just after the irradiation test described in this section, the ratio of the dark currents in irradiated and non-irradiated cells was approximately 2. It is a consequence of the too high dark current in non-irradiated cells, which were not

connected to the high-voltage and thus accumulated a high ion density. However, one month later the dark current in the irradiated cells was about three orders of magnitude higher than in non-irradiated ones.

It might be noted here that the model given above in no case pretends to be conclusive. Only a separate study of different kind can answer the question about the origin of strip conductivity.

Electrical properties of strips from “Karlsruhe II”

As it was shown in section 4.6.1, the wire-supporting strips of gold plated chambers, which were irradiated in an α -beam developed high conductivity after 0.2 C/cm. It can be interesting to know the time evolution of the strip conductivity, since it can explain the nature of the effect.

The resistance of the bottom strip (positioned 10 cm from the irradiated region) from the Au01 chamber (see section 4.6.1) in air was measured several days after stop of the chamber irradiation [9]. It was, on the average, 30 MOhm/cell. After approximately two weeks it was measured again and was already, on the average, 20 GOhm/cell for the strips that were close to the irradiated region, and by about 1000 times higher for the strips more distant from the irradiated region. Two months later the average of it was about 250 GOhm/cell for the strips close to the irradiated region and about 500 times higher in the distant strips.

Then, we positioned the “Karlsruhe II” Au01 strip in a box filled with the mixture Ar/CO₂ (80/20) and applied a voltage of 1000 V. As can be seen in figure 5.13, the current in the strips that were close to the irradiated region dropped from 4 nA/cell (corresponding to 250 GOhm) to 10 pA/cell (corresponding to 10¹⁴ Ohm).

It was estimated also that the gas system in Karlsruhe II contained more than 3000 ppm of water. Let us suppose a linear dependence of the strip conductivity on the water concentration. Then, extrapolating the results of the test with water addition (6000 ppm) to 3000 ppm, we would expect a dark current of more than 25 nA/cell. This current corresponds to a conductivity lying in the region between those of Au1 and Au10 chambers. Thus the high dark currents in Karlsruhe II can be attributed to the high water content (better substantiated in the tests with 40 cm long chambers, see section 5.2.4).

5.1.2 X-ray aging tests of chambers with different cathode coatings

Introduction

One of the observations made in the aging test “Karlsruhe II” (see section 4.6.1) was the considerable difference in dark currents in the gold-plated chambers and in the uncoated Pokalon-C cathode chambers. The dark current in the uncoated Pokalon-C cathode chambers was several orders of magnitude lower than in gold-plated chambers. The lower dark current in a chamber with uncoated cathode could be attributed, for instance, to the absorption of responsible species by the

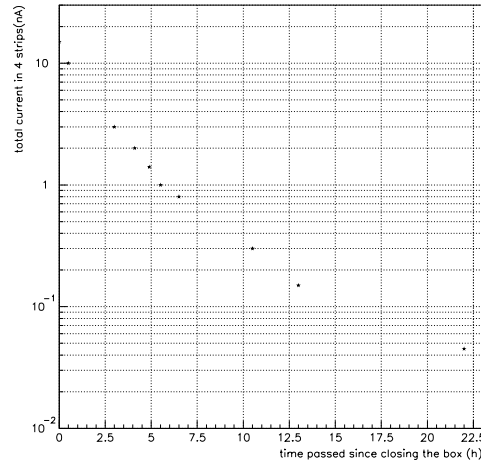


Figure 5.13: *Dark current in strips of Karlsruhe II Au01 chamber as a function of time passed since closing of the box and flushing.*

Pokalon-C. Whether the dark current depends on the cathode coating, was to be checked in the following test.

Experiment

The constructional parameters of chambers were the same as shown in figure 5.1. The two chambers made for this test were completely identical, except that one had an uncoated Pokalon-C cathode and the other gold-coated. The gas flow was identical to that used in section 5.1.1 and is shown in figure 5.14. The uncoated chamber was placed upstream (nearer to the X-ray tube) from the gold-plated chamber. The chambers had a standard open geometry according to the construction of the OTR chambers. The gas exchange inside the chambers resulted from diffusion, convection, laminar flow.

The construction of the box was specified in section 5.1.1. The parameters of the test are listed in table 5.1. It is to be noted that the main goal of the test was to study the effect causing high dark currents. Therefore, a low flow of 0.1 vol/h was chosen because the dark current started growing in the previous tests after we changed the flow from 1 vol/h to 0.1 vol/h (see figure 5.6).

Results

The aging test of the chambers filled with the counting gas $\text{Ar}/\text{CF}_4/\text{CO}_2$ was performed up to a dose of 5.3 C/cm. The currents are shown in figure 5.15. We

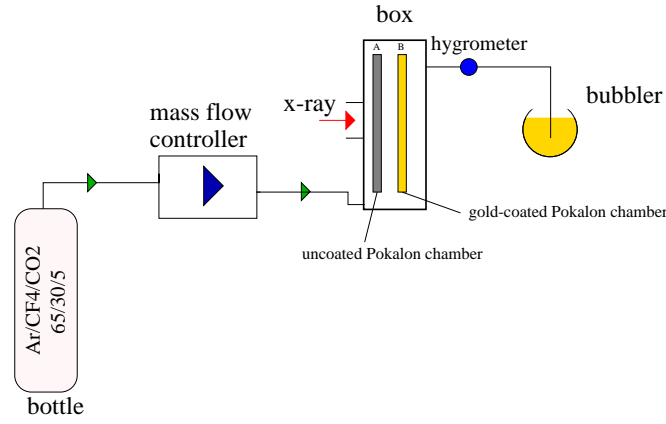


Figure 5.14: The gas system in the aging test with one gold-plated chamber and one uncoated chamber. The gas and irradiation is the same for both chambers, the only considerable difference between them were the coating of the cathode.

parameter	value
gas	$\text{Ar}/\text{CF}_4/\text{CO}_2 \rightarrow \text{Ar}/\text{CF}_4/\text{CH}_4$
flow	0.1 vol/h
HV	1700 V
current density	$1.2 \mu\text{A}/\text{cm}$

Table 5.1: Main parameters of the aging test with different cathode materials. After 5.3 C/cm the mixture $\text{Ar}/\text{CF}_4/\text{CO}_2$ was replaced by $\text{Ar}/\text{CF}_4/\text{CH}_4$.

observed a difference in the currents of the order of 30% at the beginning caused, presumably, by a higher photoemission quantum yield of the golden surface in comparison to the uncoated Pokalon-C surface. Therefore, we increased the HV in the uncoated chamber to 1750 V to equalize the currents. Irradiation continued at the same conditions up to a dose of 3.7 C/cm, where both chambers started to develop dark pulses (see measurements below). To get rid of the dark pulses, we increased the flow from 0.1 vol/h to 3 vol/h. Several days later, the dark pulses almost disappeared and after scanning with ^{55}Fe we again reduced the flow to 0.1 vol/h and irradiated up to 5.3 C/cm. As can be seen, the gain drops by 10% when changing the flow from 1 vol/h to 0.1 vol/h. Probably, the counting gas contained a relatively large concentration of electronegative contaminants as oxygen reaching the gas through the windows. After changing the mixture to $\text{Ar}/\text{CF}_4/\text{CH}_4$, and irradiating for additional 0.6 C/cm, we observed a rapid loss in the currents of 20% and 45% in gold-plated and uncoated chambers, respectively.

The continuous drift of the current downwards during test with $\text{Ar}/\text{CF}_4/\text{CO}_2$ was not related to anode aging since the ^{55}Fe spectra did not show any gain losses

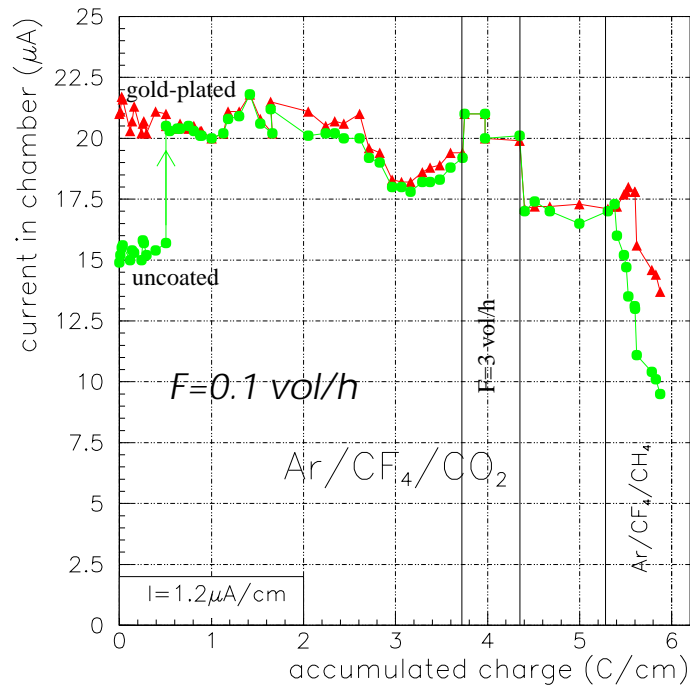


Figure 5.15: Behaviour of the currents in the aging test. At the beginning the current in the gold-plated chamber was higher, probably, because of a higher photoemission quantum yield of the golden surface in comparison with uncoated Pokalon-C. The HV in the uncoated chamber was increased to 1750 V to equalize the currents. Clear continuous gain reduction can be seen after changing the mixture.

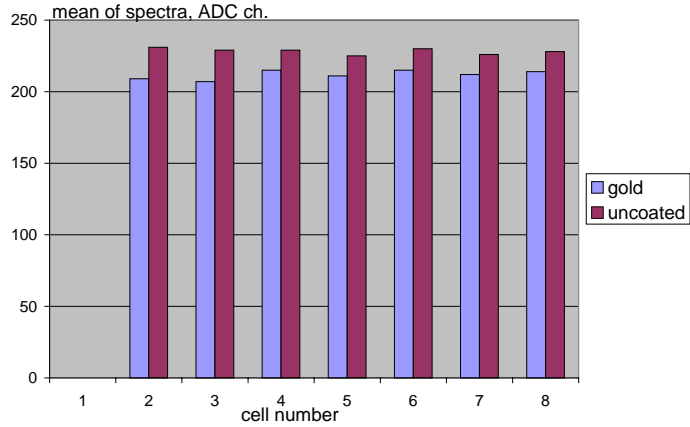


Figure 5.16: Distribution of ⁵⁵Fe spectrum mean values at a dose of 4 C/cm. Cells 3,4,5,6 in both chambers were irradiated.

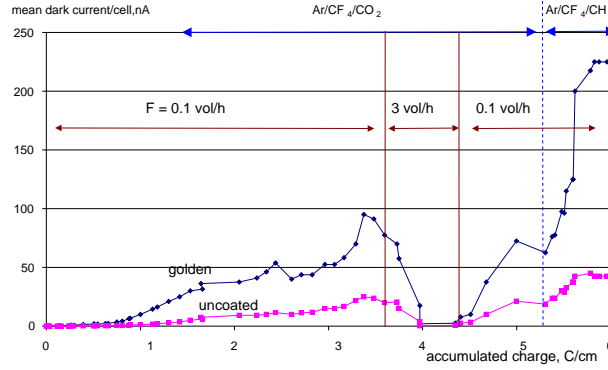


Figure 5.17: Cell-averaged dark currents as functions of accumulated charge. After boosting the flow to 3 vol/h, the dark current dropped considerably. After setting the flow at the previous level of 0.1 vol/h the dark current increased again and almost to the same level. Substituting the mixture for $\text{Ar}/\text{CF}_4/\text{CH}_4$ resulted in grow of the dark current.

as can be seen in figure 5.16. The current drop was attributed to the aging of the X-ray tube since the stated service life of the tube at the maximum intensity was only 500 h. Indeed, the current was approximately 30% lower than in the previous test performed 5 month earlier also at maximum intensity (see section 5.1.1). Later on, we changed this X-ray tube of the old type for a new one, with a well stabilized electron beam current.

The development of the dark currents is shown in figure 5.17. At the beginning, the dark current was very small, only several pA/cell and increased until we raised the flow. The increase in the flow led to a drop in the dark current correlating with a decrease in the dark pulse rate with a time constant of several tens of hours. After the flow was decreased the dark current started growing again, together with the dark pulse rate, and reached almost the same value as before. After change of the gas the dark current increased and, probably, saturated. A cathode coating dependence of the dark current was substantiated in this test since the dark current was approximately 3 times higher in the gold-plated chamber than in uncoated. However, the difference in “Karlsruhe II” test was several orders of magnitude (see section 4.6.1).

At a dose of approximately 2.6 C/cm the HV dependence of the dark current was measured (see figure 5.18). The measured values were fitted with functions $a(e^{bx} - 1)$ denoted with solid lines in the figure. As can be seen, this function describes the measurement very precisely. There has not been found any explanation for such a dependence yet.

The dark current was accompanied by “dark pulses”, which spectrum lay approximately in the same region as ^{55}Fe spectra thus complicating scanning with an ^{55}Fe source. Tests showed that dark pulses are very short, with a duration of less than 1 ns, having a high amplitude, so that they could be seen in an oscilloscope

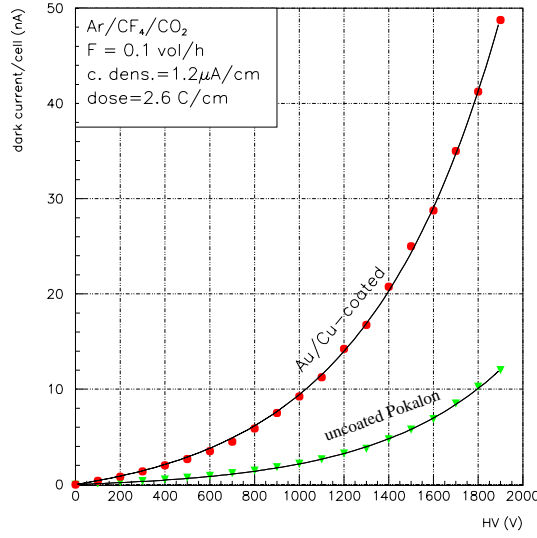


Figure 5.18: Dark current as a function of HV. Measured values for the gold-plated chamber and for the uncoated chamber are denoted with circles and triangles, respectively. The dependence is well approximated with functions $a(e^{bx} - 1)$ (denoted with solid lines) where the coefficient a is 2.26 nA and 0.456 nA for gold-plated and uncoated chambers, respectively; the coefficient is b 0.0164 V^{-1} and 0.0174 V^{-1} for gold-plated and uncoated chambers, respectively.

without a preamplifier.

Figure 5.20 shows distributions of: measured dark currents, dark-pulse rates, average dark-pulse amplitudes, estimated dark currents as contributions from dark-pulses. The estimated dark current was found as a product of the average pulse charge, measured on an oscilloscope, and the pulse rate. It should be noted that the dark currents correlated with the dark pulse frequency: gold-plated chamber had higher dark current and frequency than uncoated; a change of the flow led to a change of the dark current correlating with the dark pulse rate; dark current correlated also with dark pulse rate when varying the HV.

Any correlations between amplitudes of dark pulses and dark currents were not observed.

Finally, we made SEM analyses of the wire surface. A typical relief of the Au/W-wire surface is shown in figure 5.21, on the left. From the whisker marked with the cross we obtained the EDS spectrum, which is shown in the same figure on the right. As the figure indicates, lines of C, F, Cu, and Si were found in the whisker emission spectrum.

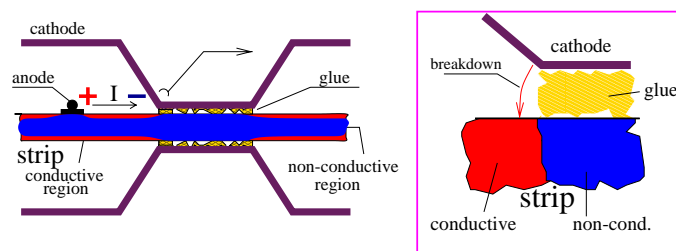


Figure 5.19: *Simplified model explaining the origin of dark pulses. Scheme of the cathode foil at the point of merging with the FR4-strip is shown magnified on the right. Conductive places on the FR4-strip are filled with red, non-conductive with blue colour.*

Discussion

Currents. According to SEM the gain loss after changing of the mixture from $\text{Ar}/\text{CF}_4/\text{CO}_2$ to $\text{Ar}/\text{CF}_4/\text{CH}_4$ resulted from deposit formation on the anode. The higher aging rate of the uncoated chamber compared to that of the gold-plated one could be attributed to higher anode voltage applied to the former: the plasma density in the avalanche increases when increasing the HV.

Dark currents. The difference in dark currents in uncoated and gold-coated chambers can be explained by lower absorption of responsible species by a gold-coated Pokalon-C foil. The dark current behaviour is also affected by the size of chambers, the irradiated region, presence of capillaries, water content, etc. Therefore, a comparison between the dark current behaviour in this test and in “Karl-sruhe II” is difficult.

It was shown before in figure 4.11, that the dark current depends on the water content. The observed flow dependence of the dark current (see figure 5.17) is consistent with previous and later tests, since the water content varies inversely with the flow.

The increase in the dark current after the change to $\text{Ar}/\text{CF}_4/\text{CH}_4$ was not expected. It could be caused, for example, by discharges via the whiskers or by an increase in the water content. The moisture content was not measured in this test.

Model explaining dark pulses. The observed correlation between the dark current and the dark pulse rate could be explained by the following model. As a result of the interaction with the gas, the FR4 strip becomes conductive in the region of the cell (see figure 5.19). A layer of Stycast between the cathode foil and the FR4-strip surface forms a non-conductive gap in the anode-cathode electric circuit. A simplified electric scheme of the model is shown in figure 5.22. The gap charges like a capacitor due to the current through the strip reaching some breakdown voltage. As the breakdown voltage is reached, a spark develops

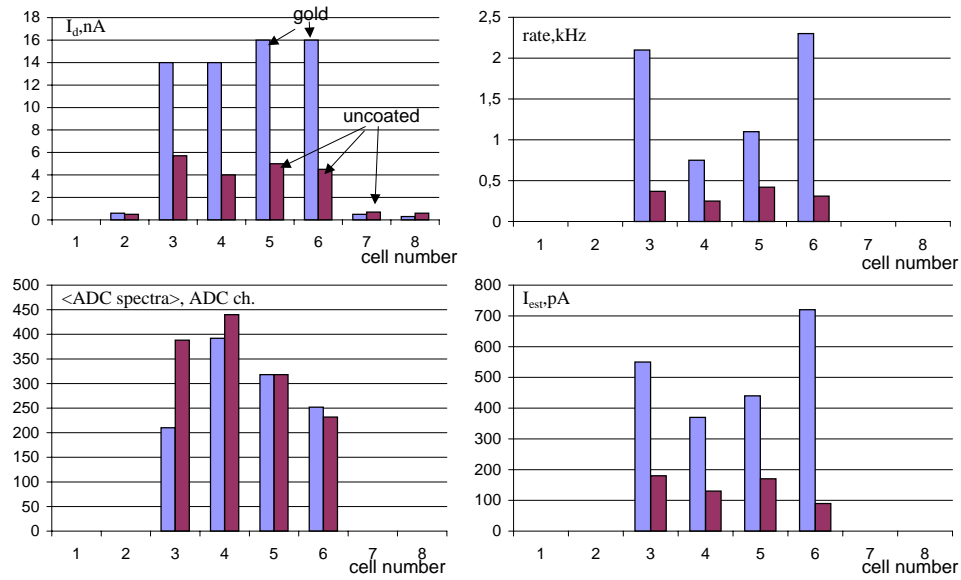


Figure 5.20: Distributions of: measured dark current, on the left at the top; dark-pulse rates, on the right at the top; average dark-pulse amplitudes, on the left at the bottom; estimated dark-pulse contribution to the dark currents, on the right at the bottom.

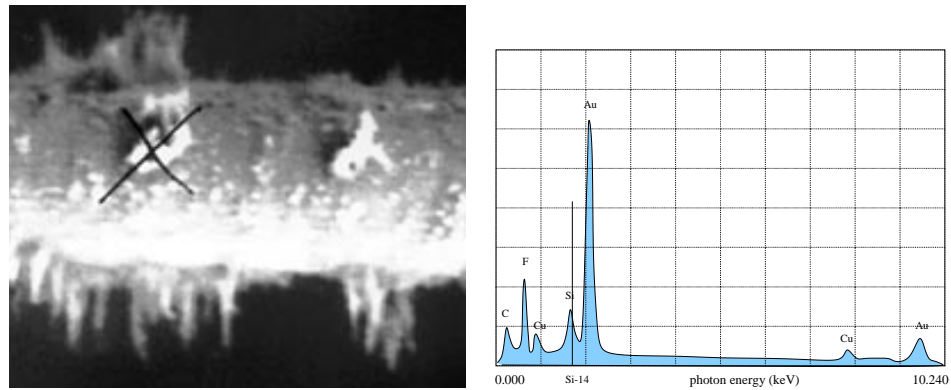


Figure 5.21: On the left side, SEM micrograph of the wire from the gold-plated chamber. After a dose of 0.6 C/cm in Ar/CF₄/CH₄ the chamber showed aging of about 20%. On the right side, EDS spectrum from the place marked with the cross.

discharging the capacitor (gap) after which the charging of the gap begins again. In an oscilloscope we see, therefore, very short pulses with the amplitude independent of the HV and not correlating with the dark currents. On the other hand, the dark pulse rate increased when increasing the dark current because the charging time of the gap varies inversely with the current.

As can be seen in figure 5.20, the current estimated as a product of the average amplitude and the rate is only approximately 3% of the measured dark current. Then, the ratio

$$\frac{C_{strip}}{C_{gap}} \approx \frac{I_{pulse}}{I_{measured}} \approx 0.03$$

should be satisfied since the strip resistance is large and its contribution to the amplitude of the dark pulse observed during the discharge of the gap (pulse duration is less than 1 ns) can be neglected.

5.1.3 Conclusion

Several conclusions can be drawn from the aging tests of 10 cm long honeycomb chambers irradiated with X-rays:

- An addition of 0.6% water vapour to the counting gas caused a jump of the dark current from 0.5 to 50 nA/cell. However, additional irradiation with addition of water did not lead to a further increase in the strip conductivity.
- The reason for the high dark current in the test “Karlsruhe II” seems to be the high water content in the gas system resulting from the use of water-transparent Kapton windows.
- The dark current was 3 times higher in the gold-coated chambers in comparison to uncoated. However, the difference in the test “Karlsruhe II” was much bigger. The difference in the dark currents was probably a result of stronger absorption of responsible species by the uncoated foil than by Au-coated one. The difference in short chambers can be smaller due to a stronger contribution of the gas exchange processes (diffusion, thermal convection).
- Neither the uncoated nor the gold-coated chamber filled with the mixture Ar/CF₄/CO₂ showed anode aging up to about 5 C/cm even with the gas flow rate as small as 0.1 vol/h. On the other hand, test with mixture Ar/CF₄/CH₄ showed a rather high anode aging rate of about 30% per 0.6 C/cm in uncoated and Au-coated chambers at the flow of 0.1 vol/h.
- The Malter effect was not observed.
- At a low flow of 0.1 vol/h we observed dark pulses of a frequency correlating with the dark current. We presented a hypothetical model suggesting that dark pulses were caused by discharges.

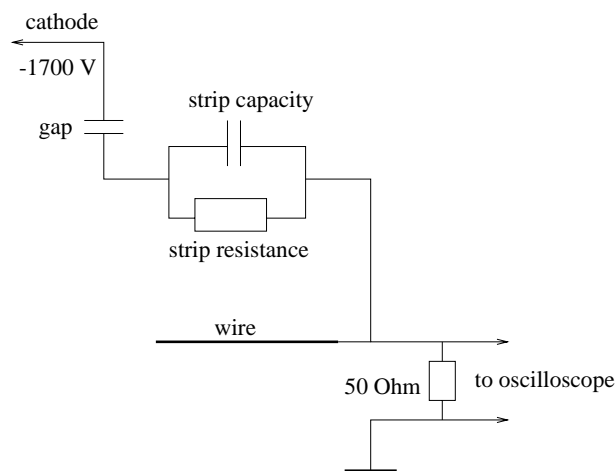


Figure 5.22: *Simplified electric scheme of the model explaining the origin of dark pulses.*

5.2 Aging studies of 40 cm long chambers

As is shown in chapter 9, 10-cm long chambers used in the previous aging tests are too short to allow a considerable accumulation of corrosive species produced in the avalanche. In longer chambers the internal “flora and fauna” is more similar to that of the OTR chambers. There are two processes increasing the gas exchange rate especially in short chambers: diffusion and thermal convection. The latter usually dominates in accelerated aging tests with chambers having open geometry like the OTR drift chambers. Suppression of thermal convection could be reached through introduction of capillaries conveying the gas directly to the cells. Therefore, the next test chambers were partially provided with capillaries.

5.2.1 Introductory test

Material and methods

We used two identical mono-layers (“A” and “B”) with a construction as shown in figure 5.23. FR4 strips were positioned symmetrically, on both sides of the irradiated region. At the bottom of each chamber the specially prepared end-pieces were equipped with 1-mm thick stainless steel capillaries. The constructional and working parameters of this test are listed in table 5.2.

Capillaries 1, 2,...,8 of chamber ‘B’ were blocked (pinched) to check how the blocking can influence the chamber behaviour.

The scheme of the gas system is shown in figure 5.24.

It should be noted that the gas flowed through the chambers, but there was no additional flushing in the box. The gas exchange in the box was thus only ≈ 0.3 l/h (0.1 vol/h). Such a low flow rate resulted in relatively high water content in

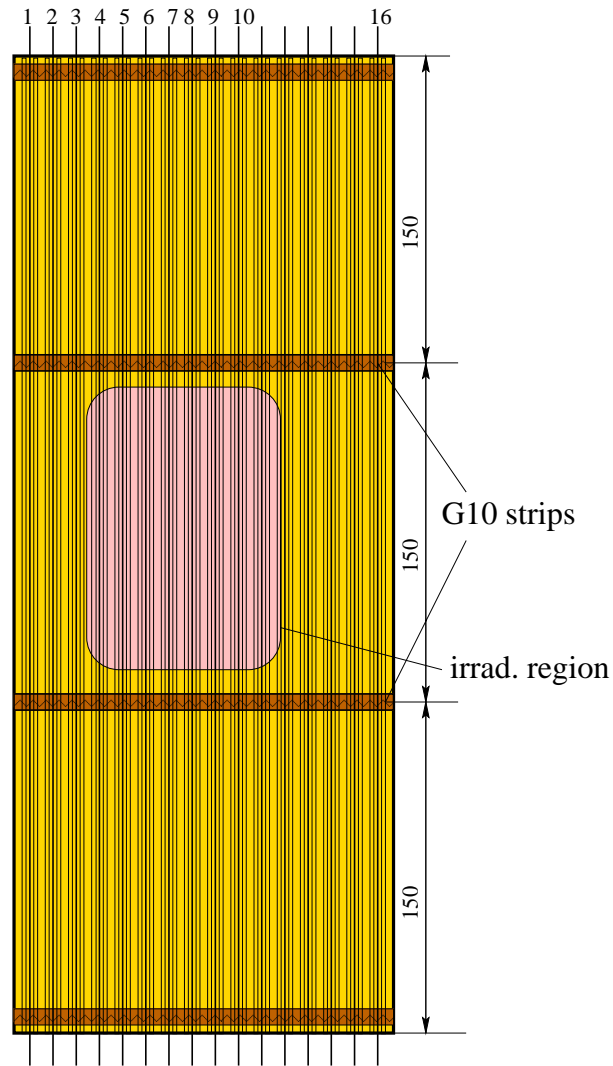


Figure 5.23: Schematic view of 45 cm long chamber used in the introductory test. The chamber was provided with capillaries (not shown in the figure).

parameter	value
chamber	45 cm x 16 cells
glue	Stycast, Traduct 2922 ^a
irradiated region	12 cm
box volume	2.4 l
box window	14 cm x 11 cm (Al-Mylar)

^aThe conductive glue Traduct 2922 was used instead of E-solder 3025 A.

parameter	value
gas	Ar/CF ₄ /CO ₂
flow (only through chamber)	1 vol/h→10 vol/h
HV	1800 V
current density	0.6 μ A/cm
water/inp	<10 ppm
water content in the box	O(500 ppm)

Table 5.2: Construction and introduced materials (top) and main working parameters (bottom) in the introductory test.

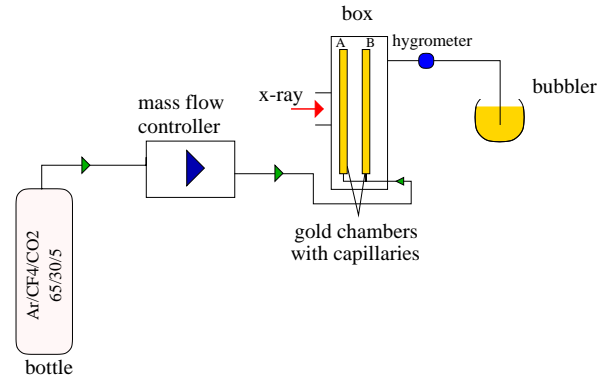


Figure 5.24: Gas system used in the introductory test.

the box, of the order of 500 ppm in spite of the low water content at the input (10 ppm). Most probably, the fraction of other atmospheric pollutants such as O_2 and N_2 was also relatively high. At the beginning the gas flow was 1 chamber volume per hour through the capillaries and changed to 10 chamber volumes per hour after 2.7 C/cm.

Wire ruptures

We observed a dangerous effect which had never been observed in the OTR before: wire ruptures. For the first time the wires started rupturing in cells with blocked capillaries after 1.2 C/cm and in normal cells after 2.2 C/cm. After each rupture the box was opened, the damaged wire was disconnected, then, the box was closed and flushed for several days. Since the wire started rapidly breaking in cells with blocked capillaries causing long shutdowns, all the wires with blocked capillaries were disconnected. The first cell (11 of 'A') with normal, not blocked, capillaries went out of operation at 2.2 C/cm. Afterwards, cell 10 of 'B' died at ≈ 2.7 C/cm. Initially, cells **3,4,5,6,7,8,9,10,11** of chamber 'A' and cells **4,5,6,7,8,9,10,11** of chamber 'B' were irradiated (the HV was on). The cells denoted with a bold font died.

A further test was made only with chamber "A". To check the influence of the flow on the rupture rate, we increased the flow 10 times. The wire rupture rate seemed to increase after increasing the flow: two more cells, 3 and 6 of 'A', broke during the following ≈ 1 C/cm. The total number of damaged cells in chamber "A" was 5. The cells did not show any "bad" symptoms before ruptures. The dark currents were not higher than the average dark current before breaking. The electrical resistance of broken wires against the cathode was in the region of O(100 Ohm).

Other results

The chambers were irradiated up to ≈ 2.7 C/cm at $F = 1$ vol/h = 0.15 l/h. The cell-averaged currents in chambers 'A' and 'B' are shown in figure 5.25. According to the current, we did not observe anode aging in the test.

The dark currents are shown in figure 5.26. We could see that the maximum dark current was 27 nA, not dangerous for the OTR. After we switched off the HV in the chamber 'B' (see figure 5.25), the dark current in chamber 'B' started falling (the dark current was measured at the normal HV of 1800 V, of course) while the dark current in chamber 'A' continued growing.

After we had stopped irradiating, we flushed the chambers in the counting gas at 40 °C for several days. Then the chambers were exposed to air to measure the dark current in humid environment. As a result of the heating procedure, the dark currents decreased by several orders of magnitude even at the high humidity of air.

After 2.7 C/cm, we made a transversal and longitudinal scanning with an ^{55}Fe source. The results are shown in figure 5.27. According to this figure, we observed

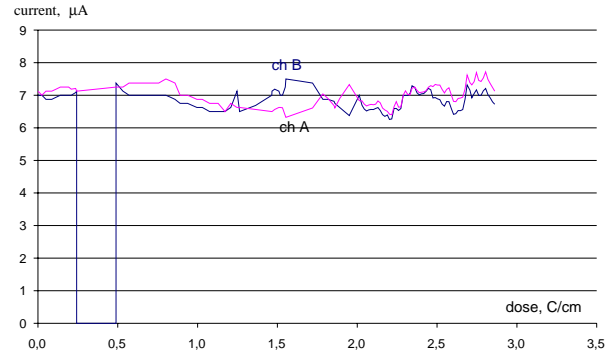


Figure 5.25: Cell-averaged p/T -corrected currents in chambers 'A' and 'B'. The x -axes represents the accumulated charge in chamber 'A'. Plotting the currents as functions of dose accumulated in one of the chambers is convenient since it allows the time-related comparison of curve fluctuations.

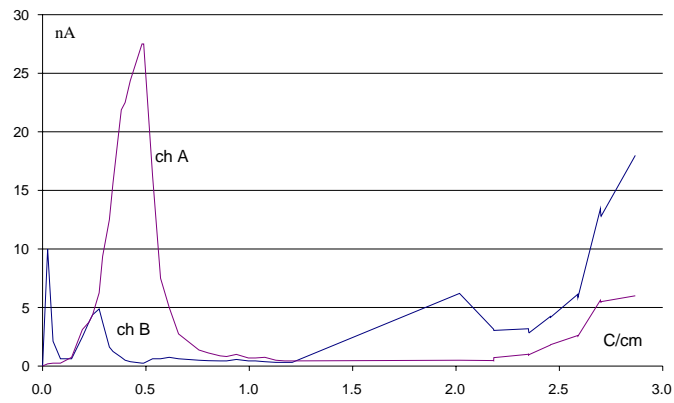


Figure 5.26: Cell-averaged dark current. The x -axes represents the accumulated charge in chamber 'A'.

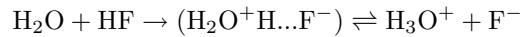
a gain drop in the irradiated region. It should be remarked that this drop is not constant but rather increasing toward the center of the irradiated region.

Such a gain loss distribution could be a result of the inhomogeneous irradiation intensity. Therefore, we measured the current density within the irradiated area. For this purpose, we moved a 4 mm thick lead plate step by step vertically along the chambers shielding the irradiated chamber area from 0% up to 100% measuring the current in the cells. The results are shown in figure 5.28. The irradiation from the X-ray tube seems to have been uniform.

We observed very intense sparking in the reference cell 15 of chamber 'A' when measuring ^{55}Fe pulses. The sparking was so fierce that the CAEN tripped at $I_{max}=10\text{ }\mu\text{A}$. After opening the chamber, we observed an about 1 cm long black-shaded spot on the wire and on the cathode in this cell far away from the irradiated region. The wire was quite tense and direct contact with the cathode was unlikely.

Discussion. At the very beginning, the dark current in chamber B was with 90 nA rather high. Most likely, some insulator between the cathode, which was under high-voltage, and the wall of the box drew the current. The dark current in chamber B temporarily fell probably due to a decrease in the humidity.

The subsequent increase in the dark current, correlating in both chambers, was caused by FR4-strips, which were not dry yet but already absorbed a considerable portion of HF. According to chapter 9, 0.6 atoms of F per one free electron are produced in the avalanche. F lives only microseconds if traces of water are present, forming HF. The latter penetrates a FR4-strip and dissociates due to reaction with water building weakly dissociated hydrofluoric acid



The higher concentration of HF and H_2O leads to a higher density of charge carriers and thus to a higher current.

The drop of the dark currents just after 0.5 C/cm was, probably, a result of dehydration of the FR4-strips. The increase in the dark current after 1.2 C/cm was probably caused by frequent opening of the box for disconnection of broken wires.

Naked-eye inspection. A photograph of the irradiated region of the open chamber 'A' is shown in figure 5.29. As this figure shows, the cathode foil is shaded in the irradiated region. The change of colour was especially strong under (above) the FR4-strips.

The photograph of an upper FR4-strip together with a new strip is shown in the right part of figure 5.29. The FR4-strips changed their appearance considerably. The coating of the strip seems to be etched out revealing a grid structure.

We observed that five cells went out of operation because of wire breaking. Any indications of carbon bridges on FR4 strips or something like that were not discovered. Furthermore, we checked the resistivity of the strips which was higher than the device limit (40 Mohm). Also, a black spot on the cathode near the

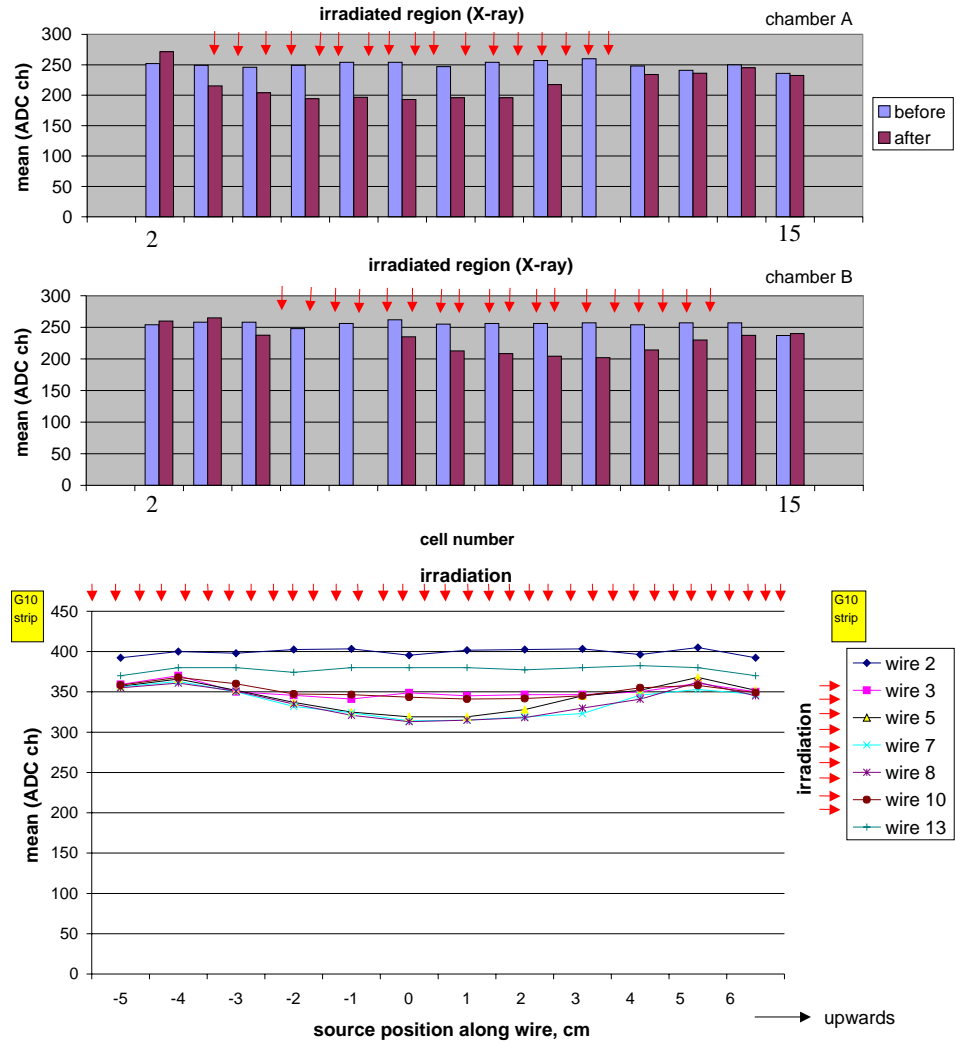


Figure 5.27: Transversal (at the top) and longitudinal (at the bottom) scanning with ^{55}Fe source.

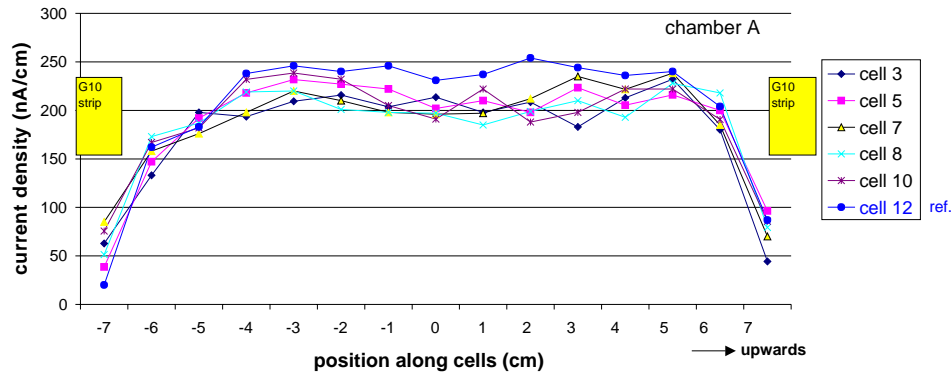


Figure 5.28: *Current density in the irradiated area measured by changing the area of the chamber shielding.*

rupture place indicated that some kind of discharge took place there. All the wires were broken approximately in the center of the irradiated region.

Wire tension measurement. We measured the tension of all the unbroken wires in the open chamber 'A' and found that a low tension was only in some cells on the edge (wire 1: 11.7 g and wire 16: 3.0 g). In all the other cells the wire tension varied from 26 to 56 g (the nominal tension is 50 g). The suspicious wire 15 had a tension of 29 g, which probably was not the reason for sparking.

Microscopy and spectroscopy

The cathodes and the wires in the regions where the wires were destroyed looked black. Six wire surfaces, three cathode pieces and a solder point of chamber 'A' were analysed under the electron microscope.

Wire 5. The wire obtained a dose of 2.7 C/cm at $F = 1$ vol/h and 1 C/cm at $F = 10$ vol/h; the observed gain loss was about 19% in the center of the irradiated region.

Figure 5.30 shows a SEM micrograph of the wire from the center of the irradiated region.

In the center of the irradiated region the surface had a structure with cracks and round black spots. The wire diameter was approximately by 5% larger in comparison with a new wire, which is shown in figure 5.31. The presence of tungsten was observed. It has to be noted that the low energy line of W (1.7 keV) dominates over the high energy W peak (9.7 keV), which gives us a hint that W is deposited above gold: if W were slightly coated with another material, the low energy lines would be stronger suppressed than the high energy ones.

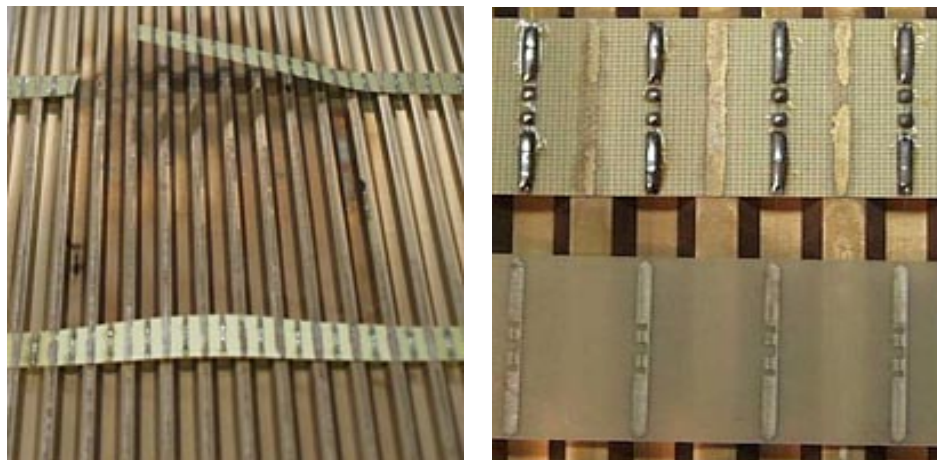


Figure 5.29: Photograph of the irradiated chamber after opening (left). On the right, photograph of FR4-strips at the end of the test (at the top) and new ones (at the bottom).

The part of the wire which was above the irradiated area looked different: the surface was clean, the EDS spectrum in figure 5.32 shows only traces of W.

Wire 8 (center of the irradiated region). The wire was irradiated up to 2.7 C/cm at $F=1$ vol/cm and then disconnected (the gain loss is 20% in the center of the irradiated area). The surface looked vesicular (see figure 5.33). The wire diameter seems to be larger by 5% than that of the reference shown in figure 5.31.

The EDS spectrum shown in figure 5.33 was measured on a small bubble. There are emission lines of oxygen (particularly strong) and W in addition to gold lines. The large peak corresponding to the low energy W line indicates that the deposit of W is on the surface, above the gold.

Cell 11, wire and cathode. The wire ruptured after a dose of about 1.5 C/cm. It has to be noted that the analysed end of the wire was not under the HV after electrical disconnection due to the rupture so that this part did not see any sparking processes after falling on the cathode. The photograph of the wire taken under the optical microscope and under the electron microscope are presented in figure 5.34 and 5.36, respectively. The wire is black and a large part of the wire cross section was etched away. An EDS spectrum is shown in figure 5.36. The peak of W dominates strongly over lines of C, O and Au.

Figure 5.35 shows peaks of chemical elements on the cathode. Besides gold and copper, we see C, O and W.

Cell 15, wire and cathode. The wire was not irradiated, the HV was usually off. No “bad” symptoms were noticed during the whole aging test until the last

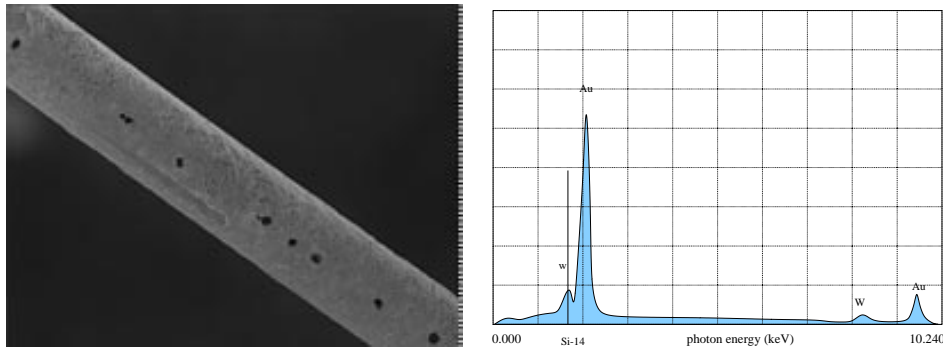


Figure 5.30: *On the left, a SEM micrograph of wire 5 is shown. The sample was taken from the center of the irradiated region. Cracks and round black spots are visible. An EDS spectrum from the whole wire surface is shown on the right. Besides Au, a peak of W can be seen.*

scanning with ^{55}Fe when the wire showed strong pulsing. We found a suspicious black-shaded region on the wire and on the cathode. A SEM micrograph and an EDS spectrum of the wire surface is shown in figure 5.38. The surface was crater-like, perhaps, due to overheating. The surface deposit consisted of C, traces of F and Cu dominated by Au.

Opposite to the black-shaded region on the wire, the cathode had a narrow, approximately 2 cm long spot of apparently pure Pokalon-C. It is not clear how this spot could be formed. An electrical contact between the cathode and the wire seems to be impossible, since the wire tension was normal.

Solder point. We analysed the solder point on the upper FR4-strip of a cell with a ruptured wire. Figure 5.37 shows the EDS spectrum of this solder point. The point had a good surface and a spectrum with a typical element composition according to [9].

Summary

Although ^{55}Fe scanning showed a gain loss of $\approx 20\%$ in the center of the irradiated region, we did not observe considerable organic deposit on the wire surface. The surface was either rather clean or covered with tungsten. The gain drop can be explained by the 5% enlargement of the wire diameter which could be caused by some corrosive species produced in the avalanche.

We observed a growth in the wire breaking rate after an increase in the flow. This growth could result from:

- an increased purity of the gas, since contaminants could react with aggressive species and thus suppress etching;

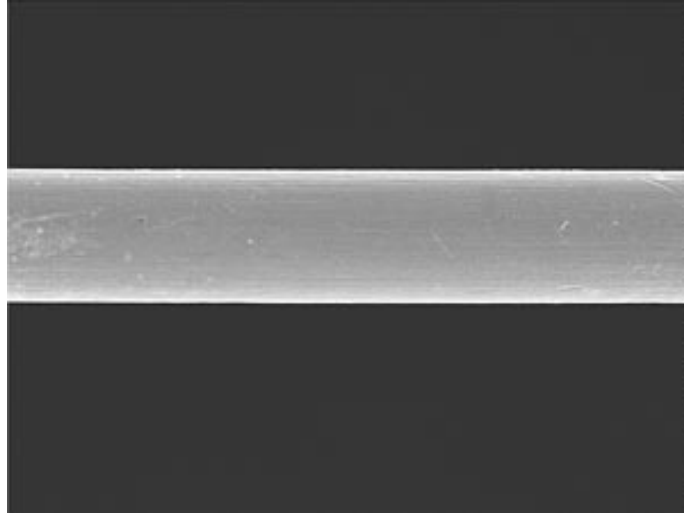


Figure 5.31: *SEM micrograph of a new wire presented here for comparison. The wire diameter was by about 5% smaller than those of irradiated wires. According to the expert, a quantitative comparison of the wire diameters on the pictures from the electron microscope is correct.*

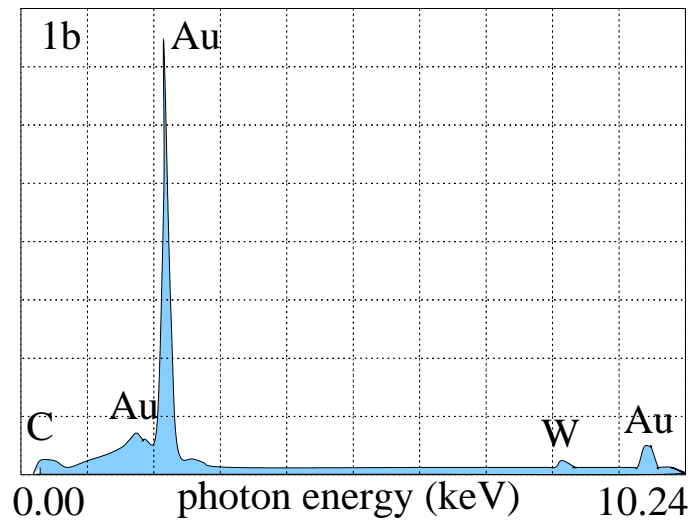


Figure 5.32: *EDS spectrum of a non-irradiated part of wire 5 downstream from the irradiated region. The spectrum indicates that the surface is clean.*

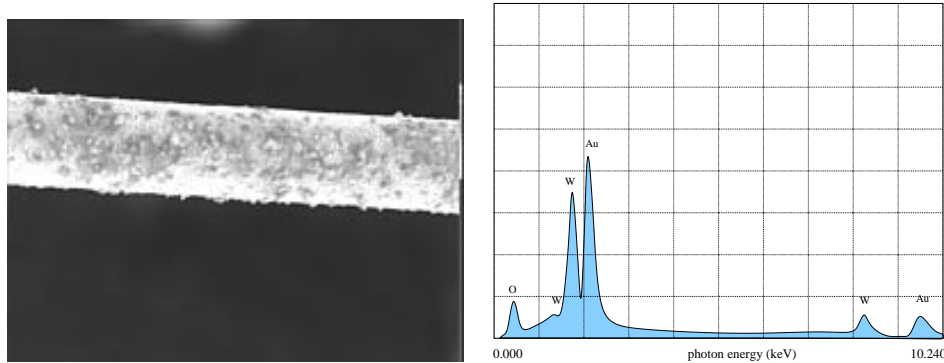


Figure 5.33: SEM micrograph of wire 8 (left). The surface seems to be covered with “discoloured” bubbles. On the right, EDS spectrum of wire 8. The large low energy W peak suggests that W is not shielded by the gold layer and is deposited in form of bubbles on the wire surface during the irradiation.

- the fact that the wires were already “worn out” during the previous test at the nominal flow;

Since this new effect is very dangerous and could destroy the detector irreversibly during several years of operation, we directed the following tests on the study of this effect.

5.2.2 Test with a water content of 50 and 200 ppm

Introduction

The anode corrosion observed in the previous “introductory test” described in section 5.2.1 was also seen in tests for the ATLAS TRT [66] using Kapton straws. There the mixture Xe/CF₄/CO₂ had a relatively high water content of several percent. The effect was not observed however with dry gas. Therefore, we made a test to study the influence of water on the wire etching rate using two boxes filled with counting gas having different water contents.

Experiment

Two identical single-layer chambers ‘A’ and ‘B’ were used. Chamber ‘A’ was in the dry gas flow, the other ‘B’ in the humid one. The chamber construction was almost identical to that used in the previous test (see figure 5.23) with some exceptions. Instead of 16, these chambers had 14 cells per monolayer. Two single-layers consisting of 28 cells were used in this test. In each single-layer 1 mono-layer was equipped with stainless-steel capillaries at the bottom. The other mono-layer was open at both ends. Each mono-layer had 4 FR4-strips. Two strips were placed symmetrically on both sides of the irradiated region at a distance of 10 cm from

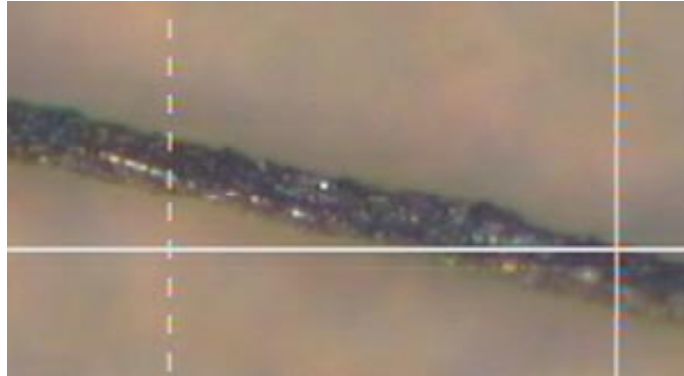


Figure 5.34: *The photograph of the broken wire 11 under an optical microscope. Black tungsten can be well distinguished from gold.*

their centres to the center of the irradiated region. The other two are placed at the ends of the chambers. In sum, each single-layer had eight FR4 strips.

A schematic view and a photograph of the test setup is shown in figure 5.39. Two identical boxes with a volume of 2.2 l were made up of hollow mono-blocks of rectangular profiles and bolted together forming a solid double-box. This double-box has a partition window as well as two exterior windows with a size of 14 cm x 13 cm made of aluminized Mylar. A 100 μm thick aluminum foil was additionally glued on the aluminum Mylar foil of the window of the dry box “A” to decrease water transparency of the window and thus the humidity. The setup had two separate gas systems: one with the pure mixture $\text{Ar}/\text{CF}_4/\text{CO}_2$ with a possible contamination due to the windows transparent for some air components; the other with $\text{Ar}/\text{CF}_4/\text{CO}_2$ and 200 ppm of water. In order to keep water in the bottle with the premixed counting gas in gas phase the bottle was heated to 40 °C with a heating tape. Although it was planned to add 1000 ppm of water to the gas, in fact, only 200 ppm of water was measured in the output gas of the bottle. Furthermore, the humidity was not constant and fluctuated by almost 30%. For information about pressure dependence of moisture content in gas containers, see [35].

The lower current in the second chamber downstream from the X-ray tube was compensated increasing the HV by 20 V. From 14 cells in each mono-layer only the central wires: 4, 5, 6, 7, 8, 9, 10, 11 cells were connected to the HV. The electrical connection inside the box was accomplished with silver wires having Rilsan tubes as insulators. Although the HV was applied to the cathode the electrical connection of wires was made taking into account a possible increase in the voltage on wires due to ruptures. After an external disconnection of a broken wire from the measuring circuit, the internal connection has to be high-voltage stable so that the box need not be opened after each rupture as in the previous test 5.2.1.

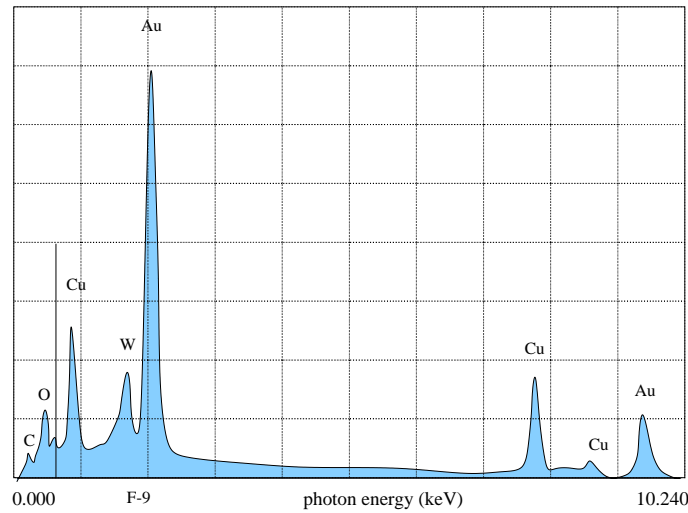


Figure 5.35: EDS spectroscopy of the cathode at the place where wire 11 was broken.

The construction features and operating parameters are summarized in tables 5.3.

The current of $0.6 \mu\text{A}/\text{cm}$ was $O(10)$ times higher than in the hottest region of the OTR. Therefore, in the test the HV was 1800 V, slightly higher than in HERA-B (1750 V), to partially compensate the space charge. The gas flow was one chamber volume per hour through the chambers and 1 box volume per hour through the boxes at the beginning. After $2.7 \text{ C}/\text{cm}$ it was increased 10 times to check the influence of the flow on rupture rate.

It should be remarked that the O_2 content dropped by a factor of three when the gas outputs of the boxes, which were connected directly to atmosphere through 3 m long pipes, got connected to the bubblers. A 3 cm high oil column in a bubbler produces an additional pressure in the boxes of about 2 mbar. Because of the high flow and the large distance to the bubblers (3 m), the gas could not diffuse back from the bubblers into the boxes.

Before starting the aging test a dehydration procedure was performed where the double-box was heated to 40-43 degrees and flushed with a dry gas for a week. After that at room temperature, the water content was measured to be on a level of 50 ppm.

Slow control

The automatic slow control program performed the measurement of:

- currents and dark currents in all the irradiated cells (the dark current was measured every three hours switching off the irradiation for 15 minutes);

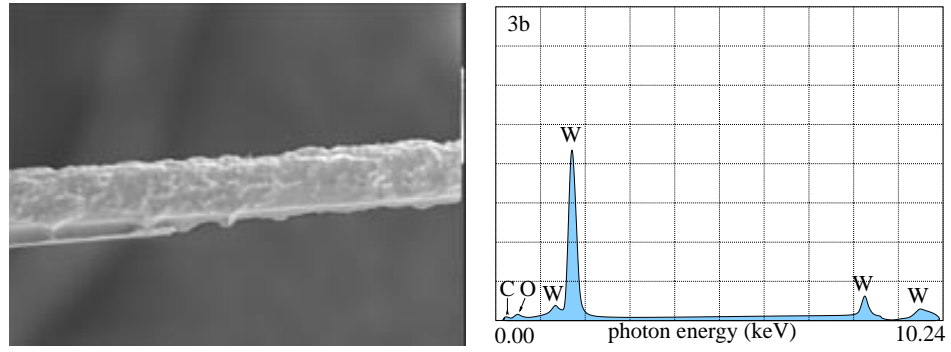


Figure 5.36: SEM micrograph of wire 11 at the same place as in figure 5.34 (left). More than a half of the wire volume has been etched away. On the right, the EDS spectrum from the same wire.

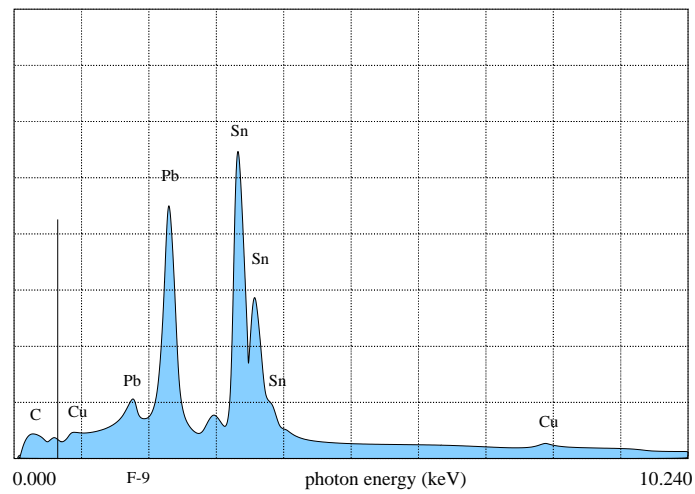


Figure 5.37: EDS spectrum of a solder point.

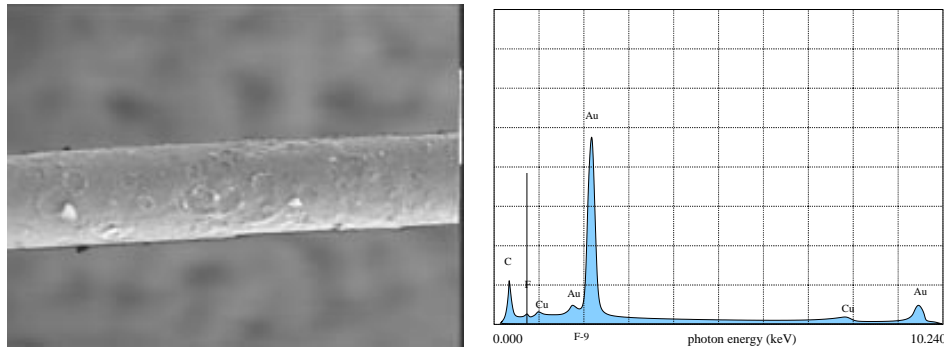


Figure 5.38: *SEM micrograph (left) and EDS spectrum (right) of the “anomalous” region of the non-irradiated “hot” wire 15.*

- the current and the dark current in one reference cell, which was connected to the HV only for 5 seconds per measurement cycle (15 minutes);
- temperatures of the double-box and of the gas bottle;
- atmospheric pressure.

Results

Ruptures. The wires started breaking already after 0.3 C/cm in both gas systems. In sum, 5 wires ruptured in the “dry” gas system and 2 wires in the “humid” one before 0.55 C/cm. All of them were equipped with capillaries. Then, the “dry” chamber was opened to investigate wires and the cathode under the electron microscope (see below). During this procedure the “humid” chamber was exposed to air for several hours, closed again and after flushing with the “humid” counting gas was irradiated further. We did not observe any rupture up to 1.8 C/cm when we stopped the test. It could be concluded that the presence of some amount of water suppresses the wire rupture rate. To validate these results, we dried out the chamber again, connected four “new wires” with capillaries to the HV, which were not under the HV before and exchanged the “humid” gas for a dry one. During an additional irradiation up to 0.6 C/cm, two “new wires” and all the “old wires” (the wires that were irradiated and under the HV from the beginning of the test) with capillaries and also two “old wires” with open geometry without capillaries broke.

To summarize, the start of the wire breaking was in both the “dry” and the “humid” chambers (irradiated in parallel) after about 3 C/cm. At 0.55 C/cm the test with “dry” chamber where the number of broken wires reached 5 was terminated, whereas the “humid” chamber was temporarily exposed to humid air and irradiated further. After this exposure we did not observe any further wire ruptures for

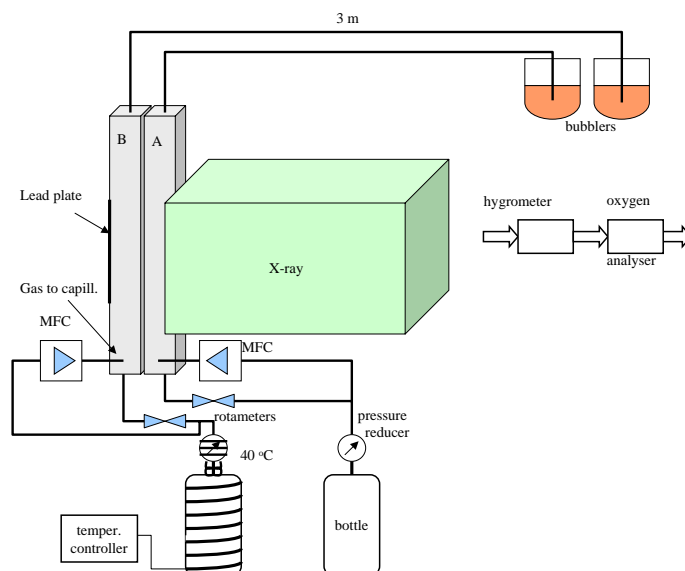


Figure 5.39: Schematic view (top) and photograph (bottom) of the aging setup.

parameter	value
chamber length	44 cm
chamber width	14 cells/monolayer
glue	Stycast E-solder 3025
irradiated region	12 cm
box volume	2 x 2.2 l
box window	14 cm x 13 cm
gas	Ar/CF ₄ /CO ₂
flow	1 vol/h
HV	1800 V
current density	0.6 μ A/cm
H ₂ O inp	<10 / 200 ppm
H ₂ O outp	50 / 250 ppm
O ₂ inp	30 ppm
O ₂ outp	200 / 300 ppm

Table 5.3: *Main constructional parameters and working parameters of the test.*

additional 1.2 C/cm. Then this chamber was dried out and tested in dry gas. The wire ruptures started again.

Currents and dark currents. The currents of cells in the "dry" chamber are shown in figure 5.40. As can be seen, there was no gain drop up to 0.55 C/cm.

The dark currents were highly different and strongly fluctuating in the "dry" gas system. In the "humid" system the dark currents were unstable either dehydration procedures (from 0 to 0.6 and from 1.8 C/cm). Dark currents in the "humid" chamber are shown in figure 5.41. The chamber started showing distinct stabilization effects after being exposed to air (from 0.6 to 1.8 C/cm). Certainly, dark currents of this order are not dangerous for the OTR system.

Transient aging. The current behaviours of the cells with capillaries in the two gas systems were different just after irradiation breaks as shown in figure 5.42. As we mentioned above, the irradiation was not continuous but was interrupted for 15-30 minutes after each time period of 3 hours for dark current measurements. If the p/T-corrected current in the chamber with a humidity of 250 ppm was nearly the same before and after the irradiation breaks, the current in the "dry" cells with capillaries (H₂O=50 ppm in the box) was approximately by 8% higher after than before each irradiation break. Just after start of the irradiation the currents in these cells began falling continuously reaching equilibrium with a time constant of approximately 12 minutes. This effect is reminiscent of the effect observed in ATLAS [4] and referred to as "transient aging". This transient decrease of the

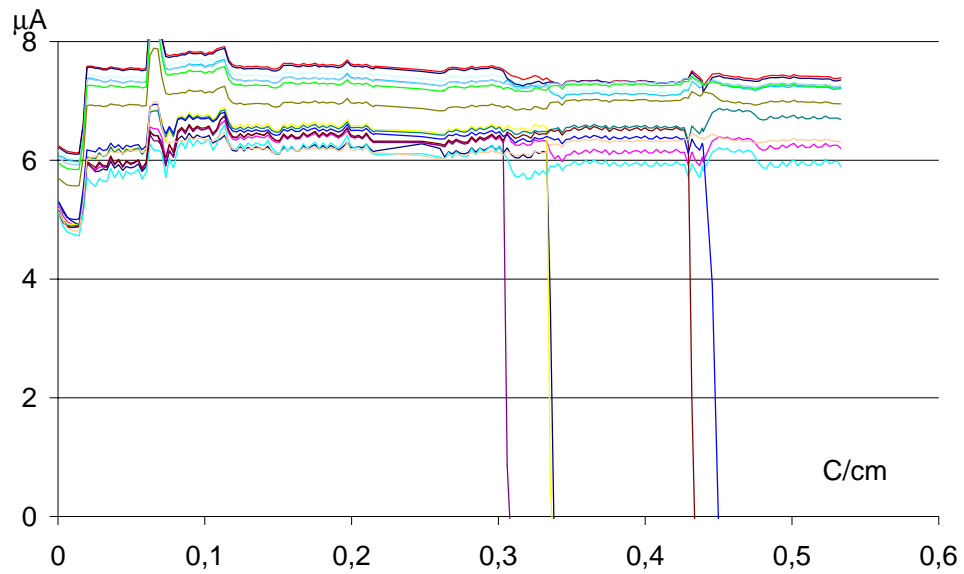


Figure 5.40: Pressure and temperature corrected currents in the "dry" cells. The first cell broke at 0,3 C/cm, the 5-th at 0,45 C/cm.

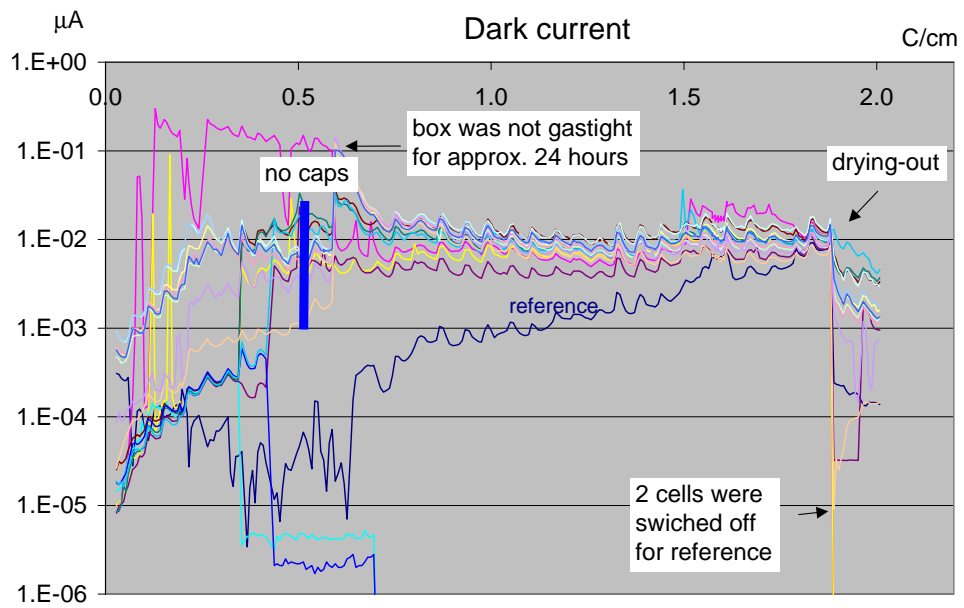


Figure 5.41: Dark current in the "humid" chamber where the gas contained 200 ppm water.

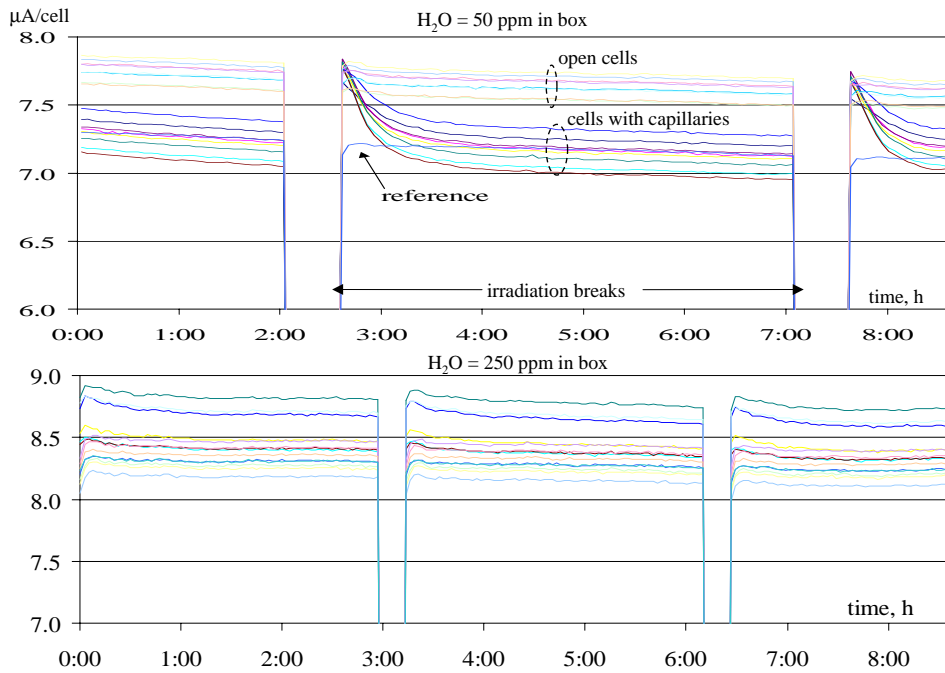


Figure 5.42: Transient aging: temporary current drop in "dry" cells with capillaries. The transient aging was not pronounced in open cells due to probably higher gas flow (thermal convection). In humid gas the responsible species were, most likely, neutralized by water.

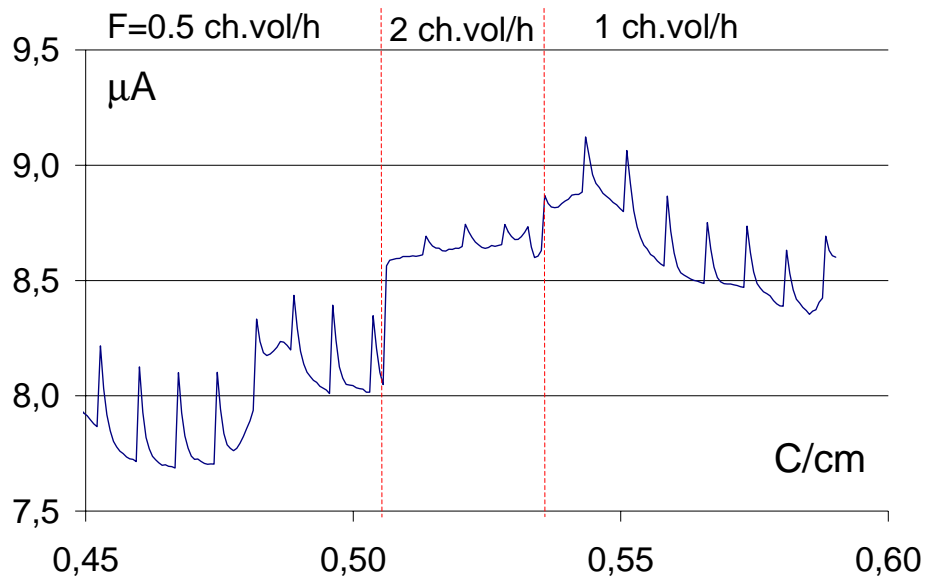


Figure 5.43: Cell-averaged current vs dose in "dry" cells with capillaries. Spikes of the curve were caused by the transient aging effect. The amplitude of the spikes depended on flow rate.

current, which we also called “transient aging”, was dependent on the flow rate as can be seen in figure 5.43. At higher flow the transient aging was less pronounced.

Apparently, the same effect was observed in the α -setup and described in 6.3. The effect is, most likely, caused by relatively long-lived, electronegative species produced in the avalanche. The fact that the “transient aging” did not appear in the “humid” chamber gave us a hint that the responsible species may be F_2 , since F_2 is the most electronegative gas and reacts with water.

Visual inspection. The photograph of the open chamber which was tested from the very beginning in the dry gas and which showed five wire ruptures is presented in figure 5.44. All the broken wires were ruptured approximately in the center of the irradiated region as denoted in the figure by the blue circle.

Black shaded spots can be distinctly seen on the edge of the irradiated region. EDS spectra of the cathode measured directly from the black spot and from a normal non-shaded area near the shaded region are shown in figure 5.45. The comparison indicates that the black deposit on the cathode is tungsten, which was probably etched away from the wire.

Also the wires were investigated by the electron microscopy. In figure 5.46 one can compare diameters of a non-irradiated wire, and two irradiated wires in the middle of the irradiated region. The diameter of the non-irradiated wire is the smallest.

The irradiated wires did not have the pure golden surface but were usually slightly covered with whiskers from which EDS spectra showed mostly lines of tungsten. Figure 5.47 shows a photograph with large magnification (left) and an EDS spectrum (right) of a whisker on the surface of wire 6. According to the X-ray spectroscopy, the whisker mainly consisted of tungsten with a small amount of oxygen, fluorine and nickel. It might be mentioned here that the nickel emission was probably observed due to a partial irradiation of the probe carrier with the electron beam (explanation by an expert).

As a continuation of this test, we checked also the aging behaviour of straws in the same setup. The test is described in the following section.

5.2.3 Aging test with straws

From detailed investigations of ATLAS straws it is well known that they have a good radiation resistance. Since straws were discussed as a back-up solution for the inner part of the OTR in HERA-B, it was interesting to check both honeycomb cells and straws under the same conditions. Therefore, the setup and parameters of the test were chosen to be exactly the same as in the previous test in the dry gas system.

A straw tube drift cell consists of a multi-layer cathode (see section 1.2.2) with an outer diameter of 4.9 mm, a 25 μm gold-plated wire, ULTEM end-pieces. For more details see papers [54, 3].

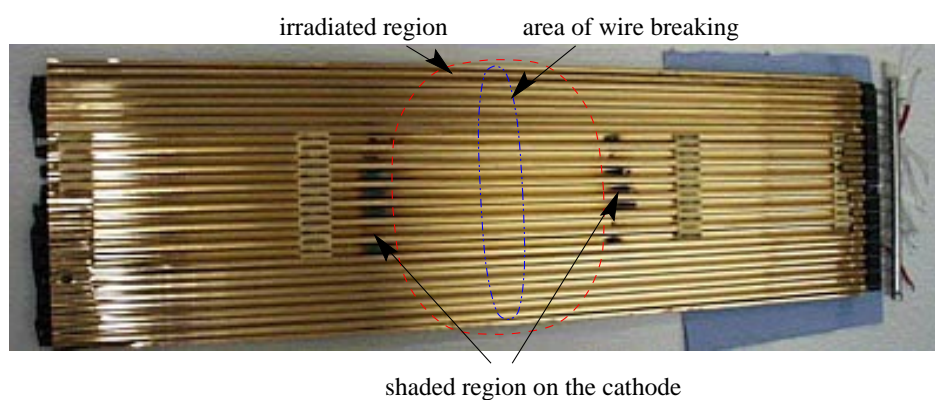


Figure 5.44: Photograph of the open “dry” chamber.

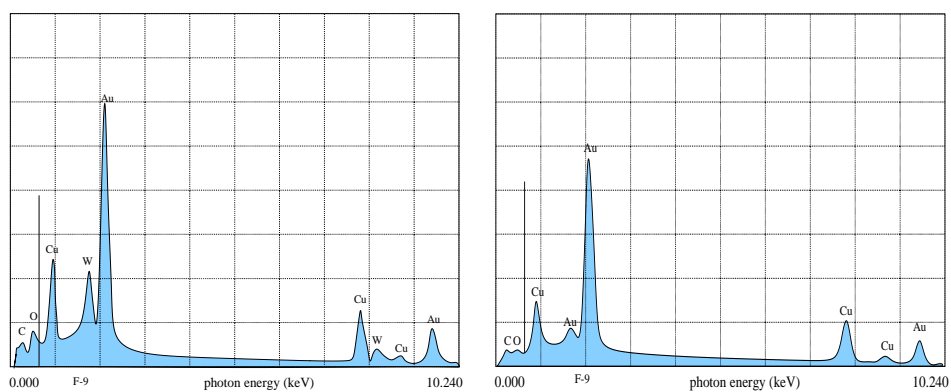


Figure 5.45: EDS spectra from the shaded region (left) and near it (right) on the cathode above the irradiated region (see figure 5.44).

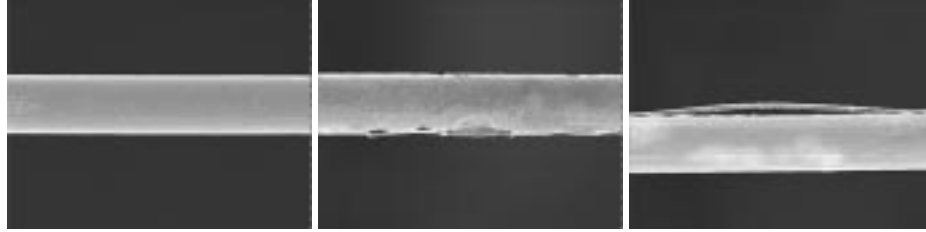


Figure 5.46: SEM micrographs of a non-irradiated wire (left), irradiated wire 6 in the middle of the irradiated region (middle) and irradiated wire 7 in the middle of the irradiated region (right). All these cells had no broken wires until the end of the test (0.55 C/cm).

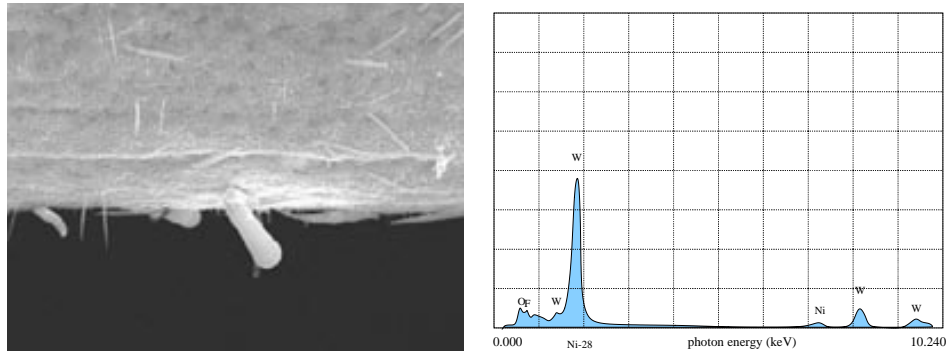


Figure 5.47: Photograph of wire 6 with high magnification (left) and EDS spectrum from the large whisker on the photo (right).

Setup. This aging test was a continuation to the test described in section 5.2.2 using the same parameters. The straw chamber (40 cm long, single-layer with 28 cells) was positioned in the box where the “dry” chamber was irradiated before. A photograph of the tested straws is shown in figure 5.48. In parallel, in the other gas system a chamber that was designated in section 5.2.2 as “humid” chamber was irradiated. Some of the cells of this chamber which were not under the HV before were connected to the HV. The gas mixtures filling the boxes with straws and honeycomb chambers had approximately the water content of 100 ppm and 120 ppm, respectively: slightly higher than in test 5.2.2 due to an increase in air humidity (the humidity is higher in summer than in winter).

Results The wires of the straws and the wires of the honeycomb chamber started breaking approximately at the same time, after a dose of 0.6 C/cm. Half of all the irradiated wires in the chamber and the same fraction of wires in the honeycomb chambers died before 1.1 C/cm. The currents in the honeycomb chamber and in the straw chamber are shown in figure 5.49. There is no indication of anode aging. We did not observe any other aging effects except wire ruptures. It should be noted that the dark current in straws, which did not have FR4 strips, was 3 orders of magnitude lower than in honeycomb chambers.

5.2.4 Test with a water content of 350 and 700 ppm

Purpose

The aging tests discussed before in sections 5.2.1, 5.2.2, 5.2.3, gave us a hint that the wire rupture rate varies inversely with the water content. However, according to figure 4.11, at higher humidities another aging effect starts showing up: the increase in the wire-supporting strip conductivity. Therefore, the main purpose of this test was to determine an optimal humidity level.

Setup

We used the same type of chambers as in the test before, where the water content was 50 ppm and 200 ppm. One half of the chamber was shielded with an aluminium plate with a thickness of approximately 0.5 mm as shown in figure 5.51 to suppress the irradiation intensity in one half of the cells approximately two times. The different intensity was needed to study the intensity dependence of aging effects.

The setup shown in figure 5.50 was improved compared to the previous test. To insure a stable gas humidity, we used an ice box embedded in a normal household refrigerator. To reduce the temperature fluctuation, we updated the fridge with a special temperature controller, stabilizing the temperature with a precision of 1 degree. Reducing the temperature of the ice box to $-14\text{ }^{\circ}\text{C}$ and applying a pressure of 2.3 bar, we humidified the counting gas to 700 ppm. A part of the gas with a water content of 700 ppm flowed into one box “B”, the other part, mixed with the dry gas through flow resistors (capillaries), into the other box “A”. The flow

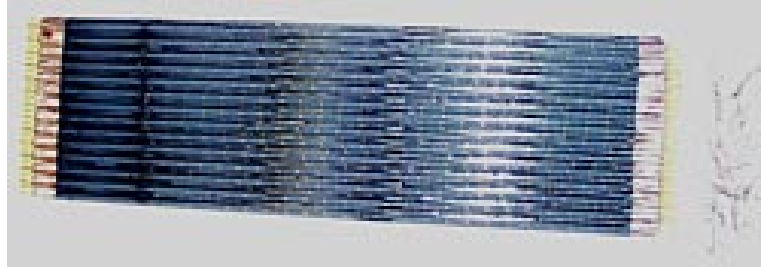


Figure 5.48: *Photograph of the straws used in the test.*

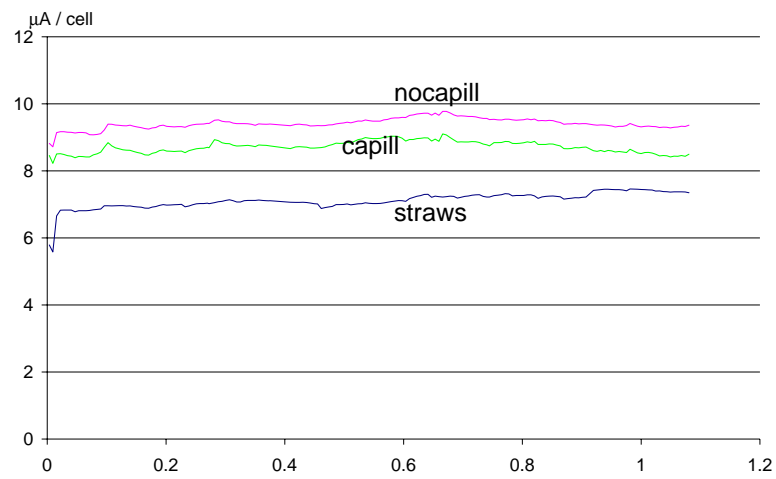


Figure 5.49: *Currents with the p/T -correction in the straw chamber and in the honey-comb chamber having cells with capillaries and without.*

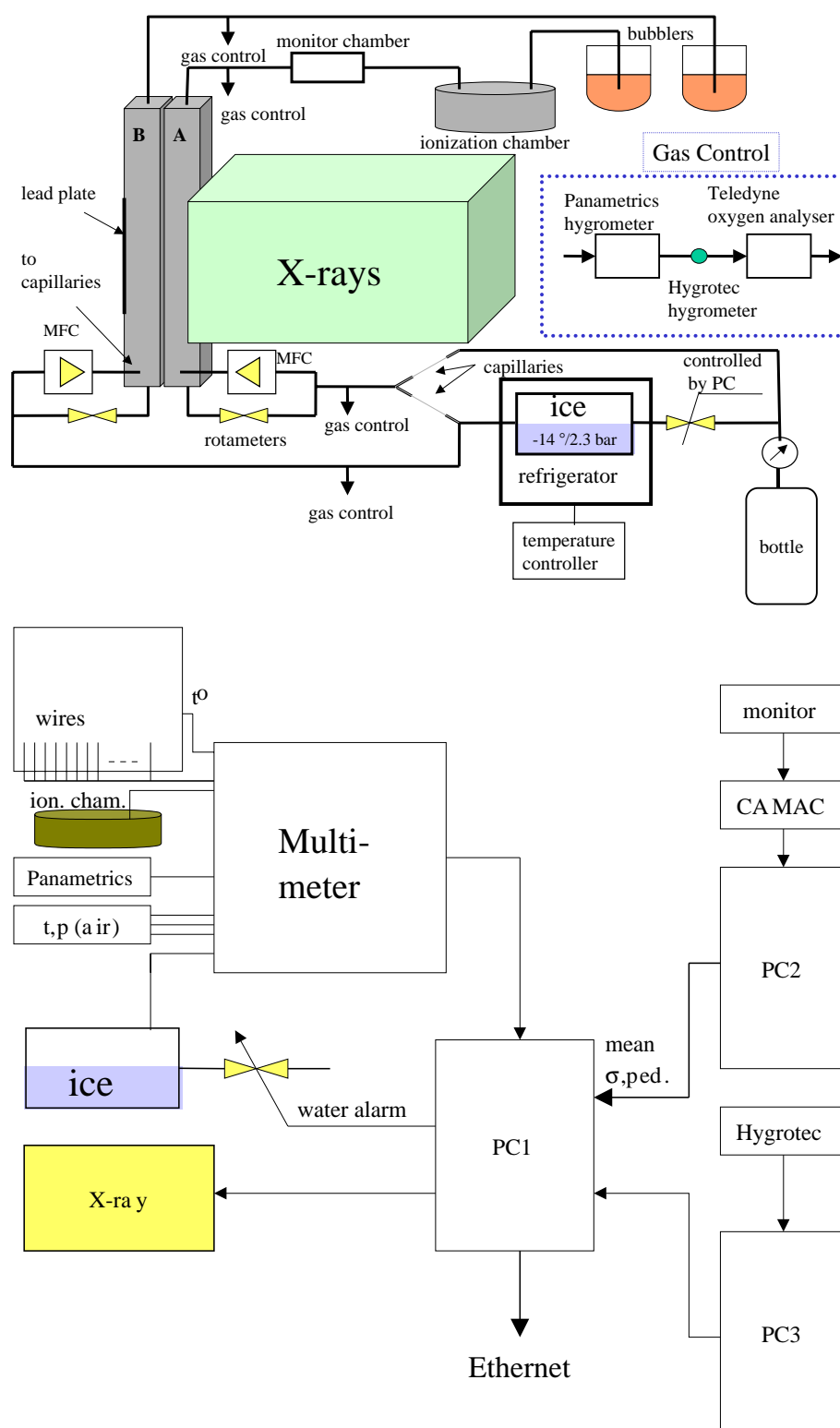


Figure 5.50: The gas flow in the aging test (top) and readout system (bottom).

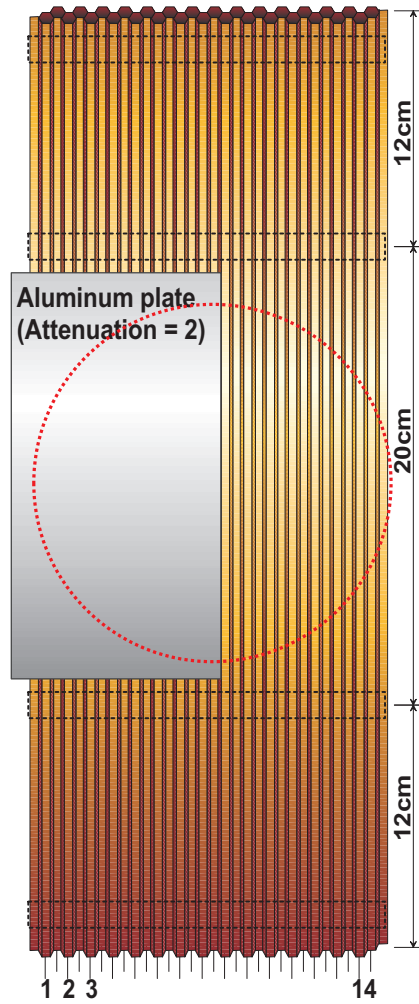


Figure 5.51: Chamber used in the test. The construction is the same as in the test 5.2.2. The aluminium plate was added to reduce the irradiation intensity in one half of the chamber by a factor of 2.

through the boxes was regulated with rotameters and the flow through chambers (capillaries) was regulated with mass flow controllers.

To summarize:

- 50% cells had open geometry and the other had capillaries at input;
- 50% cells were irradiated with an intensity of $0.4 \mu\text{A}/\text{cm}$ and the other with a two times lower one;
- 50% cells used the counting gas with a water content of 350 ppm and the other with 700 ppm.

The boxes were flushed for 7 days before starting the irradiation test.

The gas control system included Panametrics and Hygrotec hygrometers, as well as a Teledyne oxygen analyzer. All devices were connected one after another. The gas was analysed occasionally in places denoted in figure 5.50 by “gas control”. The test parameters are presented in table 5.4.

parameter	value
gas	Ar/CF ₄ /CO ₂
flow	1 vol/h
HV	1800 = V
current density	0.4, 0.8 $\mu\text{A}/\text{cm}$
H ₂ O content/inp	350 / 700 ppm
H ₂ O content/outp	400 / 750 ppm
O ₂ content/inp	30 ppm
O ₂ content/outp	200 / 300 ppm

Table 5.4: *Main working parameters of the aging test.*

Supplement: monitor and ionization chambers. Production of relatively long-lived electronegative species which probably give rise to the “transient aging” (see section 5.2.2) can be also observed in the drift chambers that are directly supplied with the output gas of the irradiated chamber. Therefore, the output of chamber “A” was connected to a “monitor chamber” and an “ionization chamber”. The monitor chamber was a cylindrical proportional chamber with a diameter of 15 mm irradiated with an ⁵⁵Fe source. Due to a larger diameter and lower electric field it was more sensitive to electronegative species than, for example, a honeycomb chamber with 5 or 10 mm cells.

The ionization chamber had a drift distance of approximately 10 cm between two electrodes on which an alternating voltage of several hundred volts was applied. The gas in the drift volume was ionized by an alpha source. The ionization chamber was very sensitive to electronegative species in the thermal electron energy region. Indeed, the reduction in the current was proportional to the concentration of electronegative species. As the field was relatively small, of the order of 100 V/cm,

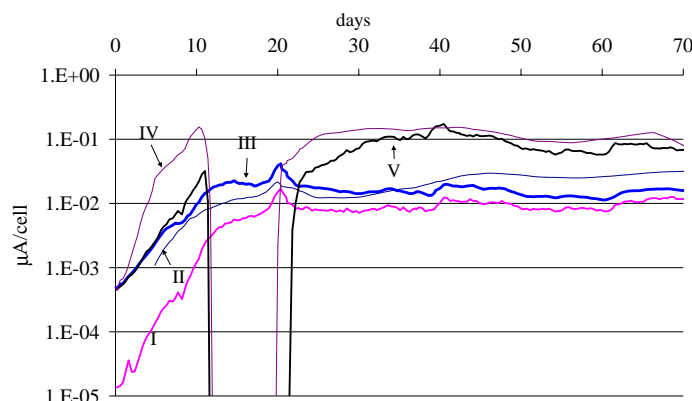


Figure 5.52: Behaviour of the dark currents. I: 350 ppm/0.4 $\mu\text{A}/\text{cm}$; II: reference wire; III: 350 ppm/0.8 $\mu\text{A}/\text{cm}$, IV: 700 ppm/0.4 $\mu\text{A}/\text{cm}$; V: 700 ppm/0.8 $\mu\text{A}/\text{cm}$. Denotation X ppm/ Y $\mu\text{A}/\text{cm}$ means the cells with a water content of X ppm and irradiated under the intensity of Y $\mu\text{A}/\text{cm}$.

and the drift gap relatively large, 10 cm, the probability for a free electron drifting a relatively long time in the gap to be attached by an electronegative molecule is much higher than in honeycomb chambers.

Data Acquisition System. A scheme of the data acquisition system is shown in figure 5.50. As can be seen, we recorded the currents and dark currents from each irradiated wire and one reference wire, the room temperature, the air pressure and the temperature of the ice box. In addition, we supplemented our data-base with continuous recording of the current in the ionization chamber, and some ^{55}Fe spectrum parameters (mean, rms, pedestal) from the monitor chamber. One hour long irradiation interruptions were made every 10 hours to measure the dark currents and the transient aging effect in the monitor and ionization chambers.

Results

We did not observe any of the aging effects up to ≈ 4.5 C/cm where the test was finished. The currents in different cell groups are shown in figure 5.53.

The dark currents, which are shown in figure 5.52, continuously increased during the first two weeks and saturated on some levels depending on humidity and intensity.

To see a possible correlation between the dark currents, currents and humidity in all the 8 cell groups, the distribution of dark currents and currents is shown in figure 5.54. The dark currents in cells with higher irradiation and higher humidity were higher. The observed humidity dependence was also seen in the previous measurements (see figure 4.11). Figure 5.55 shows the correlation between dark currents and intensities (currents) in cell groups with different intensities, water contents, cells with and without capillaries. A linear intensity dependence of the

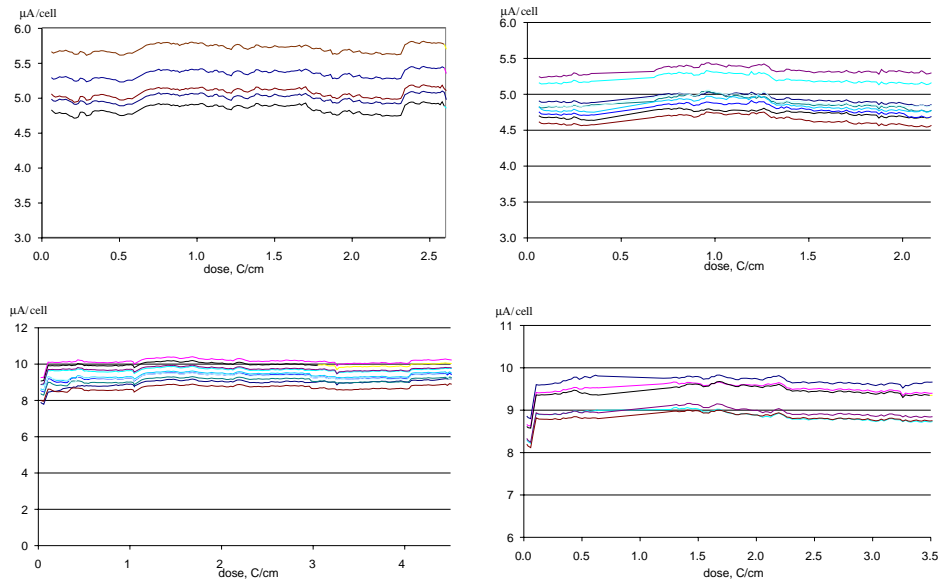


Figure 5.53: *Currents with p/T-correction from the cells with a current density of 0.4 $\mu\text{A}/\text{cm}$ and a water content of 350 ppm (left, top); 0.4 $\mu\text{A}/\text{cm}$ and 700 ppm (right, top); 0.8 $\mu\text{A}/\text{cm}$ and 350 ppm (left, bottom); 0.8 $\mu\text{A}/\text{cm}$ and 700 ppm (right, bottom).*

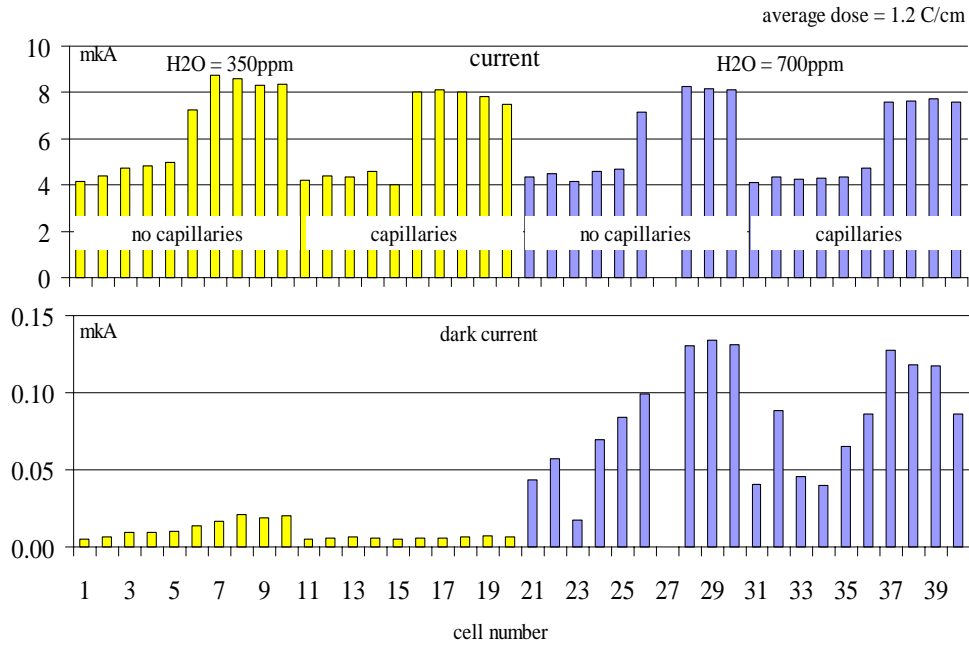


Figure 5.54: *Distribution of currents and dark currents.*

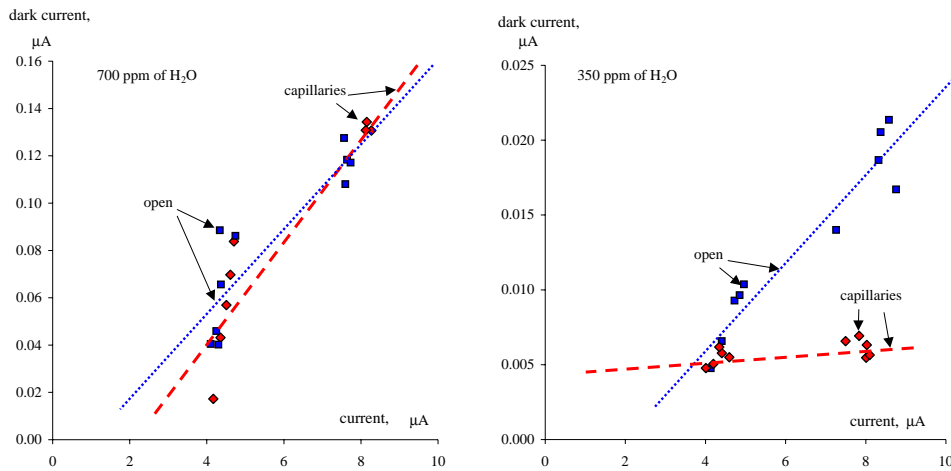


Figure 5.55: Dark current vs current in different cell groups.

dark current can be assumed according to this figure. In order to investigate the humidity dependence of the dark current in a larger humidity range we increased the humidity in the gas system containing previously 700 ppm water to 1000 ppm and irradiated the chamber under the same conditions until the dark currents were saturated. The combined results of the previous test 5.2.2, made with the humidity of 50 and 200 ppm, and of this test are shown in figure 5.56. It should be remarked that contrary to the previous measurement, shown in figure 4.11, the saturated dark current is plotted in this figure.

The current drops due to the transient aging effect in the honeycomb chambers in both gas systems were approximately 1% of the average current. This is consistent with other tests performed at the humidity higher than 100 ppm. The fluctuations of the ^{55}Fe spectrum mean values measured in the monitor chamber connected to the output gas of one of the irradiated boxes (see figure 5.50) were not correlated with irradiation interruptions. However, the current in the ionization chamber showed clear correlation with irradiation interruptions as can be seen in figure 5.57.

5.2.5 Irradiation in dry environment

Chamber "A" (tested before at the humidity of 350 ppm) remained in the same gas box as in the previous test 5.2.4. Additionally, a new chamber with the same construction as the old one was positioned in the other gas box. Both chambers were dried out and irradiated further under the same conditions except that the humidities were 80 ppm and 120 ppm in the gas systems with the new and old chambers, respectively. The difference in humidity levels was a result of different window constructions in the different boxes (see the description of the double-box

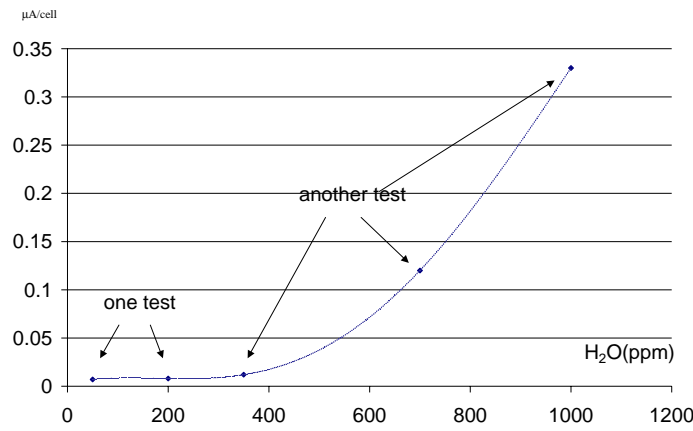


Figure 5.56: Saturated dark current as a function of water content. The results from the previous test performed with a water content of 50 and 200 ppm are also included.

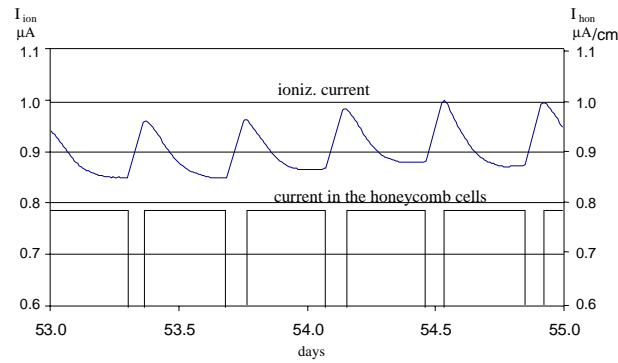


Figure 5.57: Behaviour of current in the ionization chamber.

in section 5.2.2).

Results. We irradiated the chambers up to 1.2 C/cm. The cells started dying after approximately 0.2 C/cm in the “old” chamber, with 80 ppm of water. Figure 5.58 shows the lethal dose of the cells versus their average intensity. In this figure 50% of the first dying cells irradiated with low intensity and the same fraction of wires seeing high intensity were compared.

The average intensities and average dying dose in the cells with low intensity vs those with high intensity are listed in the following table.

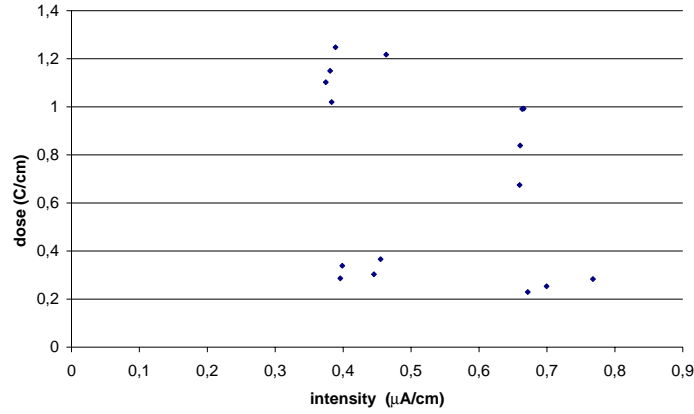


Figure 5.58: Dose at which wires broke vs average intensity. The points can be combined into four groups. Two lowest and two upper groups correspond to the cells with a humidity of 80 ppm and 120 ppm, respectively; the two left and two right groups correspond to average intensities of ≈ 0.4 and ≈ 0.7 $\mu\text{A}/\text{cm}$, respectively.

intensity $\mu\text{A}/\text{cm}$	dose C/cm
0.41	0.78 ± 0.07
0.68	0.61 ± 0.1

As these values indicate, wires which had 1.66 times higher intensity broke, on the average, after 1.28 times lower doses. According to the standard deviations, the results are consistent with the statement that anode etching rate does not depend on the intensity.

The wire rupture rate in the cells with capillaries was approximately 20% higher than in the cells with open geometry.

Discussion. According to the results, the anode corrosion was strongly suppressed by water. Therefore, we assume that fluorine is responsible. Also, it is known that the F atom is very small and, likely, can permeate through a 400 nm thick layer of gold (see table 1.3) and attack the tungsten. The wire becomes thicker, the golden layer splits off.

However, other results were obtained in another setup described in [28], where a closed purification gas system as in the Outer Tracker was tested (see a description of the OTR gas system in section 1.3.4): although the water content was measured to be below 20 ppm, no anode aging was observed up to 2.35 C/cm made at an intensity of 0.2 C/cm. Therefore, the anode etching needs further investigation.

Wire swelling and gold corrosion was also observed in aging tests of the ATLAS TRT straws with a different gas mixture: Xe/CF₄/CO₂ [66]. A significant increase in the oxygen concentration of the gold coating was found. Although the anode etching was observed at a relatively high humidity of several percent, the onset of

this effect was seen after 4 C/cm, that is at much higher doses. However, we did not investigate honeycomb chambers for doses larger than 5 C/cm. We exclude the full responsibility of oxygen in our case because:

- Oxygen does not react with water.
- Production of oxygen in the avalanche in the mixture Ar/CF₄/CO₂ (65:30:5) is very small due to: the very small cross section for electron impact dissociation of CO₂, and the small fraction of CO₂ in the gas. A simple estimation cannot substantiate the etching of half of the wire volume by oxygen after 0.3 C/cm.
- A reproducible anode etching in mixtures without CF₄ leading to wire ruptures after 0.3 C/cm has, to our knowledge, not been reported.

One of the reasons for the intensity dependence of the etching rate (see figure 5.58) could be the non-zero water content. Indeed, fluorine reacts with water rather fast (after 20 μ s, if the water content is 100 ppm, see table 9.3). Thus we would expect that the onset of wire etching occurs when water is completely consumed in the reaction with fluorine or other species. Consequently, the etching rate is proportional not to the intensity I but instead to $I - I_a$ where I_a is the maximal intensity at which all the produced fluorine atoms (molecules) are bound to water.

5.2.6 Conclusion

Here we summarise the significant observations in the tests with 40 cm long chambers irradiated with X-rays over a region of 12 cm diameter. The tests were made only with the mixture Ar/CF₄/CO₂ and a gas flow rate, mainly, of 1 vol/h. We did not observe any gain loss, related to polymer formation on the anode wire (anode aging) and we did not observe the Malter effect either. The saturated dark current in honeycomb chambers versus humidity was summarised in figure 5.56. The dark currents in straws were 3 orders of magnitude lower than in honeycomb chambers due to the presence of wire-supporting strips in the latter.

We observed that wire corrosion, which was also observed in “Karlsruhe III” (see section 4.6.2), led to wire ruptures already after 0.3 C/cm when the humidity was about or lower than 100 ppm. The tests showed clear evidence that the anode corrosion was strongly suppressed by water. Indeed, each test with the humidity of less than 120 ppm showed first ruptures already after 0.7 C/cm. Whereas, no rupture was observed at a water content of 350 ppm or more up to 4.5 C/cm. The results concerning the anode wire corrosion are summarised in table 5.5. The investigation under the electron microscope showed that the diameters of wires increases in the process of irradiation and the gold-coating on the wires peels off. The X-ray spectroscopy of heavily etched wires showed only tungsten and gold on spots where gold peeled off. On other spots where W was deposited (for example, in form of whiskers) above the gold surface of the anode or the cathode we found also oxygen.

N	Sect.	Remarks	Dose C/cm	H ₂ O ^a		O ₂ ^a		Ruptures in cells with capillaries	Ruptures in cells without capillaries
				inp	out	inp	out		
1	5.2.1	after each rupture the box was opened for internal disconnection, which considerably increased humidity; all wires had capillaries; some capillaries were blocked	3.7	<10	500			after 1.2 C/cm cells with blocked capillaries started breaking, followed by other cells after 2.2 C/cm	
2	5.2.2		0.55	<10	50	30	200	ruptures started after 0.3 C/cm; 5 ruptures before 0.55 C/cm	no ruptures
3	5.2.2	chamber was dried out at 40 °C at the beginning, water inside the cells can be very low if absorbed by plastic after this procedure	1.8	200	250	30	300	2 wires broke at 0.4-0.5 C/cm; no further ruptures	no ruptures
4	5.2.2	chamber was used in test 3, some wires not under the HV before were additionally connected to the HV	1.2	<10	120	30	250	“old” wires started breaking after 0.3 C/cm; “new” one after 0.6 C/cm	2 “old” cells died at 1.2 C/cm
5	5.2.3	straw chamber was used; test was made in parallel with test 4	1.2	<10	100	30	200	ruptures started after 0.6 C/cm; 50% of cells died before 1.2 C/cm	
6	5.2.4		4.5	350	400	30	200	no ruptures	no ruptures
7	5.2.4		3.5	700	750	30	300	no ruptures	no ruptures
8	5.2.4	chamber was used in test 6	1.2	<10	80	30	250	onset of ruptures after 0.23 C/cm; the half died before 0.35 C/cm	onset of ruptures after 0.28 C/cm; the half died before 0.4 C/cm
9	5.2.4	test made in parallel with test 8	1.2	<10	120	30	250	onset of ruptures after 0.67 C/cm; the half died before 1 C/cm	onset of ruptures after 1.2 C/cm; the half died before 1.5 C/cm

^aApproximate time-averaged values of water and oxygen content in ppm during the test are given.

Table 5.5: Summary of results concerning the humidity dependence of the anode corrosion effect.

Since anode etching was strongly suppressed by water, we believe that fluorine is responsible: fluorine is very aggressive and rapidly reacts with water (see table 9.3).

The cells with capillaries started usually dying faster than those without capillaries. However, in test 8 (see table 5.5) this effect was not significant. The influence of capillaries can be explained by the fact that the water content in open cells and in the box are approximately equal but the water content in cells with capillaries is smaller because they are supplied with the gas having in the “dry” case a humidity of less than 10 ppm. The main conclusion which can be drawn from the tests described in this chapter is that the water content should be regulated in the OTR in the region of 300-700 ppm.

We believe that the intensity dependence of etching rate is as follows:

$$E \sim I - I_a(p(n_{H_2O}))$$

where $I_a(p(n_{H_2O}))$ is the irradiation intensity at which all produced fluorine get bound by water (so that E depends on the water content, n_{H_2O}).

A low water content leads to wire corrosion, and reversely, a too high water content strongly increases the wire-supporting strip conductivity.

Chapter 6

Aging tests with an α -source

6.1 Introduction

According to the previous tests described in chapter 4 (see also later tests by the HERA-B muon group [27]), drift chambers age differently under different types of irradiation. As was also shown, the Malter effect rapidly appeared in OTR aging tests made with certain hadronic beams already after doses of $O(1 \text{ mC/cm})$ and did not appear with X-rays or electrons at 4 orders of magnitude higher doses. This observation implies that it is important to try different types of irradiation in aging tests. According to section B.1, an α -particle produces an about 100 times larger number of free electron-ion pairs than an X-ray photon. The high ionization leads to high plasma densities in the avalanche, possibly resulting in higher polymerization rates. Therefore, it was useful to make the following tests with α -particles.

6.2 Setup

The test chamber is shown in the left part of figure 6.1. It had a similar construction as the double-strip chamber in the X-ray aging test shown in figure 5.1. In the central area, with a width of 4 cells and a length of 25 mm, holes with a diameter of $200 \mu\text{m}$ were drilled to be able to irradiate with an α -source.

The chamber was placed horizontally in a box of 250 cm^3 volume equipped with a window with an area of 70 cm^2 made of aluminized Mylar + $100 \mu\text{m}$ thick aluminium foil.

The scheme of the gas system is shown in figure 6.1. The gas was fed into the box via an about 18 m long stainless steel pipe. For this test, mostly the gas mixture $\text{Ar}/\text{CF}_4/\text{CO}_2$ was used.

For the irradiation a ^{241}Am source ($E_\alpha \approx 4.5 \text{ MeV}$) with an activity of 15 MBq was used. Because the α -source was inside the box and could not be removed, we could not measure dark currents without background radiation from the source

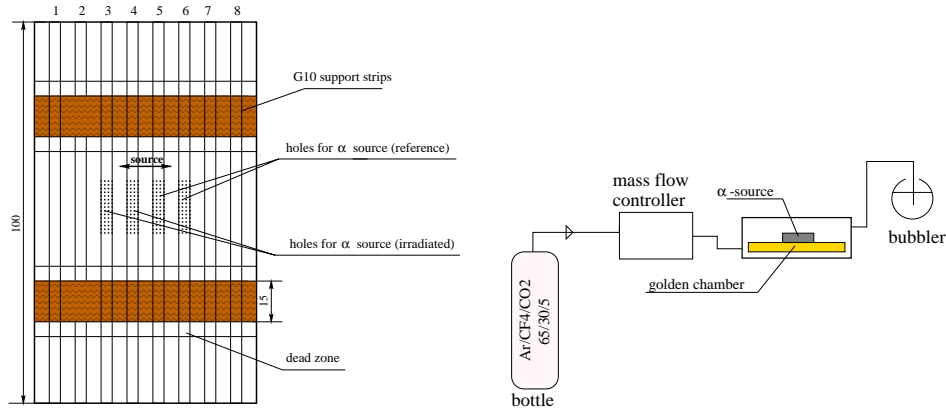


Figure 6.1: *On the left, chamber construction for the aging test with alpha-irradiation. On the right, the gas system used in the test with alpha-irradiation.*

(mainly 60 keV photons) even if the source was moved sideways from the perforation. To reduce the background, the source was placed on a lead plate when moved to the side for dark current measurements.

In order to prevent a drift of the electrons through the holes into the cells (see section 6.3) the source had to be electrically insulated from the cathode and biased by applying a voltage of 9 V relative to the cathode from a battery. The source should not be grated by the perforated region during movements since fine fragments scratched from the insulating layer on the source can block the holes or can deposit on the wire surface. Therefore, the source was moved on Kapton foil rails.

6.3 Specific problems with perforated chambers

In a number of tests it was found that the current in a cell irradiated with the α -source consisted of two parts. In addition to the current generated by the ionization caused by an α -particle inside the cell, there was another part induced by electrons drifting into the cell through the holes from the highly ionized region, with a thickness of 1 mm, above the holes, between the surface of the perforated cathode and the bottom surface of the α -source. Indeed, the approximate scheme of the electric field in that region is shown in figure 6.2. A large part of the electrons drifting along the field lines get into the chambers through the holes.

The electrons could be kept from moving into the cell by a voltage of about 5 to 6 V applied to the source relative to the cathode. The above conclusions were drawn from the measured dependence of the current on the voltage applied to the source relative to the cathode (see figure 6.3).

The current measured with an unbiased source was not stable. Just after high

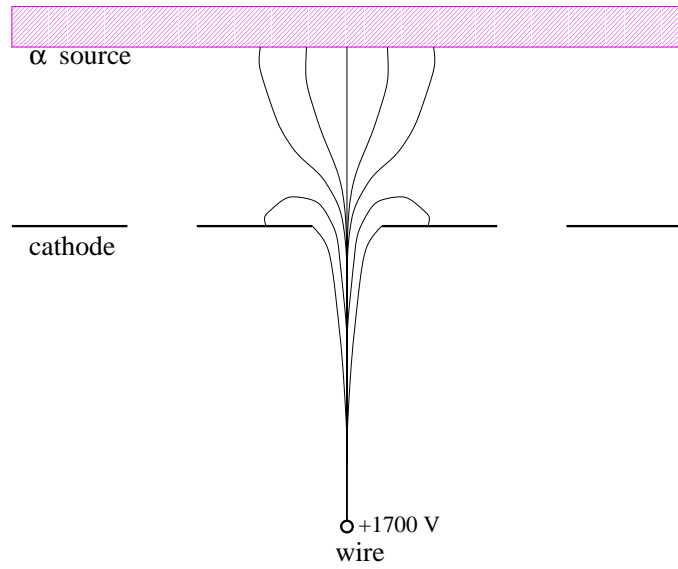


Figure 6.2: *Approximate scheme of electric field in region between source and perforated cathode.*

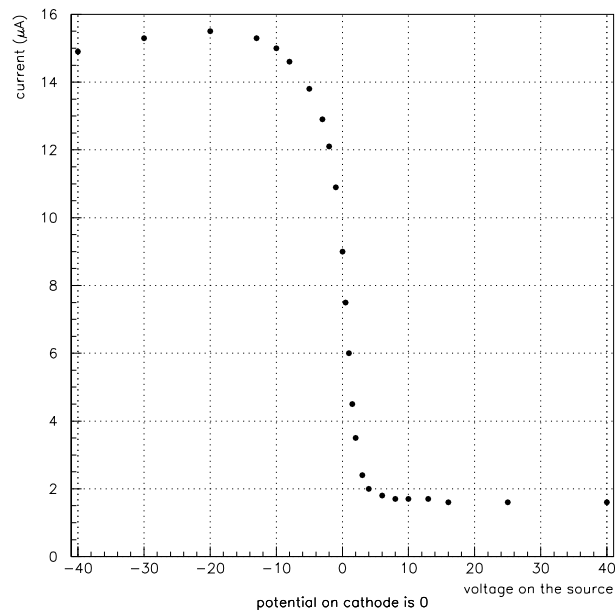


Figure 6.3: *Current as a function of bias voltage applied on the source relative to the cathode.*

flow gas flushing the current was high, about $17\ \mu\text{A}$, then it fell and settled down on some level roughly exponentially with a time constant corresponding approximately to the time of one gas exchange in the box. The level on which the current settled down depended on the gas flow. For example, at $F = 1\ \text{vol/h}$ it was about $6\ \mu\text{A}$ and at $F = 2\ \text{vol/h}$ it was about $9\ \mu\text{A}$. This behaviour of the current was reproducible. It could be explained by the following model.

The electric field in the region between the cathode and the source is very low, less than $50\ \text{V/cm}$, in comparison with more than $1500\ \text{V/cm}$ inside the cell. A free electron, slowly drifting in a low field, has a high probability to be attached to an electronegative molecule. Therefore, the flux of the ionization electrons going through the holes depends sensitively on the concentration of these molecules. After high-rate flushing the gas system is clean and the current is high. Then, due to, for example, contamination with atmospheric components the concentration of electronegative gases increases and reaches an equilibrium at some level. Hence, the current goes down and settles on a corresponding level.

In order to prevent a drift of the electrons through the holes into the cells the source was biased in all the consequent tests. To bias the source, a voltage of $9\ \text{V}$ relative to the cathode was applied from a battery.

6.4 Detection of electronegative species produced in plasma chemistry

Experiment

The high sensitivity of the current to the concentration of an electronegative gas, as described in the section above, could be exploited for the detection of electronegative species produced in the avalanche.

After high-rate flushing in $\text{Ar}/\text{CF}_4/\text{CO}_2$ the flow was set to a relatively low rate of $2\ \text{vol/h}$ and we started the test switching on the high-voltage only for a short time to measure the current. The current was dropping from about $17\ \mu\text{A}$ roughly exponentially with a time constant of about $1/2$ hour (see figure 6.4). After several hours it became stable at the level of about $12\ \mu\text{A}$. Our interpretation: this decrease of the current was caused by an increasing contamination of the gas with atmospheric components or from outgassing. As the gas system reached an equilibrium, the current stopped falling.

Afterwards, we switched on the HV continuously. The current started falling down roughly exponentially with a time constant of about $1/2$ hour and settled down on the level of $9\ \mu\text{A}$. This decrease of the current can be explained to be caused by electronegative species produced in the avalanche. A similar behaviour of the current was observed at $F = 1\ \text{vol/h}$. This suggests that the time constant for build-up of electronegative species is similar to the time for one volume exchange indicating that the life time of the relevant electronegative species is more than 1 hour.

The same test was made with an Ar/CO_2 (80/20) mixture at approximately

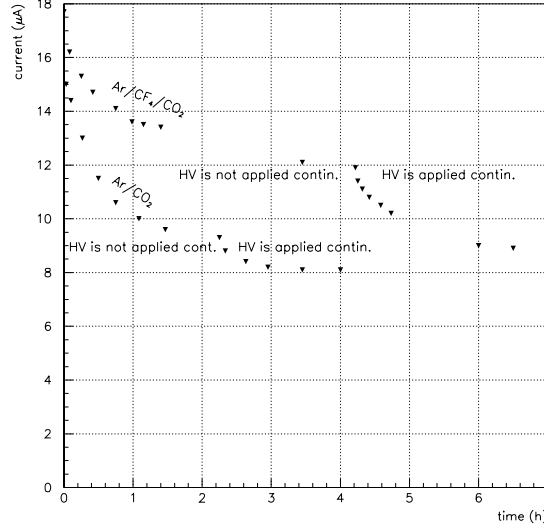


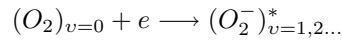
Figure 6.4: Current as a function of time passed after high-rate flushing using unbiased source.

the same gas gain and flow rate ($HV = 1400$ V, $F = 2$ vol/h). The first drop of the current was approximately the same as with the Ar/CF₄/CO₂ mixture, but the second drop, presumably caused by species produced in the avalanche, was about 3 times smaller (see figure 6.4).

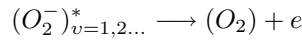
Model

From the atmospheric pollutants only oxygen and, much weaker, water are known to attach electrons. As can be seen in the figure 6.3, the electric field in the region between the α -source and the cathode is of the order of 10 V/cm. The effective electron energy in this region calculated using *Magboltz* is of the order of 0.05 eV, i.e. free electrons have thermal energies. Only electron attachment to O₂ is possible in the thermal energy region: water can attach electrons at energies around 7 eV, which are reached only close to the anode.

According to [21], the low energy electron attachment to O₂ is a three-body attachment reaction:



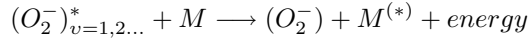
which continues like



parameter	value
gas	Ar/CF ₄ /CO ₂
flow	1 vol/h
HV	1830 V
current density	1.8 μ A/cm, 0.4 μ A/cm
irr.cell numbers	3, 4

Table 6.1: *Main parameters in the first aging test with an alpha-source (The humidity was not measured).*

or



where M is the third body and v is a vibrational level. The attachment of low energy electrons leads to the formation of unstable excited negative ions which can either auto-neutralize or be quenched by collision with molecules. The attachment coefficient could be found e.g in [22] and depends on the buffer gas in the range of 2 orders of magnitude. Such a strong variation makes it difficult to estimate the electron attachment coefficient for our mixture. Using the electron attachment coefficient η of the order of 10^{-30} cm⁶/s as a guidance, we would obtain the fraction of O₂ to be of the order

$$\frac{\Delta I}{I\eta n^2\tau} = O(10^2 \text{ ppm})$$

where $\frac{\Delta I}{I}$ is the relative current drop, $n = 2.6 \times 10^{19}$ 1/cm³ is the buffer gas concentration and $\tau \approx 1$ μ s is the electron drift time in the given region calculated using *Magboltz*. A check of the oxygen content with an analyzer was measured to be approximately 150 ppm, which substantiated this theoretical analysis.

In chapter 9 it will be shown that mostly HF is produced due to avalanche processes, if traces of water are present (At a water concentration of 100 ppm the typical reaction time between atomic F and H₂O is ≈ 20 μ s, while for the reaction F+F=F₂ it takes 25 s). According to [22], HF has a positive electron affinity and, therefore, can attach low energy electrons in three-body processes. Because HF is a highly corrosive gas, it is poorly studied and the electron attachment coefficient is not known.

As a conclusion to this test we should stress that carrying out aging tests using chambers with the perforated cathode one should be careful. The deviation of the current can be caused not by gas gain variation but rather by some other effects not relating to aging.

6.5 First aging tests

The parameters of the test are listed in table 6.1.

The cells 3 and 4 were subjected to a total radiation dose of about 0.7 C/cm at a current density of about $1.8 \mu\text{A}/\text{cm}$ (unbiased source) and 0.12 C/cm at a current density of about $0.4 \mu\text{A}/\text{cm}$ (biased source). The ^{55}Fe pulse height spectra did not show any observable fall of the gas gain in the irradiated region (at least, the gas gain loss was less than 2%).

The current measured with the α -source moved away from the perforated region (but still in the gas box) showed fluctuations (5-10%) about a mean value of about 100 pA to 400 pA depending on the actual source position. This current is consistent with being caused by background from the source. Above that no increase in the dark current was observed.

6.6 Aging tests with $\text{Ar}/\text{CF}_4/\text{CH}_4$ and $\text{Ar}/\text{CF}_4/\text{CO}_2$

As was shown in section 6.5, none of the aging effects was observed in $\text{Ar}/\text{CF}_4/\text{CO}_2$. We decided to check whether the test under the same parameters except that the mixture was changed to $\text{Ar}/\text{CF}_4/\text{CH}_4$ would show anode aging since anode aging was observed in the previous tests with hadronic irradiation. After an observation of gain loss the mixture was replaced by $\text{Ar}/\text{CF}_4/\text{CO}_2$ to see whether the gain could be recovered.

This aging test was made with the same setup and chamber as in the earlier test described in section 6.5 except now cells 5 and 6 were irradiated. The parameters of the test are listed in table 6.2.

parameter	value
gas	$\text{Ar}/\text{CF}_4/\text{CH}_4 \rightarrow \text{Ar}/\text{CF}_4/\text{CO}_2$
flow	1 vol/h, 5 vol/h
HV	1830 V
current density	$0.8 \mu\text{A}/\text{cm}$ at the start
irr.cell numbers	5, 6

Table 6.2: *Main parameters in the aging test.*

Measured variables

During the aging tests the following quantities were measured: the current in every irradiated cell, the overall dark current, ambient temperature, atmospheric pressure, humidity of air. In regular time intervals, we moved the source from the permanently irradiated cells to the reference cells 3 and 4 and measured the “reference current”. The humidity was not measured in the test (the fact that the water can strongly influence etching was not known at that time). Since the box was rather small containing large windows on both sides, the moisture content is expected to have been relatively high of several hundred ppm.

Results

The behaviour of the total current in the irradiated cells is shown in figure 6.5. As can be seen, during irradiation in Ar/CF₄/CH₄ up to 0.4 C/cm the current dropped by 70%. Afterwards, we increased the flow from 1 vol/h to 5 vol/h and the chamber recovered by 50% after 0.1 C/cm. Then, we reduced the flow again to 1 vol/h and changed the mixture to Ar/CF₄/CO₂. After 1.5 C/cm the current was restored. However, a comparison of the means of the spectra showed an approximately 15% gain loss in the irradiated cells relative to the gains in non-irradiated ones. The difference between the two measurements of the relative gain probably resulted from the large uncertainties when dividing the currents in radiated and reference cells (the current depends also on the source position on the perforated region).

Discussion. The gain loss occurred, presumably, due to polymerization of the anode wire in CH₄ plasma. Such a high aging rate could be explained by very high plasma densities in the avalanches caused by alphas that make ionization of 3×10^4 free electrons each. On the other hand, in the test with Ar/CF₄/CO₂ the chambers recovered. It is in good accord with a previous observation in the test “Karsruhe II”, where a clear anode aging with Ar/CF₄/CH₄ was observed and after changing to Ar/CF₄/CO₂ the gain was restored (see section 4.6.1). The gain recovery can be attributed to etching of polymers by the CF₄-plasma. However, as was shown in section 5.2, the etching in this gas, which is a positive effect here, can also become very dangerous.

6.7 Sealer paste “Sista F109” in an aging test

Introduction and setup

Since Stycast is very brittle and unsuitable for gluing gas-tight boxes, the purpose of the aging test was to validate aging characteristics of gas boxes additionally sealed with another, more flexible, glue: Sista F109.

The setup was not changed except that we placed an aluminium plate totally coated with the sealer “Sista F109” in the gas box. The plate had the dimensions of 5×3 cm so that the ratio of the pasta surface area and the box volume was realistic and comparable with that of the OTR.

It should be reminded here, for better understanding, that cell 5 and 6, which showed a gain loss of 15% in the test described in section 6.6, were irradiated further.

All experimental data (currents in irradiated and non-irradiated cells, temperature, atmospheric pressure) were recorded on the computer. The source was moved to the reference cells for 15 minutes every two days.

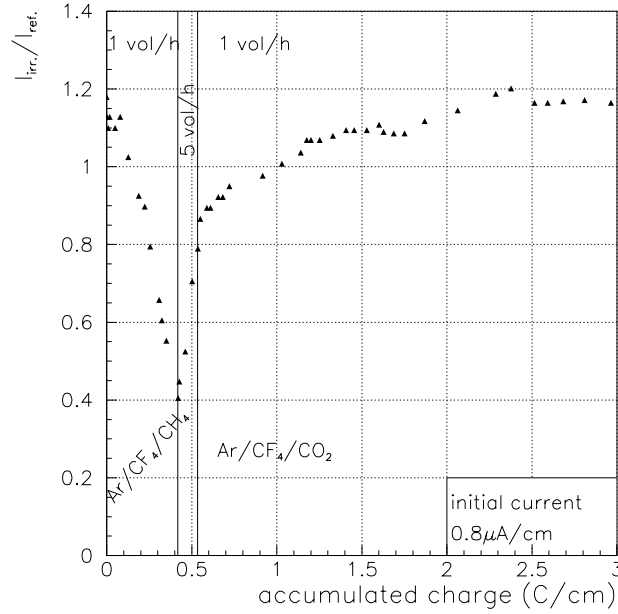


Figure 6.5: Ratio of the currents in the irradiated cells and in the reference cells.

Results

Approximately 2.2 C/cm was accumulated during the test. The development of the current is shown in figure 6.6. The average ratio of currents in irradiated cells and in the non-irradiated ones increased by 7%. The p/T-corrected distributions of the means of ^{55}Fe spectra before and after the test are shown in figure 6.7. As can be seen the observed gain loss in irradiated cells relative to the non-irradiated cells became less after the aging test with “Sista F109”.

The dark current was about 8-10 nA resulting mainly from the X-ray background of the alpha-source.

After this aging test, the total dose reached a value of about 5 C/cm in cells 5 and 6 and 1.6 C/cm in cells 3 and 4. Figure 6.8 shows a photograph of the opened chamber after this test. Despite the chamber accumulated up to 5 C/cm, we did not observe with naked eyes any considerable degradation of the chamber, however, an anode aging was observed in the following analysis.

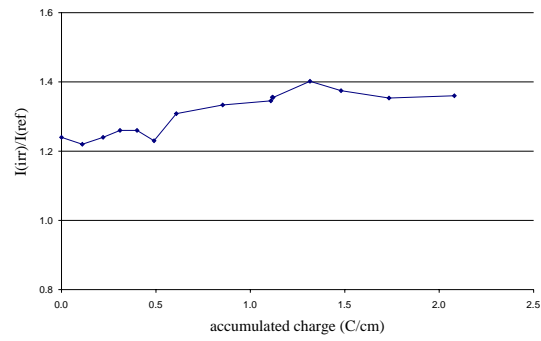


Figure 6.6: *Ratio of currents in irradiated cells and in reference cells in the test with the paste “Sista F109”.*

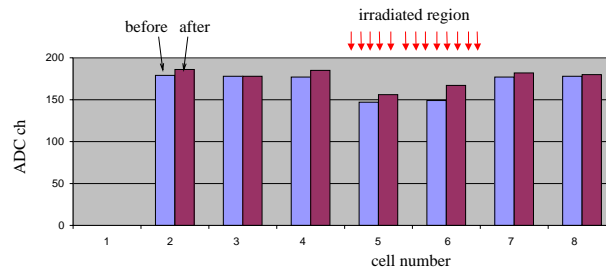


Figure 6.7: *Distribution of the mean of the spectra before and after irradiation with the sealer “Sista F109”.*



Figure 6.8: *Photograph of the opened α -chamber after a total dose of ≈ 5 C/cm for cells 5 and 6 (cell number 1 is on the left). No aging was detected optically.*

6.8 Electron microscopy and X-ray spectroscopy

The wires were investigated under an electron microscope (see figure 6.9). The light, scanty looking sediments on the wires probably were a relic of the anode aging observed in the test with the gas Ar/CF₄/CH₄.

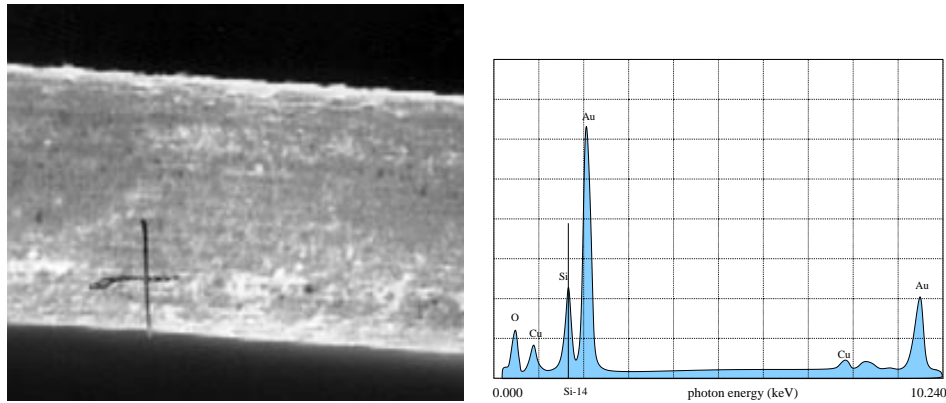


Figure 6.9: On the left, SEM micrograph of the wire 6 that received 0.35 C/cm in Ar/CF₄/CH₄ initially resulting in an anode aging of more than 70% gain loss and recovered in Ar/CF₄/CO₂ almost completely (⁵⁵Fe spectra showed a residual aging of 10%, see figure 6.7). On the right, EDS spectrum of this spot denoted by a cross on the wire shown in the figure on the left.

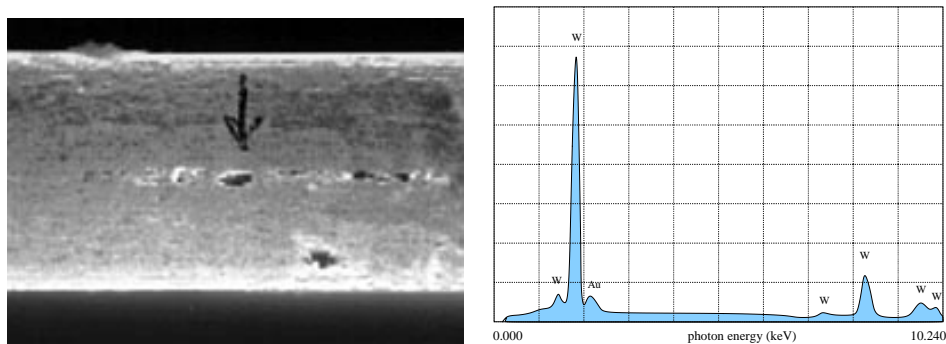


Figure 6.10: Dark spots on the golden coating of wire 6 on the left. On the right, an EDS spectrum from the spot marked by an arrow.

As can be seen from the EDS spectrum, additional elements like oxygen, copper, silicon were found. On another light spot fluorine was found. The origin of copper is not known. Although it could come from the cathode, the mechanism is

unclear.

In addition, we recognized black spots on the wire, which probably were holes in the gold coating. A photograph and an EDS spectrum from a region with a black spot is shown in figure 6.10. Both low and high energy lines of W are very pronounced. If the element is covered by some layer, then the low energy photons are suppressed more strongly than high energy ones, which means in this case that the tungsten was not covered by a golden layer at this spot.

Such holes as in figure 6.10 have never been observed on new wires [9]. This means that these holes were presumably caused by chemical attacks of radicals, produced in the avalanche.

6.9 Summary and conclusions

The following conclusions can be drawn on the basis of aging tests with an α -source using gold-coated chambers:

- a procedure for aging tests with α -sources was developed;
- production of stable electronegative species ($\tau > 1$ h) in the avalanche was observed;
- irradiation in Ar/CF₄/CH₄ caused a strong gain loss of about 70% after 0.35 C/cm;
- the chamber aged in Ar/CF₄/CH₄ recovered almost completely in the gas Ar/CF₄/CO₂;
- the dark current was below 12 nA/cell;
- tests validated the applicability of the sealer “Sista F109” to HERA-B.
- Etching effects were observed in form of appearance of holes in gold coating revealing tungsten.

Chapter 7

Aging tests with Ar/CO₂

7.1 Introduction

In order to know more about our honeycomb chambers, we decided to check the behaviour of our chamber in another well-known mixture Ar/CO₂. Some people consider this mixture as a back-up solution instead of Ar/CF₄/CO₂. In the reports of many papers (see, for example, [38]) Ar/CO₂ mixture is considered to be healthy in terms of aging characteristics. A good outcome of aging tests is not evident for the OTR, since the honeycomb chambers are equipped with FR4-strips containing silicon. Indeed, according to the analyses made in other tests, silicon was usually found in anode wire deposits (see figures 5.21, 6.9 and sections 4.2.2, 4.6.1). We suspect that silicon was usually present in test gas systems. In the report of [53, 37], silicon was a reason for rapid anode aging in drift chambers filled with the gas Ar/CO₂.

An OTR chamber filled with this gas was also tested before and described in section 4.6.2. This test became very important when the test with the mixture Ar/CF₄/CO₂ showed rapidly increasing dark currents (section 4.6.1).

7.2 X-ray aging test

Setup

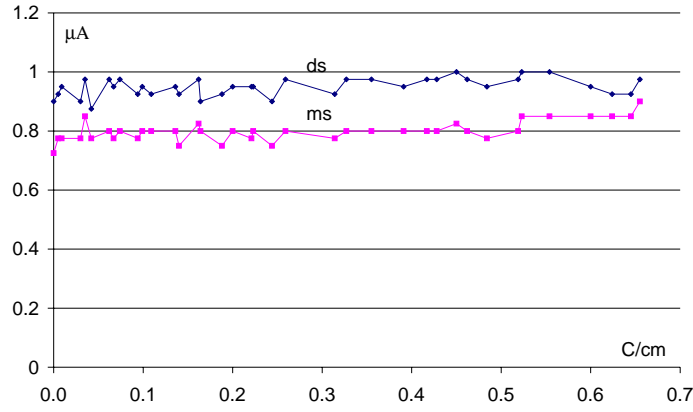
The X-ray setup and the α -setup were described in sections 5.1.1 and 6.2, respectively. The X-ray test was made with the same chambers irradiated before in **Test 1, 2, 3, 4** (see section 5.1.1).

The main parameters of the test are listed in table 7.1.

It should be noted that the HV was chosen to be 1400 V to operate at a gain of $\approx 3 \times 10^4$, the same as in the previous tests and in HERA-B (see gain-voltage dependence in Ar/CO₂ in figure B.4).

parameter	value
gas	Ar/CO ₂ (80/20)
flow	1 box.vol/h
HV	1400 V
gain	$\approx 3 \times 10^4$
current density	0.3 $\mu\text{A}/\text{cm}$

Table 7.1: Main parameters of the aging test.

Figure 7.1: Total p/T -corrected currents in double-strip (*ds*) and mono-strip (*ms*) chambers as functions of accumulated charge.

Results

Gas gain

We irradiated the chambers up to 0.7 C/cm. The total currents in the chambers are shown in figure 7.1. As can be seen, we did not observe degradation of the gain in the test. The current in the mono-strip chamber was lower than in the double-strip chamber, probably, because the mono-strip chamber was more remote from the X-ray tube (this chamber was positioned downstream from the double-strip chamber). The transversal scanning with ^{55}Fe , which is shown in figure 7.2, did not show a gain drop in irradiated cells compared to non-irradiated ones either. As this figure indicates, the gain in the mono-strip chamber was higher by $\approx 15\%$. Also, the gain in the cells of the same chamber differed considerably. It should be remarked that such a high deviation of the gain can be a consequence of the previous test with water addition made with the same chambers (see figure 5.9).

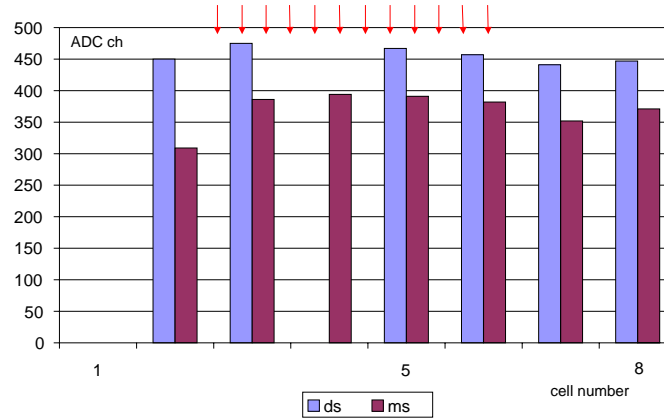


Figure 7.2: Transversal distribution of means of the ⁵⁵Fe spectra in double-strip (ds) and mono-strip (ms) chambers after the test. No loss of the gain was observed in the irradiated cells, which are denoted by red arrows.

Dark currents

The dark current in the chambers during the irradiation is shown in figure 7.3. At the beginning the dark current was high as a consequence of the previous test using the mixture Ar/CF₄/CO₂ with water addition (see section 5.1.1). The continuous decrease of the dark current to a level 40 times lower than with the mixture Ar/CF₄/CO₂ at the same flow (compare the dark current with that shown in figure 5.6) is, most likely, related to CF₄ as a responsible gas. For a more detailed discussion of the effect that causes increased dark currents see chapter 9.

7.3 Aging test with α -source

Experiment

The setup of the test was described in section 6.2. Table 7.2 lists the essential parameters of the test.

parameter	value
gas	Ar/CO ₂ (80/20)
flow	1 vol/h
HV	1500 V
current density	0.8 μ A/cm
irr.cell numbers	3, 4

Table 7.2: Main parameters in the aging test with alpha-source.

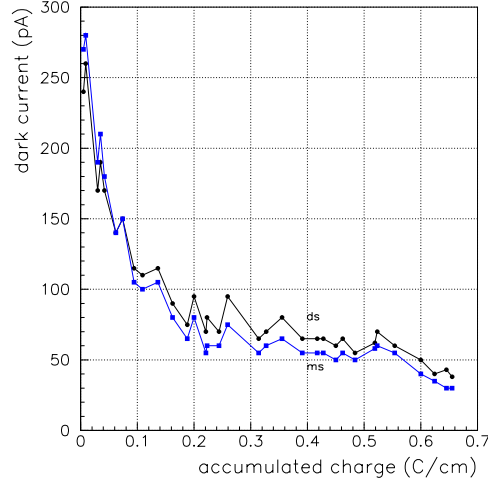


Figure 7.3: The total dark current in the cells of double-strip (ds) and mono-strip (ms) chambers. Continuous decrease of the dark current in mixture Ar/CO₂ after the test with the mixture Ar/CF₄/CO₂ was explicitly pronounced.

It should be mentioned that the HV was chosen higher than 1400 V corresponding to the nominal gain of 3×10^4 in order to partially compensate the space charge produced by the highly ionizing α -particles.

Results

Figure 7.4 shows the total p/T-corrected current in the test. According to the figure, there was no indication of anode aging. The decrease of the current at the beginning of the test can be explained as follows: At the beginning of the test the α -source was moved directly on the perforated region. Because a Kapton foil was glued on the bottom surface of the α -source to prevent electric contact, it was grated by the surface of the perforated region during movements of the source, blocking the holes with sawdust. After each movement (one movement is one polymarker in the diagram) the current dropped, on the average, by about 7%. After a slight hit made with a wrench to the box, the current recovered completely. After a dose of 0.13 C/cm we put the α -source on Kapton foil rails. As can be seen in figure 7.4, the drop of the current disappeared.

Figure 7.5 shows averages of ^{55}Fe spectra in different cells. These measurements were made after accumulating a charge of 0.8 C/cm. According to this figure, we did not observe anode aging in the test.

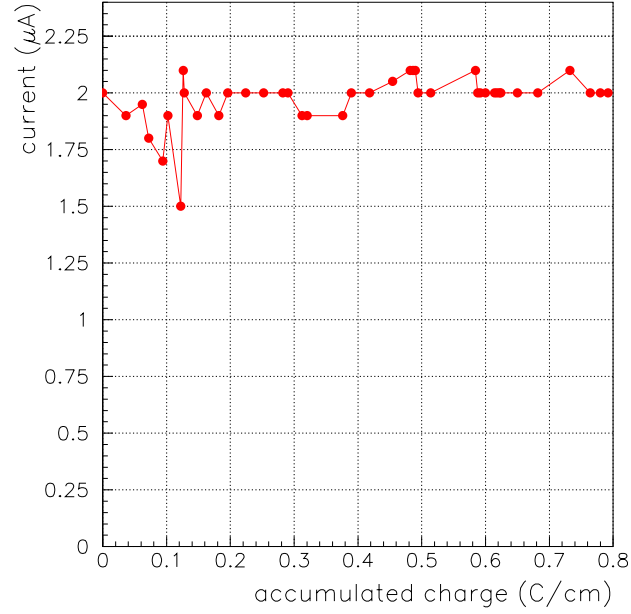


Figure 7.4: *Total p/T-corrected current in cells 5 and 6 in the test with an α -source. No aging was observed in the test.*

7.4 Conclusion

The aging tests with 10 cm long honeycomb chambers filled with Ar/CO₂ irradiated with X-rays and with α -particles showed no aging effects up to 0.8 C/cm. Unfortunately, Ar/CO₂ is not so fast as CF₄-based gases and could not provide drift times in 10 mm chambers less than 96 ns. Therefore, this mixture is considered only as a back-up if a CF₄-based mixture would fail to provide rather long stable operation of the OTR.

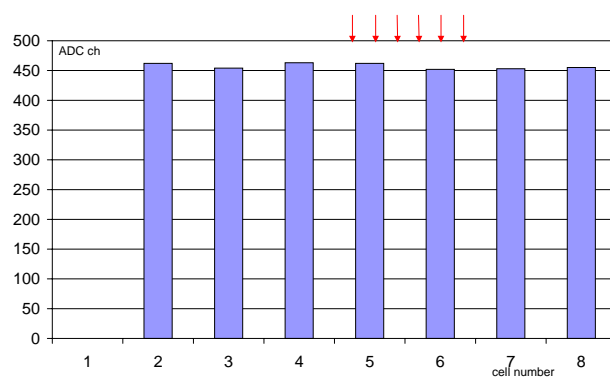


Figure 7.5: Distribution of means of ^{55}Fe spectra measured after a dose of 0.8 C/cm under irradiation with an α -source in the mixture Ar/CO_2 .

Chapter 8

HERA-B run in 2000

Facility

After an extensive R&D program, a solution for the OTR, technology and working parameters were found and the mass production of modules was started. The OTR was fully installed by January 2000. During the run 2000, before the start of the HERA upgrade shutdown at the end of August 2000, the OTR was operated in a high rate hadronic environment.

Gain control. Several cells of MC8 close to the beam were additionally irradiated with ^{55}Fe -sources installed inside the two MC8 half-superlayer boxes to keep records of the gas gain during the run 2000. The signal from corresponding wires after amplification were transferred to Analog-to-Digital Converters. The spectra were regularly measured when the beam was off. The measurement during luminosity runs was impossible due to the high HERA-B rate, which is more than four orders of magnitude higher than the irradiation rate from an ^{55}Fe -source.

Gas composition. The construction of the OTR, choice of materials, operating parameters are described in section 1.3. It might be noted here that water was not added into the gas system at that time. The water content was usually lower than 20 ppm for the whole run period. The oxygen and the nitrogen contents, varying considerably, were, on the average, 1000 and 2000 ppm, respectively (outside of the studied range). For most of the run period the gas system kept the gas composition within the range allowed by design: $(65 \pm 1)\% \text{Ar} (30 \pm 1)\% \text{CF}_4 (5 \pm 0.2)\% \text{CO}_2$ [50]. However, 1% increase in the argon fraction or the same increase in atmospheric pressure results in a 15% growth or 6% loss of the gain, respectively. Due to such a strong dependence on environmental parameters, the measured gas gain deviated up to 50% from its averaged value, which, consequently, caused relatively large systematic errors in measuring possible anode aging. In the future, it is planned to upgrade the OTR Slow Control with a gas gain monitoring system, which should stabilize the gain varying the voltage.

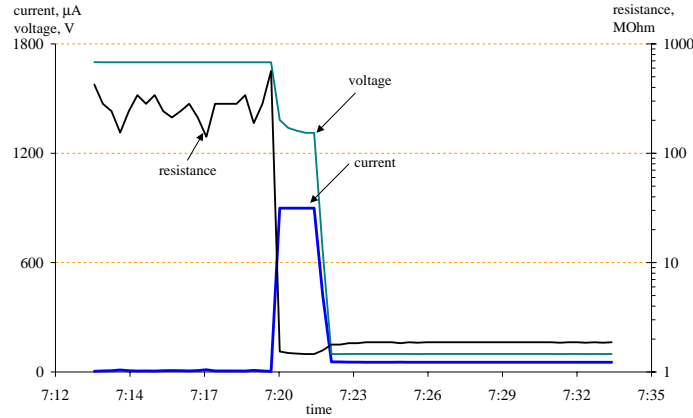


Figure 8.1: Typical short development in OTR HV channels during run 2000. The resistance of a HV group suddenly drops. If the current becomes as high as the maximum limit of the OTR HV supply of $900\ \mu\text{A}$, the HV supply starts to operate in current stabilization mode, decreasing the voltage. Typically, 2 minutes later, the Slow Control System reduces the voltage to 100 V. The resistance of a short, which is in the range from 100 kOhm to 50 MOhm, usually increases when decreasing the voltage.

Results

Some of the wires in the hottest regions accumulated up to 50 mC/cm during 14 months routine operation at target rates of 5-10 MHz. During the run over the year 2000 neither anode aging nor the Malter effect nor dark currents with ohmic behaviour were observed.

OTR HV failures. Although damages relating to aging of drift chambers were not observed, other failures, shorts, caused mainly by faulty components in the HV distribution of the detector were observed. Figure 8.1 shows a typical development of shorts. On the average, 0.2 shorts occurred during one operating hour. The operation of an affected HV channel could be restored switching off one HV group comprising 16 wires.

The sudden development of each short in the OTR was similar to the effect observed in the X-ray aging test under dry conditions. The dry operating environment of the OTR supported the idea that the OTR shorts and wire ruptures are the same effects. However, in X-ray aging tests the electrical resistance of broken wires with the cathode lay in the region of $O(100\ \text{Ohm})$. The major source of short development in the OTR was identified when the PC1+ superlayer box was opened and inspected. From 49 faulty HV groups only two were caused by shorted wires. In 39 other cases shorts were caused by formation of black thread (probably of carbon) between two electrodes of one of the two capacitors (one of which is a common filter capacitor) on the bottom side of the HV board (see figure 8.2). The other 15 capacitors on the top side of the HV-board were never shorted. The reason of the systematic difference was identified and related to the different

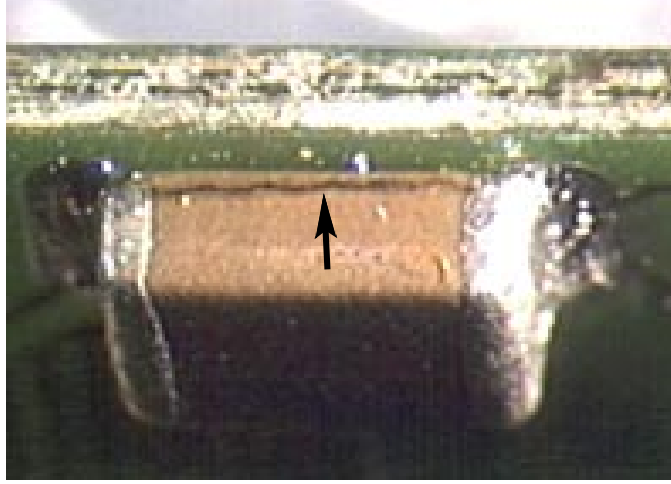


Figure 8.2: A black carbon trace forms across one of two capacitors on the bottom side of a HV boards.

super-layer	rate before repair, $\times 10^{-3}$ 1/h HV=100%	rate after repair, $\times 10^{-3}$ 1/h HV=106%	suppr. factor
PC1+	24	1.5	16
TC1-	7.5	0.8	9.4
TC1+	28	8	3.5

Table 8.1: Characteristic OTR HV failure rates observed in different half-superlayers before and after module repair.

mounting techniques used for top and bottom side elements. Since the begin of the HERA-B upgrade shutdown until the day this thesis was written, most of the bottom side capacitors on the HV boards were exchanged using clean soldering techniques, which avoids any uncontrolled deposition of soldering fluids. All “bad” wires were disconnected from the HV-boards.

Table 8.1 gives representative numbers of the failure rate before and after the repair method. As can be concluded, after the repair procedure described above, the HV failure rate was considerably reduced.

The failure rate was not constant but deviating considerably during the run 2000. Studies were launched to find possible correlations between the failure rate and environmental parameters like target rate, gas gain, gas composition, etc. The relevant data such as voltage and current in each HV channel as well as

composition of output gas of each half-superlayer box and common input are automatically stored into the Slow Control Database of HERA-B. The studies led to the conclusion that gas admixtures such as H_2O , O_2 or N_2 could have influenced the failure rate. No correlations were observed between the failure rate and the target rate. The correlation study could be helpful as a basis for the statistical comparison of failure rates before and after repairs. For more information about this study see [10].

Electron microscopy. As was mentioned above, wire ruptures were the reason for about 4% of the HV failures. In order to accumulate more information about processes causing these ruptures, some broken wires were analysed under the electron microscope. An EDS spectrum of the wire revealed that a sample wire in the burnt region near the broken end was coated with a thick deposit of C, Ag, Cl (the origin of these elements is not known). The wire surface looked already clean about 1 cm away from the end, however holes in the Au-surface showing W could still be found (of course, tungsten was seen in the burnt part as well). An analysis of the wire further away from the end showed small spots of C, but tungsten could not be found. The solder pad was analysed too. Its surface was rather clean but containing traces of carbon. Also, investigations of cathodes pieces and wires showed that burning processes which caused wire ruptures left quite localized destructions.

Conclusion

On the basis of results from the Outer Tracker run during 14 months of routine operation in hadronic environment at target rates of 5-10 MHz (dose < 50 mC/cm) several conclusions can be drawn:

- Except that O(10) wires out of 115000 ruptured, the Outer Tracker honeycomb chambers did not show any of the aging effects studied in the tests.
- HV failures caused by faulty components in the HV distribution of the detector were observed. Today the faulty component is identified and mostly repaired.

Chapter 9

Plasma chemistry in the avalanche in Ar/CF₄/CO₂

9.1 Introduction

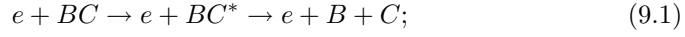
The modeling of the plasma chemistry processes in discharges is not possible in general because not all interaction cross sections of species (molecules and ions), electrons and photons with each other in plasma are known. However, for CF₄ the situation looks better. Due to the variety of applications, CF₄ was extensively studied. The modeling of the plasma chemistry in CF₄ applied to plasma etching processes showed a good agreement with experiment (see, for example, [34]).

Unlike the modeling of industrial plasma etching the modeling of drift chamber aging is more difficult because in this case the unknown impurities from leaks and outgassing play a significant role. As shown below, the presence of several ppm of water drastically changes the outcome of plasma chemistry processes. Nevertheless, measuring the water and oxygen content and considering that the content of the other impurities is negligible, we could estimate what products and in what concentration would result from the avalanche processes. Such a procedure may be not quite justified, yet can serve as a guidance for the experimental tests. Moreover, it could explain aging effects of different kinds and could show the way how to avoid dangerous phenomena.

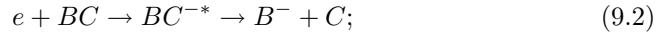
9.2 Dissociation

The dissociation of molecules plays a significant role in aging processes. On the one hand, dissociation is favourable since it contributes to radiationless energy dissipation of excited molecules and thus to the stability of chamber operation. On the other hand, it is undesirable since it leads to polymerization and/or production of aggressive species damaging the electrodes.

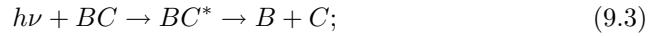
In the drift chamber dissociation follows the excitation of electronic states, which occurs mostly via electron impact



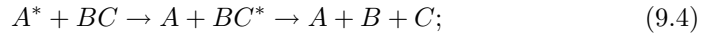
but also through dissociative electron attachment



dissociative photoabsorption

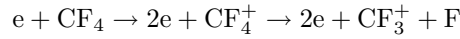


energy transfer processes

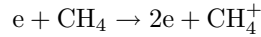


or dissociative ionization (analogical to processes (9.1, 9.3, 9.4), but B or C finishes as a positive ion).

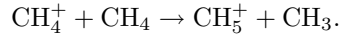
Dissociative ionization is the dominant process in dissociation of CF_4 and CH_4 species:



or



which continues according to [61] as



As an example, the dissociative mechanisms in an oxygen molecule represents typical dissociation processes in molecules. They can be illustrated by the potential energy level diagram for oxygen, which is shown in figure 9.1.

If the oxygen molecule is excited to the repulsive electronic excitation state $^3\Pi_u$, it dissociates immediately ($\tau \sim 10^{-14}$ s) [21]. The disintegration of O_2 through excitation of non-repulsive electronic excitation states like $B^3\Sigma_u^-$ can also occur. Then, the process is called predissociation. Predissociation is a rather complicated process and not clearly understood. According to [21], when excited to $B^3\Sigma_u^-$ and additionally excited to vibrational state $\nu'=3$ or 4, the system probably undergoes radiationless predissociation crossing over from $B^3\Sigma_u^-$ to the unstable state $^3\Pi_u$. From other vibrational levels the cross-over to $^3\Pi_u$ can take place through emission of a photon. In this case, the lifetime of $B^3\Sigma_u^-$ is rather long and non-dissociative relaxation channels become also probable.

Total e-impact dissociation cross sections for CH_4 , CF_4 and C_2H_6 are shown in figure 9.2. The cross section for the C_2H_6 dissociation is higher than the other two, which can be explained by the larger number of atoms in the C_2H_6 molecule. If the polymerization rate is proportional to the dissociation rate, then we should expect higher polymerization rates in the gases containing heavier hydrocarbons

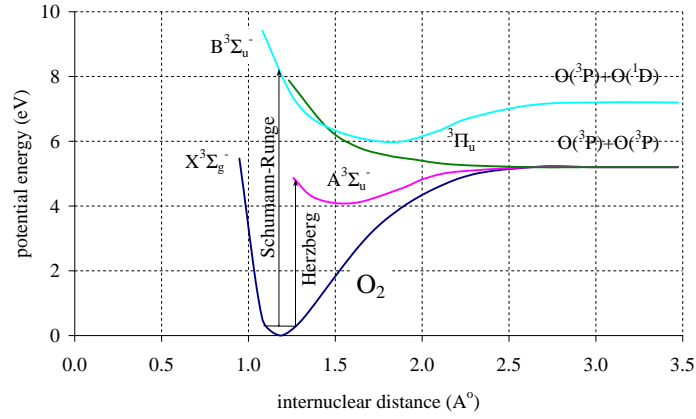


Figure 9.1: *Potential energy level diagram for oxygen [42].*

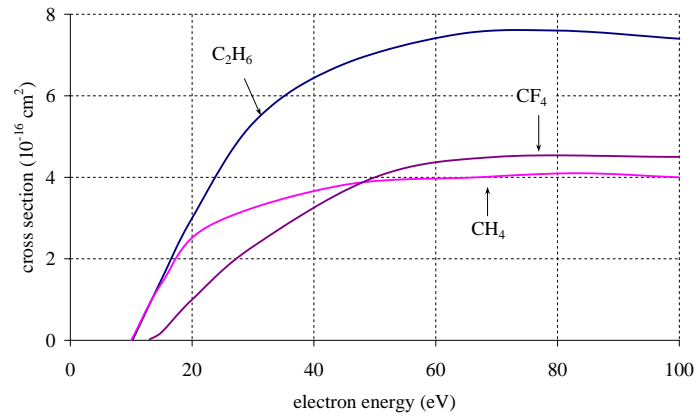


Figure 9.2: *Total electron impact dissociation cross sections for CF₄ [24], CH₄ [108], C₂H₆ [109]. The dissociation cross section for CO₂ is two orders of magnitude smaller (compare with the data in [60]). The electron energy distribution function close to the surface of the anode wire when using quenchers in small concentration could be approximated by that shown in figure 9.3.*

as quenchers, which is in agreement with the aging analysis given in [93] but contradictory to those given in [62] where the polymerization rate was observed to be in the order $\text{CH}_4 > \text{C}_2\text{H}_6 > \text{C}_3\text{H}_8$.

It should be remarked here that the curves shown in figure 9.2 do not represent total dissociation in the avalanche, since dissociation occurs not only in electron-impact collisions but also via processes (9.2, 9.3, 9.4, etc.). In the following section a calculation of the production rates of species in the avalanche taking into account only electron impact processes is presented.

9.3 Production rate of fluorine species in Ar/CF₄/CO₂

According to [60], the cross sections for CO₂ dissociation are very small, two orders of magnitude smaller than for CF₄ dissociation, and will be neglected.

The measured total ionization cross section for CF₄ was taken from [24], for argon and CO₂ in [43]. The molecule-averaged ionization cross section for the mixture Ar/CF₄/CO₂ (65:30:5) can be estimated as percentage-weighted mean of the total ionization cross sections in pure gases

$$\sigma_i(\text{Ar/CF}_4/\text{CO}_2) \approx 0.65 \times \sigma_i(\text{Ar}) + 0.30 \times \sigma_i(\text{CF}_4) + 0.05 \times \sigma_i(\text{CO}_2).$$

The cross section for the production of fluorine by neutral dissociation and dissociative ionization from electron impact on CF₄ was measured in [82]. The cross section for the production of CF₃ and also of other radicals (radicals, also called “free radicals”, are species with unpaired valence electrons) in pure CF₄ is given in [24]. According to [24],

$$\sigma(\text{CF}_3^0) \approx \sigma_{t,n}$$

where $\sigma_{t,n}$ is the total cross section for the production of neutrals. Therefore, the cross section for CF₃ production was found using the formula

$$\sigma(\text{CF}_3) \equiv \sigma(\text{CF}_3^+ + \text{CF}_3^0) \approx \sigma(\text{CF}_3^+) + \sigma_{t,n}$$

The total cross section for C, CF and CF₂ species production was found as

$$\begin{aligned} \sigma(\text{C} + \text{CF} + \text{CF}_2) &\equiv \sigma(\text{C}^+) + \sigma(\text{CF}^+) + \\ &+ \sigma(\text{CF}_2^+) + \sigma(\text{C}^0) + \sigma(\text{CF}^0) + \sigma(\text{CF}_2^0) \approx \\ &\approx \sigma(\text{C}^+) + \sigma(\text{CF}^+) + \sigma(\text{CF}_2^+) \end{aligned}$$

because the cross sections for the production of neutral C⁰, CF⁰, CF₂⁰ and CF₃⁰ are by about one order of magnitude smaller than those of the positive ions of these species [24].

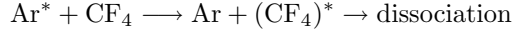
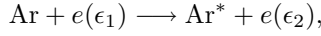
Since radicals are mainly produced due to the CF₄ dissociation and the fraction of CF₄ in the counting gas is 0.3, the molecule-averaged cross sections for the

production of free radicals in the Ar/CF₄/CO₂ mixture were found as

$$\sigma_r(\text{Ar/CF}_4/\text{CO}_2) \approx 0.3 \times \sigma_r(\text{CF}_4)$$

where $\sigma_r(\text{CF}_4)$ is the production cross section for radicals in pure CF₄. The processes concerned with the dissociation due to the attachment of electrons by CF₄ (9.2) are neglected in the last stages of the avalanche since the cross section for dissociative attachment is more than 2 orders of magnitude smaller than that of ionization in CF₄ at electron energies of 20 eV or higher (ionization of CF₄ is followed by dissociation). This can be seen in figure 2.2 (see also energy distribution function in figure 9.3).

It should be mentioned that such processes like



were not taken into account, however, can somewhat increase the cross section for free radical production in a mixture of argon and CF₄. An influence of such processes of several percent was observed in [86].

The estimated cross sections are shown in figure 9.3. Nearly all the electrons are produced in the avalanche in a region within several microns from an anode wire. Fluorine and other free radicals are mainly produced in this region. The energy distribution function $f(\epsilon, r_a)$ of electrons at the radius $r_a=12.5 \mu\text{m}$ was calculated by the Magboltz program and is shown in figure 9.3. It is normalized as follows

$$\int_0^\infty f(\epsilon) d\epsilon = 1.$$

To simplify the calculation, we can assume that the electric field and, consequently, $f(\epsilon)$ does not change significantly within several microns.

In addition, the uncertainty of the program at the given very high electric field was estimated comparing the calculation with experiment. Having experimental data for the gas gain, we compared measured and predicted Townsend coefficients.

The Townsend coefficient, α , was found from the measured high-voltage dependence of the gas gain, which is shown in figure B.1. The gas gain is given by

$$M(V) = e^{\int_{r_a}^{r_c} \alpha[E(V,r)] dr} \quad (9.5)$$

where E is the electric field at the distance r from the center of a cell, V is the high-voltage, the subscripts a and c denote the values in close proximity to the anode and the cathode, respectively. Let us solve equation (9.5) for α . From $E = \eta V/r$, where the coefficient $\eta = 1/\ln(r_c/r_a)$, follows

$$\begin{aligned} \int_{E_c}^{E_a} \alpha(E) \frac{\eta V}{E^2} dE &= \ln[M(V)] \Rightarrow \\ \Rightarrow \alpha_a(V) &= \frac{V^2}{r_a} \frac{d}{dV} \left(\frac{\ln(M(V))}{V} \right). \end{aligned}$$

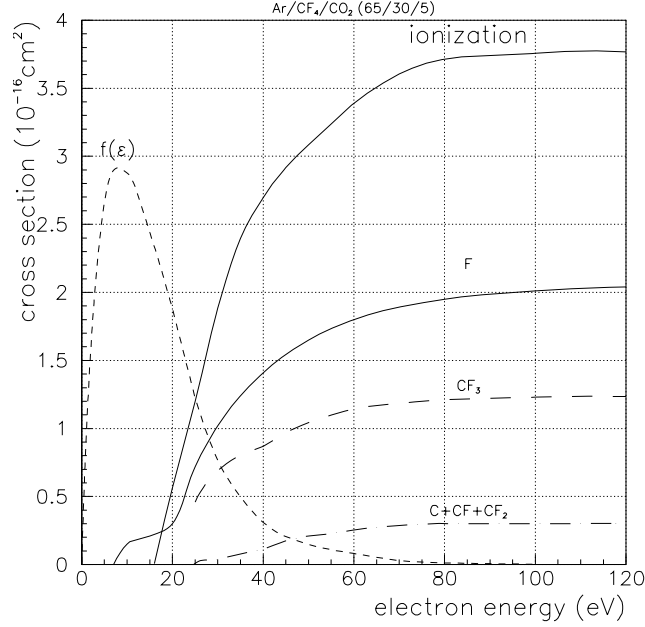


Figure 9.3: *Energy distribution function of the electrons near the anode (in arbitrary units) as well as total ionization cross section and cross sections for the production of radicals taken from [82, 43, 24] and renormalized for the mixture Ar/CF₄/CO₂.*

The Townsend coefficients obtained with the Magboltz program and from experimental data are shown in figure 9.4. To avoid a calculation of the space charge, we used data for the gain measurement between 800 V and 1500 V, where the space charge could be neglected (the attachment coefficient is also very small compared to the Townsend coefficient at the anode surface, see figure 2.9). The experimental data were fitted with a polynomial of the second degree and extrapolated to higher field. As can be seen, the difference is of several tens of percents and is acceptable for us.

Using the Mathematica program, we could find the rate ratios for production of species and production of free electrons

$$\frac{\dot{N}_{r,prod}}{\dot{N}_{e,prod}} = \frac{\int \sigma_r f(\epsilon) \sqrt{\epsilon} d\epsilon}{\int \sigma_i f(\epsilon) \sqrt{\epsilon} d\epsilon}$$

These ratios were calculated numerically with the following results:

$$\frac{\dot{N}_{F,prod}}{\dot{N}_{e,prod}} \approx 0.6; \quad (9.6)$$

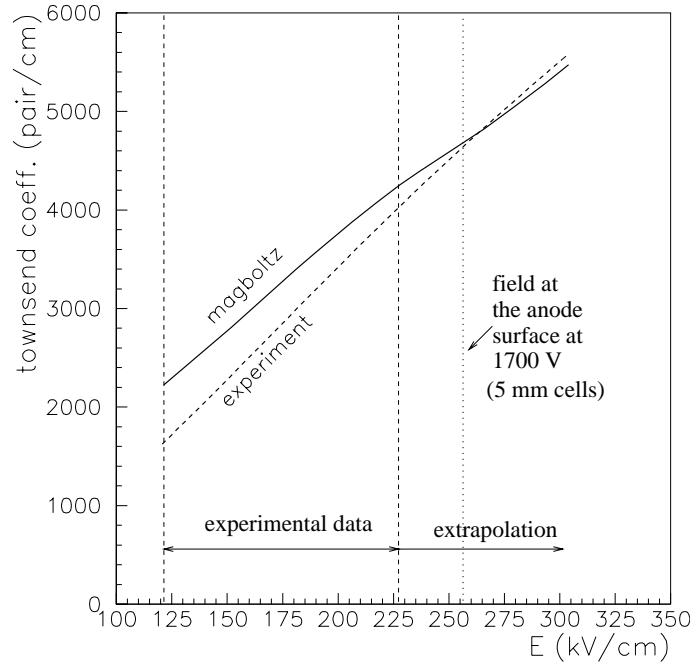


Figure 9.4: Townsend coefficients calculated by the Magboltz and found experimentally in close proximity to the anode.

$$\frac{\dot{N}_{\text{CF}_3, \text{prod}}}{\dot{N}_{e, \text{prod}}} \approx 0.43 \text{ and}$$

$$\frac{\dot{N}_{(\text{C}+\text{CF}+\text{CF}_2), \text{prod}}}{\dot{N}_{e, \text{prod}}} \approx 0.04.$$

The uncertainty of this calculation is determined by the uncertainties of the given cross sections, which is estimated to be about 20%, and by systematic errors arising when neglecting processes like (9.1, 9.2, 9.3, 9.4).

9.4 Chemistry

The rate I_A at which a chemical reaction $A+B \rightarrow C$ proceeds is expressed in terms of the amount of a product formed per unit time or the amount of a reactant used per unit time and is given by the formula $\Delta I_A = k n_B N_A$ where k is the reaction rate constant, n_B the concentration of molecules B , N_A the number of molecules A . Although there are enough reference sources for the chemical-kinetics coefficients, the constants of the reactions deviate by one or even two orders of magnitude

Reaction	Constant ^a	Ref.
$\text{CF}_3 + \text{F} + \text{M} \rightarrow \text{CF}_4 + \text{M}$	2.6×10^{18}	[80]
$\text{CF}_2 + \text{F} + \text{M} \rightarrow \text{CF}_3 + \text{M}$	1.4×10^{22}	[80]
$\text{CF} + \text{F} + \text{M} \rightarrow \text{CF}_2 + \text{M}$	6.1×10^{19}	[80]
$\text{F} + \text{F} + \text{M} \rightarrow \text{F}_2 + \text{M}$	2.9×10^{13}	[56]
$\text{CF}_3 + \text{CF}_3 + \text{M} \rightarrow \text{C}_2\text{F}_6 + \text{M}$	1.2×10^{19}	[80]
$\text{H}_2\text{O} + \text{F} \rightarrow \text{HF} + \text{OH}$	1.1×10^{13}	[56]
$\text{F} + \text{O}_2 + \text{M} \rightarrow \text{FO}_2 + \text{M}$	1.3×10^{12}	[56]
$\text{F} + \text{CH}_4 \rightarrow \text{HF} + \text{CH}_3$	2.1×10^{14b}	[56]
M \equiv collision partner (argon)		

^aUnits for two-body processes are in $\text{cm}^3/\text{mole} \cdot \text{s}$ and for three-body processes are in $\text{cm}^6/\text{mole}^2 \cdot \text{s}$.

^bThis reaction is given to show the influence of CH_4 on the F lifetime in an Ar/ CF_4 / CH_4 mixture.

Table 9.1: *Chemical reaction constants in a drift chamber with Ar/ CF_4 / CO_2 .*

Ar	CF_4	CO_2	CF_3	CH_4	H_2O	HF	F
15.8	16	13.8	10.1	13	12.6	15.8	17.7

Table 9.2: *Ionization potential (in eV) of some species that can be present in the drift chamber.*

depending on the reference paper. This concerns especially three body processes, where the reaction rate depends very strongly on the buffer gas.

Rate constants are usually given in the form $AT^B e^{E_a/RT}$ where A , B and E_a are the Arrhenius parameters, R is the universal gas constant, T is the gas temperature. The most useful, in our view, reaction rate constants were estimated for room temperature and are listed in table 9.1, together with the papers where the corresponding Arrhenius parameters were given.

Because of the high uncertainty of the rate constants, a full Monte Carlo simulation was abandoned in favour of a semi-quantitative analysis.

As shown in the previous section, predominantly CF_3^+ and F^0 are produced in the avalanche, near the anode. The production rates of C, CF and CF_2 produced as neutral or charged species are lower by more than one order of magnitude. CF_3 has a very low ionization potential of 10.1 (see table 9.2), therefore CF_3^+ is very inert, it reacts neither with the gas components Ar, CF_4 , CO_2 nor with F, nor with other CF_3^+ . Furthermore, during the drift to the cathode it remains positively charged, still attachment of water molecules is possible. An electron transfer reaction from most species to CF_3^+ is energetically forbidden. The electric field drives CF_3^+ out of the avalanche separating F and CF_3^+ species.

Let us simplify the multicomponent reaction process to a process with only

Reaction	Constant
$\text{CF}_3 + \text{F} + \text{M} \rightarrow \text{CF}_4 + \text{M}$	0.1 s
$\text{F} + \text{F} + \text{M} \rightarrow \text{F}_2 + \text{M}$	25 s
$\text{CF}_3 + \text{CF}_3 + \text{M} \rightarrow \text{C}_2\text{F}_6 + \text{M}$	0.046 s
$\text{H}_2\text{O} + \text{F} \rightarrow \text{HF} + \text{OH}$	$2 \times 10^{-5} \text{ s}^a$
$\text{OH} + \text{OH} \rightarrow \text{H}_2\text{O} + \text{O}$	0.8 s ^a
$\text{F} + \text{OH} \rightarrow \text{HF} + \text{O}$	0.014 s ^a
$\text{F} + \text{O}_2 + \text{M} \rightarrow \text{FO}_2 + \text{M}$	4 s ^a
$\text{F} + \text{CH}_4 \rightarrow \text{HF} + \text{CH}_3$	$1.8 \times 10^{-9} \text{ s}^b$
$\text{M} \equiv$ collision partner (argon)	

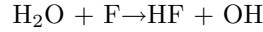
^aThe water and oxygen contents in this estimation was assumed to be 100 ppm.

^bThis reaction is given to show the influence of 5% CH₄ on F lifetime in Ar/CF₄/CH₄.

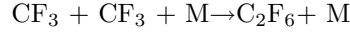
Table 9.3: *Characteristic time constants for possible reactions in a drift chamber with Ar/CF₄/CO₂ estimated for the current density of 0.6 μA/cm.*

two reacting components and a buffer gas (argon) and consider every possible combination. Characteristic time constants calculated for the reactions in this case are listed in table 9.3. The time constants are probably overestimated because we did not take into account that radicals can also be accumulated on electrode surfaces locally increasing the density of radicals and thus overall reaction rates.

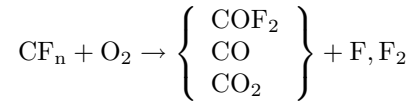
As can be seen, atomic fluorine reacts predominantly with water even if the water content is only 100 ppm:



CF₃ probably reacts as follows:



It might be noted here that oxygen, which is usually present in the counting gas as contaminant (several hundred ppm), can increase the fluorine production rate, as mentioned in [81]:



where n=1,2,3.

Thus HF and maybe C₂F₆ are predominantly produced in the drift cell during the irradiation. HF itself is not very reactive, but together with water it forms hydrofluoric acid. Hydrofluoric acid is very corrosive, it finds application in the etching of glass, metals as well as chips. Hydrofluoric acid is electro-conductive. As tests showed, the reason for the high dark currents in the cell is the strong increase in the conductivity of FR4 wire-supporting strips. A plausible explanation of this effect is the following: HF permeates the FR4 strip. If the water content in the

gas system is large, the water content in the FR4 strip is large too. Together with water, HF forms hydrofluoric acid, which is the cause of high conductivity.

According to the test results reported in 5.1.1, the conductivity of the strips, being very high just after the stop of irradiation, disappears almost completely for several months. This indicates that the conductivity is not a result of corrosion, which would cause a permanent effect, but rather of the dissociation of the species diffusing into the FR4 strip into ions. A study of the influence of hydrofluoric acid on the FR4 strip conductivity could prove this hypothesis.

In order to be sure that the aging tests give not too optimistic but more or less realistic results related to the actual setup, we estimated and compared the concentrations of the produced species in the HERA-B chamber and in test setups. The following section serve just this purpose.

9.5 Estimation of HF concentration

9.5.1 Thermal convection

The concentration of species produced in the avalanche depends inversely on the gas exchange rate. Three mechanisms play an important role in the gas exchange: diffusion, thermal convection and laminar flow. Thermal convection usually dominates in the chambers with open geometry like the OTR honeycomb chambers (if the cells are oriented vertically). The term “open geometry” means the chamber geometry that implies the use of end-pieces with openings for free gas circulation. The introduction of metal or plastic tubes (capillaries) conveying the gas to every cell can stabilize the gas flow. Thermal convection is caused by Archimedes force acting on the gas with a smaller density due to an increase in the gas temperature. The latter is caused by the avalanche processes in the chamber.

According to the measurements, the conductivity of the upper strip in the double-strip chamber was much higher than that of the lower one. This difference could be explained by an upward flow of the heated gas in vertically directed cells.

Tests (see appendix B.3) showed a difference between the cathode and box temperatures at full intensity of about $\Delta T_{c-b} = 5^\circ\text{C}$. Let us estimate the upward flow of gas in the chamber caused by thermal convection resulting from cathode heating.

In order to find the mean velocity $\langle v \rangle$ of the laminar flow of a gas, we used the Navier-Stokes equation

$$\vec{f} = \eta \cdot \Delta \vec{v}.$$

Here \vec{f} is the force acting on an elementary gas volume and $\Delta \vec{v}$ is the Laplacian of the velocity. Solving this formula for the case when the gas flows through a cylinder of radius r_c and length l , we obtained (this formula is given also in some reference books):

$$\langle v \rangle = \frac{r_c^2 \Delta p}{8\eta l}$$

where Δp is the pressure difference at the bottom and at the top of the cylinder (the cylinder axis is vertically directed), $\eta \approx 21 \cdot 10^{-6}$ Pa · s is the approximate viscosity coefficient for the counting gas.

Solving the Navier-Stokes equation for a cylinder with a wire in the center, we found that a wire reduces the gas flow in a cell by about 28% due to additional friction. Thus the mean flow velocity in the cell is given by

$$\langle v \rangle \approx 0.72 \frac{r_c^2 \Delta p}{8\eta l}$$

Or using $\Delta p = \Delta \rho g l$ where g is the standard gravitational acceleration, $\Delta \rho$ the density difference between the “inside” and “outside” gas defined by the temperature difference ΔT_{in-out} as

$$\Delta \rho \approx -\rho \frac{\Delta T_{in-out}}{T} = -\frac{p_a M_g}{RT} \frac{\Delta T_{in-out}}{T}$$

where $M_g \approx 0.055$ kg/mol is the average atomic mass of the mixture Ar/CF₄/CO₂, p_a the atmospheric pressure, R the gas constant, T the room temperature. Then, we found

$$\langle v \rangle \text{ (cm/s)} \approx \zeta \cdot \Delta T_{in-out} \quad (9.7)$$

where

$$\zeta \approx 0.72 \frac{M_g g r_c^2 p_a}{8\eta R T^2} \approx 0.2 \frac{\text{cm}}{\text{s} \cdot \text{K}}.$$

In this estimation we could roughly consider the temperature of the ambient gas to be equal to that of the box, since the hot surface of the cathode is much smaller than the inner surface of the box.

Additionally, the gas in a cell in the irradiated region is, on the average, by 1 K hotter than the cathode (the cathode is hotter by 5 K relative to the box). Indeed, the heat generation in the avalanche region causes an increase in the gas temperature, T_g

$$T_g(r) = \frac{\Phi \ln(r_c/r)}{2\pi\lambda} + T_c$$

where $\Phi = iU \approx 0.2$ W/m is the heat flow per unit length, $i = 1.2$ μA/cm the current density, $U = 1700$ V the voltage between the anode and the cathode, $\lambda \approx 0.017 \frac{\text{W}}{\text{m} \cdot \text{K}}$ the approximate heat transfer coefficient of the given mixture and T_c the temperature of the cathode. Then, the mean temperature of the gas in the cells in the irradiated region would be

$$\langle T_g \rangle = \frac{1}{\pi(r_c^2 - r_a^2)} \int_{r_a}^{r_c} 2\pi T_g(r) r dr \approx 1 \text{ K} + T_c.$$

Finally, for the length of the hot (irradiated) region $l_h = 4$ cm and the length of the cells $l_c = 10$ cm (in 10 cm long chambers) we obtained

$$\langle v \rangle \text{ (cm/s)} \approx \frac{l_h}{l_c} \zeta (\Delta T_{in-out} + 1 \text{ K}).$$

Substituting with the numerical values, we found that the gas flow velocity in 10 cm long chambers is ≈ 0.4 cm/s. The same procedure for 40 cm long chambers gives 0.15 cm/s (see details of the test in section 5.2.2).

According to [9], the mean temperature of the hottest OTR chamber cells would be by $\Delta T_{c-box} \approx 0.7$ K higher than that of the box. Using the formula (9.7), we obtained $\langle v \rangle \approx 0.05$ cm/s.

The calculation of the flow given above considers only thermal convection. To find the real flow, one should add the laminar flow which arises due to the flushing of the box. This contribution to the flow depends on box construction and is not included into the further calculation.

9.5.2 HF concentration

Knowing the gas velocity and fluorine production rate one can estimate the concentration of HF species in the box of the setup described in section 5.1.2 for $F=1$ vol/h. Here F is the flow, which can also be expressed in [l/h] (do not mix up with F , fluorine).

If there is enough water in the gas, according to formula (9.6):

$$\frac{\dot{N}_{\text{HF},prod}}{\dot{N}_{e,prod}} \approx \frac{\dot{N}_{\text{F},prod}}{\dot{N}_{e,prod}} \approx 0.6$$

At the full intensity of the X-ray tube the current I is about $5 \mu\text{A}/\text{cell}$ at 1700 V. Then, the production rate of HF in one cell would be about

$$\dot{N}_{\text{HF},prod} = \frac{\dot{N}_{\text{HF},prod}}{\dot{N}_{e,prod}} \frac{I}{e} \approx 1.9 \cdot 10^{13} \text{ s}^{-1}.$$

The concentration of HF outside the chamber in the box was considered as homogeneous. If the lifetime of the responsible species is infinitely long, the formula

$$n_{\text{HF}} \approx \frac{\dot{N}_{r,prod}}{F}$$

could be used for an estimation of the average HF concentration, n_{HF} , in the box. We would obtain $n_{\text{HF}} \approx 20$ ppm for $F = 1$ vol/h = 0.5 l/h and $n_{\text{HF}} \approx 200$ ppm for $F = 0.1$ vol/h = 0.05 l/h (the total current in the chambers was about $20 \mu\text{A}$).

The concentration of HF in the chamber considerably depends on the position in the cell and can be estimated using Fick's law under the assumption that the HF species do not react with anything and live permanently:

$$\vec{J}_{\text{HF}} = -D \text{grad } n_{\text{HF}}.$$

Here \vec{J}_{HF} is the flux of HF species, $D \approx 0.1 \text{ cm}^2/\text{s}$ the approximate diffusion coefficient of HF (no reference, taken for granted) and n_{HF} is the concentration of HF species. If the gas flow velocity \vec{v} is not zero, then this equation takes the form

$$\vec{J}_{\text{HF}} = n_{\text{HF}} \vec{v} - D \text{grad } n_{\text{HF}}.$$

Using the continuity equation

$$\frac{dn}{dt} = \frac{\partial n}{\partial t} + \text{div } \vec{\mathbf{J}}_{\text{HF}}$$

with the stationary condition $\partial n / \partial t = 0$ and considering an almost one-dimensional dependence in a relatively long drift tube, the equation can be written as

$$\langle v \rangle \frac{\partial n_{\text{HF}}}{\partial z} - D \frac{\partial^2 n_{\text{HF}}}{\partial z^2} = j_{\text{prod}}.$$

Here j_{prod} is the HF production rate per chamber unit length (it is assumed that the cells are directed vertically along the vertical z coordinate axis) and $\langle v \rangle$ is the average gas velocity in the cell.

This equation was solved for chambers with open geometry in different setups: in a 10 cm long chamber under the conditions described in section 5.1.2, in a 40 cm long chamber under the conditions given in section 5.2.2 or in a 2 m long OTR chamber under HERA-B conditions at 40 MHz target interaction rate. The solutions are shown in figure 9.5. The currents in the OTR chambers under HERA-B conditions were found using available experimental data [99].

Due to the strong thermal convection in chambers with an open geometry the concentration of relatively long-lived species in the irradiated cells in the X-ray setup and in HERA-B chambers are comparable despite much higher intensity of irradiation in accelerated aging tests. When using capillaries to control the gas flow, the concentration of long-lived species is much higher. The use of longer chambers leads to a reduction of the diffusion contributing to gas exchange and consequently to more realistic conditions.

Let us return to the discussion about the development of conductivity in the wire-supporting strips (see section 9.4). Usually we observed that wire supporting strips above the irradiated region developed a much higher conductivity than lower ones which is consistent with figure 9.5. However, there are discrepancies. According to figure 9.5, the HF concentration in the boxes and in the irradiated cells of the X-ray setups are comparable. Since the HF concentration in non-irradiated cells should be the same as in the box (we again assume that HF are stable molecules), then, the conductivities of strips in non-irradiated cells and in irradiated cells should be comparable. However, aging tests contradict to these predictions: the strip conductivity in the irradiated cells is much higher than in non-irradiated ones. Also, the conductivity of strips in 10 cm long chambers was much lower than in 40 cm long ones, which does not comply with the HF concentrations shown in figure 9.5. Moreover, in the test “Karlsruhe II” (section 4.6.1) the conductivity of the bottom strips which were 10 cm from the center of the irradiated region was three orders of magnitude higher than that of the upper but remoter strips. Probably, the species responsible for the rise of the strip conductivity (which could be HF) are not long-lived, i.e. the lifetime is considerably shorter than 1 hour (the characteristic time of the gas exchange in the tests and the OTR), or could be absorbed by the cathode foil or by the walls of the box or by other materials.

Besides, long-lived species are not responsible for etching of the anode wire either. According to results presented in section 5.2.2, the wire rupture occurs in the middle of the irradiated region, however, it should occur in the upper part if caused by long-lived species.

9.6 Concluding remarks

According to the presented model for the production of species in a drift chamber under irradiation using Ar/CF₄/CO₂, the following conclusions can be drawn:

- The presence of water can strongly change the outcome of chemical reactions occurring in the chambers during the irradiation. Water can bind fluorine by the formation of HF.
- The species HF is dominantly produced in the avalanche, if the water content is large enough to bind produced F and F₂.
- The concentration of HF was estimated in HERA-B and X-ray setups. The concentration of long-lived species in chambers with open geometry in accelerated aging tests and in the OTR chambers at 40 MHz are comparable. The concentration of long-lived species increases when reducing the gas flow in the cells.
- The HF concentration in chambers with open geometry is of the order of several tens of ppm if HF is long-lived.
- The estimation of the concentration of long-lived species given in this chapter cannot clearly explain the appearance of the strip conductivity and the wire etching effects.

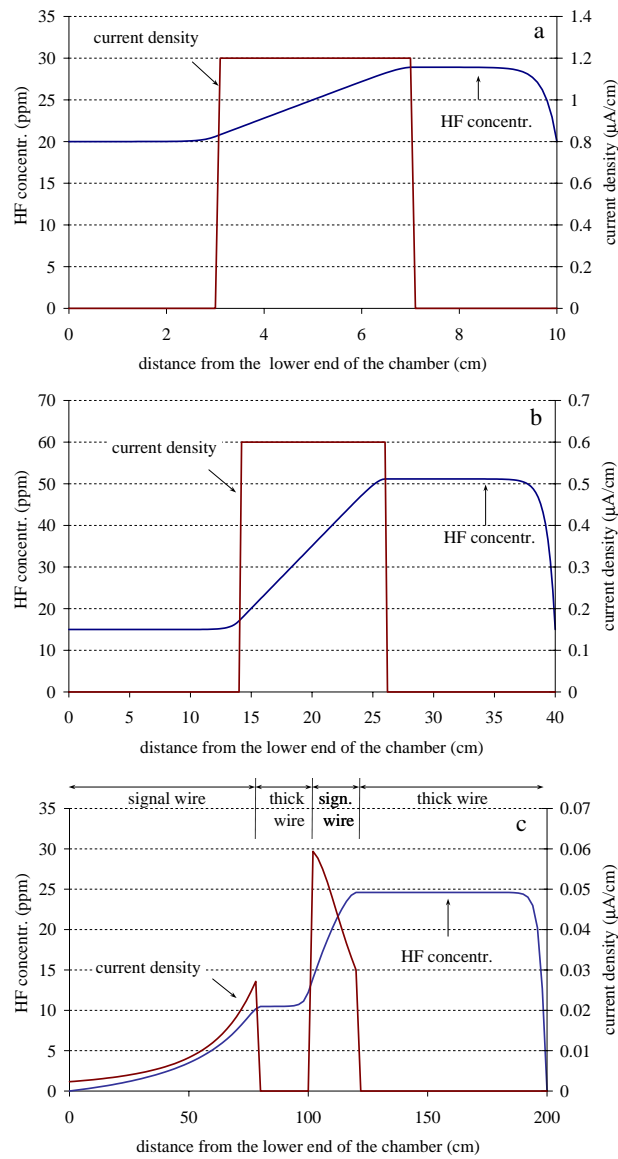


Figure 9.5: Longitudinal concentration profile for HF species in chambers from different setups. The profile, if properly rescaled, can also be applied for other long-lived species. Figures 'a' and 'b' show the HF concentrations in 10 cm long and 40 cm long chambers, respectively (aging tests were described in sections 5.1.2 and 5.2.2). It was estimated that the HF concentration in the box is 20 ppm and 15 ppm in the 'a' and 'b' setups, respectively. For comparison, figure 'c' shows the HF concentration in an OTR chamber at an operation rate of 40 MHz.

Chapter 10

Summary and conclusions

Since its approval, the initial design of the Outer Tracker (honeycomb chambers [47]) had to undergo quite some metamorphosis. All the changes were made on the basis of the extensive aging study program carried out before and after the work on this thesis started. For better clarity this thesis also includes the overview of aging investigation (chapter 4) performed by different groups using different kinds of irradiation facilities. Summaries and conclusions drawn from these aging studies were given at the end of each chapter describing one test series. This chapter summarizes more concisely the main results and achievements.

Malter effect. The first prototypes of honeycomb chambers with soot-enriched Pokalon-C cathode foil and with methane-containing mixtures, (Ar)CF₄/CH₄, showed self-sustaining (Malter-like) currents in hadronic radiation environments after a collected charge of only the order of 1 mC/cm. In table 5.5 the development of the Malter effect in different tests was summarized. The chambers rapidly failed due to the Malter effect in HERA-B, in a 350 MeV/c π /proton beam and in a 100 MeV α -beam whereas they did not clearly show this effect with low energy protons, α -sources or electrons. No indication of this effect was observed with X-rays up to 5 C/cm (corresponding to more than 8 years of operation in the “hottest” Outer Tracker regions). The rapid development of the Malter effect with higher energy hadrons (but not, for example, with an α -source) probably resulted from production of heavily ionizing nuclear fragments which has a lower or no probability by low energy beams.

Anode aging. Clear rapid anode aging with a gain loss rate of the order of 100-1000 $\frac{\%cm}{C}$ was seen with the mixtures CF₄/CH₄ and Ar/CF₄/CH₄ in hadronic environments. When using these mixtures, anode aging was sometimes observed also with X-rays. However, the chambers which were aged during runs with methane-containing mixtures were rejuvenated during irradiation after the mixtures were replaced by Ar/CF₄/CO₂.

Dark current. Strong dark currents ($>0.3 \mu A/cell$) were observed in honeycomb chambers when the humidity of the gas was rather high (>1000 ppm). These dark currents are characteristic for the special chamber design since they

Effect	Conditions	Solution
Malter Effect	CF ₄ /CH ₄ or Ar/CF ₄ /CH ₄ uncoated foil	Ar/CF ₄ /CO ₂ Au-coating
Anode Aging	CF ₄ /CH ₄ or Ar/CF ₄ /CH ₄	Ar/CF ₄ /CO ₂
Dark Current	H ₂ O > 1000 ppm	H ₂ O-control
Anode Etching	H ₂ O < 100 ppm	H ₂ O-control

Table 10.1: *Main changes of the initial parameters introduced according to aging tests.*

are caused by increased conductivity of the wire-supporting FR4 strips, which are indispensable components of the chamber construction. Although the characteristic current-voltage dependence was continuous, it was non-linear. The dark currents increased at the beginning of the irradiation and saturated typically after 0.3 C/cm. The saturated dark current in honeycomb chambers versus humidity was shown in figure 5.56. The results indicate that dark currents arise due to impermanent electrolytic processes caused by ion charge carriers rather than because of a permanent chemical change of FR4. The effect can be explained by the production of HF which reacts with water forming slightly conductive hydrofluoric acid.

Anode etching is potentially very dangerous since it caused wire rupture already after 0.3 C/cm when the counting gas Ar/CF₄/CO₂ was very dry (humidity lower than 100 ppm). The tests aimed at the study of wire etching are summarised in table 5.5. Electron microscopy showed that wires swell (the diameters increase by several percent) and the gold-coating on the wires peels off. Each investigated broken wire ruptured approximately in the center of the irradiated zone of the corresponding cell. The X-ray spectroscopy of heavily etched wires did not reveal any presence of other species except tungsten (and gold) on spots where the gold coating was removed by plasma etching. However, oxygen usually accompanied tungsten if it was deposited (for example, in form of whiskers) above the gold surface of the anode or the cathode. It can be concluded that fluorine is responsible for anode etching since this effect was effectively suppressed by adding some 300 ppm of water. Anode etching correlated with another effect, “transient aging” (which seemed to be not relating to damage of chambers, in fact). The latter effect is a temporary drop of the gain during high rate operation which recovers during irradiation breaks (see also reports [4, 14]). Most likely, this effect is caused by neutral, long-lived ($\tau > 1$ h), electronegative species produced in the avalanche. The effect was considerably reduced (similar to anode etching) when water was added in concentrations of more than 200 ppm. The “transient aging” becomes less pronounced when increasing the flow. The effect probably arises due to the avalanche production of F₂, a very electronegative gas.

New design. Tables 1.3, 1.2 give a list of materials, gas mixture, technology and operating parameters found and validated in the aging tests. Further aging

tests showed that the OTR honeycomb chambers can operate up to 5 C/cm without noticeable degradation of the functional characteristics. The most important changes introduced according to the extensive studies are as follows (see also table 10.1):

- Methane, used as a quencher, was replaced by CO₂, and gold-coating of the cathode was applied. These two changes helped to avoid the Malter effect and anode aging. The corresponding investigations were performed by the HERA-B Outer Tracker group and described in chapter 4.
- Aging tests of gold-coated Pokalon-C chambers with Ar/CF₄/CO₂ did not show a significant gain loss and the Malter effect up to 5 C/cm, but other effects showed up: high dark currents and anode etching. According to the aging tests detailed in sections 4.6.2 and 5.2, the gas moisture has to be controlled: high water content, typically above 1000 ppm, resulted in dark currents due to increasing wire-supporting strip conductivity; conversely, low humidity, of about 100 ppm or below, led to a rapid enhancement of the etching rate of anode wires. However, contradictory results were obtained in another setup reported in [28], where a closed purification gas system as in the Outer Tracker was tested (see a description of the OTR gas system in section 1.3.4): although the water content was measured to be below 20 ppm, no anode etching was observed up to 2.3 C/cm.

Furthermore, it might be worth to mention that in all the tests, carried out in different environments, the shorter chambers showed much higher resistance to irradiation than longer ones. Developments of anode aging, the Malter effect, conductivity of strips, anode etching, etc. were not so pronounced in short 10-15 cm long chambers as in longer 30-100 cm long chambers. As was shown by semiquantitative estimates (section 9.5), this difference can be explained by a very effective gas exchange in short chambers due to higher contributions from diffusion and thermal convection to the total gas exchange in shorter chambers (if the chambers were positioned vertically and had a free gas circulation).

In addition to aging tests, other interesting observations were presented, for example, the wire offset effect on the gas gain and operating stability was measured and described in appendix A.

Besides the aging measurements, there were also made semiquantitative analyses of the counting gas properties, like high electron drift velocity and quenching mechanism (see chapter 2). For a better understanding of the aging results (mainly concerning anode etching and dark currents), production of species in the avalanche, chemistry and concentration of HF (if traces of water are present) were also estimated (see chapter 9).

The wire chamber aging phenomena obviously constitute one the most complex and multifaceted subjects in R&D of particle detectors today. Given insufficient knowledge of the gas composition, an attempt to analyze plasma chemistry in the avalanche turned out to be too negative in this thesis. However, in perspective, aging investigations with a broader application of the latest, highly sensitive

gas-analyzing facilities monitoring the gas composition can be highly rewarding. Indeed, they will advance the predictive power of aging modeling, allow faster and more refined selection of appropriate materials, stimulate the improvement of production technique and thus significantly speed up the development of charged particle detectors capable of operating in unprecedentedly severe irradiation environments.

Appendix A

Study of the eccentricity and wire tension influences on the chamber operation

Setup

To study the effect of wire eccentricity on the chamber operation, two chambers with different constructions were used. One chamber was 12 cm long and had 7 cells. It was constructed to measure eccentricity effects with wires offset in the direction perpendicular to the chamber plane. The offset was changed from 0.06 mm (the half-width of a FR4 strip plus the half-width of the wire) to 1.8 mm by turning the spreading bolts (see figure A.1). All the wires had the standard tension of 50 g. The measurement of the offset was made with an approximate uncertainty of 0.05 mm.

The other chamber was 14 cm long and had 8 wires offset by 0.2 mm in the direction parallel to the chamber plane. The wires had also a standard transverse offset of 0.06 mm because of a non-zero thickness of the FR4 strips. The wire tensions in the chamber are given in table A.1.

The gas gain was found measuring the ratio of peak positions of ^{55}Fe spectra

cell num.	tension, g
1,2	60
3,4	50
5,6	40
7,8	30

Table A.1: *Wire tensions in different cells of the test chamber.*

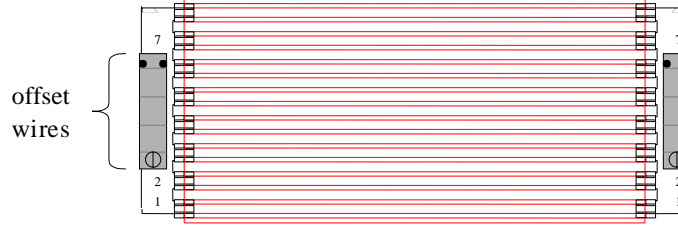


Figure A.1: Chamber with wires offset in the direction perpendicular to the chamber plane.

from offset wires and from reference wires: 1, 2 and 7. Thus any environmental effects, for example, temperature and atmospheric pressure were considerably compensated. The two chambers described above were tested for the following parameters:

parameter	value
gas	Ar/CF ₄ /CO ₂ (65:30:5)
flow	1 vol/h
HV	1700/1750/1800 V

Results

Test with an offset perpendicular to the chamber plane

The eccentricity dependence of the gas gain is shown in figure A.2. It is to be noted that the measurement of the offsets of wires 3 and 4 were made independently. Nevertheless, their curves agree well. This indicates that the method used in this test gives correct and rather precise measurements of the offset dependence of the gain. Because of some difficulties in measuring the offsets of wires 5 and 6, their values are not shown in the figure.

The offset was increased until reaching unstable operation. Thus the most right points in the figure correspond to the maximal offsets at yet stable operation. The difference in the maximal “safe” offsets of wires 3 and 4 could result from different production qualities of the wires and cells.

In addition, the offset dependence of the gain can be calculated employing the fact that the gain G only depends on the charge q of a wire in a cylinder,

$$G = f(q) = f(CU)$$

where C is the capacity of the wire in the cylinder and U the voltage applied between the wire and the cylinder. Then, a relative increase in the capacity due to a deviation of the wire position from the center is equivalent to a relative increase in the voltage. Using the empirical voltage dependence of the gain (see section

B.1) and the formula for the capacity of a wire with a radius r_1 and a length l offset by a distance d inside the cylinder with a radius r_2 , we obtain:

$$C = \frac{2\pi\epsilon_0 l}{\log(x + \sqrt{x^2 - 1})}$$

where

$$x = \frac{1}{2} \left(\frac{r_1}{r_2} + \frac{2(r_2^2 - d^2)}{r_1 r_2} \right)$$

The prediction is also shown in figure A.2 (solid line).

In figure A.3, the results were compared with the tests made in ATLAS [25]: straws with a diameter of 4 mm, 30 μm wire, gas = Ar/CF₄/CO₂ (63:22:15), HV = 1547 V. As can be seen, the ATLAS curve rises slightly faster (probably because of the smaller diameter of the cells).

An increase in the relative width of the ADC spectra was not observed except for very big offsets. For example, figure A.4 shows a typical spectrum from wire 4 without offset and at an offset of 1.5 mm. According to this figure, the spectrum measured at an offset of 1.5 mm is wider by 25%.

Test with an offset parallel to the chamber plane

Figure A.5 shows ⁵⁵Fe peak positions from different cells with different wire tensions. Neither a HV instability nor wire tension dependence of the gain was observed in the test. From the very beginning wire 8 showed dark pulses, which are presumably a result of a production defect. Despite a lateral offset of 0.2 mm we did not observe any increase in the gain relative to that of a standard chamber.

Conclusion

The following conclusion can be drawn for the obtained results:

- a good agreement between the measurement and the prediction observed up to an offset of 1.2 mm;
- stable operation was possible up to an offset of 1.3 -1.8 mm and a gain increase by a factor of 3.

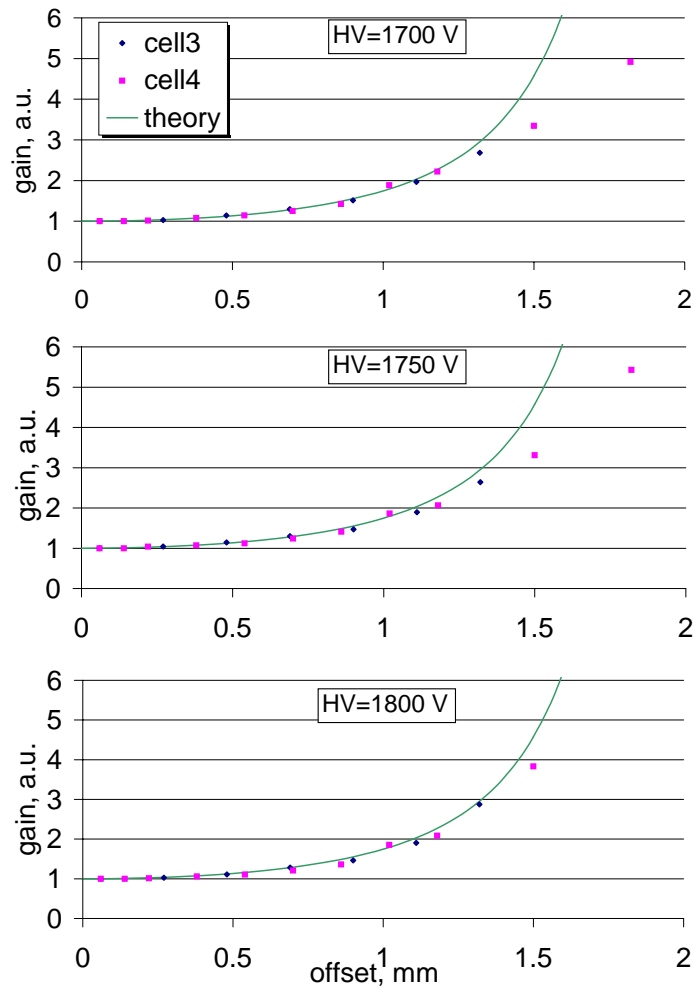


Figure A.2: Gas gain as a function of the wire offset in the direction perpendicular to the chamber plane.

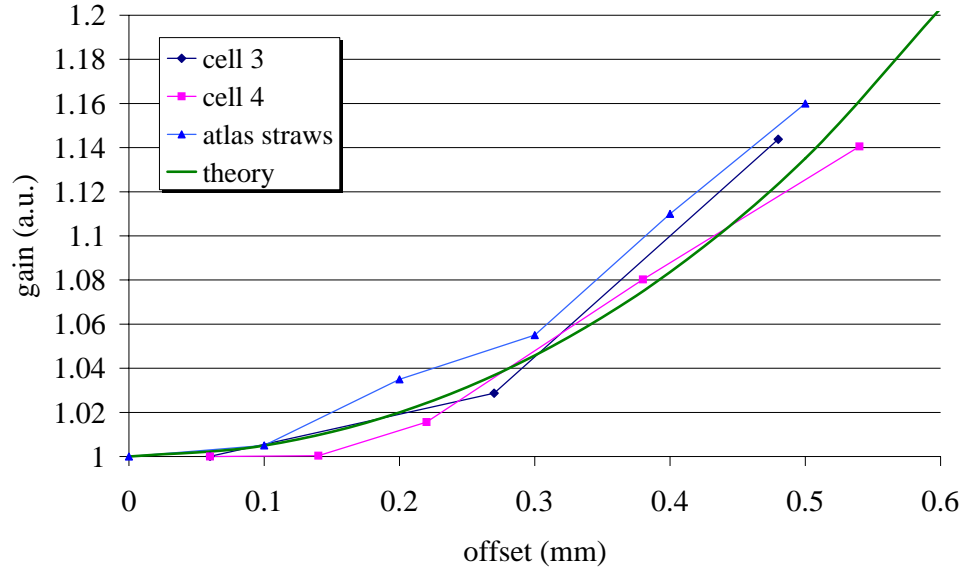


Figure A.3: Offset dependence of the gas gain obtained for 1750 V in comparison with ATLAS straws.

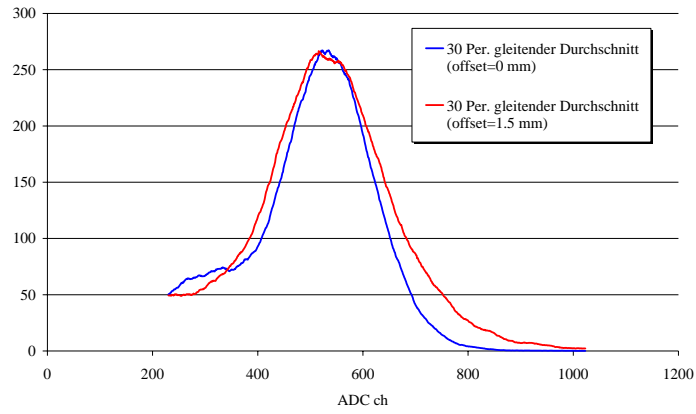


Figure A.4: Moving average from ADC spectra at no offset and at an offset of 1.5 mm.

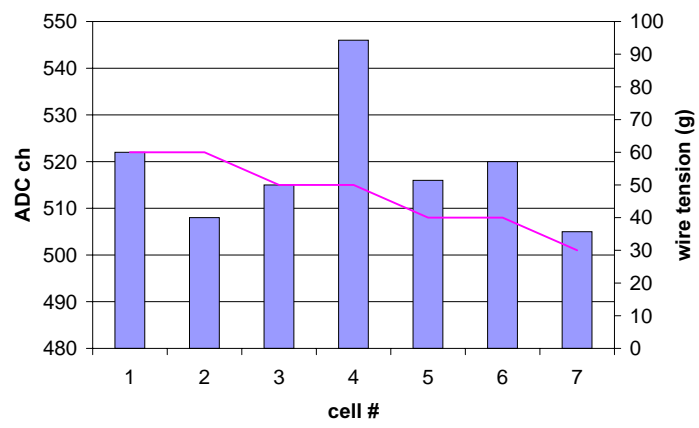


Figure A.5: ^{55}Fe peak positions in cells with different wire tensions.

Appendix B

Useful tests

B.1 Gas gain and counting characteristic in the gas Ar/CF₄/CO₂

Before making an aging test we measured the HV dependence of the current both with X-ray radiation at a minimal intensity of the tube and with an α -source. The gain was calculated dividing the anode current by the ionization current. The results are shown in figure B.1.

As the figure shows, a gas gain measured with X-rays (the ionization current was about 1.3 pA/cm) at 1700 V was $\approx 3 \times 10^4$. If irradiating with an α -source (the ionization current was about 80 pA/cm) the space charge reduced the gas gain by a factor of about 7 owing to the space charge.

The HV dependence of the counting rates measured with the α -source at different thresholds are shown in figure B.2. The counting rate curve measured with the α -source had a well pronounced plateau at the rate of 39000 counts/s.

From these data we can estimate the ionization made by an α -particle in the cell:

$$\frac{200 \times 10^{-12} \text{ A}}{(39000 \text{ Hz})(1.6 \times 10^{-19} \text{ C})} \approx 3.2 \times 10^4 \quad \text{ion pairs.}$$

The energy loss of an 4.5 MeV α -particle in the gas Ar/CF₄/CO₂ (65/30/5) was calculated with the Bethe-Bloch formula using experimental data for argon and CO₂ in [92] and for CF₄ in [24]. The results are shown in figure B.3. As can be seen, an α -particle loses about 700 keV within first 5 mm of its trajectory. The energy $W \approx 30.2$ eV is required to produce an electron-ion pair in the mixture Ar/CF₄ (66/34) by an α -particle [86]. If we use this value of W , we obtain that an 4.5 MeV α -particle should produce ionization of about $(700 \times 10^3 \text{ eV})/30.2 \text{ eV} \approx 2.3 \times 10^4$ electron-ion pairs in a 5 mm cell.

The difference between estimated and measured values can have different reasons and a discussion of them goes beyond the frame of this thesis.

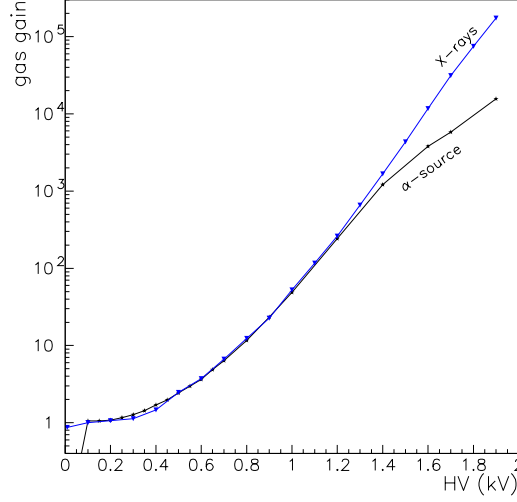


Figure B.1: Gas gains in $\text{Ar}/\text{CF}_4/\text{CO}_2$ (65:30:5) in 5 mm cells measured with X-rays and with an α -source as functions of voltage.

B.2 Gas gain in Ar/CO_2

Before starting aging test with Ar/CO_2 (see section 7), we measured the HV dependence of the gas gain. The results are shown in figure B.4.

According to the figure, the gain of $\approx 3 \times 10^4$ measured with X-rays for the minimum ionization current of 1.3 pA/cm obtained from the tube corresponds to the HV of 1400 V. The aging tests using Ar/CO_2 was made at this high-voltage.

B.3 Measurement of the cathode heating

Since convection is caused by temperature differences, it is instructive to measure an increase in the cathode temperature caused by currents in the chambers. Using this measurement, we estimated the gas flow in the open cells in section 9.5.1. Because the gas gain is very sensitive to the cathode temperature, we can find the cathode temperature measuring the current development after the start of irradiation.

We used the same setup as described in section 5.1.2. Figure B.5 shows the current development with different time scales and the time evolution of the box temperature. As can be seen on the short-scale diagram, the current, being about $13.5 \mu\text{A}$ in the gold-plated chamber and $13.2 \mu\text{A}$ in the uncoated cathode chamber at the very beginning, increased saturating on a level higher by about 15% than

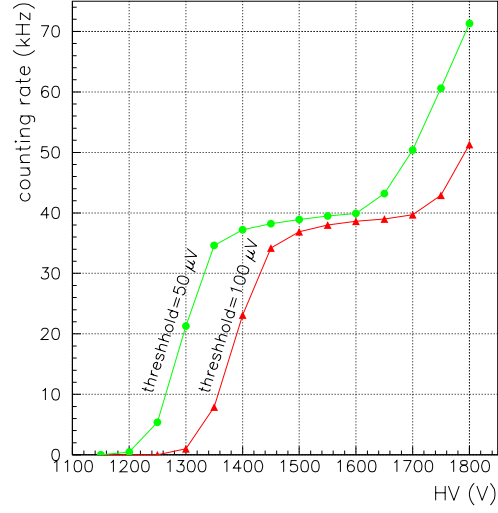


Figure B.2: Counting rate characteristic measured with an α -source. The flat parts of the curves are referred to as plateaus. Below the plateau not all the ionizing particles are counted due to an insufficient gas gain, above the plateau noise and secondary avalanches start contributing to the counting rate.

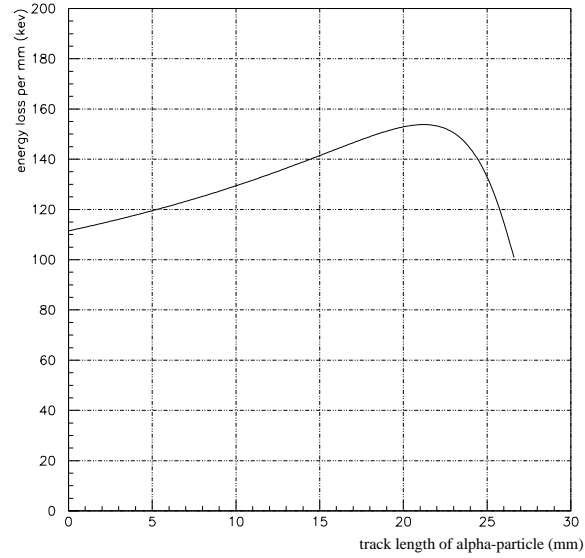


Figure B.3: Energy loss of an α -particle with an energy of 4.5 MeV in the gas $\text{Ar}/\text{CF}_4/\text{CO}_2$ calculated with the Bethe-Bloch formula.

the initial value with a time constant of about 1.5 minutes. In the middle diagram we see that the current continued increasing with a time constant of about 100 minutes correlating with an increase in the box temperature. We interpret the first fast increase in the current as a result of the cathode warming and the long-term current increase as a result of the box warming. Indeed, it is not difficult to estimate that the time constant for the temperature change of the cathode foil should be approximately 1.5 minutes (and that of the gas inside the cell about 10 s). Using the temperature dependence coefficient of the current obtained from the middle and the lowest diagram, we obtained that the increase in the temperature is approximately 5-6 °C.

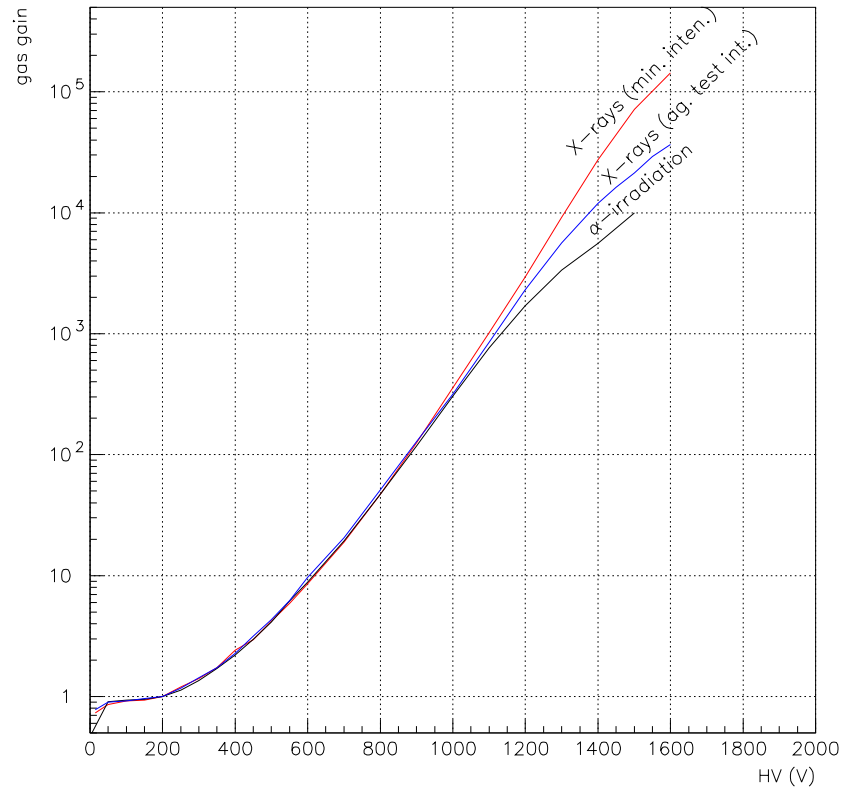


Figure B.4: Gas gain in the mixture Ar/CO_2 (80:20) in 5 mm cells as a function of HV measured at different irradiation intensities and with different types of radiation. The gain reduction when irradiating with an α -source was caused by the high local space charge resulting from the high local ionization density produced by α -particles.

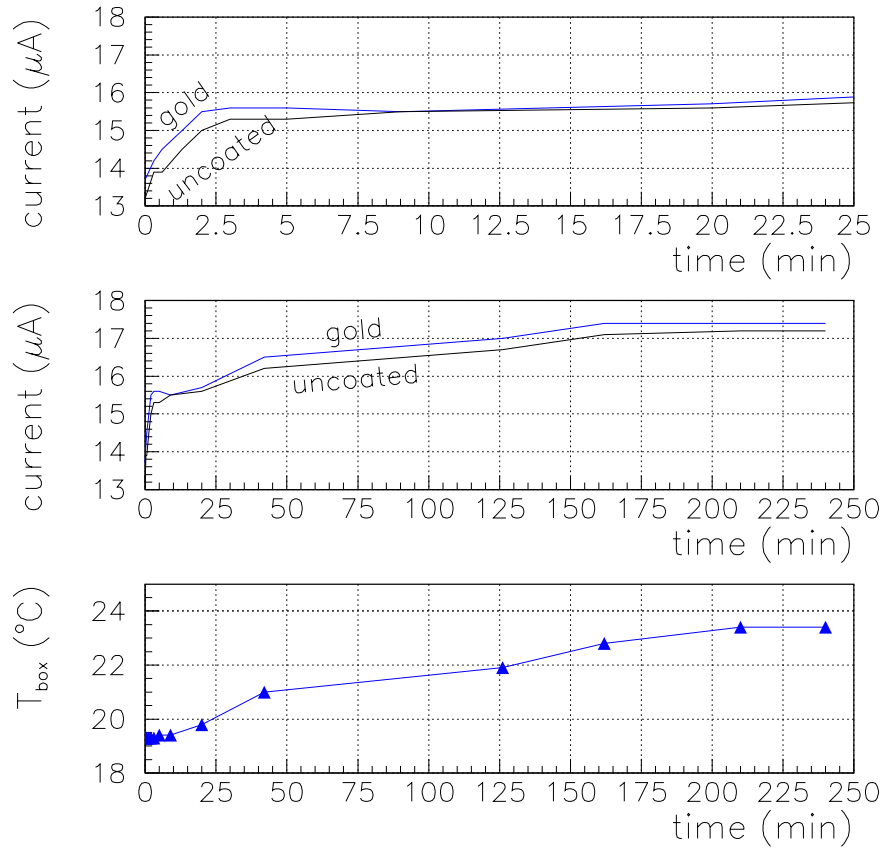


Figure B.5: Currents in the gold-plated chamber (red line) and in the uncoated chamber (green line) just after the beginning of the irradiation in a short-time scale (at the top) and in a long-time scale (in the middle) and the box temperature (at the bottom).

Bibliography

- [1] The columbia encyclopedia, 2001. <http://www.bartleby.com>.
- [2] G. Alexeev et al. *Technical Design Report for the D0 Forward Muon Tracking Detector Based on Mini-Drit Tubes*, 1997. D0 Note 3366.
- [3] ATLAS Collaboration. *The ATLAS Technical Proposal for a general Purpose pp Experiment at the Large Hadron Collider at CERN*, 1994. CERN/LHCC/94-43.
- [4] ATLAS Collaboration. *ATLAS Inner Detector Technical Design Report*, 1997. CERN/LHCC/97-17 ATLAS TDR.
- [5] F. Bakker et al. *Nucl. Instr. Meth.*, A(330):44–54, 1993.
- [6] K. H. Becker. *Electron Collision with Molecules, Clusters, and Surfaces*. Plenum, New York, 1994.
- [7] K. Berkhan et al. Large system experience with the asd-8 chips in the hera-b experiment. In *Proceedings of the 5th Snowmass Workshop on Electronics for LHC*, 1999. CERN-99-09.
- [8] L. Boesten et al. *J. Phys.*, B(25):1607, 1992.
- [9] G. Bohm. private communications.
- [10] G. Bohm and A. Schreiner. *Correlation Report*, 2001. HERA-B-01-003.
- [11] R. A. Bonham. *Jpn. J. Appl. Phys.*, (33):4157, 1994.
- [12] C. Brundle et al. *J. Chem. Phys.*, (53):2196, 1970.
- [13] B. R. Bulos and A. V. Phelps. *Phys. Rev.*, A(14):615–629, 1976.
- [14] M. Capeans. *Nucl. Instr. Meth.*, A(337):122–126, 1993.
- [15] M. Capeans et al. *Nucl. Instr. Meth.*, A(446):317, 2000.
- [16] M. Capeans, C. Padilla, and C. Stegmann. *Module Production Guide*, 1998. HERA-B internal note.

- [17] G. Charpak et al. *Nucl. Instr. Meth.*, A(99):279–284, 1972.
- [18] L. G. Christophorou et al. *Nucl. Instr. Meth.*, A(309):160–168, 1991.
- [19] D. W. Clegg and A. A. Collyer, editors. *Irradiation effects on polymers*. Elsevier Applied Science, London and New York, 1991.
- [20] G. R. Cook. *J. Chem. Phys.*, (43):1794, 1965.
- [21] L. G. Cristophorou. *Atomic and Molecular Radiation Physics*. Wiley, 1971.
- [22] L. G. Cristophorou. *Electron-Molecular Interactions and their Applications*. Academic Press, 1984.
- [23] L. G. Cristophorou et al. *Nucl. Instr. Meth.*, (163):141, 1979.
- [24] L. G. Cristophorou, J. K. Olthoff, and M. V. Rao. *J. Phys. Chem. Ref. Data*, (25):1341, 1996.
- [25] P. Cwetanski, A. Romaniouk, and V. Sosnovtsev. *Studies of wire offset effects on gas gain in the ATLAS TRT straw chamber*, 2000. ATL-INDET-2000-016.
- [26] M. Danilov et al. *Study of Drift Chamber Aging with Propane*, 1988. DESY 88-090.
- [27] M. Danilov et al. *Aging tests of the proportional wire chambers using Ar/CF₄/CH₄ (74:20:6), Ar/CF₄/CH₄ (67:30:3), Ar/CF₄/CO₂ (65:30:6) mixtures for HERA-B Muon Detector*, 2000. ITEP 43-00.
- [28] K. Dehmelt. *Reinigung eines zähl-gases mit cf₄ für das äußere spurkammer-system bei hera-b unter hoher strahlenbelastung*. Master’s thesis, Universität Hamburg, 1999.
- [29] R. W. Ditchburn. *Proc. Roy. Soc.*, A(229):44, 1955.
- [30] R. Donaldson and M. Gilchriese, editors. World Scientific, Singapore, 1990.
- [31] C. Duncan and I. Walker. *J. Chem. Soc. Faraday Trans.*, II(68):1800, 1972.
- [32] C. Duncan and I. Walker. *J. Chem. Soc. Faraday Trans.*, II(70):577, 1974.
- [33] K. M. Ecklund et al. *Etching of copper coated Mylar tubes with CF₄ Gas*, 1996. SLAC-PUB-7175G.
- [34] D. Edelson and D. L. Flamm. *J. Appl. Phys.*, (56):1522, 1984.
- [35] A. Ehrich. *Chem. Technik.*, (45):236–238, 1988.
- [36] J. S. Escher. *Semiconductors and semimetals*, (15):195, 1981.

- [37] T. Ferguson et al. *Aging Investigation of CMS EMU Prototype Chambers*, 1999. CMS Note 1999/011.
- [38] B. Foster. Workshop on radiation damage of wire chambers. In *LBL Workshop* [69], pages 227–229, 313. LBL-21170.
- [39] T. Fox. Gasanalyse für das äußere spurkammersystem des hera-b experimentes. Master's thesis, Universität Rostock, 1999.
- [40] J. Friedland et al. *Rev. Sci. Instr.*, (24):109, 1953.
- [41] L. S. Frost and A. Phelps. *Phys. Rev.*, A(136):1538, 1964.
- [42] F. R. Gilmore. *J. Quant. Spectr. Rad. Trans.*, (5):369, 1965.
- [43] I. S. Grigoriev and E. Z. Meilikhov. *Handbook of physical quantities*. Kurchatov Institute, Moscow, 1997.
- [44] O. Grimm. Driftgeschwindigkeit- und signalverstärkungsmessungen für das äußere spurkammersystem des hera-b detektors. Master's thesis, Universität Hamburg, 1998.
- [45] H.-B. O. T. Group. Archive of the otr meetings and the otr newsgroup, 1997-1998.
- [46] F. Guarino et al. *Outgassing studies of materials for the TRT construction*, 1999. ATL-INDET-99-011.
- [47] E. Hartouni et al. *HERA-B Design Report*, 1995. DESY-PRC 95/01.
- [48] B. Hasse et al. *Vakuum in Forschung und Praxis*, (3):181–185, 1997.
- [49] A. P. Heinson and D. Rowe. *Nucl. Instr. Meth.*, A(321):165, 1992.
- [50] HERA-B Collaboration. *HERA-B Report on Status and Prospects October 2000*, 2000. DESY PRC 00/04.
- [51] G. Herzberg. *Molecular Spectra and Molecular Structure. II. Infrared and Raman Spectra of Polyatomic Molecules*. Van Nostrand Reinhold, New York, 1945.
- [52] D. Hess. Workshop on radiation damage of wire chambers. In *LBL Workshop* [69], pages 15–23. LBL-21170.
- [53] H. Hilke et al. *Nucl. Instr. Meth.*, (217):298, 1983.
- [54] K. Hoepfner et al. *Status report: HERA-B Outer Tracker Chambers Based on Straws Tubes*, 1999. HERA-B 99-182.
- [55] M. Jibaly et al. *Nucl. Instr. Meth.*, A(283):692–701, 1989.
- [56] W. E. Jones and E. G. Skolnik. *J. Chem. Rev.*, (76):563–592, 1976.

- [57] I. Juricic and J. A. Kadyk. *IEEE Trans. Nucl. Sci. NS-34*, 1:481, 1987.
- [58] J. A. Kadyk. *Nucl. Instr. Meth.*, A(300):436, 1991.
- [59] J. A. Kadyk et al. *Nucl. Instr. Meth.*, A(300):511–517, 1991.
- [60] L. J. Kieffer. *A Compilation of Electron Collision Cross-Section Data for Modeling Gas Discharge Lasers*, 1973. JILA COM-74–11661.
- [61] I. Knunjanz, editor. *Chimitcheskii Enziklopeditcheskii Slovar*. 1983. in Russian.
- [62] H. Kobayashi et al. *Macromolecules*. Number 7. 1974.
- [63] H. Kolanoski. Investigation of aging in the hera-b outer tracker drift tubes. to be published in the Proceedings.
- [64] H. Kolanoski. private communications.
- [65] M. Kollefrath et al. *Nucl. Instr. Meth.*, A(419):351, 1999.
- [66] A. Krivchitch. Oxygen and the anode wire swelling under the high accumulated dose, 2001. talk presented at Vienna Conference of Instrumentation.
- [67] K. Kuroki, D. Spence, and M. Dilon. *J. Chem. Phys.*, (96):6318, 1992.
- [68] M. Kushner. *J. Appl. Phys.*, (53):2923, 1982.
- [69] Lawrence Berkeley Laboratory. *Workshop on Radiation Damage of Wire Chambers*, 1986. LBL-21170.
- [70] S. A. Lawton and A. V. Phelps. *J. Chem. Phys.*, (69):1055–1068, 1978.
- [71] L. C. Lee et al. *J. Chem. Phys.*, (67):1237, 1977.
- [72] T. Lohse et al. *HERA-B an Experiment to Study CP Violatio in the B System Using an Internal Target at the HERA Proton Ring. Porposal*, 1994. DESY-PRC 94/02.
- [73] L. Malter. Thin film field emission. *Phys. Rev.*, (50):48, 1936.
- [74] A. Mann and F. Linder. *J. Phys.*, B(25):533, 1992.
- [75] D. M. Manos et al. *Plasma Etching*. Academic, Boston, 1989.
- [76] K. Martens et al. *Nucl. Instr. Meth.*, A(343):258–262, 1994.
- [77] C. E. Melton et al. *Phys. Rev.*, (96):673, 1954.
- [78] H. Milloy and R. Watts. *Aust. J. Phys.*, (30):73, 1977.
- [79] R. Mir et al. *Study of Straw Chamber Lifetime with Argon Ethane*, 1989. SLAC-PUB-4857, UWSEA PUB 89-02.

- [80] A. P. Modica and S. J. Sillers. *J. Chem. Phys.*, (48):3283, 1968.
- [81] C. J. Mogab. *J. Appl. Phys.*, (49):3796, 1978.
- [82] S. Motlagh and J. Moore. *J. Chem. Phys.*, (109):432, 1998.
- [83] R. Openshaw. *IEEE Transaction of Nuclear Science*, 36(1), 1989.
- [84] R. Openshaw et al. *Nucl. Instr. Meth.*, (307):298, 1991.
- [85] D. Rapp and W. E. Francis. *J. Chem. Phys.*, (37):2631–2645, 1962.
- [86] G. F. Reinking et al. *J. Appl. Phys.*, (60):449, 1986.
- [87] M. B. Robin. *Higher Excited States of Polyatomic Molecules*, volume I. Academic, New York, 1974.
- [88] A. Romaniouk. private communications.
- [89] A. Romaniouk. *Choice of Materials for the Construction of the TRT*, 1998. ATL-INDET-98-211.
- [90] O. P. Rustgi. *J. Opt. Soc. Am.*, (54):464, 1964.
- [91] J. A. R. Samson. *J. Opt. Soc. Am.*, (55):420, 1964.
- [92] F. Sauli. *Principle of operation of multiwire proportional and drift chambers*, 1977. CERN 77-09.
- [93] F. Sauli. *When everything was clear*, 1986. CERN-EP/86-24.
- [94] B. Schmidt and S. Polenz. *Nucl. Instr. Meth.*, A(273):488, 1988.
- [95] U. Schwanke. Aufbau und durchführung von testexperimenten mit waben-driftkammern für das hera-b experiment. Master’s thesis, Humboldt-Universität zu Berlin, 1996.
- [96] H. Sipila et al. *Nucl. Instr. Meth.*, (217):282, 1983.
- [97] B. M. Smirnov. *Uspekhi fizicheskikh nauk*, (121):231, 1977. in Russian.
- [98] B. M. Smirnov. *Excited atoms*. Energoatomizdat, Moscow, 1982. in Russian.
- [99] C. Stegmann. private communications.
- [100] T. D. Strickler. *J. Chem. Phys.*, (41):1783–1789, 1964.
- [101] K. Tachibana and A. V. Phelps. *J. Chem. Phys.*, (71):3544–3546, 1979.
- [102] Y. Tanaka. *J. Opt. Soc. Am.*, (48):304, 1958.
- [103] W. E. S. Unger et al. *Materialprüfung*, 37:233–237, 1995.

- [104] U. Uwer et al. *Aging of Gaseous Detectors*, 1999. HERA-B-99-065.
- [105] D. D. V. Bezzubov. *Gas contamination after passing through various types of flexible plastic tubes*, 1995. D0 Note 1524.
- [106] J. Va'vra. *Nucl. Instr. Meth.*, A(252):547, 1986.
- [107] M. Walter. private communications.
- [108] H. Winters. *J. Chem. Phys.*, (63):3462–3466, 1975.
- [109] H. Winters. *Chem. Phys.*, (36):353–364, 1979.
- [110] H. F. Winters and M. Inokuti. *Phys. Rev.*, A(25):1420, 1982.
- [111] J. Wise et al. *A Chemical Model for Wire Chamber Aging in CF_4/iC_4H_{10} , Gases*, 1992. LBL-32895.
- [112] T. Zeuner et al. *Nucl. Instr. Meth.*, A(446):325, 2000.

Lebenslauf

Name:	Alexander Schreiner
9/1986 - 06/1993	Studium an der Universität in Nowosibirsk in der Fachrichtung Physik
06/1991 - 06/1993	Wissenschaftliche Mitarbeit
08/1993-02/1994	Weltraumforschungsinstitut, Kirgisistan
08/1993	Entwicklung von Mikrostreifen-Gasdetektoren für Satelliten beim KEDR Experiment in Nowosibirsk
5/1998 - 12/2001	Wissenschaftliche Mitarbeit beim HERA-B Experiment in Zeuthen

Selbständigkeitserklärung

Hiermit erkläre ich, die vorliegende Arbeit selbständig ohne fremde Hilfe verfaßt zu haben und nur die angegebene Literatur und Hilfsmittel verwendet zu haben.

Alexander Schreiner
5. Juli 2001